"High temperature thermoelectric transport in quaternary copper selenides and ternary Zintl-antimonides"

Dissertation

zur Erlangung des akademischen Grades
"Doktor der Naturwissenschaften"

am Fachbereich Chemie,
Pharmazie und Geowissenschaften der

Johannes Gutenberg-Universität Mainz

Wolfgang G. Zeier
geboren in Bad Brückenau

Mainz 2013

Dekan: [redacted]

1. Berichterstatter [redacted]

2. Berichterstatter [redacted]

Tag der mündlichen Prüfung: 29/05/2013

Für meine Familie

Die experimentellen Arbeiten, die dieser Arbeit zugrunde liegen, wurden in dem Zeitraum vom 1. Oktober 2010 bis 1. Februar 2013 unter der Leitung von [redacted] an der *Johannes Gutenberg-Universität Mainz* und [redacted] durchgeführt.

The work for this thesis was carried out at the *Johannes Gutenberg-Universität Mainz* and the *California Institute of Technology* in the period between October 1st 2010 and February 1st 2013, under the guidance of [redacted] and [redacted].

Publications

1. Heinrich C.P., Day T., **Zeier W.G.**, Snyder G.J., Tremel W., "Anion substitution induced point defect scattering in the thermoelectric solid solution $Cu_2ZnGeSe_{4-x}S_x$" *in preparation*

2. **Zeier W.G.**, Pei Y., Day T., Schechtel E., Heinrich C.P., Kieslich G., Snyder G.J., Tremel W., "Influence of the chemical potential on the carrier effective mass in the thermoelectric solid solution $Cu_2Zn_{1-x}Fe_xGeSe_4$" *in preparation*

3. **Zeier W.G.**, Heinrich C.P., Day T., Panithipongwut C., Kieslich G., Snyder G.J., Tremel W., "Bond strength dependent electronic phase transformation in the solid solution $Cu_2ZnGeSe_{4-x}S_x$" *in preparation*

4. Kieslich G., Veremchuck I., Antonyshyn I., **Zeier W.G.**, Birkel C.S., Weldert K., Heinrich C.P., Visnow E., Panthöfer M., Burkhard U., Grin Y., Tremel W., "Using crystallographic shear to reduce lattice thermal conductivity: high temperature thermoelectric characterization of the spark plasma sintered Magneli phases $WO_{2.90}$ and $WO_{2.722}$" *Energy Environ. Sci. - submitted*

5. **Zeier W.G.** Pei Y., Pomrehn G., Day T., Heinz N., Heinrich C.P., Snyder G.J., Tremel W., "Phonon scattering through a local anisotropic structural disorder in the thermoelectric solid solution $Cu_2Zn_{1-x}Fe_xGeSe_4$" *J. Am. Chem. Soc. - Article ASAP* doi:10.1021/ja308627v

6. Zevalkink A.*, **Zeier W.G.***, Pomrehn G.*, Schechtel E., Tremel W., Snyder G.J., "Thermoelectric transport properties of Sr_3GaSb_3 - A chain based Zintl compound" *Energy Environ. Sci.* **2012**, 5, 9121-9128 doi:10.1039/C2EE22378C (*equal contribution authors)

7. Birkel C.S., **Zeier W.G.**, Douglas J., Lettiere B., Mills C.; Seward G., Birkel A., Snedaker M., Zhang Y., Snyder G.J., Pollock T., Seshadri R., Stucky G., "Rapid microwave preparation of thermoelectric TiNiSn and TiCoSb half-Heusler compounds" *Chem. Mater* **2012**, 24, 2558-2565 doi:10.1021/cm3011343

8. **Zeier W.G.***, Zevalkink A.*, Schechtel E., Tremel W., Snyder G.J., "Thermoelectric properties of Zn-doped Ca_3AlSb_3" *J. Mater. Chem.* **2012**, 22, 9826-9830 doi:10.1039/C2JM31324C (*equal contribution authors)

9. **Zeier W.G.**, LaLonde A., Gibbs Z.M., Heinrich C.P., Panthöfer M., Snyder G.J., Tremel W., "Influence of a nano phase segregation on the thermoelectric properties of the p-type doped stannite compound $Cu_{2+x}Zn_{1-x}GeSe_4$" *J. Am. Chem. Soc.* **2012**, 134, 7147-7154 doi:10.1021/ja301452j

10. **Zeier W.G.**, Panthöfer M., Janek J., Tremel W.,Thermoelektrische Verbindungen. Strom aus Abwärme" *Chem. Unserer Zeit* **2011**, 45, 188-200 doi:10.1002/ciuz.201100393

11. Zevalkink A., Toberer E.S., **Zeier W.G.**, Flage-Larsen E., Snyder G.J., "Ca_3AlSb_3: an inexpensive, non-toxic thermoelectric material for waste heat recovery" *Energy Environ. Sci.* **2011**, 4, 510-518 doi:10.1039/C0EE00517G

12. **Zeier W.G.**, Roof I.P., Smith M.D., zur Loye H.-C., "Crystal growth of Ln_3GaO_6 (Ln = Nd, Sm, Eu and Gd): Structural and optical properties" *Solid State Sci.* **2009**, 11, 1965-1970 doi:10.1002/chin.201005015

13. Roof I.P., Jagau T.-C., **Zeier W.G.**, Smith M.D., zur Loye H.-C., "Crystal growth of a new series of complex niobates, $LnKNaNbO_5$ (Ln = La, Pr, Nd, Sm, Eu, Gd, and Tb): Structural properties and photoluminescence" *Chem. Mater.* **2009**, 21, 1955-1961 doi:10.1021/cm9003245

Acknowledgments

First of all I have to thank Prof. Dr. [redacted] for everything he has done for me during my time as an undergrad and during grad school. I doubt that anything that I have experienced in the last years would have been possible without him. I could not have asked for a better boss in terms of academic and mentoring support. Thank you for always sending me abroad for more research, for letting me conduct the research for my thesis with [redacted], and giving me the space for my research, while being there with support and advice, whenever I needed it. There are no words to express my gratitude and appreciations. Thank you!

To my research advisor, Dr. [redacted]. It has been a pleasure to work with you and I appreciate the way I was adopted as a visiting grad student. Research at Caltech has been a lot of fun, due to a perfect mixture of motivation, knowledge, and funny discussions about just anything. I have learned more about thermoelectrics and myself than I could have ever imagined. Thank you for always trying to push me in any way possible for you. Thank you for everything!

To the [redacted] group I want to say thank you for being a lot of fun. Thank you, [redacted], for making me enjoy synthesis at home. Sharing a glove box and collaborating with you has been fun and very productive as well. I am glad that we met in our first year, we would not stand where we are now, if we hadn't. I have to thank [redacted] for all the fruitful discussions and all the ranting with me. Thank you Dr. [redacted] for all the help and support I got from you. Especially the initial work on the powder consolidation and all of out discussions about thermoelectrics and soccer. [redacted], [redacted], and [redacted], thanks for the fun in the office and definitely the fun during all the nights we spent out partying. Together with Dr. [redacted] I couldn't have asked for better friends in Mainz. Also thanks to Dr. [redacted] for helping me find a post doc position and for the fruitful collaborations we had. I would like to thank Dr. [redacted] for his initial help with the structural refinements and understanding X-ray refinements. Many thanks to [redacted] for the help with some of the sample preparations. I also have to thank [redacted] for her help with the differential scanning calorimetry in Mainz.

I also want to thank everyone in the [redacted] group for putting up with a sometimes obnoxious and loud german. I have enjoyed working with everyone of you and I will always remember the good nights and group meetings with a lot of beer. I will miss working with you guys. I have to thank [redacted] for our collaboration within the Zintl project. It was a lot of fun, I learned a lot from you, and I think we were a good team. I will always appreciate having been able to work with you. Thank you for the Hall measurements at Jet Propulsion Laboratory, whenever they were necessary. [redacted], you have been a great friend for all these years and I will miss you. I have to thank you for helping me with the Scanning Electron Microscopy but your being around was more important. I would like to thank Dr. [redacted] and [redacted] for their help with the hot press and instruments. [redacted], I always had a lot of fun hanging out with you and I am very happy to call you my

friend. I am very grateful for Dr. [redacted] and [redacted] help with understanding and modeling thermal transport. Furthermore I have to thank Dr. [redacted] for leaving me some of his figures on PbTe and band engineering for this thesis. I will miss spicy lunch! Thank you, [redacted], for the help with the band gap measurements. Special thanks to [redacted] for performing the band structure calculations, which have been very helpful to understand the transport properties of these materials. I also have to thank Dr. [redacted] and Prof. Dr. [redacted], I have learned a lot from you guys during my first stay at Caltech in 2010. Thank you [redacted] for everything, including the help with the high temperature XRD stage. It has been a pleasure to work with so many intelligent scientists. I also want to thank Prof. Bill Johnson, who provided the equipment for the ultrasonic measurements of the samples.

I want to thank the Carl-Zeiss foundation for the fellowship and with it the financial support during my time as a Ph.D. student. This fellowship helped me to be more independent in my research. Furthermore I want to thank the Graduate School of Excellence "MAterials Science IN MainZ" (MAINZ) and their financial support through the Excellence Initiative (DFG/GSC 266), which has made it possible to attend conferences and summer schools. Especially the support for the flights to Pasadena has been very helpful for this thesis. I also have to thank the Jet Propulsion Laboratory, National Aeronautics and Space Administration, for their financial support within the Zintl project and for providing measurement time whenever it was needed. Many thanks to Dr. [redacted] for discussions and all the help and advice you gave me. Furthermore I want to thank [redacted], Dr. [redacted] and Dr. [redacted], who always helped me with any issues regarding paperwork and MAINZ.

Finally, my family and friends have to be acknowledged. My parents have always supported me during my studies and my Ph.D., and the financial and mental support during this time made this thesis possible. Thank you for always being supportive of all the crazy travels and times I have gone through. I doubt this will end. I will always be grateful for everything you two have done for me. My sister [redacted], you have always been there for me whenever I needed an advice or just someone to listen to, also my brother-in-law [redacted], and especially my cute nephew [redacted]. I love you guys. Thank you [redacted] for being a great roommate and awesome friend in Mainz. Meeting you in my first week in Mainz in 2005 made this time of my life a very good one. Thanks for putting up with all my problems and rants in the last years. I wish you and [redacted] a happy life and I will always be around to somehow give back what you guys gave me in the last years! Dr. [redacted] all these years would have been less fun without us teaming up, I can't express how much I appreciate my time in Mainz with you. [redacted] and [redacted], I think we were all an awesome team during our studies and I am very happy to have met you guys. Of course thanks to all the other great people that I have met in Mainz. I will always look back to the time with you guys and smile. Thank you Dr. [redacted], [redacted], [redacted], Dr. [redacted], and Dr. [redacted] for being such great roommates in Pasadena. Living with you has always been a pleasure, I love you guys, and I will always

miss this. Thank you [redacted] for your friendship, many things would have not been possible without you. [redacted], [redacted], [redacted], and [redacted] have been mentioned above but their names should be here as well. [redacted], thank you so much for being around in the states, too. A lot of my life would have been less fun without you being around, knowing that I can always count on you. I am looking forward to being roommates during my time as a post doc.

Abstract

This manuscript discusses the structural chemistry of quaternary, tetrahedrally bonded copper selenides and Zintl compounds and their thermoelectric properties. Different materials compositions are investigated, the influence of different dopants considered, and effects of the structural and micro structural aspects on the thermoelectric transport are discussed. In the ongoing search for new materials for thermoelectric applications such as waste heat recovery and power generation, materials composed of inexpensive and earth abundant elements need to be explored and their thermoelectric efficiencies improved. The thermoelectric efficiency is determined by the figure of merit $zT=\alpha^2 T/\rho\kappa$. Thus, an ideal thermoelectric material requires a large Seebeck coefficient α, low electrical resistivity ρ, and low thermal conductivity κ.

Engineering nanostructure in bulk thermoelectric materials has recently been established as an effective approach to scatter phonons, reducing the phonon mean free path, without simultaneously decreasing the electron mean free path for an improvement of the performance of thermoelectric materials. In this work, the synthesis, phase stability, and thermoelectric properties of the solid solutions $Cu_{2+x}Zn_{1-x}GeSe_4$, x = 0 - 0.1 are reported. The substitution of Zn^{2+} with Cu^{+} introduces holes as charge carriers in the system and results in an enhancement of the thermoelectric efficiency. Nano sized impurities, formed via phase segregation at higher dopant contents, have been identified and are located at the grain boundaries of the material. The impurities lead to enhanced phonon scattering, a significant reduction in lattice thermal conductivity, and therefore an increase in the thermoelectric figure of merit in these materials. This study also reveals the existence of an insulator-to-metal transition at 450 K.

Then, inspired by the promising thermoelectric properties of $Cu_{2+x}Zn_{1-x}GeSe_4$, the synthesis and characterization of the solid solution $Cu_2Zn_{1-x}Fe_xGeSe_4$ is described. Upon substitution of Zn with the isoelectronic Fe no charge carriers are introduced in these intrinsic semiconductors. However, a change in lattice parameters, expressed in an elongation of the c/a lattice parameter ratio with minimal change in unit cell volume, reveals the existence of a 3-stage cation restructuring process of Cu, Zn, and Fe. The differences in bonding interaction between the cations and the anions lead to different bond lengths and bond angles, resulting in the observed trend in the lattice parameters. The resulting local anisotropic structural disorder leads to phonon scattering not normally observed resulting in an effective approach to reduce the lattice thermal conductivity in this class of materials.

In the family of Zintl antimonides, Ca_3AlSb_3 seems to be an interesting compound with a peak zT of 0.8 obtained at 1050 K upon doping with Na^{+} for Ca^{2+}. A previous investigation of Ca_3AlSb_3 shows an intrinsic semiconductor with a very low lattice thermal conductivity ($0.6\,Wm^{-1}K^{-1}$ at 870 K) due to a relatively complex crystal structure. This work explores the influence of the substitution of Al with Zn on the thermoelectric transport properties of the $Ca_3Al_{1-x}Zn_xSb_3$ system, and compares the effects of Na- and Zn-doping on hole carrier concentrations, mobilities of the charge carriers, and the thermoelectric figure of merit. Furthermore a report on the influence of the grain size in these materials on the thermoelectric transport will be made. Ultimately, it is found that while larger grain size has little effect on the high temperature properties, the reduction of grain boundary surface area improves the figure of merit at intermediate temperatures. This work shows the common strategy to use

nano structured materials does not always lead to an improved figure of merit. Other competing factors such as a reduction in mobility may overwhelm the improvement of the lattice thermal conductivity.

Finally, the closely related compound Sr_3GaSb_3 is investigated. Although the crystal structure of Sr_3GaSb_3 contains infinite chains of corner-linked tetrahedra, in common with Ca_3AlSb_3 and $Ca_5Al_2Sb_6$, it has twice as many atoms per unit cell (N=56). This contributes to the exceptionally low lattice thermal conductivity (κ_L = 0.45 $Wm^{-1}K^{-1}$ at 1000 K) observed in Sr_3GaSb_3. High temperature transport measurements reveal that Sr_3GaSb_3 is a nondegenerate semiconductor (consistent with Zintl charge-counting conventions) with relatively high p-type electronic mobility ($\sim$ 30 $cm^2V^{-1}s^{-1}$ at 300 K). To rationally optimize the electronic transport properties of Sr_3GaSb_3 in accordance with a single band model, doping with Zn^{2+} on the Ga^{3+} site was used to increase the p-type carrier concentration. In optimally hole-doped $Sr_3Ga_{1-x}Zn_xSb_3$ (x= 0.0 - 0.1), a maximum figure of merit of greater than 0.9 at 1000 K is demonstrated.

Abstract - German

Dieses Manuskript beschreibt den Zusammenhang zwischen der Strukturchemie von quaternären, tetraedrisch gebundenen Kupfer-Seleniden und Zintl-Verbindungen und deren thermoelektrischen Eigenschaften. Unterschiedliche Zusammensetzungen der Materialien werden untersucht, der Einfluss verschiedener fester Lösungen betrachtet und die Auswirkungen der Struktur und des Gefüges auf den thermoelektrischen Transport diskutiert. In der fortwährenden Suche nach neuen Materialien für thermoelektrische Anwendungen, wie Wärmerückgewinnung und Stromerzeugung, müssen kostengünstige Materialien und häufiger vorkommende Elemente erkundet und ihre thermoelektrische Effizienz verbessert werden. Die thermoelektrische Effizienz wird durch die Gütezahl $zT{=}\alpha^2 T/\rho\kappa$ bestimmt, bei der ein ideales Thermoelektrikum einen großen Seebeck-Koeffizienten α, einen niedrigen spezifischen elektrischen Widerstand ρ und eine geringe thermische Leitfähigkeit κ besitzt.

Nanostrukturierung von thermoelektrischen Materialien ist ein etabliertes und äußerst wirksames Konzept zur Streuung von Phononen, wodurch die mittlere freie Weglänge der Phononen verringert wird und somit zu einer Verbesserung der Leistung der thermoelektrischen Materialien führt. In dieser Arbeit wird die Synthese, die Stabilität und die thermoelektrischen Eigenschaften der festen Lösungen $Cu_{2+x}Zn_{1-x}GeSe_4$, x = 0 - 0,1 betrachtet. Die Substitution von Zn^{2+} mit Cu^{+} erzeugt Löcher als Ladungsträger und führt zu einer Erhöhung des thermoelektrischen Wirkungsgrades. Nanometer große Verunreinigungen, durch eine Phasensegregation entstanden, wurden identifiziert und sind an den Korngrenzen des Materials zu finden. Durch diese Verunreinigungen ergibt sich eine signifikante Reduktion der Wärmeleitfähigkeit des Gitters aufgrund einer erhöhten Streuung der Phononen an den Korngrenzen, welches eine Erhöhung des thermoelektrischen Gütefaktors in diesen Materialien nach sich zieht. Des Weiteren zeigt diese Arbeit auch die Existenz eines Isolator-Metall-Überganges bei 450 K.

Inspiriert durch die vielversprechenden thermoelektrischen Eigenschaften von $Cu_{2+x}Zn_{1-x}GeSe_4$, wird die Synthese und die Charakterisierung der festen Lösung $Cu_2Zn_{1-x}Fe_xGeSe_4$ beschrieben. Die Substitution von Zink mit dem isoelektronischen Eisen erzeugt keine Ladungsträger in diesem intrinsischen Halbleiter. Allerdings wird eine Änderung der Gitterparameter mit dem Dotierungsgrad offenbart, der sich in einer Streckung des c/a-Verhältnisses ausdrückt und bei x = 0,7 ein Maximum aufweist, was durch das Vorliegen eines dreistufigen Kationenumstrukturierungsprozesses von Cu, Zn und Fe erklärt werden kann. Die Unterschiede im Bindungscharakter zwischen den Kationen und Anionen führen zu unterschiedlichen Bindungslängen und Bindungswinkeln, welches sich in dem beobachteten Trend der Gitterparametern ausdrückt. Die daraus resultierende lokale anisotrope strukturelle Unordnung führt zu einer Streuung der Phononen und zu einem bisher nicht bekannten, effektiven Ansatz zur Reduktion der Wärmeleitfähigkeit des Gitters in dieser Materialklasse.

In der Klasse der Zintl Antimonide scheint Ca_3AlSb_3 eine interessante Verbindung sein, mit einer Gütezahl zT von 0,8 bei 1050 K. Vorangegangenen Untersuchungen von Ca_3AlSb_3, in der ein Substitution von Kalzium mit Natrium vorgenommen wurde, zeigen einen intrinsischen Halbleiter mit sehr niedriger Wärmeleitfähigkeit des Gitters von 0,6 $Wm^{-1}K^{-1}$ bei 870 K, was auf eine komplexe Kristallstruktur zurückzuführen ist. In dieser Arbeit wird der Einfluss

der Substitution von Aluminium mit Zink auf die thermoelektrischen Transporteigenschaften untersucht und ein Vergleich der Auswirkungen einer Substitution von Natrium und Zink in Hinblick auf die Ladungsträgerkonzentrationen, die Mobilitäten und die thermoelektrische Gütezahl angestellt. Des Weiteren wird der Einfluss der Korngrößen in diesen Materialien auf den Transport untersucht. Es zeigt sich, dass die Größe der Körner bei hohen Temperaturen wenig Einfluss auf den Transport hat, während bei mittleren Temperaturen die thermoelektrische Gütezahl verbessert wird. Diese Arbeit zeigt, dass die allgemein anerkannte Strategie zur Nanostrukturierung nicht immer zu einer Verbesserung der thermoelektrischen Eigenschaften führen muss, sondern auch konkurrierende Faktoren wie die Verringerung der Mobilität der Ladungsträger und eine Änderung der thermischen Leitfähigkeit gegeneinander abgewogen werden sollten.

Abschließend wird die verwandte Verbindung Sr_3GaSb_3 untersucht, welche, aufgrund der größeren Elementarzelle, eine außergewöhnlich niedrige Wärmeleitfähigkeit des Gitters von $0{,}45\,\mathrm{Wm^{-1}K^{-1}}$ bei 1000 K besitzt. Messungen der Transporteigenschaften bei hohen Temperaturen zeigen einen nicht entarteten Halbleiter mit relativ hohen Mobilitäten der Löcher ($\sim 30\,\mathrm{cm^2V^{-1}s^{-1}}$ bei 300 K). Um die thermoelektrischen Eigenschaften gezielt zu optimieren wurde Gallium mit Zink substituiert, um mehr Lochzustände zu erzeugen, was zu einer thermoelektrischen Gütezahl von 0,9 bei 1000 K führt.

Contents

List of Figures

List of Tables

List of Symbols, Notations, and Abbreviations

a - lattice parameter
a_0 - equilibrium lattice parameter
$a(x)$ - composition dependent lattice parameter
a_p - lattice parameter of pure end member
α - Seebeck coefficient / Thermopower
α_A - absorption coefficient
α_T - thermal expansion coefficient
B - quality factor
BSE - back scattered electron
BTE - Boltzmann transport equations
B_T - bulk modulus
b - lattice parameter
$b(XX)$ - number of bonds
C - heat capacity / specific heat
c - lattice parameter
D - sample density
D_M - mass diffusion coefficient
ΔT - temperature difference
DFT - density functional theory
DOS - density of states
DSC - differential scanning calorimetry
d - thermal diffusivity
dq_T - Thomson heat
dq_P - Peltier heat
E - electric field
E_g - band gap
EDS - energy dispersive X-ray spectroscopy
$E(\vec{k})$ - band dispersion
E_A - activation energy
$e(X)$ - number of valence electrons per anion
$e(M)$ - number of valence electrons per metal cation
e - electron charge
ϵ - reduced carrier energy
ϵ_F - Fermi energy
ϵ - anharmonicity parameter

FP-LAPW - full-potential linearized augmented plane-wave
f - Fermi-Dirac distribution function
f_0 - Fermi-Dirac distribution function at equilibrium
f_i - fraction of atoms i
GGA - generalized gradient approximation
$g(\omega)$ - vibrational density of states
Γ_{exp} - experimental disorder scattering parameter
Γ_m - mass disorder scattering parameter
Γ_S - strain disorder scattering parameter
γ - Grüneisen parameter
h - Planck constant
η - reduced electrochemical potential
η_C - Carnot efficiency
η_e - electrical efficiency
i^+ - electrical current
J_e - electrical current density
K_S - spring constant
k_B - Boltzmann constant
$\vec{k}$ - electron wave vector
κ - thermal conductivity
κ_L - lattice thermal conductivity
κ_{el} - electronic thermal conductivity
κ_L^p - lattice thermal conductivity of a crystal without disorder
κ_{min} - minimum lattice thermal conductivity
κ_b - bipolar contribution to the thermal conductivity
L - Lorenz number
l - phonon mean free path
l_D - diffusion length
λ - scattering parameter
M - atomic mass
$\bar{M}$ - average mass per atom
m_b^* - band effective mass
m_d^* - density of states effective mass
μ_T - Thomson coefficient
μ - charge carrier mobility
μ_H - Hall mobility
μ_0 - intrinsic carrier mobility
N - number of atoms
N_V - band degeneracy
$N(E)$ - density of states
n - charge carrier concentration/density
n_H - Hall carrier concentration

n_i - occupation number of vibrational states
ν - wave number
ν_g - phonon group velocity
ν_p - phonon phase velocity
∇T - temperature gradient
P - power
PF - power factor
PBE - Perdew, Burke, and Enzerhof
p - momentum
$\pi_{a,b}$ - Peltier coefficient
QBSD - quadrant back scattering detector
q_J - Joule heat
q - heat flow
R - electrical resistance
R - ideal gas constant
R_a - atomic distance
$R_{a,0}$ - equilibrium atomic distance
R_H - Hall coefficent
R_{wp} - profile residual
r_H - Hall factor
ρ - electrical resistivity
SEM - scanning electron microscopy
SE2 - secondary electron detector
σ - electrical conductivity
T - temperature
T_C - temperature on the cold side
T_H - temperature on the hot side
TB-mBJ - modified Becke-Johnson semi-local exchange potential
TGA - thermogravimetric analysis
t - thickness
τ_D - diffusion time
τ - scattering relaxation time
τ_N - phonon scattering relaxation time for normal scattering
τ_U - phonon scattering relaxation time for Umklapp scattering
τ_B - phonon scattering relaxation time for boundary scattering
τ_{PD} - phonon scattering relaxation time for point defect scattering
τ_{EP} - phonon scattering relaxation time for electron-phonon scattering
Θ_D - Debye temperature
u - disorder scaling parameter
V - voltage
V - volume
VEC - valence electron concentration

V_0 - minimum band energy
v_d - electron drift velocity
v_m - average velocity of sound
v_l - longitudinal speed of sound
v_t - transverse speed of sound
XRD - X-ray diffraction
ZT - device thermoelectric figure of merit
zT - materials thermoelectric figure of merit
Z - formula units per unit cell
ω - phonon frequency
ω_D - Debye frequency
Ω - average volume per atom

1 Introduction

Todays world is facing threats like climate change due to the combustion of fossil fuels, while the worlds demand for more and more energy is ever more increasing. The slowly receding supply of fossil fuels and with it the increasing price has led to a renewed interest in renewable energy technologies. For example Germany, which decided in 2011 to shut down all nuclear power plants, is having a closer look into new technologies like e.g. photovoltaics, wind energy, batteries, supercapacitors, and thermoelectricity.

Especially thermoelectric materials can be a potential route to increase the efficiency of existing technologies through the recovery of waste heat and its conversion into useful electrical energy.[1, 2, 3, 4]

It is therefore necessary to explore new compounds for a possible use as thermoelectric materials with a focus on understanding the structure and property relationships in order to be able to optimize thermoelectric efficiencies.

1.1 Summary

This chapter starts with an overview on the fundamentals of thermoelectric energy conversion. The basic transport phenomena, thermoelectric effects, and the required materials properties are discussed in detail. Combining these effects and the materials properties leads to the dimensionless thermoelectric figure of merit, zT. In modern thermoelectric materials the figure of merit approaches unity, however higher figure of merits are needed for a more efficient energy conversion.

An overview over the state of the art materials is given along with a discussion on some approaches for higher figure of merits in thermoelectric materials, including the optimization of the charge carrier density, resonant scattering, band engineering, and approaches to a lower thermal conductivity. This chapter is mainly designed to give an overview on the transport phenomena and provide a rough literature review. A more thorough description of transport will be made at the beginning of each transport chapter.

The remainder of this chapter focuses on the literature overview and background of the materials considered in this thesis: $Cu_2M^{II}GeSe_4$, Ca_3AlSb_3, and Sr_3GaSb_3. In particular the section on Zintl-phases will touch some of the reasons why this class of materials is suited for the investigation of structure-property relationships in thermoelectric materials. Finally, the discussion will close with a summary and a motivation of the research conducted for this thesis.

1.2 Transport Phenomena and Thermoelectric Energy Conversion

Basic solid state transport phenomena of an electrical conductor or semiconductor can usually be investigated through two very basic methods. Either an electric field, a temperature gradient, or both can be applied to observe different effects.[5]

Applying an electric field E across a material will lead to an electrical current in the material which is defined by the the electrical current density J_e and the electrical conductivity σ:[6, 7]

$$J_e = \sigma E \ . \tag{1.1}$$

On the other hand, applying a temperature gradient ∇T will lead to a heat flow q (when no electric current is allowed to flow) due to the thermal conductivity κ of a material, with:[6, 7]

$$q = -\kappa \nabla T \ . \tag{1.2}$$

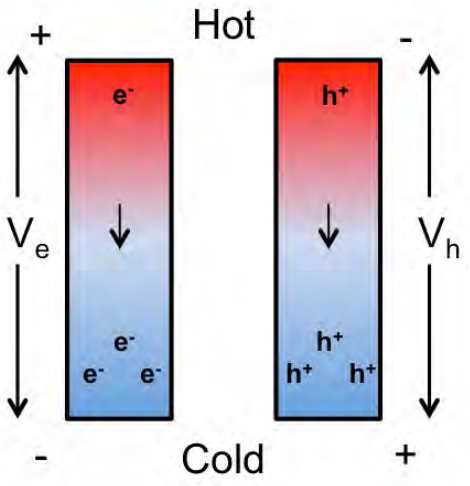

Figure 1.1: Schematic of the Seebeck effect. Charge carriers diffuse in response to a temperature gradient from the hot side to the cold side, until the resulting voltage counterbalances the heat flux.

Both transport phenomena, electrical conductivity and thermal conductivity, are intrinsic properties of a bulk material. However, there is a phenomenon which causes an electrical flow in response to a temperature gradient, without an external electrical field. This, so called thermoelectric current, is caused by the Seebeck effect. In 1821, Thomas Johann Seebeck, realized that an electric current flows around a closed circuit made up of different electrical conductors when the junctions are subject to different temperatures.[8, 9, 10, 11, 12] The Seebeck effect originates in the appearance of an electromagnetic force, which is caused by the diffusion of charge carriers, electrons or holes, along the temperature gradient from the hot side to the cold side. This is best visualized by an analogy to a gas in a tube. The gas molecules/atoms at the hot side have a higher thermal energy and diffuse to the cold side. In other words, the hot gas expands and the cold gas contracts.[13] This effect is also observed for electrons and holes (see Figure 1.1). The diffusion from the hot to the cold side causes a voltage V

and the carriers diffuse until the resulting voltage counterbalances the heat flux. For small temperature differences ΔT, the resulting thermoelectric voltage is found to be proportional to the temperature difference, with the Seebeck coefficient α:[8]

$$\alpha = \frac{V}{\Delta T} \, . \tag{1.3}$$

The Seebeck coefficient (or thermopower) is negative when the conduction is dominated by electrons and positive when holes are the dominant charge carrier type. The Seebeck coefficient is an intrinsic property of a solid material under open circuit conditions, however, it can only be measured when in contact with another material (i.e. closed circuit conditions), which leads to the common misconception that a junction between two materials is necessary for a thermoelectric voltage to occur.

However, if we consider the situation where an electric current flows from one substance (a) to another (b), then heat may either be absorbed or given out at the junction, depending on the direction of the current.[5] This effect has been reported by Jean Peltier in 1834, when he passed a small external current across a bismuth-antimony thermocouple. This Peltier heat dq_P was found to be proportional to the magnitude i^+ and the duration of the applied external current:[8]

$$dq_P = \pi_{a,b} i^+ \, . \tag{1.4}$$

The coefficient of proportionality is the so called Peltier coefficient $\pi_{a,b}$. The Peltier effect, as well as the Seebeck effect, is a reversible effect and should not be confused with the irreversible Joule heating q_J, which occurs when an electrical current flows through a material with the resistivity ρ ($q_J = J_e \rho$).[5, 8]

In 1854 William Thomson (later Lord Kelvin) applied the first and second law of thermodynamics on thermoelectricity and decided there should be a thermodynamical connection between the Seebeck and the Peltier effect. After analyzing the situation and realizing that experimental evidence was not in agreement with the theoretical connection, he postulated a third thermoelectric effect, the so called Thomson effect.[5, 8] An electrical current that passes through a conductor, when there is also a temperature gradient ∇T present, produces a Thomson heat dq_T:[5]

$$dq_T = \mu_T J_e \nabla T \, . \tag{1.5}$$

The Thomson coefficient μ_T depends on the temperature of the conductor and has a positive sign if heat is absorbed, i.e. when a current flows to the hot region. The Kelvin (or Thomson) relations relate Seebeck coefficient α, Peltier coefficient $\pi_{a,b}$, and Thomson coefficient μ_T:[5]

$$\mu_T = \frac{T d\alpha}{dT} \; and \; \pi_{a,b} = T\alpha \, . \tag{1.6}$$

Considering all transport phenomena and thermoelectric effects, good thermoelectric materials should have a large Seebeck coefficient α. Furthermore, the heat flow q from the hot to the cold side should be as small as possible to keep a stable temperature gradient ∇T along

the material. Therefore, small thermal conductivities are desired, as can be seen in Equation 1.2. Good thermoelectric materials also need to have good electrical conductivities σ (or a small electrical resistivity $\rho = 1/\sigma$), to keep the Joule heating low and the power output P high (with $P = V^2/R$, for a total resistance R).[7] However, the combination of these materials properties is usually difficult to obtain, since they are highly interdependent. For example, high α usually corresponds to a low σ and vice versa. Therefore different strategies need to be employed to obtain a good thermoelectric performance.

1.3 Thermoelectric Figure of Merit

A thermoelectric generator converts heat q into electrical power P with a certain electrical efficiency η_e. This efficiency strongly depends on the temperature difference ΔT and is limited by the Carnot efficiency η_C ($\eta_C = \Delta T/T_H$) and is typically defined as:[9, 14, 15, 16]

$$\eta_e = \eta_C \cdot \frac{\sqrt{1+ZT}-1}{\sqrt{1+ZT}+\frac{T_C}{T_H}}\,, \tag{1.7}$$

for an optimized current. With the device figure of merit ZT and the temperatures of the hot side and the cold side, T_H and T_C, respectively. Since the device figure of merit is not easily calculated, the average materials figure of merit zT can be used to assess the efficiency of thermoelectric material:[15, 17]

$$zT = \frac{\alpha^2\sigma}{\kappa}T\,. \tag{1.8}$$

Figure 1.2 shows published figure of merits for some common state of the art thermoelectric materials.

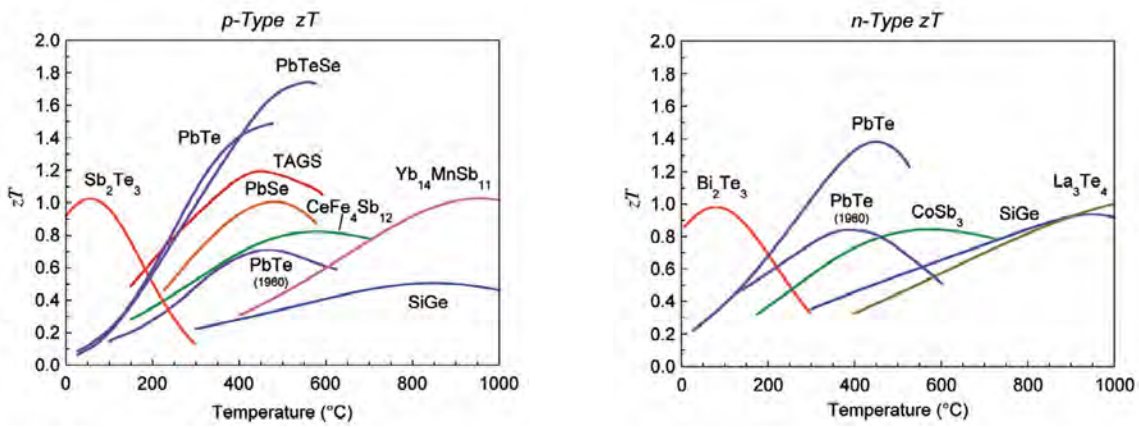

Figure 1.2: Overview of zT-values for different p-type (left) and n-type (right) materials.[18] TAGS stands for $(GeTe)_{1-x}(AgSbTe2)_x$. Note that different materials have their maximum figure of merit in different temperature regimes.

As mentioned above, high thermoelectric efficiencies are achieved for high Seebeck coefficients, high electrical conductivities (or low electrical resistivities), and low thermal conductivities. However, these materials properties are strongly coupled and the desired combination is difficult to obtain.

The thermal conductivity, for instance, has two primary contributions, a lattice thermal conductivity κ_L and an electronic contribution κ_{el}:[3, 19]

$$zT = \frac{\alpha^2\sigma}{\kappa_L + \kappa_{el}}T \ . \tag{1.9}$$

While the lattice contribution to the thermal conductivity can be independently altered (see Section 1.3.3 and Chapter 5), the electronic part directly depends on the electrical conductivity, expressed in the Wiedemann-Franz law:[3, 9, 14, 20]

$$\kappa_{el} = L\sigma T = Ln e \mu T \ , \tag{1.10}$$

with the Lorenz number L (L = 2.44x10^{-8} WΩK^{-2} for free electrons), the charge carrier concentration n, the mobility of the charge carrier μ, and the electron charge e. As mentioned, a high electrical conductivity is important for a good thermoelectric material, however, as can be seen in Equation 1.10, this also leads to a higher electronic contribution to the thermal conductivity.

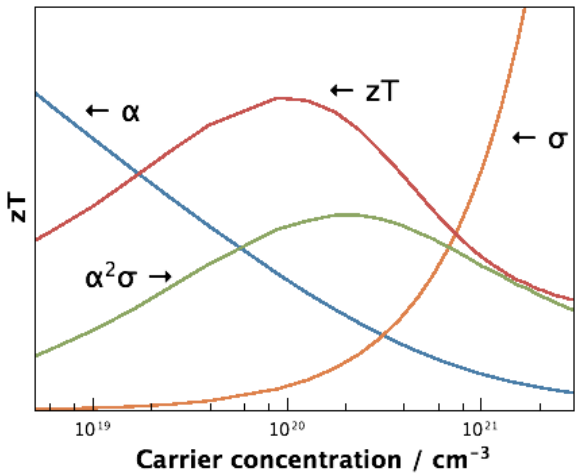

Figure 1.3: Influence of the charge carrier concentration on the Seebeck coefficient α, the electrical conductivity σ, the power factor $\alpha^2\sigma$, and the figure of merit zT. While the electrical conductivity increases with increasing carrier concentration, the Seebeck coefficient decreases. It can be seen, that an optimum carrier concentration exists, which will lead to a maximum figure of merit in a material.

In addition to a low thermal conductivity a high power factor PF ($PF = \alpha^2\sigma$) is required for a high figure of merit. Equation 1.10 shows the dependence of the electrical conductivity on the charge carrier concentration n and the mobility of the charge carriers μ. However, the Seebeck coefficient does also strongly depend on the charge carrier concentration of the material. For a degenerate system (high carrier concentrations) the Seebeck coefficient is given by:[3, 19]

$$\alpha = \frac{8\pi^2 k_B^2}{3eh^2} m_d^* T \left(\frac{\pi}{3n}\right)^{\frac{2}{3}} \ , \tag{1.11}$$

while at lower carrier concentrations (non-degenerate semiconductor) α is proportional to ln(1/n).[9, 10] This means the Seebeck coefficient decreases with increasing carrier concentration. Here m_d^* stands for the density of states effective mass, k_B is the Boltzmann constant, and h the Planck constant. Furthermore, even the Lorenz number is not constant and does to some extent depend on the location of the Fermi level and therefore the carrier concentration (see Equation 5.30).[21] The influence of the charge carrier concentration on the Seebeck coefficient, the electrical conductivity, and the electronic contribution to the thermal conductivity reveals the need to precisely control the charge carrier density in a material, so that reasonable values of α and σ are obtained at an optimum carrier concentration (see Figure 1.3).

Achieving an optimum carrier concentration in a material is crucial for a maximum figure of merit of a given thermoelectric material. However, different approaches to higher figure of merits have been chosen as well. For instance, the thermopower of a material can be increased by increasing the density of states of a material at the Fermi level, either by resonant impurities or multiple bands via band engineering. Furthermore, reducing the thermal conductivity via alloying, nano structuring, and employing glass-like materials has also been shown to increase the figure of merits in some materials.

1.3.1 Enhancement of Thermopower

As seen in Section 1.3 a high Seebeck coefficient is desired, while an optimum carrier concentration for a decent electrical conductivity might result in too low carrier concentrations for an actual high Seebeck coefficient. However, considering Equation 1.11, the Seebeck coefficient does not depend on charge carrier density only. The density of states effective mass m_d^* at the Fermi level has an influence on α as well, and materials with a high effective mass are desired.[19, 22, 23, 24, 25]

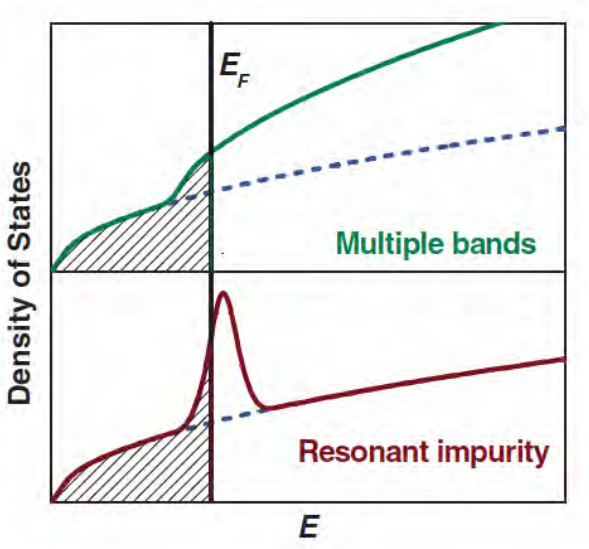

Figure 1.4: Schematic of the influence of multiple bands and resonant states on the density of states (DOS). Both mechanisms increase the Seebeck coefficient, either through a larger number of conducting bands (N_V) or a higher density of states effective mass m_d^* at the Fermi level E_F.[25]

A high density of states and therefore a high density of states effective mass can be achieved due to either a large number of conducting bands N_V (also called band degeneracy),[26] or via flat bands giving a high band effective mass m_b^*:[9, 24, 25]

$$m_d^* = N_V^{2/3} m_b^* \,. \tag{1.12}$$

One approach to a high density of states (or flat bands) at the Fermi level can be achieved through the introduction of resonant states via doping. This concept has first been proposed by Heremans *et al*. in 2008.[27] Doping bulk PbTe with Tl introduces new energy levels (or resonant states) leading to a higher density of states and an increased Seebeck coefficient in this material. This has also successfully been shown for doping with Al and Cr in PbTe or PbSe.[28, 29, 30] Figure 1.4 shows the influence of resonant states and multiple bands on the density of states at the Fermi level.[25]

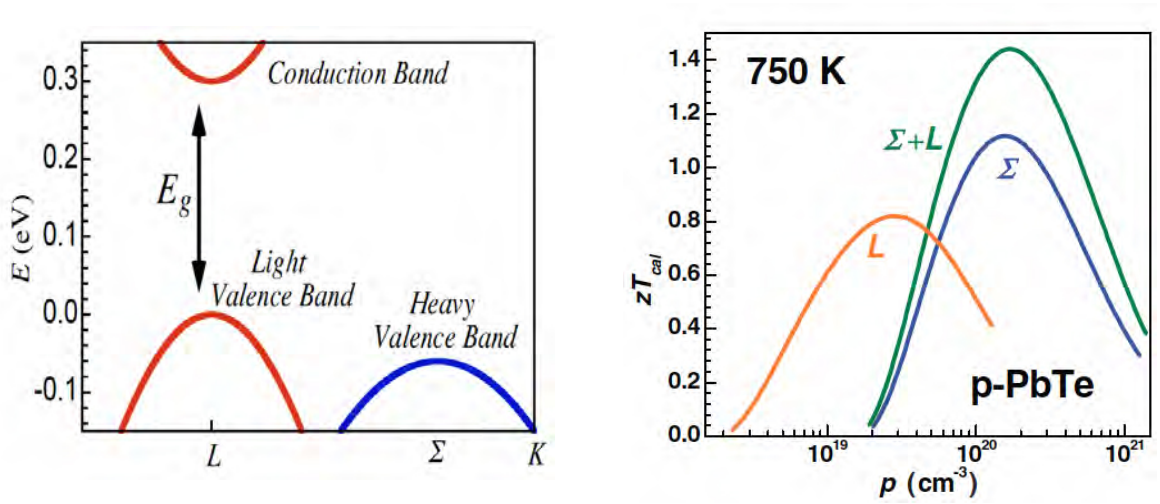

Figure 1.5: Left: Light and heavy valence band in PbTe for different symmetry points in the Brillouin zone. PbTe exhibits a valence band with a larger (heavier) effective mass at lower energies. Right: Figure of merit zT for different carrier concentrations n and the influence of the different valence bands. After shifting the Fermi level to lower energies due to a larger doping level, the heavier valence band contributes to the transport and increases the zT.[18, 25]

However, a high band effective mass (i.e. flat bands) will unfortunately result in a low electron (or hole) mobility, because the mobility is inversely proportional to the effective mass ($\mu \propto 1/m_b^*$).[3, 19, 24] And a low charge carrier mobility will inevitably lead to a low electrical conductivity (see Equation 1.10). For a material with an optimized carrier concentration, the figure of merit zT depends on the quality factor B, which is determined by the lattice thermal conductivity κ_L, the mobility of the charge carriers, the band effective mass, and the band degeneracy (number of bands contributing to the conduction):[18]

$$B \propto \frac{\mu N_V m_b^{*3/2}}{\kappa_L} \,. \tag{1.13}$$

Besides increasing the effective mass for a high quality factor, there are approaches to increase the band degeneracy, and lowering the lattice thermal conductivity for a high ther-

moelectric figure of merit. These approaches will be discussed in the following sections.

1.3.2 Band Engineering

Following the expression for a high quality factor B (Equation 1.13), thermoelectric materials with a large number of band degeneracy N_V are beneficial for a high figure of merit. In other words, having multiple bands with comparable energies (within a few k_BT) contributing to the electronic transport from either degenerate band extrema (orbital degeneracy) or multiple carrier pockets in the Brillouin zone (see Figure 1.6) due to high crystal symmetry. While it is not possible to change the N_V of a material (since this would mean a change in symmetry and crystal structure), it is possible to converge several bands to achieve a larger, combined N_V.[18, 25, 31, 32]

Lead chalcogenides, for example, have a highly symmetric crystal structure (NaCl-type) and therefore a very high band degeneracy. The band structure of PbTe shows a light valence band at the L-point, with a direct band gap E_g to the conduction band, and a heavier valence band at the Σ-point, which is lower in energy (see Figure 1.5 left). A higher doping level would inevitably move the Fermi level into the direction of the heavier valence band and therefore increase the thermopower, leading to a higher figure of merit for both bands contributing to the transport at an optimum carrier concentration (see Figure 1.5 right).[18]

Furthermore, both valence bands exhibit different temperature dependencies (see Figure 1.6). At a certain temperature both bands converge, leading to an effective band degeneracy of 12-16 and therefore increasing the figure of merit to $zT \sim 1.8$.[31]

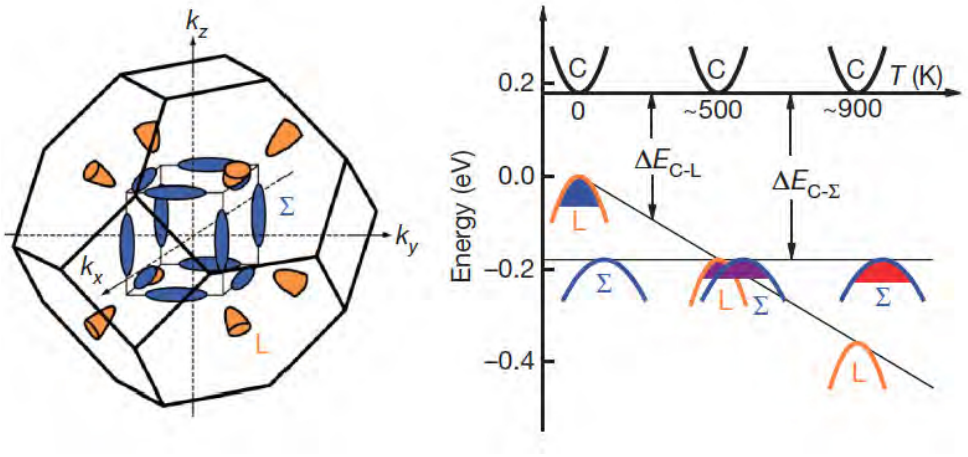

Figure 1.6: Left: Number of carrier pockets in the first Brillouin zone of PbTe, showing a band degeneracy of N_V equals 4 for the L-point and 12 for the Σ-point, due to the exceptionally high crystal symmetry. Right: Temperature dependence of the two valence bands. At a specific temperature both bands converge, leading to a combined band degeneracy of 12-16 and therefore an increased figure of merit in this temperature regime.[18, 31]

Increasing the band gap of a material via alloying also leads to an increase in the figure of merit of a material.[25] At higher temperatures, minority carriers get excited across the band gap and the thermopower starts to decrease due to the contribution of minority carriers. If

there are electrons and holes present, the resulting Seebeck coefficient will be the sum of their contributions, with:[8]

$$\alpha = \frac{\alpha_n \sigma_n + \alpha_p \sigma_p}{\sigma_n + \sigma_p} , \tag{1.14}$$

and therefore the thermoelectric voltage will be lowered. Hence, a decrease of the figure of merit will occur at higher temperatures due to the decreasing thermopower. Alloying a compound to widen the band gap will therefore not only shift the maximum of the zT to higher temperatures, it will also lead to higher figure of merits, since larger values of the Seebeck coefficient can be obtained at higher temperatures (see Equation 1.11 and Figure 1.7).

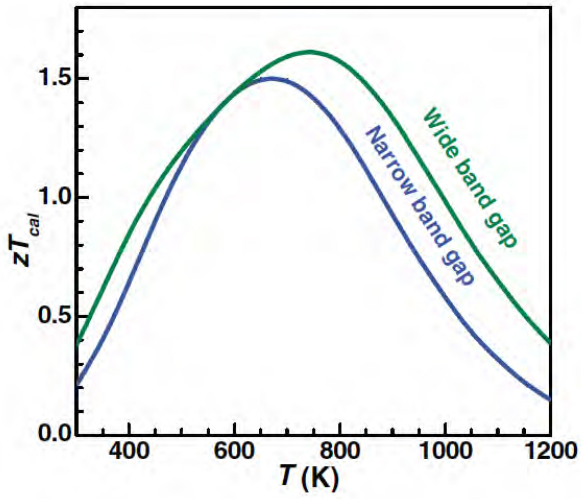

Figure 1.7: Influence of the band gap on the temperature dependence of the figure of merit. For larger band gaps the carrier activation across the band gap occurs at higher temperatures, leading to a higher peak and integrated zT, before the influence of the minority carriers lead to a decrease in the thermoelectric voltage.[25]

1.3.3 Reduction of Thermal Conductivity

In order to obtain high thermoelectric efficiencies a low lattice thermal conductivity κ_L is desired for a large quality factor. The lattice thermal conductivity of a material is caused by lattice vibration waves or phonons, propagating through the lattice and therefore carrying heat. These phonons have group velocities v_g, mean free path lengths l between scattering events, and the amount of heat transported is proportional to the heat capacity C. This leads to a lattice thermal conductivity in analogy to kinetic gas theory of:[19]

$$\kappa_L = \frac{1}{3} C v_g l \, . \tag{1.15}$$

For materials with low lattice thermal conductivities, materials with low heat capacities are required, which can usually be found in materials with weak bond strengths, heavy atoms, or large unit cell volumes.[19]

Lowering the phonon mean free path in a material is one possible approach to a lower

lattice thermal conductivity. This can easily be achieved via alloying with other elements to create point defect scattering,[33] successfully shown for thermoelectric materials in Heusler compounds,[34] skutterudites,[35, 36] lead telluride,[37] and SiGe.[38, 39] Point defect scattering (or alloy scattering) is an effective way to scatter high frequency phonons, which are usually not heavily scattered by phonon-phonon scattering.[33, 40, 41] Furthermore the use of nano structuring or interfaces to reduce the phonon mean free path has shown to be effective for scattering low frequency (large wavelength) phonons, achieving low κ_L.[42, 43, 41, 44, 45, 46]. However, oftentimes these point defects, interfaces, and nano structures not only scatter phonons but charge carriers as well, leading to a reduction in the mobility and therefore decreasing the quality factor (Equation 1.13).[41]

This problem has lead to the search for materials within the "phonon-glass electron-crystal" concept.[47] Utilization of the materials' structure, e.g. use of filling atoms in skutterudites,[48, 49, 50, 51] or clathrates,[52, 53, 54] exhibit glass-like thermal properties, with still high mobilities due to a crystalline behavior.

1.4 Pertinent Materials

1.4.1 $Cu_2M^{II}GeSe_4$

This section is in parts an adapted reproduction, from *J.* Am. Chem. Soc **2012**, 134, 7147-7154 and *J.* Am. Chem. Soc **2013** - accepted manuscript.[55, 56] Reproduced with permission of the American Chemical Society Copyright 2012 and 2013.

In an attempt to broaden the quest for abundant materials with low thermal conductivities Chen *et al*. have reported on the transport properties of quaternary tetrahedrally bonded Cu_2(Zn/Cd)$SnSe_4$.[57, 58, 59] Despite being wide band gap compounds with low electron mobility, these materials exhibit fairly good thermoelectric performance upon "doping" due to the very low intrinsic thermal conductivities, leading to a maximum zT of 0.95 at 850K for $Cu_2ZnSn_{1-x}In_xSe_4$.[57, 58, 59, 60]

There exists a whole family of structurally related quaternary compounds of the formula Cu_2-II-IV-S_4(Se_4), with II = Mn, Fe, Co, Ni, Zn, Cd, Hg and IV = Si, Ge, Sn, crystallizing in either tetragonal or orthorhombic crystal structures.[61] Many of these compounds have been synthesized and characterized, for instance for their electronic properties,[62, 63, 64] optical properties,[65] thermal properties,[66], and magnetic properties.[67, 68] The structural robustness of this class of compounds makes systematic substitution and hence the study of their properties possible.[67, 69, 70, 71, 72] Recently $Cu_2ZnSnSe_{4-x}S_x$ (CZTSSe), and related compounds, have attracted attention for the use in photovoltaics, due to possible band gap tuning,[73, 74, 75, 76] leading to efficiencies around 10% of laboratory fabricated photovoltaic devices.[73, 77, 78]

Structurally derived from the diamond structure, the structures of these so called "adamantine" compounds, have been synthesized and structurally characterized.[61, 63, 80] In these diamond like structures, each atom is coordinated by four nearest neighbors, forming a tetrahedrally bonded structure.[79] In the tetragonal unit cell system there exist two structurally similar but distinct structure types, namely stannite and kesterite. The crystal structures of

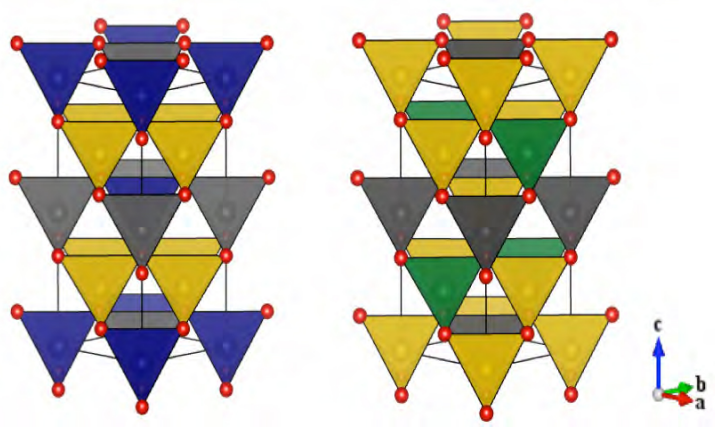

Figure 1.8: Crystal structures of stannite-type (left) and kesterite-type (right) $Cu_2M^{II}GeSe_4$. Cu atoms are yellow, Ge atoms are gray, M^{II} atoms are blue (stannite) or green (kesterite), and Se atoms are red, with the tetrahedral coordination of the elements indicated.[55] Note the difference in the ordering of the metal cations. While Cu resides on the 4*d*-Wyckoff position (0, $\frac{1}{2}$, $\frac{1}{4}$) in the stannite type, it shares this lattice site with M^{II} in the kesterite structure.[79]

the stannite-type and the kesterite-type $Cu_2M^{II}GeSe_4$ are shown in Figure 1.8.

These multinary chalcogenides, form binary, ternary, and quaternary compounds where the two substructures are populated with cations and anions, respectively. The binary compounds $A^{II}X^{VI}$ (e.g. ZnSe) crystallize in the cubic-sphalerite structure type (space group $F\bar{4}3m$). Lowering the symmetry by ordered cation substitution with two metals leads to the chalcopyrite structure type $A^{I}B^{III}X_2^{VI}$ ($I\bar{4}2d$), with the mineral chalcopyrit $CuFeS_2$ as the prototype. This ordered substitution doubles the translational period along the z-direction leading to a tetragonal structure crystal system. Due to different interactions between the metals and the anions, resulting in different bond length and bond angles, a tetragonal distortion takes place resulting in a $c/2a$-ratio < 1.[79]

A further decrease in symmetry leads to the stannite type structure ($I\bar{4}2m$) or (with even further reduced symmetry) the kesterite type structure ($I\bar{4}$). This decrease in symmetry is achieved by substitution of elements but also through metal ordering, e.g. metal ordering leads from stannite (prototype Cu_2FeSnS_4) to kesterite (prototype Cu_2ZnSnS_4).[79] In the stannite type Cu is located on the Wyckoff position 4*d* (0, $\frac{1}{2}$, $\frac{1}{4}$), M^{II} occupies 2*a* (0,0,0), and Ge is located on site 2*b* (0, 0, $\frac{1}{2}$), while selenium coordinates all cations on Wyckoff position 8*i*-site (0.2449, 0.2449, 0.1298). All site occupancies are 100% and each unit cell contains two chemical

Table 1.1: Crystallographic data of stannite-type $Cu_2M^{II}GeSe_4$ (space group $I\bar{4}2m$).[61]

Atoms	Wyckoff	Position	Point symmetry	Occupation
M^{II}	2a	(0, 0, 0)	$\bar{4}2m$	1.0
Cu	4d	(0, $\frac{1}{2}$, $\frac{1}{4}$)	$\bar{4}$..	1.0
Ge	2b	(0, 0, $\frac{1}{2}$)	$\bar{4}2m$	1.0
Se	8i	(0.2449, 0.2449, 0.1298)	..m	1.0

Table 1.2: Crystallographic data of kesterite-type $Cu_2M^{II}GeSe_4$ (space group $I\bar{4}$).[80]

Atoms	Wyckoff	Position	Point symmetry	Occupation
M^{II}	2d	$(\frac{1}{2}, 0, \frac{1}{4})$	$\bar{4}$..	1.0
Cu1	2a	(0, 0, 0)	$\bar{4}$..	1.0
Cu2	2c	$(0, \frac{1}{2}, \frac{1}{4})$	$\bar{4}$..	1.0
Ge	2b	$(\frac{1}{2}, \frac{1}{2}, 0)$	$\bar{4}$..	1.0
Se	8g	(0.756, 0.756, 0.8722)	1	1.0

formulas (Z=2).[61, 81] The crystallographic positions for both structures are given in Tables 1.1 and 1.2.

In the kesterite type structure (see Figure 1.8), however, Cu is located at the Wyckoff position 2*a*-site and the 2*c*-site with equal parts. The M^{II} cation occupies the 2*d*-site sharing it with Cu.[79] In other words, while M^{II} and Ge share the z = 0 and z = $\frac{1}{2}$ metal layers, Cu occupies the z = $\frac{1}{4}$ and z = $\frac{3}{4}$ layer only, whereas in kesterite all layers are occupied with Cu sharing with either the M^{II}-cation or the Ge.[80]

Both structure types are closely related and there is a high degree of possibility for anti site disorder, especially since the kesterite structure evolves from metal ordering, occurring concurrently with a symmetry decay from the stannite type. There is further indication that the synthetic procedure might have an influence on the obtained crystal structures.[79, 81, 82] Given the high degree of similarity of the prototype structures of kesterite and stannite, Cu_2ZnSnS_4 and Cu_2FeSnS_4, respectively, many investigations have been undertaken to analyze the solid solutions of this system. Kesterite and stannite are found coexisting adjacent with no indication of miscibility,[80] while there seems to be a discontinuity of the lattice parameters, showing an inversion of the trend of the unit-cell parameters, observed in the range 60-70 mole % in Cu_2ZnSnS_4.[80, 83] Neutron diffraction studies by Susan Schorr on these multinary chalcogenides suggest a 3-stage cation restructuring process originating from a crossover from the stannite to the kesterite structure type.[81, 82]

In this thesis, the solid solutions $Cu_{2+x}Zn_{1-x}GeSe_4$, $Cu_2Zn_{1-x}Fe_xGeSe_4$, and $Cu_{2+x}Zn_{1-x-y}Fe_yGeSe_4$ have been synthesized and characterized for a possible application as thermoelectric materials. The solid solution of $Cu_2Zn_{1-x}Fe_xGeSe_4$ has been synthesized by Caldera *et al.*,[84] and the lattice parameters have been reported. These materials have been mainly characterized for their magnetic properties, and $Cu_2FeGeSe_4$, for example, exhibits antiferromagnetic behavior with a Neel-temperature of 20 K.[68]

1.4.2 Zintl-Phases

This section is an adapted reproduction of the Diploma thesis from Wolfgang Zeier, 2010.[85]

Zintl phases are intermetallic solids, which include an electropositive metal, such as alkali and alkaline earth metals, and a metallic but more electronegative partner (mostly semimetals, e.g. Si, P, As, Sb). These compounds contain chemical bonds that demonstrate both ionic and covalent character.[86, 87]

The *Zintl-Klemm* formulation provides an explanation for the properties of these com-

pounds. The more electropositive metal transfers all valence electrons to its more electronegative partner, and the resulting anion forms a covalently bonded superlattice, structured according to its valence electron concentration (*VEC*).[86, 87] This model is referred to as the *Zintl-Klemm-Busmann* concept.[86]

For a binary compound M_mX_x, with the cation M and the anion X, the *VEC* is given by:[88]

$$VEC(X) = \frac{m \cdot e(M) + x \cdot e(X)}{x} , \tag{1.16}$$

where $e(M)$ and $e(X)$ are the number of valence electrons for the metal and anion, respectively. The number of bonds $b(XX)$, formed by the anions, is given by:[88]

$$b(XX) = 8 - VEC(X) . \tag{1.17}$$

This formulation is simply a restatement of the octet rule for the formation of elemental structures. In the *Zintl-Klemm-Busmann* concepa these compounds form the structures of the elements of the 4th to 7th main group, according to their valence electron configuration.[88]

Consider the Zintl compound NaTl. Sodium is the more electropositive partner, so it transfers one electron to thallium to form Tl^-. This results in a *VEC* of four for Tl^-, which is the same valence electron configuration as of carbon. According to the octet rule carbon has to form four bonds, which results in the diamond structure. Thus in NaTl, the Tl^- forms a diamond-like, tetrahedral coordinated superlattice with covalent Tl-Tl bonds and Na^+ in the tetrahedral holes.[87]

Other examples are the compounds FeS_2 (pyrite) and CaSi. In pyrite the iron transfers two electrons to two sulfur atoms, which leads to a formal S^- with a *VEC* of 7 and S_2^{2-}-pairs form in analogy to Cl_2.[88] As expected from the Si^{2-}-species in CaSi, with a *VEC* of 6, chains similar to S^0 can be found.

Clearly the term Zintl phase can apply to more than just binary compounds, it comprises a vast number of compounds (ternaries, clusters with molecular motifs, etc.), and a detailed discussion can be found elsewhere in the literature, e.g. [86].

Due to the covalent character of the anionic bonding in the superlattice and the ionic cation-anion interaction, the properties of the Zintl phases differ from the properties of intermetallic compounds.[87] Similar to ionic materials a band gap (< 1 eV) forms between the filled anionic valence band and the empty cation conduction band.[87] Zintl phases are also referred to as polar intermetallics and they exhibit properties of both ionic and covalent materials, such as brittleness but metallic or semiconducting behavior.[87, 88]

Materials with good thermoelectric properties can be found in a wide range of compounds. Some thermoelectrics have high mobilities and low effective masses of the charge carriers, while more ionic materials exhibit low mobilities and high effective masses.[3] The interdependence of the transport properties on the figure of merit is the reason why good thermoelectric compounds might be completely different materials. This leads to an important question: Are there interesting compounds located in the middle of this wide range between intermetallics and ionics with good thermoelectric properties?

One possible class of compounds are these Zintl phases. As mentioned they exhibit both

ionic and metallic behavior, which led to a recent research focus on Zintl phases for thermoelectric materials, e.g. [89, 19, 90].

Probably the best example for a focus on Zintl phases is the compound $Yb_{14}AlSb_{11}$. Doping on the Al-site with Mn^{2+} leads to a $zT > 1.3$ for $Yb_{14}Mn_{1-x}Al_xSb_{11}$ at the optimized doping level of $x = 0.6$ and 0.8.[91] The high zT of this material is mainly due to the glass-like thermal conductivity.[19, 89, 92] The complexity of the structure with a large number of atoms per unit cell (104 atoms) leads to an intrinsically low lattice thermal conductivity.[19, 89] Furthermore, the heavy atoms of this compound result in a low group velocity of the phonons, which leads to an additional decrease of the lattice thermal conductivity.[19] Magnetic investigations suggest a contribution of the d^5-spin-state of the Mn^{2+}-cations to the high zT-value due to coupling with the holes.[90, 91, 93] The compound $Yb_{14}AlSb_{11}$ seems to be a very promising candidate and a very good example for the research on Zintl phases, due to good electrical properties and a low thermal conductivity - which leads to a successful combination of the electron-crystal phonon-glass approach - and the ability of precise doping on the Yb or Al-site.[19, 89].

As seen in Section 1.3 the thermoelectric properties strongly depend on the carrier concentration of a material, and a control over the carrier concentration is necessary for a good thermoelectric material.[19] Zintl phases are valence compounds with semiconducting behavior. The anions form the valence band, with only small cation contributions, and the cations the conduction band. Due to the small impact of the cations on the electronic structure of the valence band, acceptor doping on the cation site allows a precise adjustment of the Fermi level and carrier concentration, usually without a huge disruption of the band structure.[19, 94]

Zintl phases offer the desired characteristics for thermoelectric materials. They often exhibit complex crystal structures resulting in a low thermal conductivity, they form small band gap semiconductors, and their rich crystal chemistry leads to the possibility of precise tuning of the transport properties.[94] On the fundamental level, there is a need to explore Zintl compounds and their thermoelectric properties in respect to their crystal structure. A comparison of the electrical and thermal transport properties might lead to an insight in the structure-property relationships in Zintl compounds and maybe opening new approaches to enhanced thermoelectric efficiencies.

1.4.3 Ca_3AlSb_3

This section is in parts an adapted reproduction, from *E*nergy Environ. Sci. **2011**, 4, 510-518 and *J*. Mater. Chem **2012** 22, 9826-9830.[95, 96] Copyright 2011 and 2012 The Royal Society of Chemistry.

First reported by Cordier *et al*.,[97] Ca_3AlSb_3 crystallizes in the orthorhombic crystal system (space group *P*nma) with 28 atoms in the unit cell. Four Sb atoms coordinate the Al atoms, forming slightly distorted tetrahedra. These tetrahedra connect to one-dimensional corner-sharing infinite chains in the *b*-direction, in analogy to the structure of $(SiO_3)_n^{2-}$ in the chain-silicates.[98] A perspective along the $AlSb_4$ tetrahedral chains can be viewed in Figure 1.9.

The Al-Sb distances of 270.9-273.9 pm are shorter than the sum of the radii for the metals or the ions and are in the range of the covalent radii. Therefore a mainly covalent Al-Sb bond

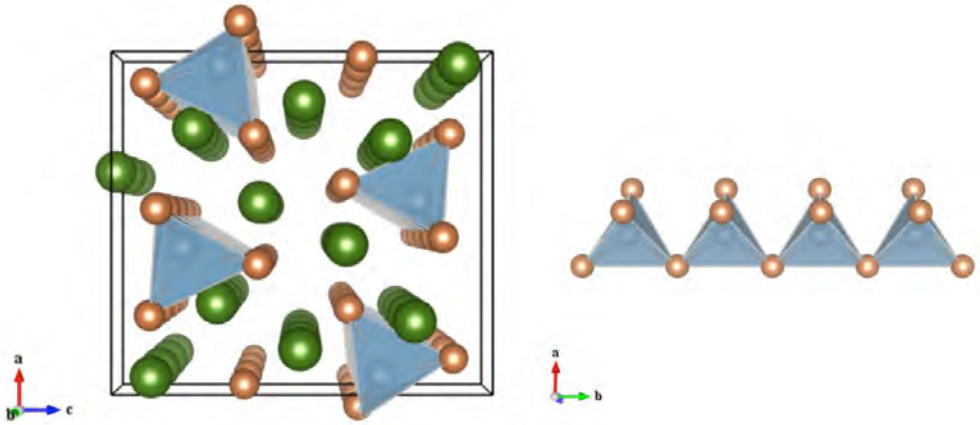

Figure 1.9: Crystal structure of the orthorhombic Zintl-phase Ca_3AlSb_3 (space group *P*nma) viewed along the *b*-direction (left). Ca atoms are green, Al atoms blue, and Sb atoms are orange. Al is tetrahedrally coordinated by Sb and forms linear chains (right) of corner sharing tetrahedra in the direction of *b*.[97]

seems to exist,[97] probably due to the similar electronegativities of antimony and aluminium. The chains are arranged in a pseudo hexagonal pattern with the Ca^{2+} cations between the chains, with a charge of -1 for the double bonded pnicogen atoms and a charge of -2 for the single bonded antimony.[97] This is in accordance with the *Zintl-Klemm-Busmann* concep (see Section 1.4.2). A charge of -1 for Sb leads to a valence electron concentration *VEC* of 6, which has to form two bonds according to the octet rule, while a charge of -2 leads to a *VEC* of 7 resulting in one bond. The aluminium has to have a valence state of -1, leading to a *VEC* of 4, which results in the observed tetrahedral coordination.

The Zintl-phase Ca_3AlSb_3 has recently been investigated for its thermoelectric transport properties and the electronic and thermal transport properties have been reported.[95] Through substitution of sodium for calcium, control and optimization of the hole carrier concentration

Table 1.3: Crystallographic data of Ca_3AlSb_3.[97]

Space group	a / Å	b / Å	c / Å	Z
*P*nma	12.835(5)	4.489(2)	14.282(5)	4
Atoms	**Wyckoff**	**Position**	**Point symmetry**	**Occupation**
Sb1	4c	(0.0393, $\frac{1}{4}$, 0.3509)	.m.	1.0
Sb2	4c	(0.1129, $\frac{1}{4}$, 0.8890)	.m.	1.0
Sb3	4c	(0.2555, $\frac{1}{4}$, 0.6199)	.m.	1.0
Ca1	4c	(0.2711, $\frac{1}{4}$, 0.2806)	.m.	1.0
Ca2	4c	(0.8487, $\frac{1}{4}$, 0.5050)	.m.	1.0
Ca3	4c	(0.0598, $\frac{1}{4}$, 0.1104)	.m.	1.0
Al	4c	(0.0659, $\frac{1}{4}$, 0.7032)	.m.	1.0

Table 1.4: Crystallographic data of Sr_3GaSb_3.[99]

Space group	a / Å	b / Å	c / Å	β / °	Z
$P2_1/n$	11.762(4)	14.509(5)	11.749(4)	109.96	8
Atoms	Wyckoff	Position	Point symmetry	Occupation	
Sr6	4e	(0.0772, 0.0665, 0.1638)	1	1.0	
Sb6	4e	(0.1099, 0.7587, 0.3988)	1	1.0	
Sb1	4e	(0.1148, 0.0908, 0.4263)	1	1.0	
Ga2	4e	(0.1292, 0.2450, 0.3219)	1	1.0	
Sr2	4e	(0.1370, 0.7502, 0.1579)	1	1.0	
Sr3	4e	(0.1395, 0.4291, 0.1817)	1	1.0	
Sb5	4e	(0.1556, 0.4001, 0.4498)	1	1.0	
Sr1	4e	(0.3504, 0.5758, 0.0230)	1	1.0	
Sb4	4e	(0.3658, 0.2372, 0.3199)	1	1.0	
Ga1	4e	(0.3719, 0.0911, 0.1888)	1	1.0	
Sr5	4e	(0.4041, 0.2836, 0.0915)	1	1.0	
Sb3	4e	(0.6089, 0.0936, 0.2046)	1	1.0	
Sr4	4e	(0.6187, 0.4044, 0.4622)	1	1.0	
Sb2	4e	(0.6496, 0.4329, 0.2261)	1	1.0	

has been obtained, since sodium has one less valence electron to donate compared to calcium which leads to the introduction of holes as charge carriers. Ca_3AlSb_3 was found to have an exceptionally low lattice thermal conductivity (0.6 $Wm^{-1}K^{-1}$ at 1050 K), due in large part to its complex unit cell. The combination of a reasonable bandgap, good carrier concentration control, and low thermal conductivity yields a thermoelectric figure of merit of 0.8 at 1050 K.[95]

1.4.4 Sr_3GaSb_3

This section is in parts an adapted reproduction, from *E*nergy Environ. Sci. **2012**, 5, 9121-9128.[100] Reproduced with permission of The Royal Society of Chemistry Copyright 2012.

Sr_3GaSb_3 is the only compound known to crystallize in a unique, chain-based structure that, according to Schäfer *et al*., can be considered a connecting link between the structures based on either linear chains or isolated tetrahedra-pairs formed by all other known A_3MPn_3 compounds (A = Ca, Sr, Ba, M = Al, Ga, In, and Pn = P, As, Sb).[99] The monoclinic structure, with 56 atoms per unit cell, of Sr_3GaSb_3 (space group $P2_1/n$) contains infinite, close packed, non-linear chains of corner sharing tetrahedra, characterized by four-tetrahedra repeat units, as shown in Figure 1.10 a). This four-tetrahedra periodicity in Sr_3GaSb_3 leads to a larger unit cell than that of Ca_3AlSb_3, which is only one tetrahedron wide along the chain direction. The chains in Sr_3GaSb_3 are aligned along the [101] direction, shown pointing into the page in Figure 1.10 b). A single chain is highlighted in red. Note that while the chains appear to overlap with nearby chains to form zigzagging planes, staggering along the [101] direction prevents strong interactions between neighboring chains.

In accordance with the *Zintl-Klemm-Busmann* concept for Ca_3AlSb_3, Sr_3GaSb_3 forms these tetrahedra resulting in a valence-balanced compound. While the basic bonding environment

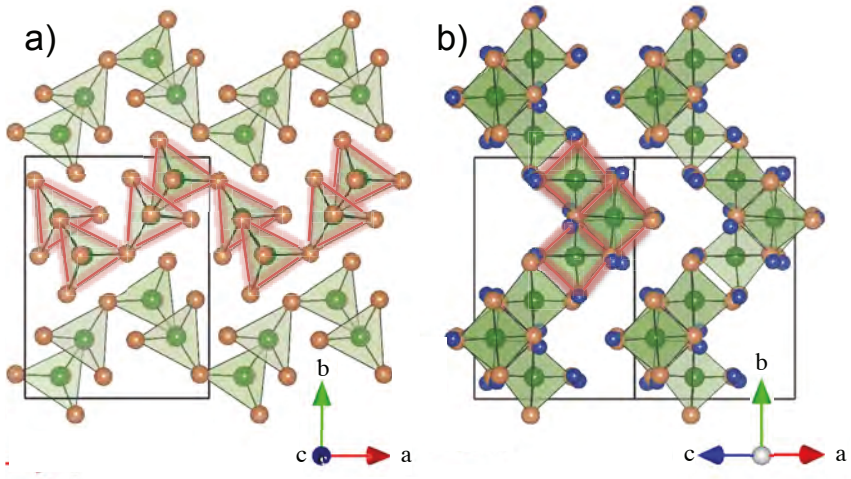

Figure 1.10: a) Sr_3GaSb_3 contains unique chains of corner-sharing $GaSb_4$ tetrahedra, formed from four-tetrahedra repeat units. Ga atoms are green, Sb are orange, and Sr atoms are not shown. b) The structure of Sr_3GaSb_3 viewed down the [101] axis, with chains going into the page (Sr atoms shown in blue). In both orientations, a single chain is highlighted in red.[100]

is the same as in the Ca_3AlSb_3 compound, the bigger size of the Sr^{2+} cation inevitably leads to a different structure, compared to Ca_3AlSb_3.

1.5 Summary of Research and Motivation

This thesis addresses the structural and thermoelectric properties of materials and tries to link the structure to the properties in Zintl compounds and quaternary copper selenides. Different materials compositions are investigated, the influence of different dopants considered, within transport models from common solution to the Boltzmann transport equation, and effects of structural and micro structural aspects on the thermoelectric transport are discussed.

For most of this work, the compound $Cu_2ZnGeSe_4$ and its solid solutions are considered. This class of compounds has a high structural robustness regarding the substitution with different elements,[86] which should inevitably lead to the possibility of precise doping in these materials to obtain an optimum charge carrier concentration. Combined with the low intrinsic thermal conductivities of these compounds an attempt is made to investigate and to institute a whole, new range of possible thermoelectric materials. Different materials compositions are investigated in order to combine structural and doping effects for a thorough characterization of their impact on the materials properties. First the solid solution $Cu_{2+x}Zn_{1-x}GeSe_4$ is investigated for its transport properties, upon the substitution of Zn^{2+} with Cu^{+} and the introduction of charge carriers. It is shown that the substitution not only introduces holes, but also creates a charge imbalance in this material, leading to a phase segregation, which in turns lowers the thermal conductivity in this material.

Then the system $Cu_2Zn_{1-x}Fe_xGeSe_4$ is considered. The isoelectronic substitution of Zn with Fe and the inherent structural complexity resulting from alloying influences the thermal transport properties greatly. To finalize the analysis of this class of compounds, the solid so-

lution $Cu_{2+x}Zn_{1-x-y}Fe_yGeSe_4$ is characterized in an attempt to combine the previous results, showing a certain degree of band engineering, leading to a dependence of the effective mass on the composition.

In addition to the work on the $Cu_2M^{II}GeSe_4$ compounds, this thesis discusses the transport in the Zintl compounds Ca_3AlSb_3 and Sr_3GaSb_3. The solid solutions of $Ca_3Al_{1-x}Zn_xSb_3$ and $Sr_3Ga_{1-x}Zn_xSb_3$ were synthesized and the thermoelectric transport properties measured. The influence of the grain size and the grain boundaries on the transport is discussed and an attempt will be made to relate the difference of the thermal transport properties of both compounds to the difference in their crystal structures.

Zintl compounds, characterized by covalently bonded "substructures," surrounded by highly electropositive cations, have recently attracted attention due to their often complex crystal structures.[19, 89] In general, the lattice thermal conductivity of Zintl compounds trends with unit cell complexity;[101, 102] e.g. $Yb_{14}AlSb_{11}$, containing 104 atoms per unit cell, exhibits one of the lowest known lattice thermal conductivities of any bulk material.[91] In contrast, the electronic mobility in Zintl compounds is more difficult to predict, though the nature of the covalently-bonded substructure is thought to play a major role. For example, a relatively high electronic mobility has been demonstrated in AM_2Sb_2 (A = alkaline or rare earth, M = transition metal) compounds which form 2-dimensional covalent planes ($\mu \sim 100\,cm^2V^{-1}s^{-1}$),[103, 104, 105], while $Yb_{14}AlSb_{11}$, characterized by isolated $AlSb_4$ tetrahedra and Sb_3 moieties, exhibits extremely low carrier mobility ($\sim 5\,cm^2V^{-1}s^{-1}$).[91] This is not true in all cases however; despite highly covalent, 3-dimensional anionic structures, the clathrate compounds generally do not exhibit high carrier mobility, due to disorder on the anionic sites.[54, 106]

Bridging these well-characterized 3-, 2-, and 0-dimensional structures are the relatively little-known 1-dimensional, chain-forming Zintl compounds. The Zintl compounds Ca_3AlSb_3 and Sr_3GaSb_3 form distinct structures, characterized by infinite chains of corner-sharing $AlSb_4$ or $GaSb_4$ tetrahedra, respectively. While these compounds exhibit similar crystal structures, Sr_3GaSb_3 has twice as many number of atoms per unit cell and a significantly higher density compared to Ca_3AlSb_3. Their similar but distinct crystal structures, the possibility of doping and therefore optimized carrier concentrations provide a good model system to relate structure to thermoelectric properties in this class of compounds.

2 Experimental Methods

2.1 Summary

This chapter discusses the synthesis and characterization of the pertinent materials of this thesis and the synthetic procedures for the different materials are given in detail in the first part of the chapter. The quaternary copper selenides were synthesized via a classical "shake and bake" route and mechanical alloying has been employed for the synthesis of the Zintl phases.

The last section focuses on the different characterization techniques and the instruments that were used for the chemical characterization as well as the characterization of the transport properties. While some techniques will only be roughly described, a more thorough description of the transport measurements will be provided.

2.2 Synthesis

The synthesis of inorganic, crystalline solids is generally limited by mass diffusion. The primary goal during synthesis is thus to reduce the time for diffusion to occur and therefore for the atoms to react with each other. In general, the diffusion time (τ_D) is given by:[7]

$$\tau_D = l_D^2 / D_M \, , \tag{2.1}$$

where l_D is the diffusion length and D_M is the mass diffusion coefficient. Since the diffusion coefficient has an energy activated behavior in a solid, synthesis is often employed at high-temperatures, which results in relatively large diffusion coefficients. This is sometimes called the "shake and bake" route, which employes thorough mixing of the elements followed by high temperature annealing steps to obtain phase pure compounds. One alternative to this route is the reduction of l_D, which can be achieved via mechanical alloying (or high energy ball-milling).

The final synthetic step is the sintering of powders to produce dense samples that can be characterized by a variety of techniques. The samples discussed in this work were sintered via pressure-assisted sintering, or hot pressing (for details see Section 2.2.3).

2.2.1 Quaternary Copper Selenides

$\mathbf{Cu_{2+x}Zn_{1-x}GeSe_4}$

This section is an adapted reproduction, from *J.* Am. Chem. Soc **2012**, 134, 7147-7154.[55] Reproduced with permission of the American Chemical Society Copyright 2012.

Bulk samples of polycrystalline $Cu_{2+x}Zn_{1-x}GeSe_4$ with compositions of x = 0, 0.025, 0.05, 0.075, and 0.1 were prepared via solid state reactions using elemental powders of Cu (Alfa Aesar, 99.999 %), Zn (Sigma Aldrich, 99.995 %), Ge (Chempur, 99.99 %), and Se (Alfa Aesar, 99.999 %). Phase purity of the starting materials was verified by X-ray diffraction and all synthetic procedures were carried out in a N_2 dry box. Annealing was performed in evacuated quartz ampoules, which were preheated at 1073 K under dynamic vacuum for 5 hours to ensure dry conditions.

The starting elements were thoroughly ground, sealed in quartz ampoules, heated to 923 K at 5 K/min, and annealed for 48 hours. The ampoules were cooled at 5 K/min and the obtained materials were ground, sealed in quartz ampoules again, and then reannealed at 1073 K for 96 hours with the above mentioned heating and cooling rates. It was found that the second annealing step was necessary to prevent the formation of the binary and ternary compositions. The quartz ampoules were 10-12 cm in length and 11 mm inner diameter with a maximum amount of 1.5 g of starting materials within the ampoule. This ampoule geometry was found to prevent significant loss of selenium at higher temperatures, indicated by red selenium precipitation present on longer ampoules. The obtained powders were hand ground and consolidated into 1-1.5 mm thick, 12 mm diameter disks at 873 K for 5 hours under a pressure of 40 MPa by induction hot pressing in high density graphite dies.[107] The resulting samples have more than 97 % theoretical density, determined from the geometric densities.

$Cu_2Zn_{1-x}Fe_xGeSe_4$

This section is an adapted reproduction, from *J.* Am. Chem. Soc **2013** - accepted manuscript.[56] Reproduced with permission of the American Chemical Society Copyright 2013.

Bulk samples of polycrystalline $Cu_2Zn_{1-x}Fe_xGeSe_4$ with compositions of x = 0, 0.1, ..., 0.9, 1.0 were prepared via solid state reactions using elemental powders of Cu (Alfa Aesar, 99.999 %), Zn (Sigma Aldrich, 99.995 %), Fe (Alfa Aesar, 99.998 %), Ge (Chempur, 99.99 %), and Se (Alfa Aesar, 99.999 %). Phase purity of the starting materials was verified by X-ray diffraction and all synthetic procedures were carried out in a N_2 dry box. Annealing was performed in evacuated quartz ampoules, which were preheated at 1073 K under dynamic vacuum for 5 hours to ensure dry conditions.

The starting elements were thoroughly ground, sealed in quartz ampoules, and annealed in a first step for 48 hours at 923 K and 673 K, for $x < 0.4$ and $x \geq 0.4$, respectively. In a following second step, the harvested powders were reannealed for 96 hours at 1073 K and 873 K, respectively. Heating and cooling rates for all procedures in the horizontal tube furnaces were 5 K/min. It was found that the second annealing step was necessary to prevent the formation of the binary and ternary compositions. The quartz ampoules were 10-12 cm in length and 11 mm inner diameter with a maximum amount of 1.5 g of starting materials within the ampoule. This ampoule geometry was found to prevent significant loss of selenium at higher temperatures, indicated by red selenium precipitation present in longer ampoules. The obtained powders were hand ground and consolidated into 1-1.5 mm thick, 12 mm diameter disks at 873 K for 5 hours under a pressure of 40 MPa by induction hot pressing in high density graphite dies.[107] The resulting samples have more than 95 % theoretical density,

determined from the geometric densities.

$Cu_{2+x}Zn_{1-x-y}Fe_yGeSe_4$

Bulk samples of polycrystalline $Cu_{2+x}Zn_{1-x-y}Fe_yGeSe_4$ with compositions of x = 0.025 and y = 0.975, 0.8, 0.7, and 0.6 were prepared via solid state reactions using elemental powders of Cu (Alfa Aesar, 99.999 %), Zn (Sigma Aldrich, 99.995 %), Fe (Alfa Aesar, 99.998 %), Ge (Chempur, 99.99 %), and Se (Alfa Aesar, 99.999 %). Phase purity of the starting materials was verified by X-ray diffraction and all synthetic procedures were carried out in a N_2 dry box. Annealing was performed in evacuated quartz ampoules, which were preheated at 1073 K under dynamic vacuum for 5 hours to ensure dry conditions.

The starting elements were thoroughly ground, sealed in quartz ampoules, and annealed in a first step for 48 hours at 673 K. In a following second step, the harvested powders were reannealed for 96 hours at 873 K. Heating and cooling rates for all procedures in the horizontal tube furnaces were 5 K/min. It was found that the second annealing step was necessary to prevent the formation of the binary and ternary compositions. The quartz ampoules were 10-12 cm in length and 11 mm inner diameter with a maximum amount of 1.5 g of starting materials within the ampoule. This ampoule geometry was found to prevent significant loss of selenium at higher temperatures, indicated by red selenium precipitation present in longer ampoules. The obtained powders were hand ground and consolidated into 1-1.5 mm thick, 12 mm diameter disks at 873 K for 5 hours under a pressure of 40 MPa by induction hot pressing in high density graphite dies.[107] The resulting samples have more than 95 % theoretical density, determined from the geometric densities.

2.2.2 Zintl-Phases

$Ca_3Al_{1-x}Zn_xSb_3$

This section is an adapted reproduction, from *J*. Mater. Chem **2012** 22, 9826-9830.[96] Reproduced with permission of The Royal Society of Chemistry Copyright 2012.

Bulk, polycrystalline $Ca_3Al_{1-x}Zn_xSb_3$ samples with compositions x = 0.00, 0.01, 0.02, and 0.05 were prepared by ball milling followed by hot pressing from elemental Ca (Sigma-Aldrich, 99.9%, dendritic pieces), Al (Alfa Aesar, 99.9%, shot), Zn (Alfa Aesar, 99.99%, shot), and Sb (Alfa Aesar, 99.9999%, shot). The elements were slivered into small pieces and loaded into stainless-steel vials with stainless-steel balls in an Ar dry box. The precursors were milled for 90min using a SPEX Sample Prep 8000 Series Mixer/Mill. The resulting powder was consolidated by induction hot pressing in high density graphite dies.[107] The die was slowly heated up to 973 K in two hours then held at this temperature at a pressure of 40 MPa for four hours, and five hours for x = 0.01, respectively. After a stress free two hour cool down, the resulting ingots were sliced into 1-1.5 mm thick disks, 12 mm in diameter, and characterized.

$Sr_3Ga_{1-x}Zn_xSb_3$

This section is an adapted reproduction, from *E*nergy Environ. Sci. **2012**, 5, 9121-9128.[100] Reproduced with permission of The Royal Society of Chemistry Copyright 2012.

Bulk, polycrystalline $Sr_3Ga_{1-x}Zn_xSb_3$ samples with compositions x = 0.00, 0.02, 0.05, 0.07, and 0.1 were prepared by ball milling followed by hot pressing, starting with elemental Sr, Zn, Sb, and GaSb. A GaSb precursor was synthesized from Ga (99.99 % shot, Sigma-Aldrich), and Sb (99.9999 %, shot, Alfa Aesar) in an evacuated quartz ampoule which was held at 1000 K for 12 hours followed by water-quenching. The refined X-ray diffraction data of the GaSb precursor is shown in the Supporting Information in Chapter 8. The elements (99 % pieces Sr, 99.99 % Zn shot, and 99.9999 % Sb shot from Alfa Aesar) were cut into small pieces and loaded with the GaSb precursor in stoichiometric amounts into stainless-steel vials, with stainless-steel balls in an Ar dry box. The mixtures were milled for 90 min using a SPEX Sample Prep 8000 Series Mixer/Mill. The resulting powder was consolidated by induction hot pressing in high density graphite dies.[107] The die was heated to 873 K in 2 hours and held for 1.5 hours, followed by a 30 min ramp to 973 K, at which point a pressure of 120 MPa was applied. These conditions were maintained for 2 hours, followed by a 2 hour pressure-free cool down. The resulting ingots, which were sensitive to air and moisture, were sliced into disks, using a low-speed diamond saw and non-aqueous lubricant, for characterization. The characterized specimens were roughly 1-2mm in thickness.

2.2.3 Pressure-Assisted Sintering

A rapid hot press has been employed for the consolidation of the powdered materials. The custom-built hot press system at Caltech has been developed to rapidly consolidate thermoelectric materials over a large temperature range (400-2300 K) within an inert atmosphere, this is referred to as rapid hot pressing. The heat in this system is provided by an induction coil operated in the RF range applied directly to a graphite die acting as a susceptor. Utilizing the hydraulic control system during processing, the consolidation of samples can be monitored to determine the minimum required pressing time.[107] The synthesized powder or ball-milled elemental powders are loaded into a high density graphite die in an argon glove box.

Before the power is loaded into a die, a grafoil sheet is used to cover the inside of the die, furthermore a circular piece of grafoil and a graphite anvil (spacer) are inserted into the base of the die. The settled powder is then compressed by hand using a long graphite plunger, after which the final grafoil, spacers, and (shorter) plunger are be inserted. In case of the copper selenides, more spacers have been used in order to obtain three consolidated disks in one press run. The basic setup of the pressing procedure and a picture taking at Caltech can be seen in Figure 2.1. After loading the sample into the die and placing the die in the induction coil, the chamber door is closed, a small load of about 5 MPa, and a vacuum is applied to the chamber. When an acceptable vacuum has been reached, the desired load is applied to the die, the chamber is backfilled with Ar and flowed through the chamber, and the induction heating power supply is turned on and heating begins.

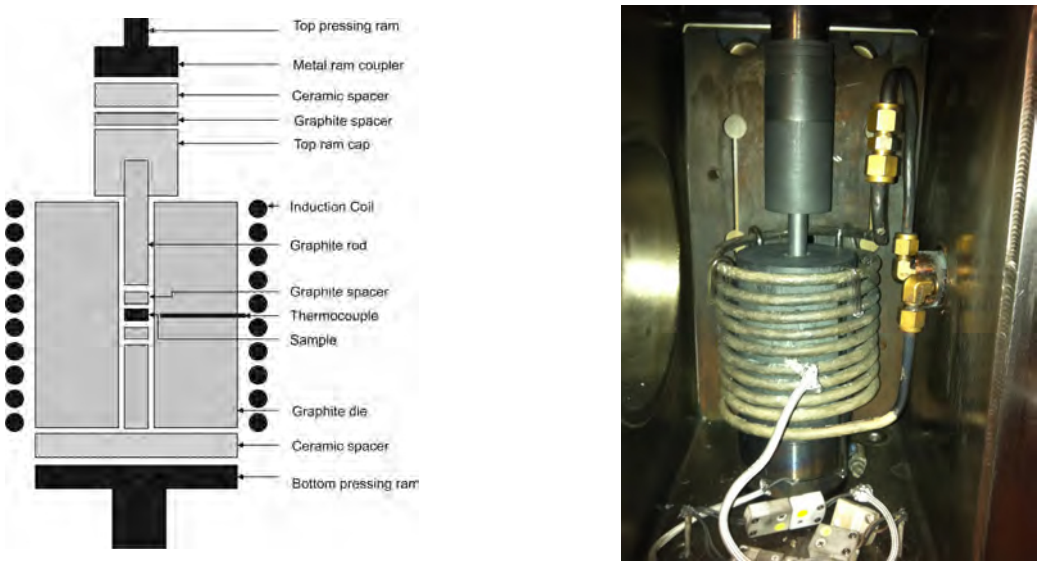

Figure 2.1: Schematic of induction hot press setup (left) and picture of hot press taken at Caltech (right).[107] The powdered sample is loaded into the die and covered with grafoil on all sides. Pressure is attained with a graphite plunger and the induction coil is utilized to heat up the die.

2.3 Characterization

2.3.1 Chemical Characterization

X-ray diffraction measurements for the copper selenides were performed on a Siemens D5000 powder diffractometer with a Braun M50 position sensitive detector and $CuK_{\alpha 1}$ radiation [Ge (220) monochromator] with a step size of 0.0078°. Data were collected over a time of 14 hours. X-ray diffraction measurements on the Zintl-phases and high temperature X-ray diffraction were performed on a Philips PANalytical X'Pert Pro with CuK_{α} radiation and a step size of 0.0084°. The usual time for data collection was two hours. For the high temperature diffraction, the samples were kept at the target temperatures for 30 min before the measurement started, in order to ensure equilibrium conditions. Rietveld and Pawley refinements were performed with TOPAS Academic V4.1,[108] applying the fundamental parameter approach, as implemented in TOPAS, using the crystallographic data from Section 1.4. The instrumental measurement uncertainty for the determination of the lattice parameters is approximated to be 0.003 Å.

Scanning electron microscopy (SEM) images and energy-dispersive X-ray spectroscopy (EDS) of the consolidated materials were taken using a Zeiss 1550 VP SEM in the Quadrant Back Scattering Detector (QBSD or BSE) and the Secondary Electron Detector (SE2) mode. For scanning electron microscopy, the samples were embedded in epoxy including graphite as a conductive filler, and then polished with different grid size to achieve smooth surfaces for the measurement. The sequential arrangement was: sanding paper with 240 grid, then 400, and 600 followed by 800. Afterwards pastes with polishing particles from 3 μm to 0.3 μm are used. For the study of grain sizes via fractured surfaces of the samples, the disks were broken prior to a measurement and directly mounted for SEM.

Optical absorption spectra of the roughened consolidated disks were measured at room temperature by a Cary 5000 UV-visible-near-IR spectrometer equipped with an integrating sphere. Absorption coefficients were calculated from the diffuse reflectance using the Kubelka-Munk function.

Combined thermogravimetric analysis (TGA) and differential scanning calorimetry (DSC) were performed using a Netzsch STA 449.

2.3.2 Characterization of Transport Properties

Thermal diffusivity was measured using a Netzsch laser flash diffusivity instrument (LFA 457), samples were coated with a thin layer of graphite to maximize the samples' emissivity and absorptivity to obtain strong radiation signals in the measurement. The data were analyzed using a Cowan model with pulse correction. Heat capacity (C) was estimated using the method of Dulong-Petit (C = 3R, k_B per atom) and theoretical densities were calculated from the molar mass and the lattice parameters for each composition obtained from X-ray diffraction. The Seebeck coefficient was calculated from the slope of the voltage vs. temperature gradient measurements from Chromel-Nb thermocouples.[109] Electrical resistivity, Hall coefficient, and carrier concentration were measured using the Van der Pauw technique under a reversible magnetic field of 2 T for the copper selenides and 1 T for the Zintl phases using pressure-assisted contacts. A current of 20 mA has been used to obtain Hall data of the copper selenides and 100 mA for the Zintl phases. All measurements were performed under dynamic vacuum and on multiple samples for each composition. Shown measurement data represent both heating and cooling data. The combined uncertainty for all measurements involved in zT determination is ~20 %. Normal and shear ultrasonic measurements were performed at room temperature to extract the longitudinal and transverse sound velocities, respectively. Honey was used as the couplant on a *Panametrics NDT 5800* pulser/receiver, which was employed with a *Tektronix TDS 1012* digital oscilloscope. The measurements were performed in Prof. Bill Johnson's laboratory at Caltech.

The measurement techniques for the transport properties will be described in the following.

Seebeck coefficient

For a detailed description of the Seebeck coefficient metrology, for different measurement setups, and methods the reader is referred to the articles by Martin *et al*.[110] and Iwanaga *et al*.[109]. In principle, the measurement of the Seebeck coefficient of a bulk material is relatively simple. Knowing the temperature difference and the voltage between two points of a material gives the Seebeck coefficient, see Equation 1.3. There are a few primary requirements for "good" Seebeck coefficient measurements. First the voltage and temperature must be measured at the same location and at the same time, second the probes must be in very good thermal and electrical contact with the specimen, and third the occurring voltage should be low.[109, 110]

With the measurement setup of Figure 2.2, these requirements are believed to be met.[109] The disk shaped samples are loaded into the Seebeck system (Figure 2.2 c)) and lateral spring loading ensures a good thermal contact between the thermocouples and the sample. A piece

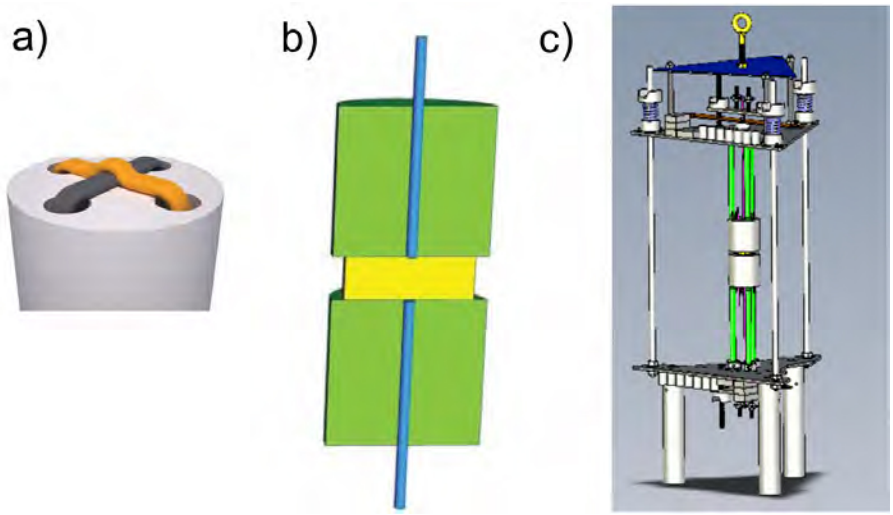

Figure 2.2: a) Schematic build-up of a thermocouple with a crossed-wire geometry. b) Schematic of the uniaxial 4-point method for the measurement of the temperature and voltage across the sample. The upper and lower green blocks represent the heaters and heat sinks, the center yellow block the sample, and the blue narrow rods represent the thermocouples. c) Schematic setup of the Seebeck instrument.[109] The heaters are used to create a temperature gradient along the sample and the thermocouples are simultaneously used to measure the voltage and temperature.

of grafoil is placed between the sample surface and the thermocouple to prevent chemical reactions at higher temperatures. The thermocouples (see Figure 2.2 a)), made of Chromel-Nb wires, are designed to measure the voltages and temperatures at the same location, to minimize errors.[109]

In this setup, the temperature of the top heater and the bottom heater (Figure 2.2 b)) oscillate around one value of temperature, which is used as the average value of the temperature. The corresponding ΔV are recorded and plotted vs. the corresponding ΔT. The slope of the voltage response to the temperature gradient yields the Seebeck coefficient. Typical deviations between data sets are within $\pm 5\ \mu V K^{-1}$ and an accuracy of 5 %-10 % is estimated for reproducible Seebeck data.[109]

Hall coefficient and Resistivity

The electrical conductivity and the Hall coefficient are important materials properties in the field of thermoelectrics, especially since transport properties are strongly dependent on the charge carrier concentration of a material. In a Hall measurement, the charge carrier concentrations can be directly calculated from the Hall coefficient. Through simultaneous measurement of the resistivity and the Hall coefficient, the Hall carrier mobility can be inferred. Especially the temperature dependence of the Hall mobility can be used to extract information about the scattering mechanism of the charge carriers.[111]

In the used instrument, the Van der Pauw technique is utilized for the measurement of the specific resistivity and Hall coefficient. Pressure assisted contacts are used to eliminate

the need for contact glue and paste, for a lower contact area (i.e. lower contact resistance) and to prevent chemical reactions with the sample. These contacts are placed on the edge of the sample disk and are all turned by 90 degrees in respect to each other (see Figure 2.3 left). To measure the resistivity, a current is passed between to adjacent contacts, while the voltage is measured between the other two. The Hall coefficient is obtained by passing a current diagonal across the sample in a magnetic field perpendicular to the sample plane. For a detailed description of the Hall measurement, the reader is referred to references [111] and [112].

While the electrical resistivity can be calculated from the resistance, the Hall coefficient R_H is calculated from the average change in resistance ΔR when changing the field ΔB:[111]

$$R_H = t\Delta R/\Delta B \,, \tag{2.2}$$

with the sample thickness t. Within the free electron or single parabolic band model, the Hall carrier concentration n_H can be calculated from:

$$n_H = \frac{1}{eR_H} \,, \tag{2.3}$$

with the elementary charge e. Especially at high temperatures where there is carrier activation across the band gap, the measured carrier concentrations tend to be overestimated. The Hall mobility μ_H is calculated from the Hall coefficient and electrical resistivity ρ:

$$\mu_H = \frac{R_H}{\rho} \,. \tag{2.4}$$

The typical measurement uncertainty is estimated to be 5 %. However, badly placed contacts and too thick samples tend to increase this error significantly. Therefore thin disks are mandatory for less noise in the Hall data.

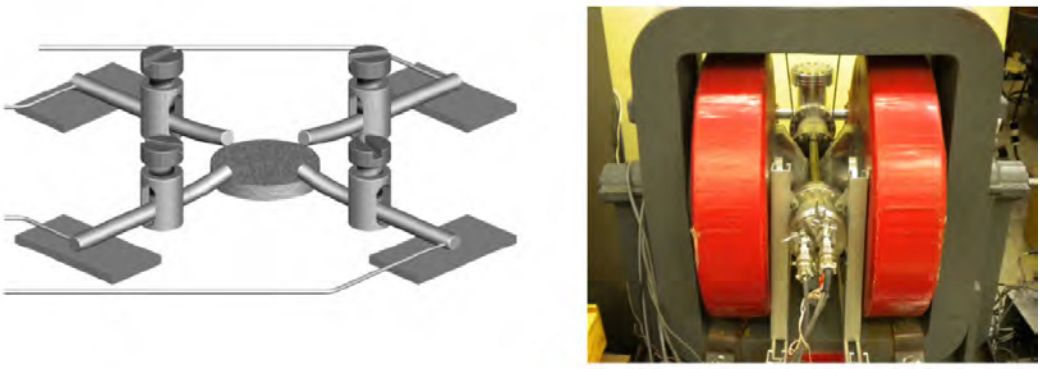

Figure 2.3: Schematic of the 4-point setup in Van der Pauw geometry, with pressure assisted contacts (left) and a picture of the Hall measurement system taken at Caltech (right).[111]

Thermal diffusivity

Thermal diffusivity was measured using the laser flash thermal diffusivity method (see Figure 2.4 a)). In this method the sample is irradiated by a short laser pulse. The temperature rise of the opposite side of the sample is then monitored using an IR detector and the thermal diffusivity d is determined from the sample thickness and the time constant of the temperature rise. The thermal diffusivity is related to the thermal conductivity κ as:[112]

$$\kappa = dDC \,, \tag{2.5}$$

with the heat capacity C and the density of the sample D. The sample disks and the standard are spray-coated with graphite on both sides, to minimize the influence of the reflectivity of the sample surface on the measurement.

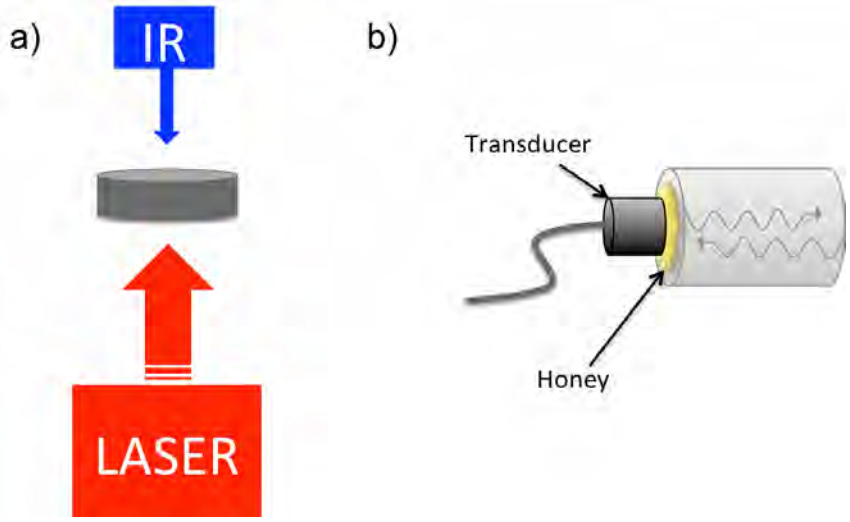

Figure 2.4: a) Schematic of the laser flash method. A LASER irradiates the sample via a short pulse, while the temperature of the opposite side of the sample is monitored by an IR detector. b) Schematic of the speed of sound measurement. The transducer introduces sound waves into the bulk sample, which travel to one end of the sample before they are reflected back. Honey is used as a couplant.

The measurement uncertainty of the laser flash diffusivity measurement is 3 %. However, errors in density and thickness of the samples will contribute to the overall measurement uncertainty of 5 %.

Speed of sound

Figure 2.4 ba) shows a schematic of the speed of sound measurement setup. A pulser/receiver introduces sound waves (frequency 1 kHz), longitudinal and transverse, respectively, into the bulk sample. These propagate to the end of the sample where they are reflected. The response is recorded via a digital oscilloscope. The speed of sound of the sample can be determined from the time between the pulse and the response and the thickness of the sample. Errors in the measurement mainly arise from the error of the thickness and if the two surfaces of

the sample disk are not parallel. These measurements are independent of the grain sizes of a material since sound waves are long wavelength phonons. However, the quality of the data generally depends on the quality of the samples and both surface defects and internal defects reduce the quality of the data. Therefore, the data was collected multiple times to minimize errors in the analysis.

2.4 Electronic Structure Calculations

Electronic structure calculations have been performed under collaboration by Gregory Pomrehn, within the Snyder group at Caltech. These results are shown in this thesis to address and further understand some of the transport properties presented in this work.

2.4.1 $Cu_2M^{II}GeSe_4$

This section is an adapted reproduction, from *J*. Am. Chem. Soc **2013** - accepted manuscript.[56] Copyright 2012 American Chemical Society.

Density Functional calculations were performed with the WIEN2K code [113] based on the full-potential linearized augmented plane-wave (FP-LAPW) method under the generalized gradient approximation (GGA) as parameterized by Perdew, Burke, and Ernzerhof (PBE).[114] A plane wave basis cutoff was $R_{mt}K_{max} = 7$, in terms of the smallest muffin tin radius and maximum plane wave vector respectively. Muffin tin radii for Cu, Zn, Fe, Ge and Se were 2.4, 2,5, 2.4, 2.3 and 2.1 a.u. respectively. Calculations were performed at the theoretical ground state lattice parameters as determined by a structural minimization of the unit cell. Atomic positions were relaxed to converged forces below 0.025 $eV/$ on each atom. An anti-ferromagnetic state was used for the initial magnetization of the density. Total energy convergence was achieved in a self consistent calculation using with a shifted 8x8x4 k-point mesh, which reduced to 32 symmetrically unique k-points. The modified Becke-Johnson (TB-mBJ)[115] semi-local exchange potential was employed, which has been shown to improve the band gap across a wide variety of semiconductors,[116] but may still fall short in these materials. This method was utilized to produce the density of states and electronic dispersions shown in this work.

2.4.2 Sr_3GaSb_3

This section is an adapted reproduction, from *E*nergy Environ. Sci. **2012**, 5, 9121-9128.[100] Copyright 2012 The Royal Society of Chemistry.

Density Functional calculations were performed with the WIEN2K code [113] based on the full-potential linearized augmented plane-wave (FP-LAPW) method under the generalized gradient approximation (GGA) as parameterized by Perdew, Burke, and Ernzerhof (PBE).[114] A plane wave basis cutoff of $R_{mt}K_{max} = 9$ was used, in terms of the smallest muffin tin radius and maximum plane wave vector respectively. Muffin tin radii were 2.4 a.u. for Sr and 2.5 a.u. for both Ga and Sb. Calculations were performed at the theoretical ground state lattice parameters as determined by structural minimization of the unit cell. Atomic positions were

relaxed to converged forces below 0.025 eV/Å on each atom. Total energy convergence was achieved in the self consistent calculations with a shifted 6x4x6 k-point mesh, which reduced to 36 symmetrically unique k-points. The modified Becke-Johnson (TB-mBJ) [115] semi-local exchange potential was employed, which has been shown to improve the band gap in *sp* bonded semiconductors.[116] This method was used to produce the density of states and electronic dispersions shown in this work.

3 Chemical and Structural Results

3.1 Summary

The purity and composition of the synthesized compounds is discussed in this chapter. Specifically powder X-ray diffraction is utilized to address phase purity. The $Cu_2M^{II}GeSe_4$ materials are all found to be phase pure, except for the composition $Cu_{2.1}Zn_{0.9}GeSe_4$, where the impurity phase $Cu_{2-x}Se$ is present with approximately 1-2 wt%, due to a charge imbalance. The Zintl phases Ca_3AlSb_3 and Sr_3GaSb_3 both show impurities of the binary and other ternary antimonides.

Rietveld and Pawley refinements have been performed on room temperature and high temperature X-ray diffraction data. While the Zintl phases and $Cu_{2+x}Zn_{1-x}GeSe_4$ do not exhibit a dependence of the lattice parameters on the composition, both $Cu_2Zn_{1-x}Fe_xGeSe_4$ and $Cu_{2+x}Zn_{1-x-y}Fe_yGeSe_4$ show a non-Vegard like behavior of the lattice parameter indicating a restructuring process, occurring upon substitution. Rietveld and occupational analyses of the compound $Cu_{2+x}Zn_{1-x}GeSe_4$ show a cation deficiency on their specific lattice sites, indicative of an interstitial occupancy of Cu and Zn.

Scanning electron microscopy has been utilized to verify phase purity, investigate grain boundaries, and microstructures of the materials. For instance micrographs of the solid solution $Cu_{2+x}Zn_{1-x}GeSe_4$ show the impurity phase $Cu_{2-x}Se$, formed through a phase segregation, as nano sized particles located at the grain boundaries between the interfaces of the bulk material.

The chemical and structural information on the compounds, presented in this chapter, are crucial for the understanding of the electronic and thermal transport properties discussed in the following chapters, since the structures and microstructures strongly affect the transport in these materials.

3.2 $Cu_{2+x}Zn_{1-x}GeSe_4$

This section is an adapted reproduction, from *J.* Am. Chem. Soc **2012**, 134, 7147-7154.[55] Reproduced with permission of the American Chemical Society Copyright 2012.

All samples were checked for phase purity prior to any transport measurements and selected powder diffraction data is shown in Figure 3.1 for each composition. In all compositions with $x < 0.075$ all reflections can be indexed to $Cu_2ZnGeSe_4$ and no secondary phase is observed. However, the samples with the nominal composition of $Cu_{2.1}Zn_{0.9}GeSe_4$ show an impurity phase of $Cu_{2-\delta}Se$ with a weight percentage of 1-2 wt% indicated by Rietveld refinement. Complete diffraction data can be seen in the Supporting Information (Chapter 8). Lattice parameters were refined and no significant change was observed upon doping Zn^{2+}

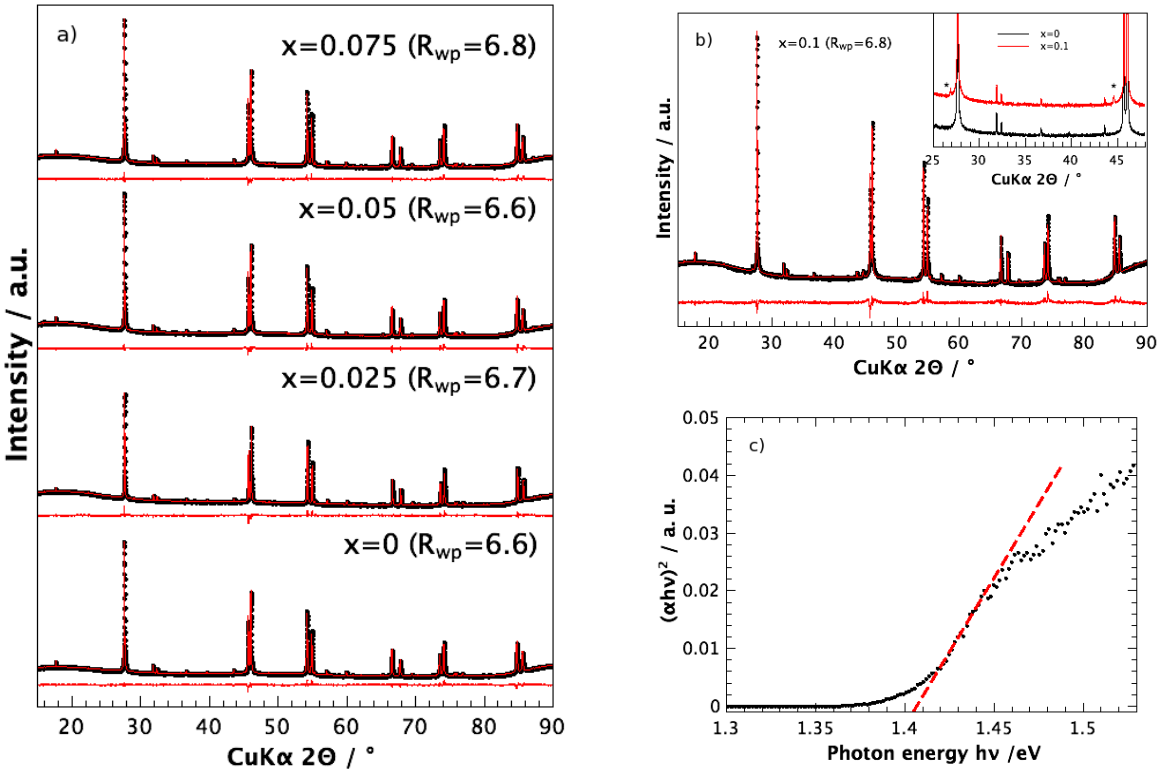

Figure 3.1: Powder diffraction data a) and b) for $Cu_{2+x}Zn_{1-x}GeSe_4$ including profile fit, profile difference and profile residuals from the corresponding Rietveld refinement. The intensities are plotted as the square root to show low intensity reflections as well. The inset in b) shows extra reflections indexed to $Cu_{2-\delta}Se$. Absorption spectrum c) of $Cu_2ZnGeSe_4$ with the band gap extrapolation indicated ($E_g \sim 1.4\,eV$).

with Cu^+ due to the relatively similar ionic radii of the species (see Figure 3.3 left). The refined parameters are given in Table 3.1.

An occupational analysis of the specific lattice sites shows occupancies of Cu^+ and Zn^{2+} below 100 % (see Figure 3.4 left). Back calculating the residual electron densities via Rietveld refinement shows a significant amount of the missing electron density on interstitial sites in this material (Figure 3.4 right). However, a detailed analysis of the interstitial occupancy cannot be performed via standard laboratory X-ray diffraction. Due to the same number of valence electrons of Cu^+ and Zn^{2+}, these cations exhibit the same scattering form factors for X-rays and can therefore not be distinguished via X-ray diffraction. In addition to the interstitial occupancy, anti site disorder of Cu and Zn cannot be ruled out, and it is therefore necessary to perform neutron diffraction and possible a pair distribution function analysis to further elucidate the underlying nature of the structure in this class of materials.

Combined TGA/DSC analysis of the material from ambient temperature to 1100 K revealed a slightly exothermic effect around 450 K corresponding to a phase transition (Figure 3.2), which has not been reported previously.[66, 65] To further investigate this phase transformation, X-ray diffraction has been performed on the consolidated disk at different temperatures (see Figure 3.3 right). The lattice parameters of the sample with the composition $Cu_2ZnGeSe_4$ (Table 3.2) increase linearly with temperature, which can be explained through thermal ex-

Table 3.1: Lattice parameters a, c, and occupation of Zn and Cu, and profile residuals R_{wp} for $Cu_{2+x}Zn_{1-x}GeSe_4$, from the corresponding Rietveld refinement.

x	a / Å	c / Å	occ (Zn)	occ (Cu)	R_{wp}
0.0	5.6128(2)	11.0480(2)	0.83	0.89	6.6
0.025	5.6084(3)	11.0397(6)	0.78	0.86	6.7
0.05	5.6139(7)	11.0470(1)	0.84	0.89	6.6
0.075	5.6130(1)	11.0489(5)	0.86	0.90	6.8
0.1	5.6096(4)	11.0542(2)	0.84	0.89	6.8

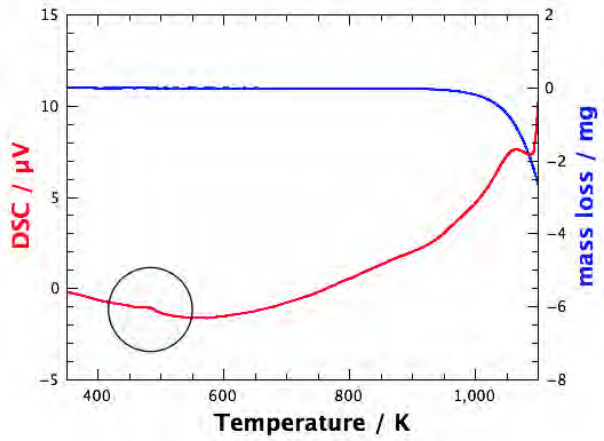

Figure 3.2: TGA/DSC data for $Cu_2ZnGeSe_4$, with the slightly exothermic effect (black circle) indicating a phase transition.

pansion of the unit cell. Therefore no structural phase transformation can be detected via standard laboratory X-ray diffraction. At present, the nature of this phase transformation remains unclear and a detailed investigation and analysis is necessary.

At room temperature the optical data in Figure 3.1 c) plotted as $(\alpha_A h\nu)^2$ against photon energy, where α_A is the absorption coefficient, h the Planck constant, and ν the wave number, gives an estimated optical band gap E_g of 1.4 eV, which is consistent with the reported data of this class of wide band gap material.[66]

Scanning electron microscopy of polished and fractured surfaces showed very high densities of the samples, in agreement with the high density values measured after hot pressing. Selected SEM micrographs of polished surfaces for different doping contents are shown in Figure 3.5. SEM micrographs are shown in backscattered (QBSD) and secondary electron mode (SE2) to distinguish between impurities, voids and the residue of polishing particles. Energy-dispersive X-ray spectroscopy was utilized to verify the stoichiometry.

Contrasts in the micrographs are due to different orientations of the grains of the compound $Cu_{2+x}Zn_{1-x}GeSe_4$ and grain sizes are between 10-20 μm. Scanning electron microscopy at higher magnifications reveal impurity phases present in the material that were undetected by X-ray diffraction. The impurity phase has been attributed to a segregation triggered by higher contents of Cu. Samples with the nominal composition of $Cu_{2.05}Zn_{0.95}GeSe_4$ show the

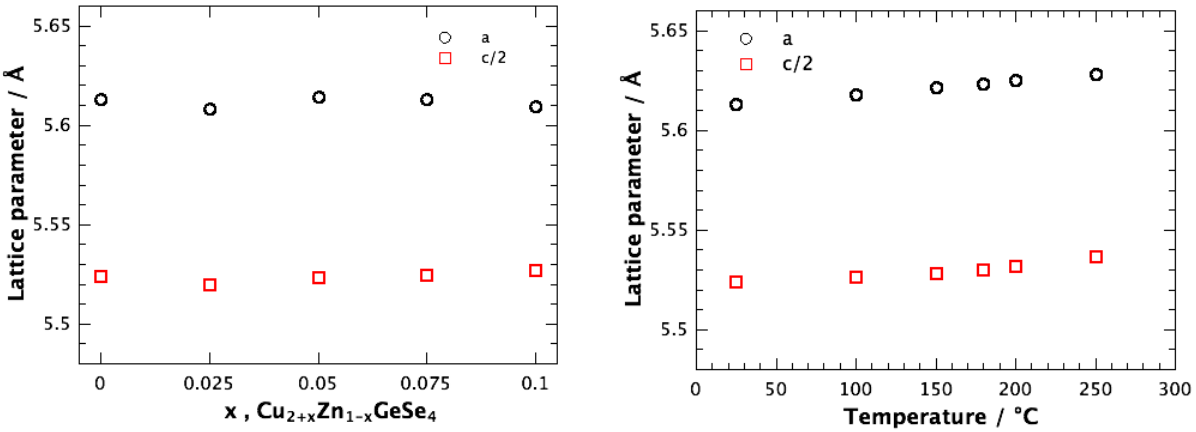

Figure 3.3: Left: Lattice parameter of $Cu_{2+x}Zn_{1-x}GeSe_4$ at room temperature with composition. No significant change is observed upon doping Zn^{2+} with Cu^{+} due to the relatively similar ionic radii of the species. Right: Lattice parameters of $Cu_2ZnGeSe_4$ with temperature. A linear increase with temperature is apparent, indicative of thermal expansion of the unit cell. No structural phase transformation is visible with laboratory X-ray diffraction.

two impurity phases CuSe and $Cu_{2-\delta}Se$ as white and black spots, respectively. However, higher Cu contents mainly lead to the formation of $Cu_{2-\delta}Se$ for $x = 0.075$ and $x = 0.1$, which is in accordance with the X-ray diffraction data for $x = 0.1$ (Figure 3.1). This phase segregation is possibly a result of a charge imbalance in the material. Substitution of Zn^{2+} with Cu^{+} leads to the formation of holes, or Se^{-} (for localized charges). For higher doping levels the excess of Cu leads to a phase segregation to form the energetically more stable species Se^{2-} in the secondary phase. It is possible that above a certain amount of excess Cu, all the extra Cu segregates in the form of $Cu_{2-\delta}Se$. The amount of the impurity phase should then be proportional to the amount of extra Cu. These impurities have grain sizes of 250 nm and smaller and are mainly located at the grain boundaries.

The Rietveld refinements of powder samples prior to the hot pressing procedure and data taken from consolidated samples do not show any significant texture in this material. We therefore believe that disks of this polycrystalline material are suitable for a thermoelectric characterization.

Table 3.2: Lattice parameters a, c, and profile residuals R_{wp} for $Cu_2ZnGeSe_4$ with temperature, from the corresponding Pawley refinement.

T / °C	a / Å	c / Å	R_{wp}
25	5.6128(2)	11.0480(2)	6.6
100	5.6176(2)	11.0523(5)	5.9
150	5.6213(2)	11.0565(5)	5.6
180	5.6235(1)	11.0600(4)	5.4
200	5.6251(2)	11.0635(7)	12.3
250	5.6281(2)	11.0737(6)	11.7

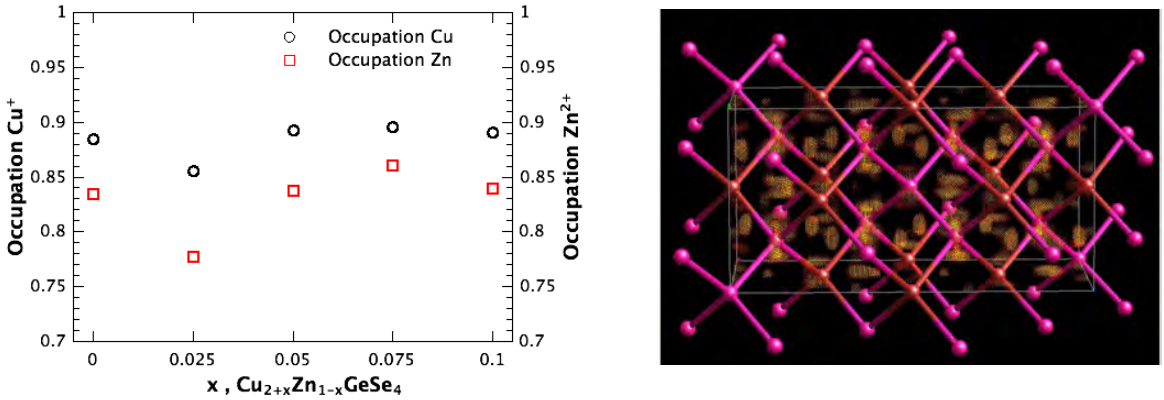

Figure 3.4: Left: Occupations of Cu^{+} and Zn^{2+} on their specific lattice sites in $Cu_2ZnGeSe_4$. Both elements show significantly lower occupations for the expected occupation of 100 %. Right: Residual electron density from the corresponding Rietveld refinement showing the missing Cu and Zn electron density on interstitial sites.

Significant weight loss does not occur until 973 K, while purged with Argon, however, measurements in dynamic vacuum lead to a significant evaporation of selenium above 723 K. The influence of different maximum temperatures on the consolidated disks can be seen in the Supporting Information in Chapter 8. Therefore, all measurements were performed up to 673 K to ensure thermal stability of the samples.

Table 3.3: Lattice parameters a, c, V, c/a-ratio, and profile residuals R_{wp} for $Cu_2Zn_{1-x}Fe_xGeSe_4$, from the corresponding Pawley refinement.

x	a / Å	c / Å	V / Å^3	c / a	R_{wp}
0.0	5.6121(2)	11.0480(2)	347.96	1.969	6.6
0.1	5.6080(3)	11.0536(2)	347.64	1.971	4.5
0.2	5.6036(2)	11.0661(1)	347.48	1.975	4.4
0.3	5.6079(9)	11.0935(3)	348.88	1.978	4.2
0.4	5.6022(6)	11.1046(3)	348.52	1.982	4.3
0.5	5.5879(6)	11.1025(1)	346.68	1.987	3.8
0.6	5.5901(5)	11.1122(1)	347.25	1.988	3.9
0.7	5.5827(2)	11.1176(2)	346.50	1.991	3.8
0.8	5.5918(2)	11.1076(1)	347.32	1.986	3.6
0.9	5.5956(0)	11.0924(8)	346.84	1.980	4.0
1.0	5.6014(6)	11.0703(8)	347.35	1.976	5.7

3.3 $Cu_2Zn_{1-x}Fe_xGeSe_4$

This section is an adapted reproduction, from *J.* Am. Chem. Soc **2013** - accepted manuscript.[56] Reproduced with permission of the American Chemical Society Copyright 2013.

All samples were checked for phase purity prior to any transport measurements and the refined powder diffraction data is shown in the Supporting Information (Chapter 8) for each

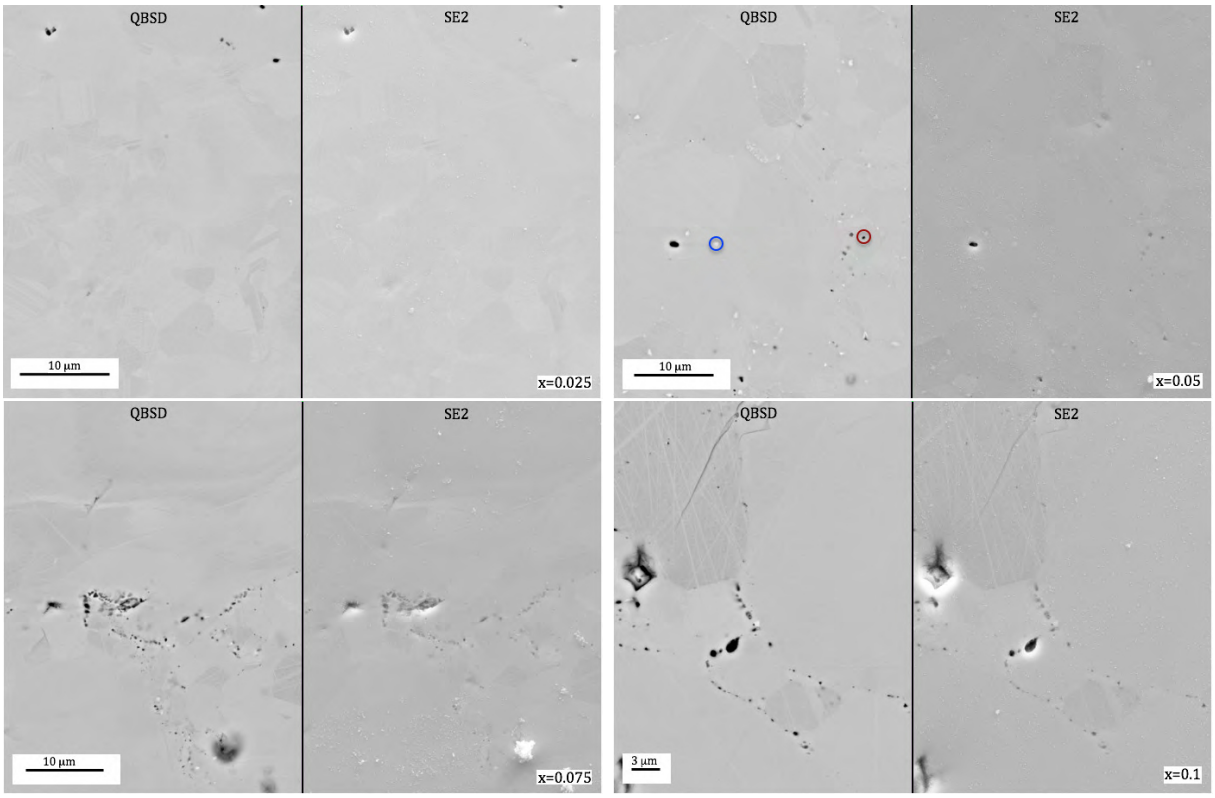

Figure 3.5: Scanning electron micrographs of polished surfaces for different doping contents x in $Cu_{2+x}Zn_{1-x}GeSe_4$ in backscattered (QBSD) and secondary electron mode (SE2). White spots (blue circle) and black spots (red circle) in samples with $x = 0.05$ reveal minor impurities of CuSe and $Cu_{2-\delta}Se$, respectively. Doping contents of $x = 0.075$ and $x = 0.1$ mainly show impurities of $Cu_{2-\delta}Se$ with sizes of 250 nm and smaller, mainly located at the grain boundaries.

composition. In all compositions all reflections can be indexed to $Cu_2Zn_{1-x}Fe_xGeSe_4$ and no secondary phases are observed. Refined lattice parameters are shown in Table 3.3. Powder X-ray diffraction data of samples prior to the hot pressing procedure and data taken from consolidated samples do not show any significant texture in this material. Therefore, properties measured on disks of this polycrystalline material are expected to be isotropic within expected experimental uncertainty and represent a scalar average of the tensor properties. Scanning electron micrographs for all compositions are shown in the Supporting Information (Chapter 8). Scanning electron microscopy confirms phase purity and similar microstructures with grain sizes between 10-20 μm throughout the whole composition range.

Pawley refinements of the powder X-ray diffraction data reveal a change in lattice parameters upon substitution of Zn with Fe as seen in Figure 3.6. Experimental c/a-ratios (see Figure 3.7) exhibit a non linear trend, showing an elongation of the c-axis with increasing Fe content until a maximum is reached at 70 % Fe content, where this trend becomes reversed. This non-Vegard like behavior has been observed by Caldera *et al.*, however they have assumed it to be not significant giving experimental uncertainty.[84] This discontinuity of the lattice parameters has also previously been observed in the solid solution $Cu_2Fe_{1-x}Zn_xSnS_4$.[80, 83, 117] A phase segregation due to the solubility limit being reached has been ruled out, since no splitting of reflections at higher diffraction angles is observed (see Figure 3.6). Furthermore

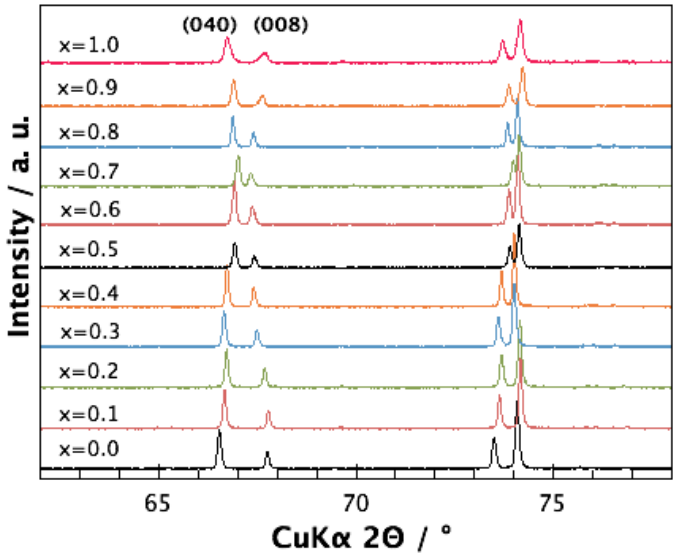

Figure 3.6: Reflections of selected Miller indices (040) and (008), showing the change in lattice parameters upon substitution. The reflections of the Miller indices do not cross over as expected for Vegard's law.

^{57}Fe Mössbauer spectroscopy on this class of compounds shows the existence of Fe^{2+} only, therefore ruling out the influence of Fe^{3+} on the crystal structure.[118]

Neutron diffraction studies by Schorr *et al.*[79, 81] on the chemically and structurally very similar solid solution $Cu_2Fe_{1-x}Zn_xSnS_4$ resolved this behavior of the lattice parameters and the c/a-ratio upon substitution, which can be described as a 3-stage cation restructuring process in the crossover from the stannite ($Cu_2ZnGeSe_4$, space group $I\bar{4}2m$) to kesterite ($Cu_2FeGeSe_4$, space group $I\bar{4}$) structure type (see Figure 3.8).[79, 81] Upon substitution of Zn, Fe starts to replace Zn on the 2*a*-site (0,0,0) as expected (Figure 3.8 b)). In the range of 0.35 $< x <$ 0.7, which is the main restructuring region, Cu depletes the 4*d*-site (0,$\frac{1}{2}$,$\frac{1}{4}$), occupying the 2*a*-site and forcing Zn on the 4*d*-site, while Fe holds its position (2*a*).[79, 81] At a substitution level of x = 0.7, the cations Fe^{2+}, Zn^{2+}, and Cu^{+} are equally distributed on the 2*a*-site (Figure 3.8 c)) and Cu and Zn on position 4*d*, exhibiting the highest c/a-ratio and highest local anisotropic structural disorder of this solid solution. With further decreasing Zn content, Cu starts to dominate position 2*a* and Fe and Cu occupy position 4*d* in $Cu_2FeGeSe_4$ (Figure 3.8 d)).[79, 81] The differences in bonding interaction between the cations and the anions lead to different bond lengths and bond angles, resulting in the observed trend in the lattice parameters.[79]

The electronic dispersion along lines of high symmetry from the DFT calculations are shown in Figure 3.9 for $Cu_2ZnGeSe_4$ in the stannite structure and $Cu_2FeGeSe_4$ in the kesterite structure. Both materials exhibit direct band gaps at the Brillouin Zone center. The stannite structured $Cu_2ZnGeSe_4$ exhibits a degeneracy of two at the valence band maximum. The two bands split apart away from the Gamma point and each exhibit parabolic behavior with averaged effective mass of 0.81 m_e and 0.23 m_e, respectively. The top valence band of $Cu_2FeGeSe_4$

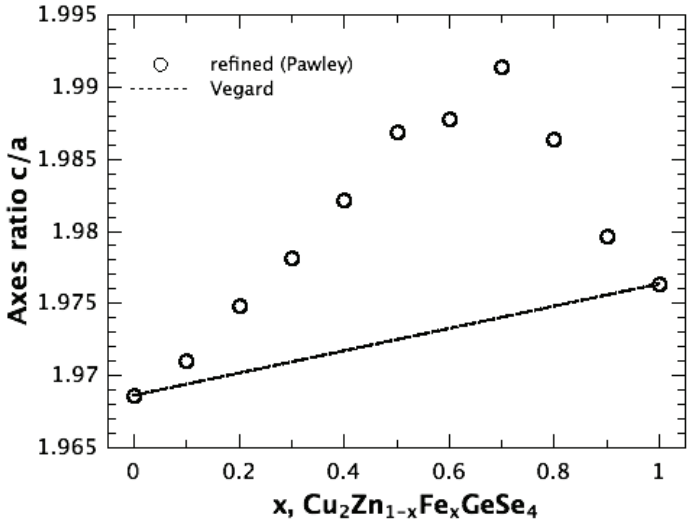

Figure 3.7: Lattice parameter ratio c/a with composition x of $Cu_2Zn_{1-x}Fe_xGeSe_4$, from a Pawley refinement. The broken line indicates the expected behavior following Vegard's law. A 3-stage cation restructuring process of Cu^+, Fe^{2+}, and Zn^{2+} results in the trend of the lattice parameters.

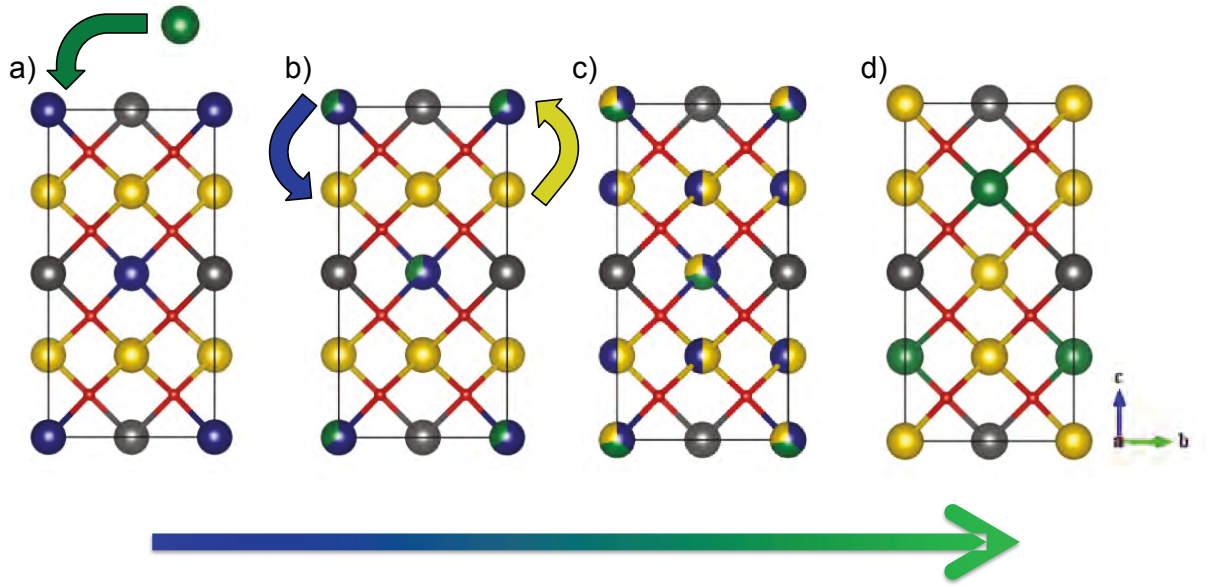

Figure 3.8: 3-stage cation restructuring process from the stannite ($Cu_2ZnGeSe_4$, a)) to kesterite ($Cu_2FeGeSe_4$, d)) structure type. Cu atoms are yellow, Ge atoms gray, Zn atoms are blue, Fe atoms green, and Se atoms are red. The sizes of the atoms in this ball-and-stick model are arbitrary and have been chosen for a better structural representation. With increasing Fe content, Fe starts to replace Zn (a). Then Cu depletes it's original site and occupies the Zn site, while forcing Zn on the Cu site, which results in the kesterite structure (d) type with further decreasing Zn content.

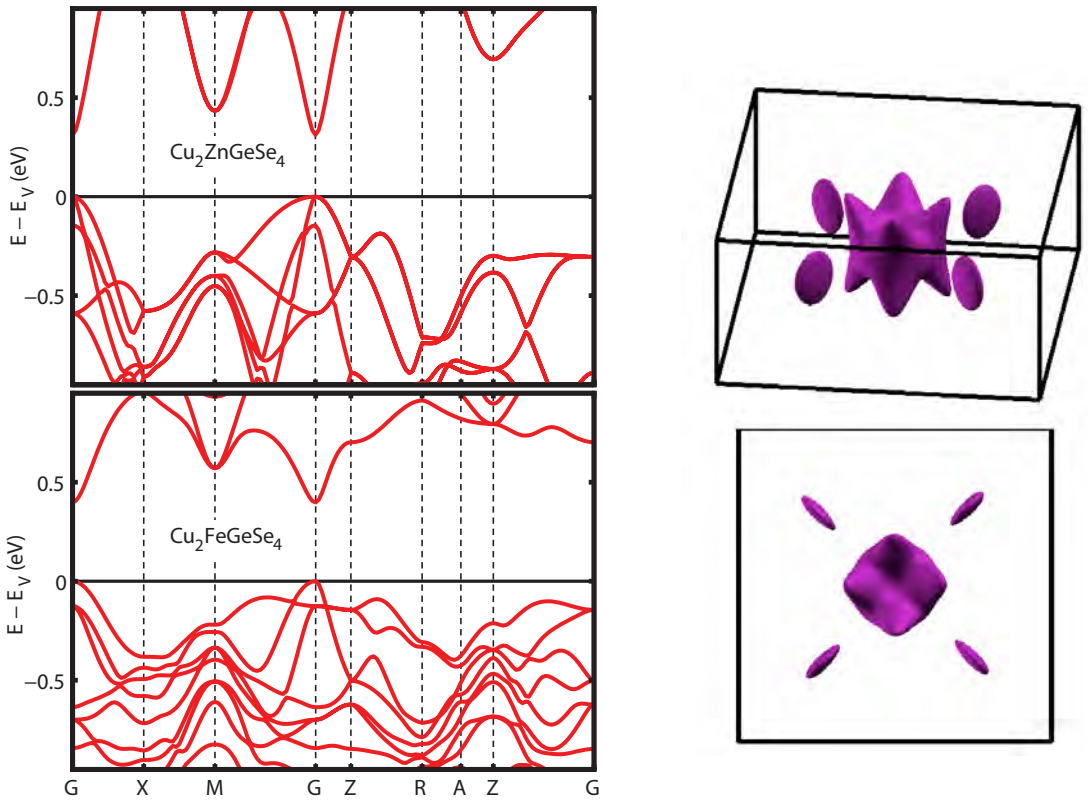

Figure 3.9: Left: Calculated band structures of stannite-type $Cu_2ZnGeSe_4$ (top) and kesterite-type $Cu_2FeGeSe_4$ (bottom). Note the heavy band, consisting mainly of Fe d-states, in the valence band contributing to the transport at higher carrier concentrations. Right: Fermi surface of kesterite - $Cu_2FeGeSe_4$ in the heavy band along k_x-k_y. The Gamma centred pocket shows non-parabolic character deeper in the valence band, while the four degenerate pockets represent the heavy valence band.

in the kesterite structure is a single band with parabolic band mass of 0.67 m_e. Around 82 meV below the valence band maximum there is another band with predominantly Fe d-state character. This band has a much heavier effective mass of 1.91 m_e and a symmetric degeneracy, N_V, of four. It is expected that this band would contribute to electronic transport due to its proximity to the valence band maximum.

3.4 $Cu_{2+x}Zn_{1-x-y}Fe_yGeSe_4$

For all compositions x was set to 0.025 and only the value of y has been altered throughout the series of solid solutions to obtain the material $Cu_{2.025}Zn_{0.975-y}Fe_yGeSe_4$. All samples were checked for phase purity prior to any transport measurements and the refined powder diffraction data is shown in the Supporting Information (Chapter 8) for each composition. In all compositions all reflections can be indexed to $Cu_{2.025}Zn_{0.975-y}Fe_yGeSe_4$ and no secondary phases are observed. Refined lattice parameters are shown in Table 3.4.

Pawley refinements of the powder X-ray diffraction data reveal a change in lattice parameters upon substitution of Zn with Fe as seen in Section 3.3. Experimental c/a-ratios (see Figure 3.10) exhibit a non linear trend, consistent with the trend seen and explained for $Cu_2Zn_{1-x}Fe_xGeSe_4$, which has been included for comparison.

3.5 Ca_3AlSb_3

This section is an adapted reproduction, from *J*. Mater. Chem **2012** 22, 9826-9830.[96] Reproduced with permission of The Royal Society of Chemistry Copyright 2012.

Following ball milling and hot pressing, $Ca_3Al_{1-x}Zn_xSb_3$ samples with x = 0.00, 0.01, 0.02, and 0.05 have geometric densities of at least 97% of the theoretical densities. As reported in Ref. [95], X-ray diffraction (Figure 3.11) and scanning electron microscopy reveal secondary phases of $Ca_5Al_2Sb_6$ and $Ca_{14}AlSb_{11}$ with 5-10 wt% and 2-5 wt%, respectively. SEM analyses of fracture surfaces reveals small grains ($< 1\,\mu$m in diameter) and porosity (0.1 μm in diameter) at the grain boundaries. However, the sample with the nominal composition of $Ca_3Al_{0.99}Zn_{0.01}Sb_3$ contains grains that are at least an order of magnitude larger, as shown with selected SEM micrographs in Figure 3.11. The larger grain sizes is possibly due to the longer pressing time for this sample. Complete XRD and SEM data can be found in the Supporting Information in Chapter 8. The relatively small grains found in all samples in this

Table 3.4: Lattice parameters a, c, c/a-ratio, and profile residuals R_{wp} for $Cu_{2.025}Zn_{0.975-y}Fe_yGeSe_4$, from the corresponding Pawley refinement.

y	a / Å	c / Å	c / a	R_{wp}
0.975	5.5940(2)	11.0755(1)	1.979	3.8
0.8	5.5937(2)	11.1089(1)	1.986	4.0
0.7	5.5846(1	11.1186(1)	1.990	4.1
0.6	5.5875(1)	11.1084(1)	1.988	4.5

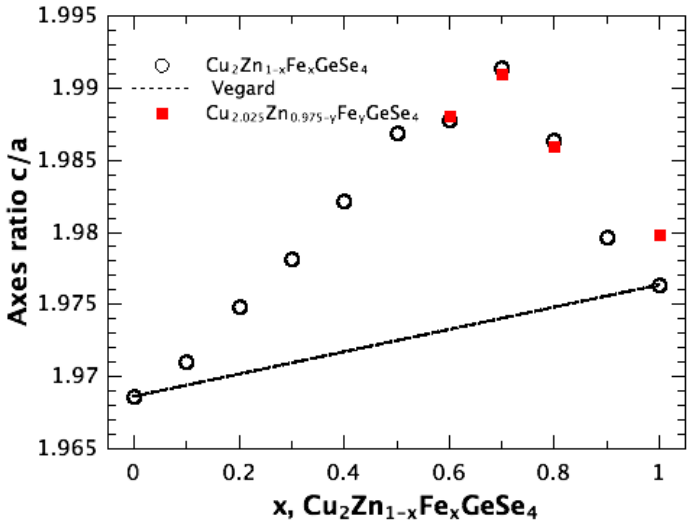

Figure 3.10: Lattice parameter ratio c/a with composition y of $Cu_{2.025}Zn_{1-y}Fe_yGeSe_4$ (red data points), from a Pawley refinement. The broken line indicates the expected behavior following Vegard's law. For comparison the data of $Cu_2Zn_{1-x}Fe_xGeSe_4$ has been included (black circles) and the x-axis has been labeled in respect to this solid solution. A 3-stage cation restructuring process of Cu^+, Fe^{2+}, and Zn^{2+} results in the trend of the lattice parameters.

study are in accordance with the broad profiles of the reflections in Figure 3.11 and therefore no significant change of the lattice parameters upon substitution with Zn can be observed.

3.6 Sr_3GaSb_3

This section is an adapted reproduction, from *E*nergy Environ. Sci. **2012**, 5, 9121-9128.[100] Reproduced with permission of The Royal Society of Chemistry Copyright 2012.

Following ball milling and hot pressing, the polycrystalline $Sr_3Ga_{1-x}Zn_xSb_3$ (x = 0, 0.02, 0.05, and 0.07) samples have geometric densities of $\sim$ 98% of the theoretical density. SEM analysis using backscattered electrons reveals small, light-colored precipitates (see upper left panel of Figure 3.12), identified by EDS as the Zintl phase Sr_2Sb_3. This phase appears to comprise approximately 1-3 vol% of each sample. X-ray diffraction confirms that Sr_3GaSb_3 and Sr_2Sb_3 were the only phases present in samples with x = 0.00 - 0.07 (shown in Figure 3.12). The inset shows a magnified view in which the most prominent Sr_2Sb_3 reflections are marked with asterisks. The fraction of this phase was comparable in each of the samples with x = 0.00 - 0.07. In the sample with nominal composition $Sr_3Ga_{0.9}Zn_{0.1}Sb_3$, additional phases were present, including $SrZn_2Sb_2$, indicating that the solubility limit of Zn in Sr_3GaSb_3 has been exceeded. The transport properties of this composition has therefore not been included in this thesis. In all samples, the grain size after hot pressing was extremely small, estimated from fracture surfaces to be in the sub-micrometer range (upper right panel in Figure 3.12), in accordance with the broad profiles of the XRD reflections. No obvious texturing was seen in the diffraction patterns. Complete XRD and SEM data can be found in the Supporting

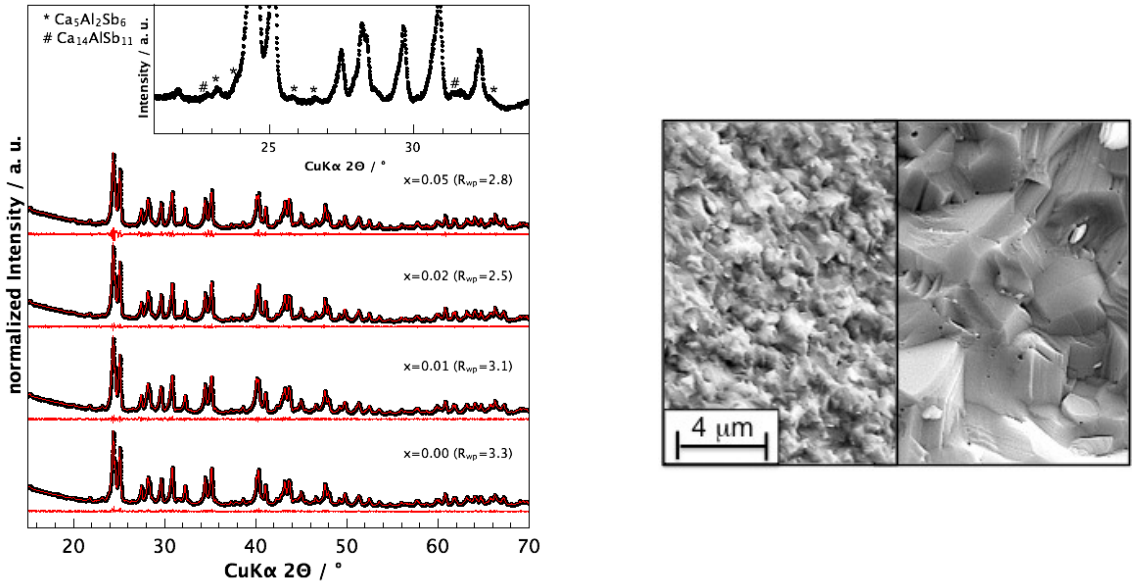

Figure 3.11: Left: X-ray diffraction data for $Ca_3Al_{1-x}Zn_xSb_3$ including profile fit, profile difference, and profile residuals from the corresponding Pawley refinement including the secondary phases of $Ca_5Al_2Sb_6$ and $Ca_{14}AlSb_{11}$. The inset shows the reflections indexed to the impurity phases, observed in all samples. Right: Selected SEM micrographs illustrating the different grain sizes of the samples. Smaller grains (left) for the compositions with x = 0.00, 0.02, and 0.05 and larger grain sizes for x = 0.01 (right). The scale bar is representative for both micrographs.

Information in Chapter 8.

Sr_3GaSb_3 forms a valence precise crystal structure that can be described within the Zintl formalism as follows: The highly electropositive Sr (3 Sr^{2+}) atoms donate their valence electrons to the anionic chains. Two of the Sb atoms making up the chains have only one covalent bond, leading to a valence state of -2, while one Sb atom is shared between two tetrahedra, leading to two covalent bonds and a valence state of -1. Assigning a valence state of -1 to the four-bonded Ga leads to overall charge balance and the formation of the covalent anionic chains.

The basic features of this simple bonding description are reflected in the calculated density of states, shown in Figure 3.13 a). The prominent Ga and Sb electronic states deep in the valence band (-4 to -6 eV) and at the conduction band minimum likely correspond to Ga-Sb bonding and anti-bonding interactions, respectively. The valence band maximum is dominated by Sb states, likely arising from non-bonding Sb lone-pairs. In contrast, the conduction band is formed primarily by Ga-Sb anti-bonding states and by Sr states at higher energies, consistent with the assumption that Sr donates its valence electrons to form the anionic substructure. A band gap of $\sim$ 0.75 eV is predicted, qualitatively consistent with the experimentally observed behavior described in Chapter 4.

The electronic band structure of Sr_3GaSb_3 is shown in Figure 3.13 b) in the k-space direction parallel to the $GaSb_4$ chains (Γ-$A_{[101]}$), and in the two perpendicular directions (Γ-Z and Γ-$A_{[\bar{1}01]}$). The k-space points Γ, A and Z are labeled in the Brillouin zone shown in the inset. The band structure is characterized by an indirect band gap ($\sim$0.75 eV) with the valence band

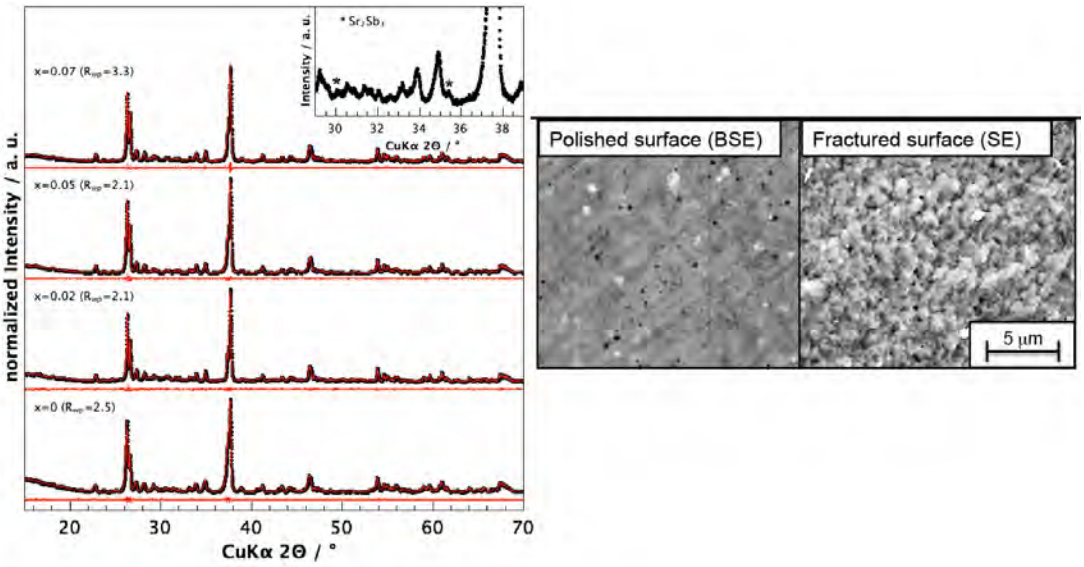

Figure 3.12: Left: X-ray diffraction data for $Sr_3Ga_{1-x}Zn_xSb_3$ including profile fit, profile difference, and profile residuals from the corresponding Pawley refinement including the secondary phase Sr_2Sb_3. The inset shows the reflections indexed to the impurity phase marked by asterisks. Right: back-scattered electron image of a polished Sr_3GaSb_3 sample reveals the secondary phase Sr_2Sb_3 as white specks, while secondary electron imaging of a fracture surface shows the very small grain size ($< 1\,\mu m$).

maximum at Γ and the conduction band minimum between Γ and Z. The upper and lower blue lines correspond to carrier concentrations of 10^{19} and 10^{20} holes/cm^3, respectively. At energies very close to the valence band maximum (0 to -0.1 eV), the dispersion is anisotropic, with the effective mass along the chains ($m^*_{[101]} = 0.18\,m_e$) smaller than the mass in the perpendicular directions ($m^*_{[\bar{1}01]} = 0.57\,m_e$ and $m^*_{[010]} = 0.66\,m_e$). In contrast, the two additional bands with maxima at $\sim$ -0.1 eV are nearly isotropic. When electrons are scattered primarily by acoustic phonons, as is the case in most known thermoelectric materials, the improvement in carrier mobility conferred by a light band mass outweighs the detrimental effect that low m^* has on α. In this case, the thermoelectric quality factor is given by $B \propto \frac{N_v}{m_i^* \kappa_L}$, where m_i^* is the mass of a single hole pocket along the conduction direction.[18, 25] This suggests that the light band mass in Sr_3GaSb_3, particularly in the direction of the chain substructures ($m^*_{[101]}$), may be advantageous.

The number of bands contributing to transport (N_v) at a given carrier concentration influences a material's figure of merit, as illustrated by the thermoelectric quality factor. If N_v is high, it is possible to simultaneously have light bands (small m_i^*) and large density of states effective mass. In Sr_3GaSb_3, only one band contributes to transport at energies very close to the valence band maximum. In heavily doped Sr_3GaSb_3 ($n > 10^{20}$ holes/cm^3), the contribution from the two bands with maxima at about -0.1 eV could potentially lead to $N_v = 3$.

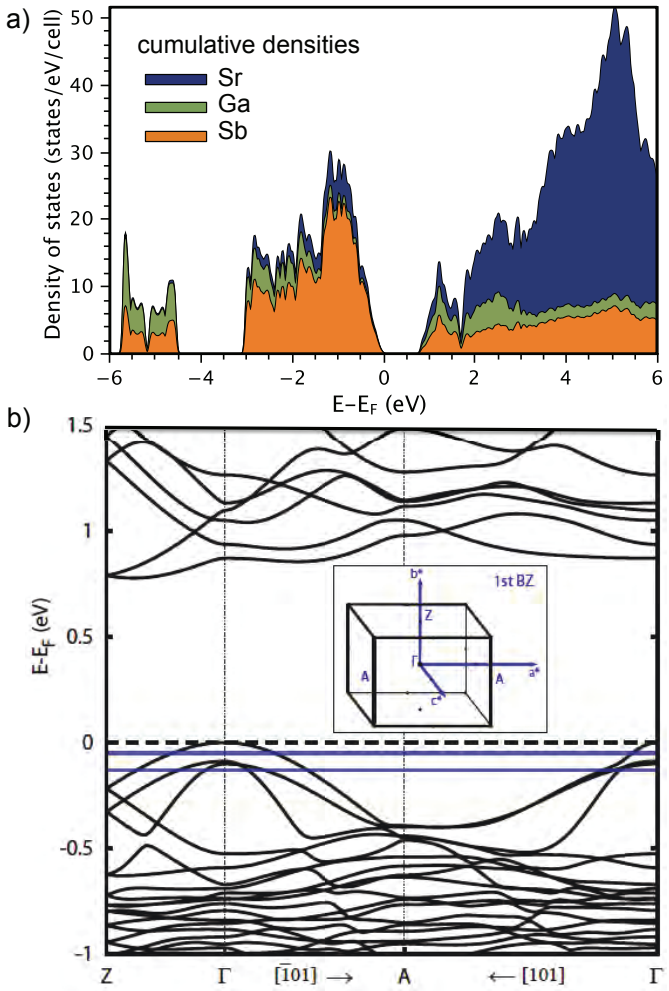

Figure 3.13: a) Density of states and b) band structure of Sr_3GaSb_3 reveal an indirect band gap of ~ 0.75 eV. The upper and lower blue lines correspond to carrier concentrations of 10^{19} and 10^{20} holes/cm^3, respectively. Inset: Brillouin zone of Sr_3GaSb_3 with selected k-space directions labeled.

4 Electrical Transport

4.1 Summary

This chapter starts with a basic introduction to electrical transport theory. The single parabolic band approximation will be introduced and with it the chemical potential, the density of states and effective mass of charge carriers within the parabolic band approximation. The different scattering types for carriers and the influence on the transport will be reviewed. Then the different solutions to the Boltzmann transport equations will be given for the electronic transport properties, which will be the foundation for the modeling of the transport in this thesis.

The substitution of Zn^{2+} with Cu^{+} introduces holes as charge carriers in the system leading to a lower thermopower and higher electrical conductivities. The resulting carrier concentrations deviate significantly from the charge carrier concentrations expected from simple charge counting, which can be attributed to the influence of the secondary phases in this system. Furthermore, a previously unknown insulator-to-metal like phase transformation is observed around 450 K in this solid solution.

In the solid solutions of $Cu_2Zn_{1-x}Fe_xGeSe_4$ and $Cu_{2+x}Zn_{1-x-y}Fe_yGeSe_4$ a partially unfilled, heavy Fe d-band contributes to the transport, supported with band structure calculations, which leads to higher carrier concentrations in a combination of intrinsic defects. Seebeck and Hall data suggest a significant change of the band effective masses, depending on the Fe content, which results in higher Seebeck coefficients.

Both, Ca_3AlSb_3 and Sr_3GaSb_3, exhibit non-degenerate intrinsic p-type semiconducting behavior showing an influence of the Zn content on the transport properties, due to higher carrier concentrations in the solid solutions. While both materials exhibit an exponential behavior of the temperature dependent Hall mobility due to barriers at the grain boundaries, e.g. oxide layers or secondary phases, an influence of the grain size on the mobility and the Hall carrier concentration can be found in the solid solution $Ca_3Al_{1-x}Zn_xSb_3$, which properties have been compared to recently published data of the sodium doped analogue.[95] Larger grain sizes lead to higher carrier mobilities due to a reduced scattering of the charge carriers on the grain boundaries.

4.2 Electronic Transport Theory

The following section is thought to give a rough overview over the basic concepts of the electronic transport in semiconductors. The concept of the single parabolic band will be highlighted and a short overview on the different scattering mechanisms will be provided. At last the common solutions of the Boltzmann transport equations, which have been employed

for the modeling of the important materials properties discussed in this chapter, will be given here. The following section is in parts an adapted reproduction of the Diploma thesis from Wolfgang Zeier, 2010.[85]

4.2.1 Electronic Transport in a Single Parabolic Band

The perhaps simplest model for the electrical conductivity of solids is the Drude model, where the electrons are described as a gas of electrons moving through the lattice of a solid. In this model, the electrical conductivity is given by a concentration of charge carriers n, which move into the direction of an applied electric field E with a drift velocity v_d. The drift velocity can be written as:[7]

$$v_d = \frac{e\tau E}{m^*} \,, \tag{4.1}$$

with the carried charge e, the effective carrier mass m^*, and the scattering relaxation time τ. The electrical current density J_e (charge per area per time) can be expressed through:

$$J_e = nev_d \,, \tag{4.2}$$

using Ohm's law for the electrical current density J_e (Equation 1.1):[7]

$$J_e = \sigma E \,,$$

leads to the electrical conductivity σ:[7]

$$\sigma = \frac{ne^2\tau}{m^*} \,, \tag{4.3}$$

showing the dependence of the electrical conductivity on the number of charged carriers, their effective mass, and the importance of the scattering relaxation time. The term $e\tau/m^*$ is defined as the mobility of the charge carriers μ, leading to a familiar expression for σ with $\sigma = en\mu$. However, in general, only the electrons near the electrochemical potential (within a few k_BT) and not all carriers in a band contribute significantly to the transport.

Solutions to the Boltzmann transport equation (BTE) are usually employed for the description and analysis of electronic transport. The electron distribution is described by the Fermi-Dirac distribution function f, which is an approximation for the non-equilibrium electron distribution, with:

$$f = (1 + exp[\epsilon - \eta])^{-1} \,. \tag{4.4}$$

Here ϵ stands for the reduced energy ($\epsilon = E/k_BT$) and η for the reduced electrochemical potential. The Fermi energy ϵ_F represents the highest occupied energy level at 0 K and the electrochemical potential is the energy at which $f = \frac{1}{2}$ for all temperatures above 0 K.[13]

Single Parabolic Band Model

One major assumption for the solutions of BTE is that the energies of the carriers can be described by an isotropic, parabolic dispersion relationship which is commonly referred to as

a parabolic band.

Band theory describes the motion of free, delocalized electrons as waves in a periodic lattice potential. Superposition of the Bloch functions lead to the band structure of a solid. In the chemical picture, the band structures and band gaps arise from the energy difference between atomic orbitals, or between bonding and antibonding interactions.[119] The energy of a band is a function of the wave vector $\vec{k}$ of the electrons and the wave vector is related to the momentum p of an electron via:[119]

$$\vec{k} = \hbar p \ , \tag{4.5}$$

with $\hbar = \frac{h}{2\pi}$. Plots of the energy vs. wave vector $E(\vec{k})$ are therefore useful for the discussion of the dynamics of electrons in solids.

Electrical conductivity arises when a band is partially filled and therefore the motion of electrons from an occupied to an unoccupied state becomes possible. This is how band theory differentiates between electrical insulators and conductors (at 0 K).[119]

The energy of an electron in the conduction band is given via the dispersion relationship, with the minimum energy of an electron in the band V_0:[119]

$$E(\vec{k}) = V_0 + \frac{\hbar^2 \vec{k}^2}{2m^*} \ . \tag{4.6}$$

This equation shows the origin of the term "parabolic band" due to the square of the wave vector. The density of states $N(E)$ for a parabolic dispersion relation under the assumption of $V_0 = 0$ is given by:

$$N(E) = \frac{(2m^*)^{3/2}}{2\pi^2\hbar^3}\sqrt{E} \ , \tag{4.7}$$

and increases as the square root of the energy. This model is commonly referred to as the single parabolic band model (SPB), if only one band contributes to the transport.

Here the electrons are treated within the free electron model, while the concept of the effective mass m^* is used to account for the electrons interaction with the lattice.[119] Electrons with a small effective mass behave as mobile particles. While "heavy" electrons have lower mobilities and are therefore less itinerant and more localized on the atoms.[119] The effective mass of a single parabolic band is defined by the relation:[119]

$$\frac{1}{m^*} = \frac{1}{\hbar^2}\frac{\partial^2 E(\vec{k})}{\partial \vec{k}^2} \ . \tag{4.8}$$

This shows that the effective mass for electrons depends on the curvature of $E(\vec{k})$ at any point in a band.[9, 119] In other words the effective mass of an electron increases with decreasing dispersion of the band, for the same number of states. In a wide band, the electron behaves as a free, nearly completely delocalized particle. In a narrow band however, a more localized description of the electrons is necessary. The concept of an effective mass can be explained with the motion of the electrons in the band. In a wide band the energy states of the electrons are distributed over a wide range of energies and fully delocalized. In a narrow

band, the electrons interact with the lattice and each other. They polarize their surroundings and a polarization cloud moves through the lattice along with the electrons. The electrons seem to have a bigger mass compared to a free electron.[119]

The bandwidth of a band depends on the bonding interactions in the solid. If the overlap of the neighboring orbitals is strong, the atomic orbitals tend to lose their identity and a wide band is formed.[120, 121] This is the case in materials with small electronegativity differences (covalent bonds), while ionic compounds have narrow bands due to a poor overlap of the atomic orbitals.[119, 121] Therefore ionic compounds usually exhibit a very low electrical conductivity, compared to metals, due to the high effective mass of the charge carriers.

Relaxation Times and Carrier Scattering

The description of transport processes using statistical mechanics, expresses the movement of all particles by the change rate of their overall distribution function which, in the steady state, can be expressed as:[122]

$$\left(\frac{\partial f}{\partial t}\right)_{field} + \left(\frac{\partial f}{\partial t}\right)_{collision} = 0 \,, \tag{4.9}$$

where the first term represents the disturbance of the distribution function by external fields and the second term the effect of collisions or scattering. The third major assumption in BTE is the assumption, that the extent of deviation of the distribution function from equilibrium is linearly to the rate of scattering:[122]

$$\left(\frac{\partial f}{\partial t}\right)_{collision} = \frac{f - f_0}{\tau} \,. \tag{4.10}$$

In other words, the relaxation of the distribution function back to equilibrium can be described by the scattering relaxation time τ.[13]

The electrical transport in a material is associated with various scattering mechanisms such as scattering on defects, impurities, electrons, holes, and the lattice.[13] The relaxation time associated with the various scattering mechanisms (s) is given by:[122]

$$\frac{1}{\tau} = \sum_{s=1}^{s} \frac{1}{\tau_s} \,, \tag{4.11}$$

with the relaxation time of the scattering mechanisms:[13, 122]

$$\tau_s = \tau_{0,s} \epsilon^{\lambda - 1/2} \,, \tag{4.12}$$

where ϵ is the reduced carrier energy ($\epsilon = E/k_B T$), k_B the Boltzmann constant, and λ a variable, which relates to the energy dependence of the carrier relaxation time.[13] The energy dependence of τ is important for the calculations of the Seebeck coefficient as discussed below and therefore a rough description of the different scattering mechanisms is important.

In the case of acoustic phonon scattering, lattice vibrations give a relaxation time with $\lambda = 0$ and $\tau_{acoustic} \propto \epsilon^{-0.5}$. Acoustic phonon scattering mainly occurs at high temperatures where

high energy electrons are present and therefore a greater number of states being available for the electrons to be scattered into. For highly degenerate electrons the mobility μ decays as T^{-1}, which is the classic metallic behavior at higher T, while μ decays as $T^{-1.5}$ in a nondegenerate material.[13, 122]

Ionized impurity scattering due to the Coulombic field of the impurities can be described via $\lambda = 2$. This scattering mechanism is limited to the lower temperature regime and the mobility increases with temperature, because higher energy electrons have higher velocities and will be less influenced by local disruptions of the Coulombic field.[122]

Energy independent scattering ($\lambda = 0.5$) occurs in the intermediate temperature regimes and can be explained as a balance between ionized impurity scattering and acoustic phonon scattering.[13, 122]

4.2.2 Electronic Transport Equations within the Single Parabolic Band Approximation

This single parabolic band approximation is the basis of the transport equations, which will be discussed in the following. This section is thought to give an overview over the transport equations, which have been used for modeling the thermoelectric transport of the pertinent materials. More information and the derivations can be found in the literature, e.g. Fistful's "Heavily Doped Semiconductors"[122] and the Ph.D Thesis by Andrew F. May, 2010[13].

Carrier Concentration

The carrier concentration of a band is obtained through the integration over all occupied states in the band, in other words an integral over the density of states $N(E)$:

$$n = \int_0^\infty N(E) f(E) dE \ , \tag{4.13}$$

with the assumption of a minimum band energy of zero ($V_0 = 0$). Substituting for $N(E)$ (Equation 4.7) and $f(E)$ (Equation 4.4) leads to:

$$n = 4\pi \left(\frac{2m^* k_B T}{h^2} \right)^{3/2} \int_0^\infty \frac{\epsilon^{1/2} d\epsilon}{1 + exp[\epsilon - \eta]} \ . \tag{4.14}$$

Defining the Fermi integrals as:

$$F_j(\eta) = \int_0^\infty \frac{\epsilon^j d\epsilon}{1 + exp(\epsilon - \eta)} \ , \tag{4.15}$$

the carrier concentration can be written as:

$$n = 4\pi \left(\frac{2m^* k_B T}{h^2} \right)^{3/2} F_j(\eta) \ . \tag{4.16}$$

The assumption of acoustic phonon scattering, with the scattering parameter $\lambda = 0$ relating to the energy dependence of the carrier relaxation time τ, with $\tau = \tau_0 e^{\lambda - \frac{1}{2}}$,[10] leads to $F_{1/2}(\eta)$.

Now, carrier concentrations can be calculated using Equations 4.15 and 4.16 and can be compared to measured Hall carrier concentrations. The reduced chemical potential η can be calculated from the measured Seebeck coefficients using Equation 4.15 and 4.20. However, scattering effects can cause a deviation between n and n_H, which has to be accounted for (with $n = r_H n_H$). This can be achieved with the Hall factor r_H which is given by:

$$r_H = \frac{3}{2} F_{1/2}(\eta) \frac{(1/2 + 2\lambda) F_{2\lambda - 1/2}(\eta)}{(1+\lambda)^2 F_\lambda^2(\eta)} \,, \tag{4.17}$$

which leads to the expression for n_H:

$$n = 4\pi \left(\frac{2m^* k_B T}{h^2} \right)^{3/2} \frac{F_{1/2}(\eta)}{r_H} \,. \tag{4.18}$$

Seebeck coefficient

The Seebeck coefficient within the single parabolic band description is given by:[13, 21, 122]

$$\alpha = \frac{k_B}{e} \left(\frac{\int_0^\infty \tau \epsilon^{\frac{3}{2}} (\epsilon - \eta) \frac{\partial f}{\partial \epsilon} d\epsilon}{\int_0^\infty \tau \epsilon^{\frac{3}{2}} \frac{\partial f}{\partial \epsilon} d\epsilon} \right) \,, \tag{4.19}$$

which leads to:

$$\alpha = \frac{k_B}{e} \left(\frac{(2+\lambda) F_{1+\lambda}(\eta)}{(1+\lambda) F_\lambda(\eta)} - \eta \right) \,, \tag{4.20}$$

when $\tau = \tau_0 e^{\lambda - \frac{1}{2}}$. For a single parabolic band, the Seebeck coefficient only depends on η, regardless of the band mass. The value of η can be estimated using Equation 4.20 and the Fermi integrals (Equation 4.15) and all other transport properties can be calculated. The band effective mass can be calculated from the chemical potential and the measured Hall carrier concentration (Equation 4.18) of a given thermopower and with it Pisarenko relations, while temperature dependent Lorenz number can be calculated with η (Equation 5.30).

4.3 $Cu_{2+x}Zn_{1-x}GeSe_4$

This section is an adapted reproduction, from J. Am. Chem. Soc **2012**, 134, 7147-7154.[55] Reproduced with permission of the American Chemical Society Copyright 2012.

The temperature dependence of the resistivity for different doping concentrations in $Cu_{2+x}Zn_{1-x}GeSe_4$ is shown in Figure 4.1. As expected for a wide band gap semiconductor,[64] unsubstituted $Cu_2ZnGeSe_4$ exhibits a high electrical resistivity at room temperature and decreases with increasing temperature. The above (see Section 3.2) mentioned phase transformation at around 450 K has a significant impact on the electrical resistivity leading to an increase in resistivity with temperature for all doping levels, similar to metallic transport behavior and the temperature of the transition seems to be composition dependent. Thus, this transition can be considered an insulator-to-metal transition.

While substitution introduces charge carriers and results in a decrease of the resistivity over orders of magnitude, the change in the resistivity does not entirely follow the trend expected

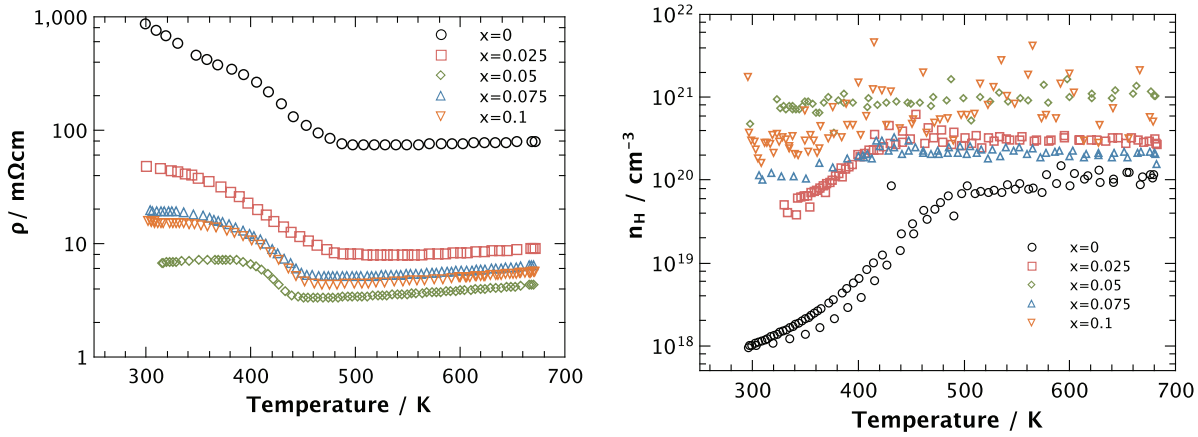

Figure 4.1: Resistivity ρ (left) and Hall-carrier concentrations n_H (right) of $Cu_{2+x}Zn_{1-x}GeSe_4$ as a function of temperature. An insulator-to-metal transition can be seen in the transport at 450 K. Note that the composition with $x = 0.05$ exhibits the lowest electrical resistivity which can be attributed to its higher Hall carrier concentration.

for the substitution with Cu^{2+} for Zn^{+}. The exception to the expected behavior is seen at the substitution level of $x = 0.05$ which shows a lower resistivity than $x = 0.075$ and $x = 0.1$. This can be explained by the charge carrier concentrations (Figure 4.1) that result for each doping level, where a higher than expected carrier concentration was observed for the $x = 0.05$ sample. Expected carrier concentrations from simple charge counting and measured Hall-carrier concentrations are shown in Figure 4.2. At a doping level of $x = 0.025$ the substitution has the expected effect on the carrier concentration, however, higher substitution levels deviate significantly from the charge carrier concentrations expected from simple charge counting. This behavior is attributed to the secondary phases in the material seen in the scanning electron micrographs (Figure 3.5). The formation of $Cu_{2-\delta}Se$ reduces the amount of Se^{2-} and Cu^{+} in the matrix. Considering the case where only Se is removed from the matrix, there would be electrons left behind in the matrix which would lead to fewer holes in the material, as compared to that expected from charge counting for each level of substitution x. In the case where only Cu is removed from the matrix, the result would be more holes left behind in the matrix. In the case of phase segregation where stoichiometric Cu_2Se is formed, the individual effects of less Se and Cu in the matrix would cancel each other out and would not impact the carrier density. However, the formation of nonstoichiometric $Cu_{2-\delta}Se$ means that more Se than Cu is removed from the matrix and the overall result is less holes in the matrix as compared to the expected number from simple charge counting, the effect of which is shown by the measured Hall carrier concentrations shown in Figure 4.2. Additionally, it is likely that CuSe forms for $x = 0.05$ due to a slight excess of Se and reduces the amount of Cu and therefore leads to more holes in the matrix.

It should be noted that measured Hall-mobilities (Figure 4.2) at room temperature of the doped materials are around 2-3 $cm^2/V{\cdot}s$ and not effected by this unexpected trend, leading to the assumption that the charge carrier concentration mainly dominates the electronic transport. The Hall voltage is positive, which is expected for p-type charge carriers (holes),

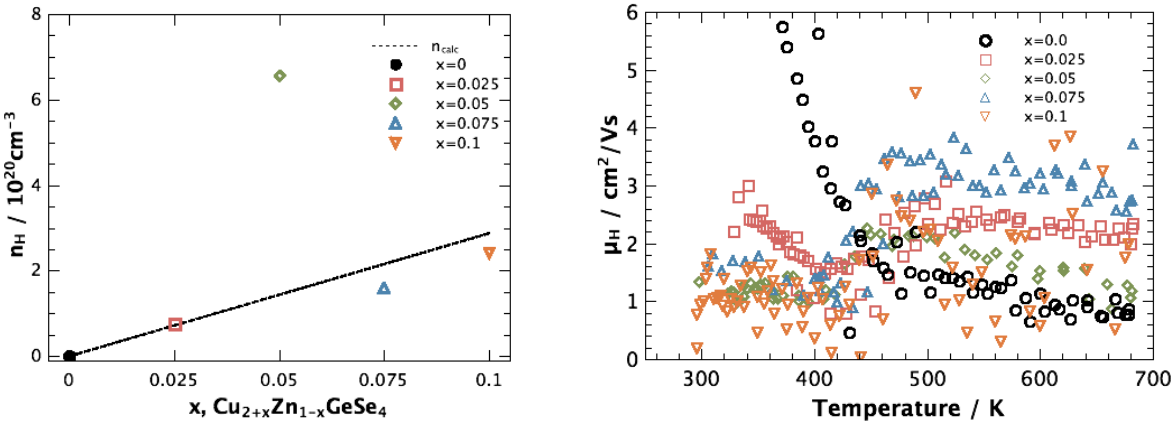

Figure 4.2: Left: Expected charge carrier concentrations n_{calc} and measured Hall-carrier concentrations n_H for $Cu_{2+x}Zn_{1-x}GeSe_4$. The deviations from the expected charge carrier concentrations can be attributed to the secondary phases, which alter the actual stoichiometry leading to defects affecting the transport. Right: Temperature dependence of the measured Hall-mobilities. The mobilities are low for a semiconductor showing some degree of localization.

and the mobilities are low for a semiconductor but high for localized charges in a very ionic environment.

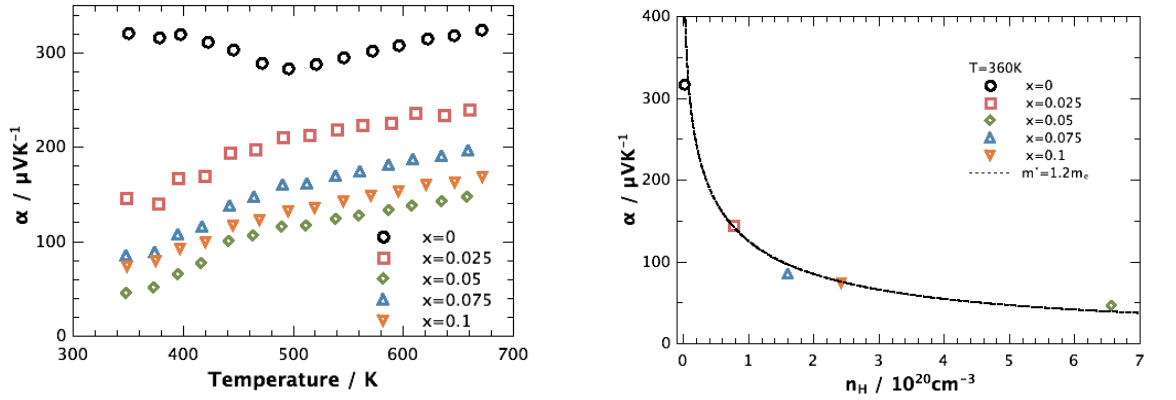

Figure 4.3: Seebeck coefficients α vs. temperature (left) of $Cu_{2+x}Zn_{1-x}GeSe_4$, showing the phase transition in the undoped sample. Experimental Seebeck-coefficients as a function of Hall carrier concentration n_H (right) at 360 K. The dotted line, which was generated using a single parabolic band approximation and an effective mass of 1.2 m_e, shows single parabolic band behavior in this materials system.

Figure 4.3 illustrates the effect of the charge carrier concentrations on the thermopower. The Seebeck coefficients are large and positive, indicating holes as the majority carrier type, consistent with the carrier concentration and Hall-mobilities acquired via Hall-measurements. The increase of the Seebeck coefficient with increasing temperature reveals that the maximum of the thermopower is not yet reached at 670 K, which is consistent with the measured wide band gap of 1.4 eV in this material (Figure 3.1 c)). Within this measurement range, thermally activated electrons do not cause a reduction in the thermovoltage. Equations 4.15, 4.16, and

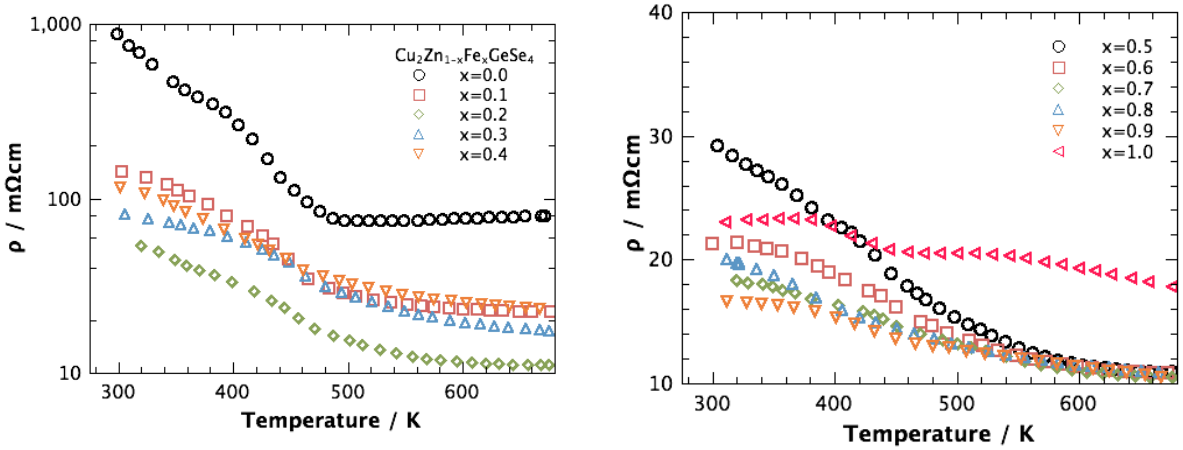

Figure 4.4: Temperature dependence of the electrical resistivity ρ of $Cu_2Zn_{1-x}Fe_xGeSe_4$ for x = 0.0 - 0.4 (left) and x = 0.5 - 1.0 (right) showing semiconducting behavior with high electrical resistivity. A previously reported phase transformation[55] is apparent for x = 0.0 and 0.1

4.20 have been used to model the relationship between carrier concentration and the Seebeck coefficient. It is assumed that only one type of carrier is present in a single parabolic band, with the assumption of acoustic phonon scattering ($\lambda = 0$). The effective mass m^* of 1.2 m_e, which was used to calculate the Pisarenko relation (Figure 4.3) at 360 K, was calculated from the experimental Seebeck coefficient and Hall carrier concentration for x = 0.025.

Because the experimental data fall on or near the generated curve it may be assumed that a heavily doped, single parabolic band is a good starting model for electronic transport of this system below the transition temperature. Substitution with Cu does not significantly change the effective mass or mobility of the holes and therefore confirms that the electronic transport is mainly governed by the charge carrier densities. This furthermore shows that the carrier mobility is not affected by nano particles of this length scale, which is expected, since the mean free paths of electrons and holes in a semiconductor are much shorter than that of phonons.[41]

In conclusion, a phase transition at 450 K has been identified, and it has an influence on the transport properties in this material, leading to an insulator-to-metal transition. Substitution of Zn^{2+} with Cu^{+} introduces holes as charge carriers, but also leads to the formation of impurities by phase segregation which greatly influence the charge carrier concentration.

4.4 $Cu_2Zn_{1-x}Fe_xGeSe_4$

This section is an adapted reproduction, from *J.* Am. Chem. Soc **2013** - accepted manuscript.[56] Reproduced with permission of the American Chemical Society Copyright 2013.

The temperature dependence of the electrical resistivity ρ for different compositions x of $Cu_2Zn_{1-x}Fe_xGeSe_4$ is shown in Figure 4.4. As expected for these wide band gap semiconductors,[55] these compositions exhibit a high electrical resistivity at room temperature, decreasing with temperature. A previously reported phase transformation[55] (see Section

4.3) is apparent for x = 0.0 and 0.1. No charge carriers are introduced directly through the substitution with isoelectronic Fe^{2+} for Zn^{2+}, however measured Hall carrier concentrations (see Supporting Information in Chapter 8) change across compositions due to the changes in character of the density of states of the valence band (see Figure 3.9) as well as the presence of intrinsic defects. However, it has to be mentioned that due to the multi-band behavior (see Figure 3.9), measured Hall carrier concentrations will not represent chemical carrier concentrations since Equation 2.3 does only apply for transport within a single band.

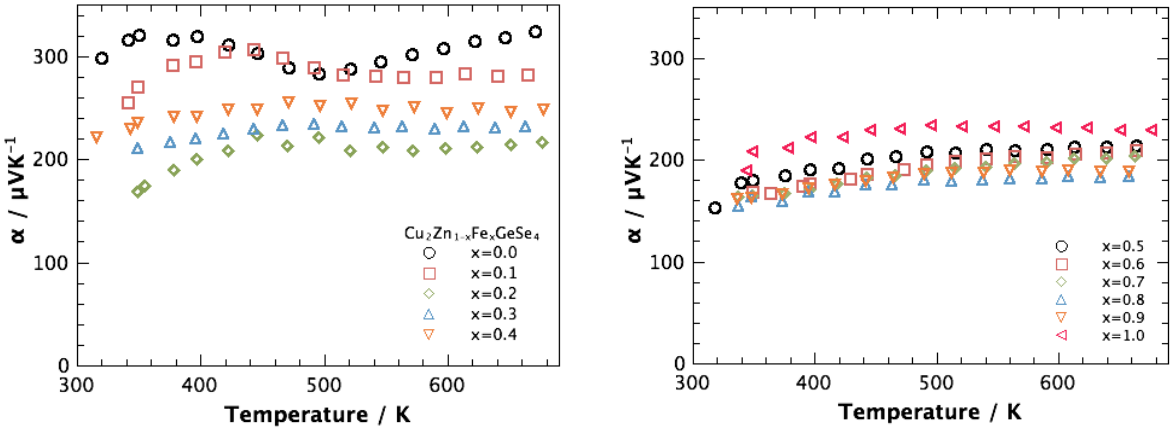

Figure 4.5: Temperature dependence of the Seebeck coefficients α of $Cu_2Zn_{1-x}Fe_xGeSe_4$ for x = 0.0 - 0.4 (left) and x = 0.5 - 1.0 (right) showing intrinsic p-type semiconducting behavior controlled by intrinsic defects. A previously reported phase transformation[55] is apparent for x = 0.0 and 0.1.

The resistivity of a composition is therefore mainly controlled by the change in mobility, due to alloy scattering, and charge carrier concentrations. The unchanged intrinsic nature of these semiconductors, upon substitution of Zn with Fe, can also be seen in the flat slope of the temperature dependent positive Seebeck coefficients (Figure 4.5), which show intrinsic p-type conduction.[55, 123] The differences in the Seebeck coefficients arise from the different carrier concentrations of the samples and an increase in the carrier effective mass with measured Hall carrier concentrations, as seen Figure 4.6. The effective masses, which have been calculated within the single parabolic band model at 360 K using Equations 4.18 and 4.20, show a linear increase with increasing carrier concentrations. Such a trend is usually attributed to a non-parabolicity of the band, which results in higher effective masses for a shift of the chemical potential deeper into the band. However, as mentioned above, this trend could also be due to the multi-band character of the valence band with the Fe-d band coming into play.

It has been shown, that substitution of Zn^{2+} with Fe^{2+} does not change charge carrier concentration as it is expected for aliovalent doping and the intrinsic nature of the solid solutions is not changed. However, the multi-band behavior in the valence band seems to play a role on the measured Hall carrier concentrations and the effective masses of the charge carriers.

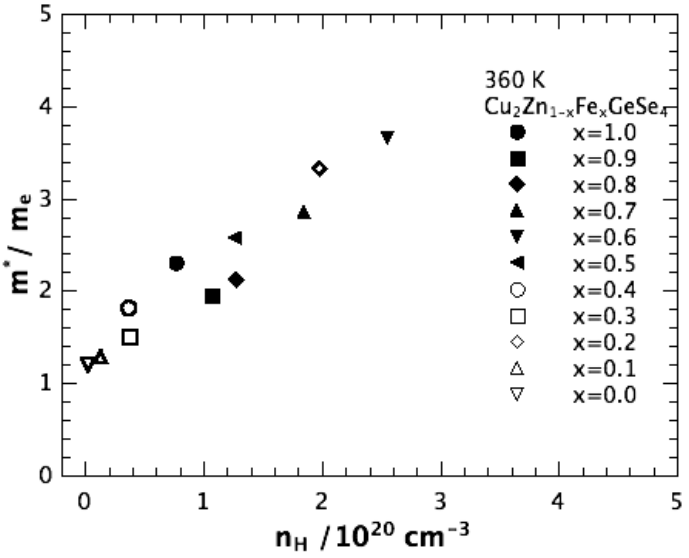

Figure 4.6: Carrier effective mass of $Cu_2Zn_{1-x}Fe_xGeSe_4$ vs. measured Hall carrier concentration showing a linear dependence usually associated with non-parabolic behavior, but possible a result of the multi-band behavior in this class of material.

4.5 $Cu_{2+x}Zn_{1-x-y}Fe_yGeSe_4$

For all compositions x was set to 0.025 and only the value of y has been altered throughout the series of solid solutions to obtain the material $Cu_{2.025}Zn_{0.975-y}Fe_yGeSe_4$ with the carrier concentrations obtained for $Cu_{2+x}Zn_{1-x}GeSe_4$ as seen in Section 4.3. The electronic transport data of the temperature dependent Seebeck coefficient, resistivity, Hall carrier concentration, and Hall mobility can be found in the Supporting Information in Chapter 8.

Due to the multi-band character upon Fe-substitution and the difficulty in controlling charge carrier concentrations in this class of materials all carrier concentrations are higher than the 7.7x10^{19} holes/cm^{-3} of x = 0.025 in $Cu_{2+x}Zn_{1-x}GeSe_4$ and therefore a change in the intrinsic nature of the electronic properties cannot be detected, which reproduces the results from Section 4.4 very well.

4.6 Ca_3AlSb_3

This section is an adapted reproduction, from *J.* Mater. Chem **2012** 22, 9826-9830.[96] Reproduced with permission of The Royal Society of Chemistry Copyright 2012.

The electronic properties of sodium doped Ca_3AlSb_3 have previously been investigated and are largely similar to those reported here with zinc as a dopant. In the following results the transport properties of the Na-doped sample that resulted in the highest figure of merit (nominal composition $Ca_{2.94}Na_{0.06}AlSb_3$) has been included as a basis for comparison.[95]

Figure 4.7 shows the measured Hall carrier concentrations as a function of temperature. Though Ca_3AlSb_3 is a classic, valence-precise Zintl compound, the undoped material has a p-type carrier concentration of 10^{18} holes/cm^3 at room temperature due to intrinsic defects. As

expected, the carrier concentration increases upon substitution of Al^{3+} with Zn^{2+} due to the introduction of holes. Doped samples behave extrinsically, with temperature independent carrier concentrations up to 700 K, after which the carrier concentration increases abruptly, likely due to carrier excitation across the band gap ($E_g \sim 0.6$ eV[95]). Zinc doping introduces significantly fewer holes than predicted, in accordance with previous attempts at doping Ca_3AlSb_3 and the closely related phase, $Ca_5Al_2Sb_6$.[95, 124, 125] Ultimately, the maximum carrier concentration achieved by doping with zinc is lower than that achieved upon sodium doping, suggesting a lower solubility limit for zinc, assuming substitution of Al with Zn.

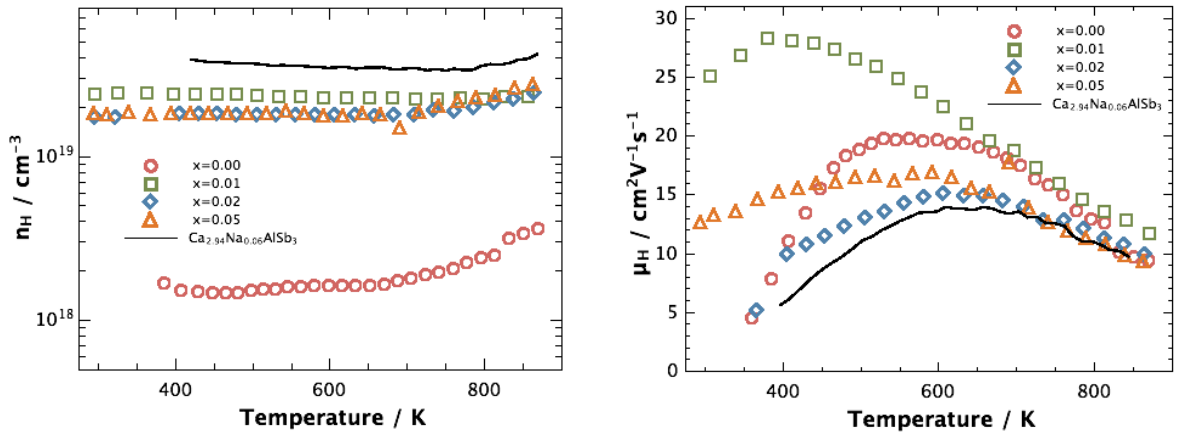

Figure 4.7: Left: Hall carrier concentration n_H with temperature of $Ca_3Al_{1-x}Zn_xSb_3$. The carrier concentration increases upon substitution due to the introduction of holes. The sharp increase of n_H is likely due to carrier excitation across the band gap. Right: Hall mobility μ_H with temperature. The increase with temperature at lower T represents an activation energy process due to grain boundaries. At higher temperatures acoustic phonon scattering dominates the carrier mobilities. Experimental data is compared to $Ca_{2.94}Na_{0.06}AlSb_3$ data (black line) from Reference [95].

Impurities at grain boundaries, such as oxidation products or possibly phases that are too small to observe by SEM, are already known to impede charge transport in Ca_3AlSb_3, leading to reduced mobility at low temperatures.[95] Grain boundaries are also a likely place for Zn to accumulate, potentially causing the reduced doping effectiveness observed in this study. This supposition is supported by the anomalous carrier concentration of the $x = 0.01$ sample, which is higher than that of the samples with $x = 0.02$ and 0.05, and may be attributable to its large grain size (see Section 3.5) and thus lower interfacial surface area.

Grain size also correlates with the carrier mobility of the $Ca_3Al_{1-x}Zn_xSb_3$ samples in this study. The Hall mobility, calculated from the measured Hall coefficient (R_H) and resistivity (ρ), is shown in Figure 4.7. For samples with sub-micron grains ($x = 0.00$, $x = 0.02$, and $x = 0.05$), the Hall mobility at low temperatures exhibits an exponential temperature dependence ($\mu_H = \mu_0 e^{-E_A/k_BT}$) indicative of a barrier at the grain boundaries, such as an oxide layer, requiring an activation energy to overcome. At higher temperatures (> 600 K) the mobility is limited by acoustic phonon scattering, for which the temperature dependence is given by $\mu_H \propto T^{-\nu}$, with ν between 1 and 1.5 for degenerate and non-degenerate behavior, respectively.[126] However, the sample with the nominal composition of $Ca_3Al_{0.99}Zn_{0.01}Sb_3$ exhibits larger Hall

mobilities than all other compositions, with acoustic phonon scattering dominating transport above 400 K. This suggests that since larger grains (see Figure 3.11) result in a lower interfacial surface area, a less pronounced activation process in the temperature dependence of the Hall mobility in this sample leads to higher mobility at lower temperatures. Additionally, larger grain sizes may cause a larger carrier mobility at lower temperatures in the sample with x = 0.01 through reduced grain boundary scattering.

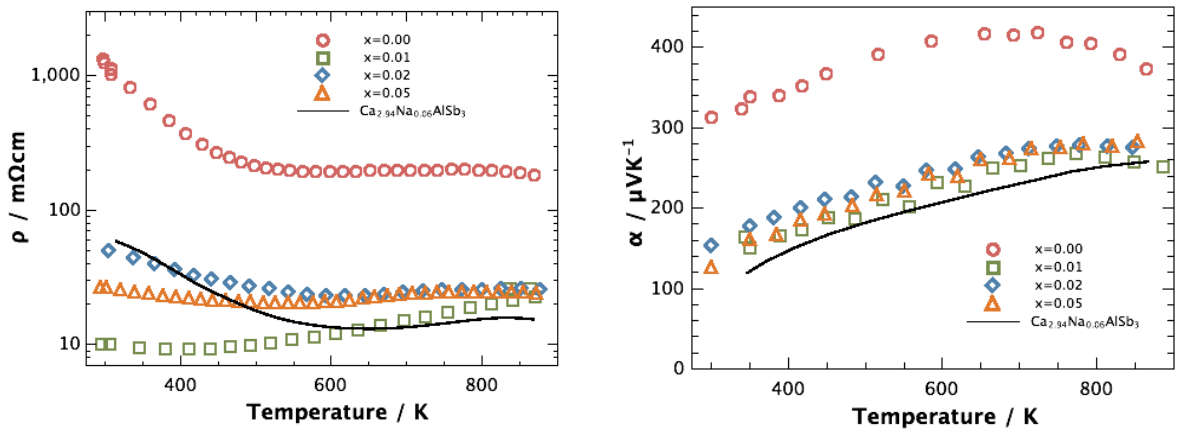

Figure 4.8: Left: Resistivity ρ of $Ca_3Al_{1-x}Zn_xSb_3$ exhibiting semiconducting behavior consistent with the Hall mobility. Right: Temperature dependent Seebeck coefficients of $Ca_3Al_{1-x}Zn_xSb_3$ showing p-type behavior consistent with the p-type carrier concentrations. Experimental data is compared to $Ca_{2.94}Na_{0.06}AlSb_3$ data (black line) from Reference [95].

The temperature dependence of the electrical resistivity (Figure 4.8), shows a decreasing trend at lower temperatures, consistent with the activated mobility behavior ($\rho = 1/ne\mu$). At higher temperatures the resistivity behaves as expected for a heavily doped semiconductor.

The Seebeck coefficients are positive, consistent with the p-type carrier concentrations, and the temperature dependence is shown in Figure 4.8. The Seebeck coefficient of undoped Ca_3AlSb_3 increases up to a temperature of 700 K, at which point thermally activated electrons reduce the thermoelectric voltage resulting in a decay of the Seebeck coefficient. As expected for a heavily doped semiconductor, the Seebeck coefficients decrease with increasing carrier concentrations. In order to compare the influence of Zn and Na as dopants on the electronic structure of this material, the Pisarenko relation of this material is shown in Figure 4.9. The experimental Seebeck and carrier concentrations were measured at 700 K, while the dashed line was generated using the single parabolic band model described in Section 4.2, with a valence band effective mass of $m^* = 0.8\,m_e$. Both Zn and Na doped materials are well described by the same model, suggesting that using Zn as a dopant does not affect the band structure of the compound.

In conclusion, the electronic properties of zinc-doped Ca_3AlSb_3 were compared to a previously reported study on sodium as a dopant.[95] A similar band mass is observed regardless of whether Zn or Na is the dopant. However, zinc exhibits a lower solubility limit than sodium resulting in lower carrier concentrations, because the optimum carrier concentration for this material cannot be reached via doping with zinc. This study also shows the effect of

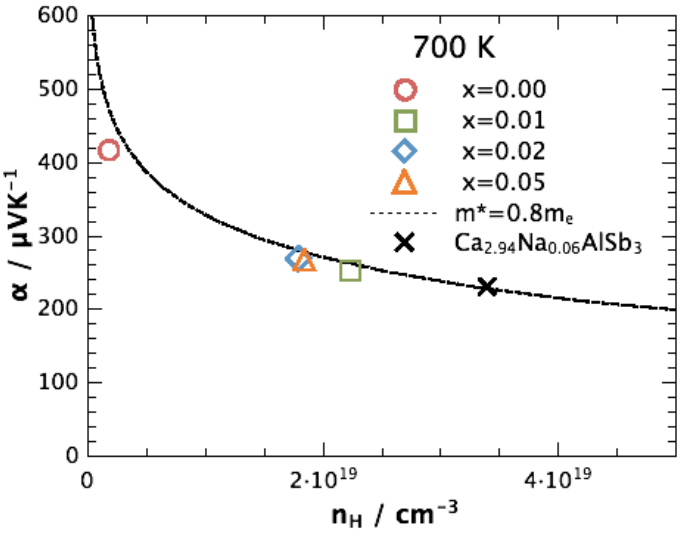

Figure 4.9: Experimental Seebeck coefficients as a function of carrier concentration of $Ca_3Al_{1-x}Zn_xSb_3$ exhibiting single parabolic band behavior. Both Zn and Na[95] doped materials are well described by the same model, suggesting that using Zn as a dopant does not affect the band structure of the compound.

different grain sizes on the thermoelectric transport properties, with larger grains leading to higher mobilities at lower temperatures, due to reduced scattering of electrons at the grain boundaries.

4.7 Sr_3GaSb_3

This section is an adapted reproduction, from *E*nergy Environ. Sci. **2012**, 5, 9121-9128.[100] Reproduced with permission of The Royal Society of Chemistry Copyright 2012.

Figure 4.10 shows the measured Hall carrier concentrations n_H of $Sr_3Ga_{1-x}Zn_xSb_3$ samples as a function of temperature. Despite Sr_3GaSb_3 being a valence-precise Zintl compound, the undoped material has an extrinsic p-type carrier concentration of 4×10^{18} holes/cm^3 at room temperature, most likely due to intrinsic defects in the crystal structure. The resistivity of undoped Sr_3GaSb_3 is very high (see Figure 4.11), decreasing due to thermal activation of carriers into the conduction band only at temperatures above 800 K.

With each substitution of Zn^{2+} on a Ga^{3+} site we expect to introduce one additional free hole (h^+), due to the difference in valence states.[19] In many Zintl compounds, this simple assumption works well for predicting n_H of doped samples (i.e. $Yb_{14}Al_{1-x}Mn_xSb_{11}$[91], $Ba_8Ga_{16-x}Ge_{30+x}$[54]), indicating that the dopant primarily substitutes on the intended crystallographic sites. However, in Sr_3GaSb_3, in common with Ca_3AlSb_3,[96] doping with Zn results in only a fraction of the predicted hole concentration. For example, when $x = 0.07$ (equivalent to a synthetic concentration of 1 at.% Zn) we would predict $n = 2.1\text{x}10^{20}$ h^+/cm^3. However, the measured n_H is only $5\text{x}10^{19}$ h^+/cm^3. If each measured hole is assumed to result from a Zn atom on a Ga site, than only *one fourth* of the synthetic Zn content resides on the

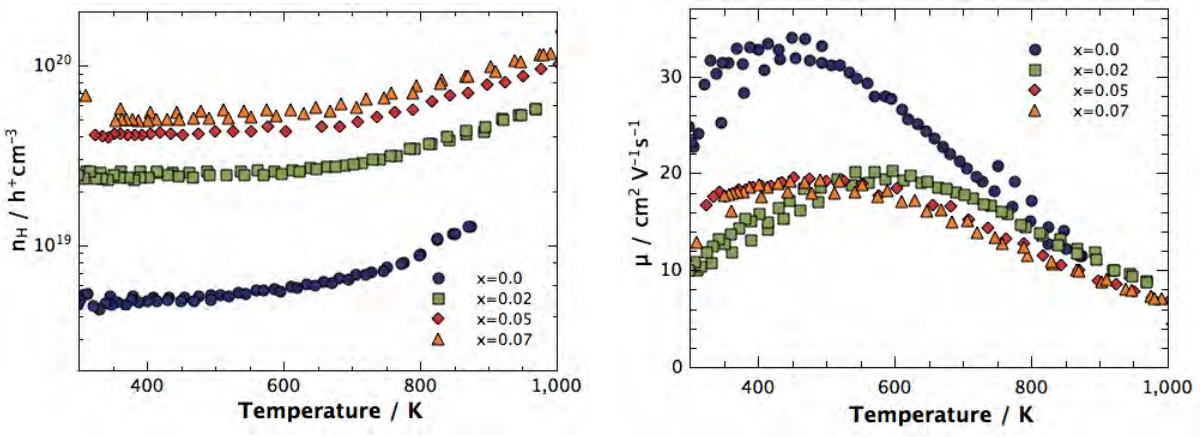

Figure 4.10: Left: Hall carrier concentration n_H with temperature of $Sr_3Ga_{1-x}Zn_xSb_3$. The carrier concentration increases upon substitution due to the introduction of holes. Right: Hall mobility μ_H with temperature. The increase with temperature at lower T represents an activation energy process due to grain boundaries. At higher temperatures acoustic phonon scattering dominates the carrier mobilities.

intended site, while the remainder may form secondary phases too small to identify or perhaps becomes trapped at grain boundaries. However, estimating the matrix Zn content from the measured Hall coefficient can be misleading. Sources of error might include Zn defects with an effective charge other than +1, formation of compensating n-type defects,[127] or a Hall factor (r_H=n/n_H) that deviates significantly from unity.[54]

As a function of temperature, n_H in $Sr_3Ga_{1-x}Zn_xSb_3$ is constant at low temperatures, indicative of extrinsic transport, and increases at high temperature as intrinsic carriers are activated across the band gap. The increase in n_H leads to the decrease in electrical resistivity with Zn-doping shown in Figure 4.10.

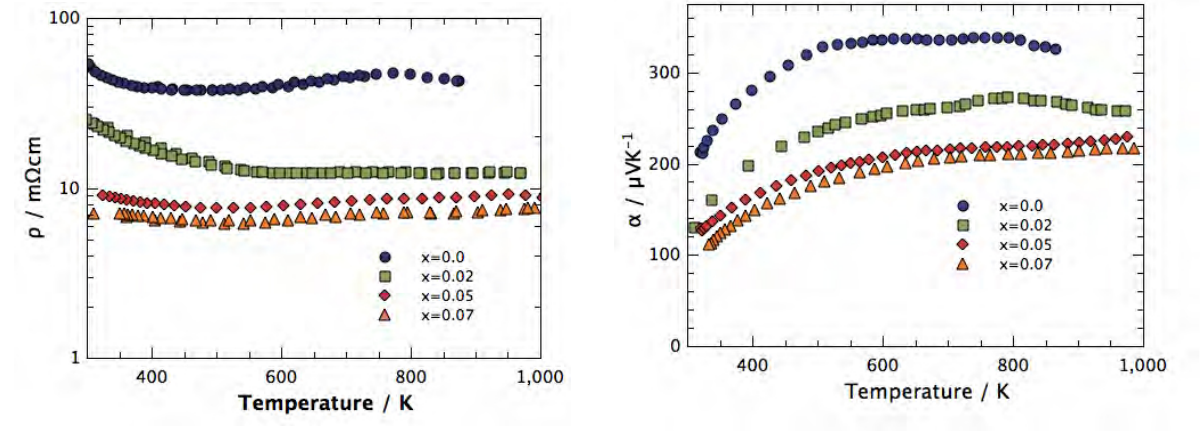

Figure 4.11: Left: Resistivity ρ of $Sr_3Ga_{1-x}Zn_xSb_3$ exhibiting semiconducting behavior consistent with the Hall mobility. Right: Temperature dependent Seebeck coefficients of $Sr_3Ga_{1-x}Zn_xSb_3$ showing p-type behavior consistent with the p-type carrier concentrations.

The Hall mobility, μ_H, is shown in Figure 4.11, calculated from $\rho = 1/n_H e\mu_H$. At low temperatures ($T < 500\,\mathrm{K}$), μ_H exhibits a positive temperature dependence that can be fit using

$\mu_H \propto e^{-E_A/k_BT}$, where E_A is the activation energy associated with a potential barrier.[128] Such behavior may arise from barriers at the grain boundaries, such as oxide layers or secondary phases, requiring an activation energy to overcome. Our previous study (Section 4.6) of Ca_3AlSb_3 indicates that with the correct processing it is possible to avoid this activated behavior, drastically increasing electrical conductivity.[96] At higher temperatures ($> 600\,K$) the mobility in $Sr_3Ga_{1-x}Zn_xSb_3$ is limited by acoustic phonon scattering, for which the temperature dependence is given by $\mu_H \propto T^{-\nu}$, with ν between 1 and 1.5 for degenerate and non-degenerate behavior, respectively.[126]

The Seebeck coefficients, α, of $Sr_3Ga_{1-x}Zn_xSb_3$ samples, shown in Figure 4.11, are positive, consistent with the p-type carrier concentrations. The Seebeck coefficient of undoped Sr_3GaSb_3 increases up to a temperature of 700 K, at which point thermally activated electrons result in a decay of α. From the resulting maximum ($\alpha_{max} \sim 340\ \mu VK^{-1}$, $T_{max} \sim 700\,K$), a rough estimate of the band gap using $E_g = 2e\alpha_{max}T_{max}$ [129] yields $E_g \sim 0.5\,eV$, which is in general agreement with the results of the DFT calculations (see Figure 3.13). As expected, the Seebeck coefficients decrease with increasing carrier concentrations. This is best illustrated by the Pisarenko relation shown in Figure 4.12, with experimental α and n_H (cross symbols) obtained at 700 K. The broken curve was generated using the single parabolic band (SPB) model described in Section 4.2 with a valence band effective mass of $m^* = 0.9\,m_e$. All of the doped samples in this study appear to be well described by $m^* = 0.9\,m^*$ at 700 K, suggesting that, within experimental uncertainty, it is not possible to see any evidence of multi band behavior at these doping levels. While not shown here, the same effective mass also provides a good fit for the experimental Seebeck coefficients at 300 K and 500 K.

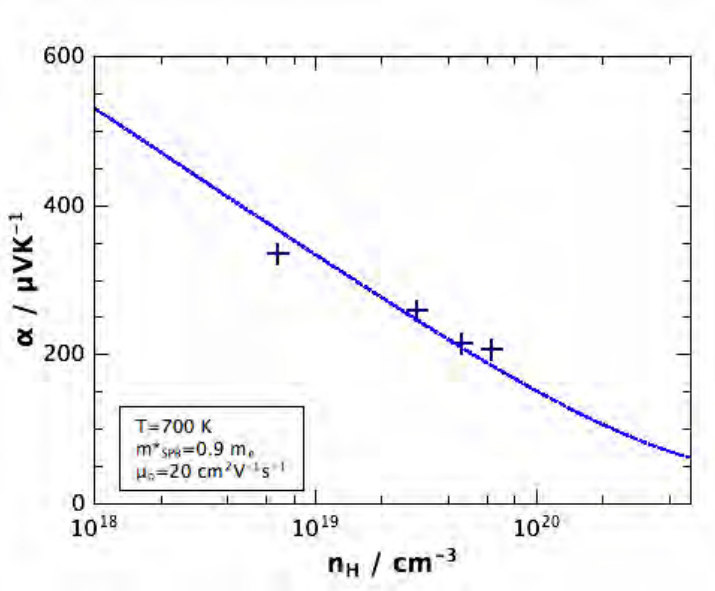

Figure 4.12: Experimental Seebeck coefficients of $Sr_3Ga_{1-x}Zn_xSb_3$ vary with carrier concentration approximately according to an SPB model at 700 K. The blue curve represents the predicted SPB behavior of α, assuming $m^* = 0.9\,m_e$, $\mu_0 = 17\,cm^2V^{-1}s^{-1}$ and $\kappa_L = 0.55\,Wm^{-1}K^{-1}$.

To investigate the possibility of anisotropic transport properties, the Hall coefficients and electrical resistivities of $Sr_3Ga_{0.93}Zn_{0.07}Sb_3$ were measured on disks cut in different directions (perpendicular and parallel to the hot pressing direction) and can be found in the Supporting Information in Chapter 8. A $\sim$ 5% disparity in resistivity measured to 1000 K appeared to stem from a higher hole concentration in the perpendicular slice, while the mobility was identical in both directions. The difference in the Seebeck coefficients at 300 K was within the measurement uncertainty of 5%. Together, these results suggest that possible anisotropy does not significantly influence transport properties in our polycrystalline samples. This is in agreement with XRD measurements, which show no signs of preferred grain orientation (see Figure 3.12).

In conclusion, the electronic properties of the Zintl compound Sr_3GaSb_3 and the influence of Ga substitution with Zn has been investigated. While zinc exhibits a lower solubility limit than expected for complete substitution, the properties are representative of a heavily doped, degenerate semiconductor with simple parabolic band behavior, which is in accordance to other Zintl compounds.

5 Thermal Transport

5.1 Summary

This chapter begins with a general discussion of the thermal conductivity of solids. The different contributions to the thermal conductivity and the heat conduction of the lattice are highlighted and general concepts are introduced. An attempt will be made to relate basic concepts such as phonon group velocity and heat capacity to a general chemistry understanding. Then the influence of different scattering mechanisms on the lattice thermal conductivity will be discussed, since it is necessary for the understanding of the data in the remainder of this chapter. Furthermore transport equations which are used in this chapter for the modeling and calculations of the minimum lattice thermal conductivity, the electronic contribution to κ, and the Lorenz numbers will be given.

In $Cu_2Zn_{1-x}GeSe_4$, a statistically significant reduction in the lattice thermal conductivity can be seen for x = 0.075 and 0.1, which can be attributed to the secondary phases at these substitution levels. The nanometer scaled impurities are mainly located at the grain boundaries, leading to an enhanced phonon scattering and therefore a significant reduction in phonon mean free path. The effect of the reduction leads to a lowering in lattice thermal conductivity of 0.3-0.5 $Wm^{-1}K^{-1}$at room temperature, with κ_L approaching the minimum value of 0.6 $Wm^{-1}K^{-1}$ at higher temperatures.

The solid solution of $Cu_2Zn_{1-x}Fe_xGeSe_4$ shows a dramatic reduction in thermal conductivity at 70 % Fe, correlating to the 3-stage cation restructuring process described in Chapter 3 where the highest local anisotropic structural disorder occurs at at 70 % Fe content. This disorder apparently reduces the lattice thermal conductivity by 15 % resulting in a minimum for the composition $Cu_2Zn_{0.3}Fe_{0.7}GeSe_4$ due to scattering of phonons by local anisotropic strain.

The lattice thermal conductivities of the Zintl phases Ca_3AlSb_3 and Sr_3GaSb_3 are investigated. The effect of different grain sizes on the thermal transport properties of Ca_3AlSb_3 is discussed, where larger grain sizes lead to higher thermal conductivities at lower temperatures, due to reduced scattering of phonons at the grain boundaries. In the compound Sr_3GaSb_3 the lattice thermal conductivity is found to be 0.4 $Wm^{-1}K^{-1}$ at 1000 K and therefore over the whole temperature range approximately 0.2 $Wm^{-1}K^{-1}$ lower than in the Zintl phase Ca_3AlSb_3, which can be attributed to the larger number of atoms per unit cell compared to Ca_3AlSb_3.

5.2 Thermal Transport Theory

Chapter 1 showed that the application of a temperature gradient ∇T will lead to a heat flow q due to the thermal conductivity κ of a material ($q = -\kappa\nabla T$, Equation 1.2. The heat flow

from the hot to the cold side of a thermoelectric module should be as small as possible to keep a stable temperature gradient along the material. Hence, small thermal conductivities are desired for good thermoelectric materials.

The following section is in parts an adapted reproduction of the Diploma thesis from Wolfgang Zeier, 2010.[85] It is thought to give a rough overview over the basic concepts on thermal transport properties.

5.2.1 Lattice Thermal Conductivity

The lattice thermal conductivity κ_L arises from quanta of lattice vibrations of a solid, the so called phonons, which propagate through the lattice with a certain specific heat C, a phonon group velocity v_g, and a mean free path l, given by Equation 1.15 for a treatment via kinetic gas theory:

$$\kappa_L = \frac{1}{3} C v_g l \ .$$

The mean free path characterizes the distance a phonon travels between random scattering events and is related to the scattering relaxation time τ via $\tau = l/v_g$. Considering the frequency ω dependence of the lattice gives:

$$\kappa_L = \frac{1}{3}\int_0^{\omega_{max}} C(w) v_g(\omega) l(\omega) d\omega = \frac{1}{3}\int_0^{\omega_{max}} C(\omega) v_g^2(\omega) \tau(\omega) d\omega \ . \tag{5.1}$$

Equation 5.1 demonstrates the importance of the heat capacity, the phonon group velocity, and the phonon mean free path on the lattice thermal conductivity. These materials properties will be discussed in the following, giving an overview on the concepts including chemical as well as structural approaches for lowering C, v_g, and l.

Lattice Vibrations

The atoms in a solid oscillate around their equilibrium positions. The vibrations are strongly coupled to neighboring atoms and are therefore not independent of each other. These vibrations can be described as standing waves in a classical treatment or in analogy to electrons as quanta of the crystal vibrational field, commonly referred to as phonons.[20] The simplest way to treat the vibrational behavior is to consider a periodic one-dimensional chain of atoms, which interact via springs (spring constant K_S) as shown in Figure 5.1.

At equilibrium, a chain of N atoms with mass M has an interatomic spacing equal to the unit cell length a_0. Within periodic boundary conditions and neglecting anharmonic forces, the solution of Newton's laws leads to the phonon frequencies $\omega_{\vec{q}}$ for a one-dimensional chain:[20]

$$\omega_{\vec{q}} = 2\sqrt{\frac{K_S}{M}}\,|sin(\vec{q}a_0/2)| \qquad \vec{q} = \frac{n\pi}{a_0} \ , \tag{5.2}$$

with the phonon wave vector $\vec{q}$. The maximum value of the vibrational frequency of the 1D periodic chain $\omega_{\vec{q}}^{max}$ is given by:[20]

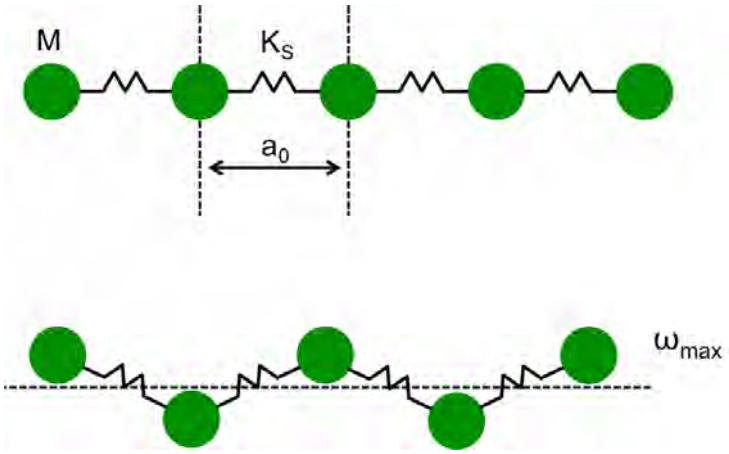

Figure 5.1: A periodic one-dimensional chain of identical masses M, connected by springs with a spring constant K_S, showing the origin of phonons from atomic vibrations. The top schematically shows no lattice vibrations while the bottom shows the maximum oscillation leading to the maximum vibrational frequency $\omega_{\vec{q}}^{max}$.

$$\omega_{\vec{q}}^{max} = 2\sqrt{\frac{K_S}{M}}\,. \tag{5.3}$$

Thus the vibrational frequency has a periodic behavior with the periodicity $(2\pi/a_0)$ of the reciprocal lattice. This is usually illustrated in phonon dispersion curves, with the phonon frequency as a function of the phonon wave vector $\vec{q}$.[20, 130]

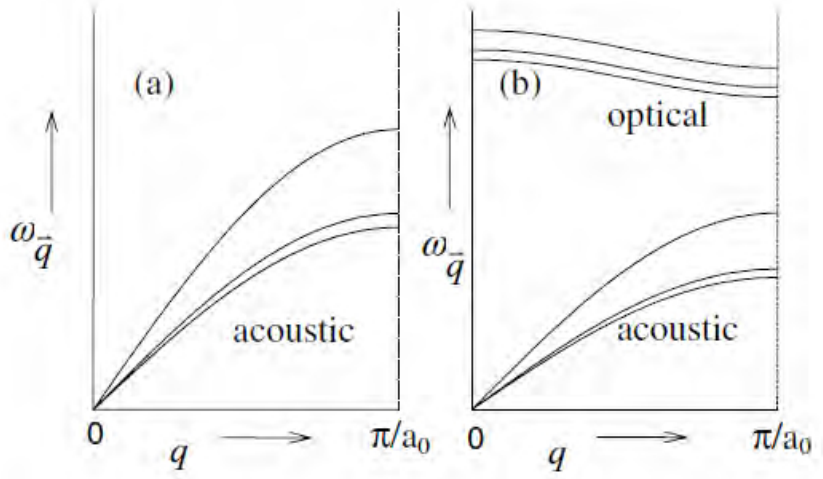

Figure 5.2: Schematic phonon dispersion curves for a given direction of $\vec{q}$ of (a) monoatomic lattice and (b) diatomic lattice.[130] An increasing number of atoms introduces more optical phonon modes, which have low phonon group velocities and therefore carry less heat than acoustic phonons.

Figure 5.2 shows phonon dispersion curves for a monoatomic lattice (a) and a diatomic lattice (b). The low-frequency acoustic branches correspond to atoms in the unit cell moving in the same phase (harmonic vibrations), whereas the high-frequency optical branches represent the anharmonic lattice vibrations. In a three-dimensional lattice with N atoms per unit cell, the harmonic and anharmonic vibrations lead to three acoustic and $3N$-3 optical branches,

respectively.[9, 20, 130]

As seen in Equations 5.2 and 5.3 the frequencies of the phonons of a one-dimensional periodic chain strongly depend on the spring constant and the atomic mass. The magnitude of the spring constant strongly depends on the bond strength of the atoms in the solid:[20]

$$K_S = \left(\frac{\partial^2 E}{\partial R_a^2}\right)_{R_{a,0}} , \tag{5.4}$$

with the distance R_a of the atoms and the equilibrium distance $R_{a,0}$, where a high bond strength leads to a high spring constant.

Hence, the phonon dispersion decreases with increasing mass of the atoms and decreasing bond strength between the atoms. This can also be expressed with the group velocity v_g of the phonons:[20]

$$v_g = \frac{\partial \omega_{\vec{q}}}{\partial \vec{q}} = a_0 \sqrt{\frac{K_S}{M}} cos(\vec{q} a_0/2) , \tag{5.5}$$

which resembles the slope of the phonon dispersion curves.[130] Therefore a low bond strength between the atoms and high atomic masses lead to low phonon group velocities and a low value of the maximum value of the vibrational frequency.

As seen in Equation 5.1, the lattice thermal conductivity depends on the group velocity of the phonons, which is difficult to access because of a broad spectrum of phonons present. However, the high energetic optical phonons have low group velocities and are not effective in transporting heat energy through the lattice, even though they might affect the heat conduction due to interactions with the acoustic phonons.[19, 130, 131] This approximation becomes more valid in materials that contain atoms with a high mass contrast, as well as a variety of chemical bonds, because these features promote a large energy gap between the acoustic and optical modes, often leading to lower group velocities.[132, 133] The acoustic phonons are the main heat conductors and for a material with low thermal conductivity the group velocity of the acoustic branches should be small.[19] Hence materials with heavy atoms and low bond strength usually exhibit low thermal conductivities.

Heat Capacity

When the temperature of a solid is raised, the supplied heat increases the occupation of the vibrational energy states of the atoms. The energy difference of the vibrational states is given by:

$$\Delta E = \hbar \omega \tag{5.6}$$

with the vibrational density of states:[134, 135]

$$g(\omega) d\omega = \frac{4\pi \omega^2 V}{v_m^3} d\omega , \tag{5.7}$$

where V is the volume, ω the vibrational frequency, and v_m the average velocity of sound. Quantum statistics leads to the occupation number of the different states (n_i):[135]

$$n_i = \frac{1}{exp\left(\frac{h\omega}{k_B T}\right) - 1} \tag{5.8}$$

However the vibrations of a solid are not an elastic continuum, because they are comprised of atoms. Each atom has three degrees of dynamical freedom and a solid containing N atoms has $3N$ degrees of vibrational freedom, which imposes a limit on the maximum frequency $\omega_{max} = \omega_D$ (Debye theory). With the Debye frequency ω_D the total number of all distinguishable phonon modes is:[134]

$$3N = \int_0^{\omega_D} g(\omega) d\omega \ , \tag{5.9}$$

with

$$\omega_D = \left(\frac{3N}{4\pi V}\right)^{\frac{1}{3}} v_m \ . \tag{5.10}$$

Considering the total energy U of the phonon modes thermodynamically leads to the heat capacity of a system of:[134]

$$C \propto \int_0^{\Theta_D/T} \frac{x^4 e^x}{(e^x - 1)^2} \left(\frac{T}{\Theta_D}\right)^3 dx \ . \tag{5.11}$$

The quantity Θ_D is known as the Debye temperature:[130, 134, 135]

$$\Theta_D = \frac{h\omega_D}{k_B} \ . \tag{5.12}$$

At temperatures above the Debye temperature with $\Theta_D \ll T$ all vibrational states are sufficiently occupied and the value of C reaches the classical value of 3R (Dulong-Petit law).[134] However, for the materials considered in this thesis, this value is likely to result in an underestimation ($\sim 10\%$) of the thermal conductivity at high temperatures.[136]

The Debye temperature Θ_D of a material can be easily estimated from the mean speed of sound v_m and the average volume per atom Ω via:[137]

$$\Theta_D = \frac{v_m \hbar}{k_B} \left(\frac{6\pi^2}{\Omega}\right)^{1/3} \ , \tag{5.13}$$

where the average speed of sound is calculated from the longitudinal v_l and transverse v_t sound velocities:

$$v_m = \frac{3}{v_l^{-3} + 2v_t^{-3}} \ . \tag{5.14}$$

Obviously large volumes of the unit cell and small number of atoms (see Equation 5.10), as well as a high mass of the atoms and a weak bond strength lead to a low Debye cutoff frequency and a low Debye temperature, which in turn leads to a low heat capacity of a solid.

Scattering Mechanisms

The use of Equation 5.1 not only shows the need for a low heat capacity and phonon group velocity, but also small phonon mean free paths or small phonon scattering relaxation times. There are different mechanisms for phonons to get scattered along their propagation through the lattice and the scattering relaxation time can be written as the sum of the different contributions using Matthiessen's rule:[39]

$$\tau^{-1} = \tau_N^{-1} + \tau_U^{-1} + \tau_B^{-1} + \tau_{PD}^{-1} + \tau_{EP}^{-1} \,, \tag{5.15}$$

with the different scattering relaxation times for normal phonon scattering (N), Umklapp scattering (U), boundary scattering (B), point defect scattering (PD), and electron-phonon scattering (EP), respectively.

For phonon-phonon scattering (normal and Umklapp-scattering), effects by normal processes (or N-processes) are ignored since they conserve the phonon wave vector. Furthermore electron-phonon scattering will not be discussed here since its effect is small compared to the other scattering mechanisms.[39]

Umklapp processes are 3-phonon processes in which the scattering processes translates the wave vector into another Brillouin zone, in other words, the crystal momentum changes due to the scattering event. The inverse phonon scattering relaxation time for Umklapp scattering is proportional to the phonon frequency ω ($\tau_U^{-1} \propto \omega^2$) showing that low frequency (or long wavelength) phonons are more heavily scattered by these phonon-phonon scattering processes.[39]

The temperature dependence of κ_L for phonon-phonon Umklapp-scattering is well described by a 1/T dependence which, in materials with low mass contrast and simple crystal structures, is given by:[102]

$$\kappa_L = \frac{(6\pi^2)^{2/3}}{4\pi^2} \frac{\bar{M} v_m^3}{T \Omega^{2/3} \gamma^2} \,, \tag{5.16}$$

where $\bar{M}$ is the average mass, v_m the average speed of sound, Ω the volume per atom and γ the Grüneisen parameter. This can also be expressed in terms of the Debye temperature shown by Klemens:[138]

$$\kappa_L \approx \frac{\pi}{2\gamma^2} \left(\frac{k_B}{h} \right)^3 \bar{M} a \frac{\Theta_D^3}{T} \,, \tag{5.17}$$

with the lattice parameter a. The Grüneisen parameter is defined as:[139]

$$\gamma = -\left(\frac{dln\omega_D}{dlnV} \right)_T = \frac{3\alpha_T B_T V}{C} \,, \tag{5.18}$$

with the linear coefficient of thermal expansion α_T and the isothermal bulk modulus B_T. The bulk modulus can be experimentally obtained from the density D and the longitudinal and transverse speeds of sound via:

$$B_T = D \left(v_l^2 - \frac{4}{3} v_t^2 \right) \,. \tag{5.19}$$

The Grüneisen parameter relates to the anharmonicity of the lattice vibrations. Low γ is achieved in materials with very low anharmonicity for example in the tetrahedrally bonded ZnSe (γ = 0.8), while very anharmonic materials exhibit Grüneisen parameters greater than 1.[139] For example, materials with free electron pairs on one atom in the unit cell exhibit a high anharmonicity usually resulting in low lattice thermal conductivities.

In the limit of acoustic phonons contributing to the thermal transport only, the temperature dependence of the lattice thermal conductivity can be expressed via:[19]

$$\kappa_L = \frac{(6\pi^2)^{2/3}}{4\pi^2} \frac{\bar{M} v_m^3}{T V^{2/3} \gamma^2} \frac{1}{N^{1/3}} \,, \tag{5.20}$$

showing the effect of the number of atoms N in a unit cell on κ_L. It is therefore practical to search for materials with a large number of atoms per unit cell.

Boundary scattering is a very effective mechanism particularly in nanostructured materials such as nanowires, thin films, and nanocomposites. The use of nano structuring or interfaces reduces the phonon mean free path due to scattering of the low frequency (large wavelength) phonons, which carry the largest portion of heat.[42, 43, 41] For example in PbTe 10 % of the heat at room temperature is carried by phonons with a mean free path of greater than 860 nm[140] and Pei *et al*.[43] have shown that a 20 % reduction in phonon thermal conductivity can be expected in PbTe by scattering the phonons with mean free paths greater than 200 nm.

Another very effective way to reduce the phonon mean free path of a material is the utilization of point imperfections or point defects. Scattering by point defects can be achieved through alloying with other elements,[33] successfully shown for thermoelectric materials in Heusler compounds,[34] skutterudites,[35, 36] lead telluride,[37] and SiGe.[38, 39] While alloying with isoelectronic elements does not introduce charge carriers into a material, it creates point defect scattering for phonons due to mass differences[141] (or mass field fluctuations) and strain field fluctuations. This strain arises from different bonding interactions and size differences between the host and impurity atoms,[34] and expresses itself in the lattice parameters.

The scattering relaxation time for point defect scattering is given by:[142]

$$\tau_{PD} = \frac{4\pi}{V} \frac{v_g(\omega) v_p^2(\omega)}{\omega^4} \left(\sum f_i \left(1 - \frac{m_i}{m}\right)^2 + \sum f_i \left(1 - \frac{r_i}{r}\right)^2 \right)^{-1} \,, \tag{5.21}$$

with the phonon group and phase velocities, v_g and v_p, respectively. Here, f_i is the fraction of atoms with mass m_i and radius r_i that reside on a site with average mass m and radius r.[142] The inverse phonon scattering relaxation time for point defects is proportional to the phonon frequency ω ($\tau_{PD}^{-1} \propto \omega^4$) showing that high frequency (or short wavelength) phonons are more heavily scattered by these static point imperfections, leading to an effective way of scattering phonons that are not influenced by phonon-phonon processes.

Following Callaway's expression to model the effect of point defect scattering on the thermal transport at higher temperatures ($\Theta_D \ll T$)[33] and combining it with the approaches of Alekseeva *et al*.[37] and Yang *et al*.[34] leads to a model in which the fractional occupancies on the lattice sites can be neglected even if the lattice parameters do not follow Vegard's law.

If only Umklapp and point defect scattering are the only scattering sources, the ratio of κ_L of the crystal with disorder to the crystal without disorder, κ_L^p, is:[34]

$$\frac{\kappa_L}{\kappa_L^p} = \frac{tan^{-1}(u)}{u} \ , \tag{5.22}$$

with the disorder scaling parameter u, which can be expressed as:[34]

$$u^2 = \frac{\pi^2 \Theta_D \Omega}{h v_m^2} \kappa_L^p \Gamma_{exp} \ , \tag{5.23}$$

where Ω is the average volume per atom, h Planck's constant, ν_m the average lattice sound velocity, and Γ_{exp} the experimental disorder scattering parameter. The disorder scattering parameter can be expressed as the sum of the contributions of the mass and strain field fluctuations, Γ_m and Γ_S, respectively. For the simple cubic case this can be expressed as:[37]

$$\Gamma_{exp} = x(1-x) \left[f_i \left(\frac{\Delta M}{\bar{M}} \right)^2 + \epsilon \left(\frac{a(x) - a_p}{x a_p} \right)^2 \right] \ . \tag{5.24}$$

Here $\bar{M}$ stands for the average atomic mass of the compound, ΔM for the mass difference between the host and impurity atom, ϵ is an adjustable anharmonicity parameter, $a(x)$ the lattice parameter with composition, and a_p the lattice parameter of the pure end member.

It is important to note that the strength of strain field fluctuation effects relative to mass fluctuation effects depends on more than just the size differences relative to the mass differences. Important considerations include the nature of the atomic bonding specific to each atom.[34]

5.2.2 Minimum Lattice Thermal Conductivity

The assumption of a minimum scattering length for phonons as a function of the phonon frequencies leads to a model of the glassy limit of the lattice thermal conductivity, initially described by Cahill *et al.*[143] and recently employed to calculate the lower bound for lattice thermal conductivities κ_{min} in thermoelectric materials by Toberer *et al.*[124]. The formulation is developed for amorphous materials as an extension of Einstein's model of a random walk of energy. It assumes that the minimum phonon mean free path is one-half of its wavelength, leading to:[143]

$$\kappa_{min} = \left(\frac{\pi}{6} \right)^{1/3} k_B \Omega^{-2/3} \sum_i v_i \left(\frac{T}{\Theta_i} \right)^2 \int_0^{\Theta_i/T} \frac{x^3 e^x}{(e^x - 1)^2} dx \ , \tag{5.25}$$

where the summation is over the two transverse modes v_t and the one longitudinal mode v_l, determined by speed of sound measurements, and:[54]

$$\Theta_i = v_i \left(\frac{\hbar}{k_B} \right) \left(\frac{6\pi^2}{\Omega} \right)^{1/3} \ . \tag{5.26}$$

In the high temperature limit, an estimation of the minimum lattice thermal conductivity

κ_{min} with an average volume Ω per atom is given by:[21]

$$\kappa_{min} = \frac{1}{2}\left(\frac{\pi}{6}\right)^{1/3} k_B \Omega^{-2/3}(2v_t + v_l) \; . \tag{5.27}$$

5.2.3 Electronic Contribution to the Thermal Conductivity

Measurements of the thermal conductivity of a material always leads to the total thermal conductivity κ, which is a sum of the three different contributions of the lattice thermal conductivity κ_L, the electronic thermal conductivity κ_{el}, and the bipolar contribution κ_b:

$$\kappa = \kappa_L + \kappa_{el} + \kappa_b \; . \tag{5.28}$$

The electronic contribution to the thermal conductivity can be expressed through the Wiedemann-Franz law as:[10]

$$\kappa_{el} = L\sigma T \; . \tag{5.29}$$

The value of the Lorenz number L for the free electron model is $2.44\,\mathrm{W\Omega K^{-2}}$. However, most materials do not exhibit values of the Lorenz number close to the free electron value and their temperature dependent Lorenz numbers should be calculated. In the limit of a single parabolic band, under the assumption of acoustic phonon scattering (λ = 0) the temperature dependent Lorenz number is found to be:[21]

$$L = \frac{k_B^2}{e^2}\frac{(1+\lambda)(3+\lambda)F_\lambda(\eta)F_{\lambda+2}(\eta) - (2+\lambda)^2 F_{\lambda+1}^2(\eta)}{(1+\lambda)^2 F_\lambda^2(\eta)} \; . \tag{5.30}$$

The reduced chemical potential η, can be calculated from the experimental Seebeck coefficients via Equation 4.20 using the Fermi integrals $F_j(\eta)$.

The term of the bipolar contribution to the thermal conductivity, occurs when a sample has both holes and electrons significantly contributing to σ. This energy transport in addition to that carried by the electrons and the holes is due to the creation of electron-hole pairs that extract an amount of energy. This may be a noticeable contribution to the electronic thermal conductivity when carrier concentrations and the mobilities are equal for electrons and holes.[130] Since only σ and therefore κ_{el} can be readily accessed through the measurements and the Wiedemann-Franz law, the bipolar term is usually neglected. If a significant significant bipolar contribution to the total thermal conductivity occurs, it is visible as an upturn in the lattice thermal conductivity data at higher temperatures.

5.3 $Cu_{2+x}Zn_{1-x}GeSe_4$

This section is an adapted reproduction, from *J.* Am. Chem. Soc **2012**, 134, 7147-7154.[55] Reproduced with permission of the American Chemical Society Copyright 2012.

Thermal diffusivity of the material was measured up to 670 K. The total thermal conductivity was calculated using $\kappa = dDC$ where d = thermal diffusivity, D = geometric density, C = specific heat capacity. Here, use of the Dulong-Petit approximation for the heat capacity (C

= 0.34 $Jg^{-1}K^{-1}$) is likely to result in an underestimation ($\sim$ 10%) of the thermal conductivity at high temperatures.[136] The temperature dependence of the total thermal conductivity is shown in Figure 5.3 and the effect of the previously mentioned phase transformation can be seen at around 450 K. The thermal diffusivity is additionally shown in Figure 5.3.

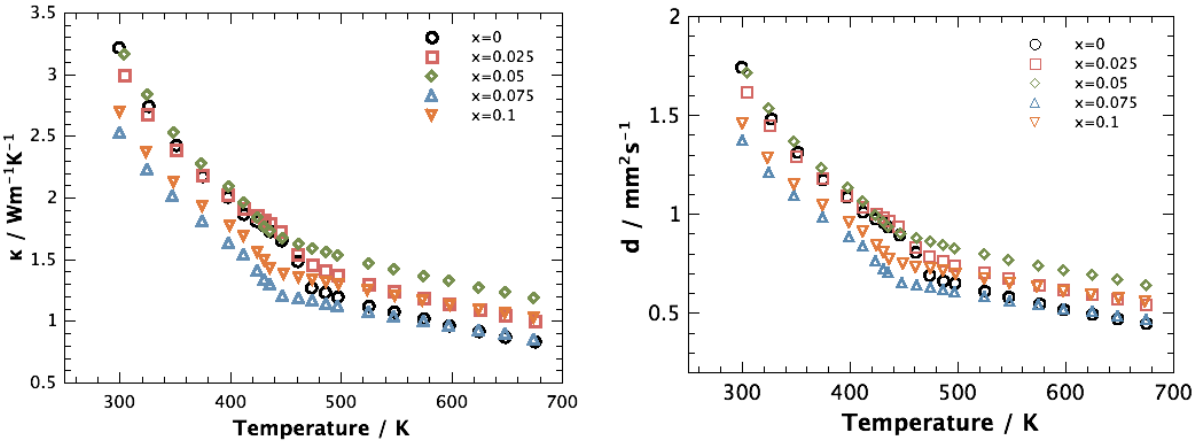

Figure 5.3: Total thermal conductivity κ (left) and thermal diffusivity d (right) of $Cu_{2+x}Zn_{1-x}GeSe_4$ as a function of temperature. The kink in the data can be attributed to the change in the electronic contribution κ_{el}.

The total thermal conductivity of a semiconducting material is a combination of lattice, electronic, and bipolar contributions ($\kappa = \kappa_L + \kappa_{el} + \kappa_b$). The Wiedeman-Franz relation $\left(\kappa_{el} = \frac{LT}{\rho}\right)$ was employed to estimate the κ_{el} contribution to the thermal conductivity. Temperature dependent Lorenz numbers (L) were calculated within the single parabolic band approximation using Equation 5.30 under the assumption of acoustic phonon scattering ($\lambda = 0$).

The electronic contribution to the total thermal conductivity (Figure 5.4) of the undoped sample is very low due to the high resistivity and increases with increasing carrier concentration. The phase transformation can be seen as well due to the change in the resistivity at the transition temperature in this material. The calculated Lorenz numbers are considerably lower than the value for the free electron model of 2.44 $W\Omega K^{-2}$.

Subtraction of κ_{el} from κ leaves the lattice and bipolar contribution of the thermal conductivity Figure (5.5). As expected for this wide band gap semiconductor there is no evidence of a significant bipolar contribution to the total thermal conductivity in this temperature range, which would be visible as an upturn in the data at higher temperatures, and the resulting thermal conductivity is hereafter referred to as lattice thermal conductivity.

The lattice thermal conductivities of $Cu_{2+x}Zn_{1-x}GeSe_4$ with x = 0, 0.025 and 0.05 are the same within the range of the measurement uncertainty for the laser flash diffusivity measurements of 3 %. This can be expected since the mass contrast between Cu and Zn is low and therefore point defect scattering, due to the mass disorder, can be assumed to be negligible. The temperature dependence of κ_L is well described by a 1/T dependence attributed to phonon-phonon Umklapp-scattering which, in materials with low mass contrast and simple crystal structures can be described by Equation 5.16. The temperature dependence of κ_{min} is given in Figure 5.5 calculated via Equation 5.25.

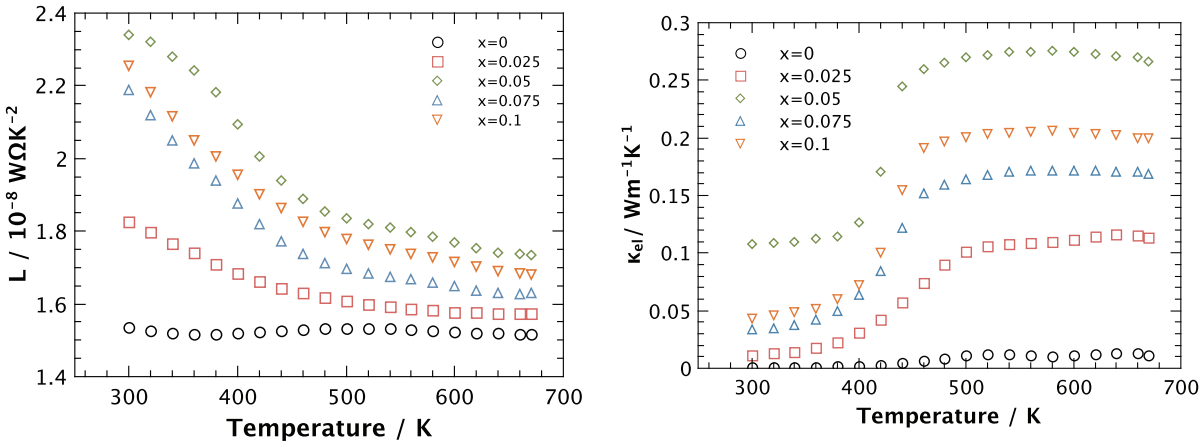

Figure 5.4: Calculated temperature dependent Lorenz number L (left) and electronic thermal conductivity κ_{el} (right) of $Cu_{2+x}Zn_{1-x}GeSe_4$. Lorenz numbers are smaller than the value for the free electron model of $2.44\,W\Omega K^{-2}$. The phase transformation is visible in the electronic thermal conductivity due to its dependence in the electrical conductivity.

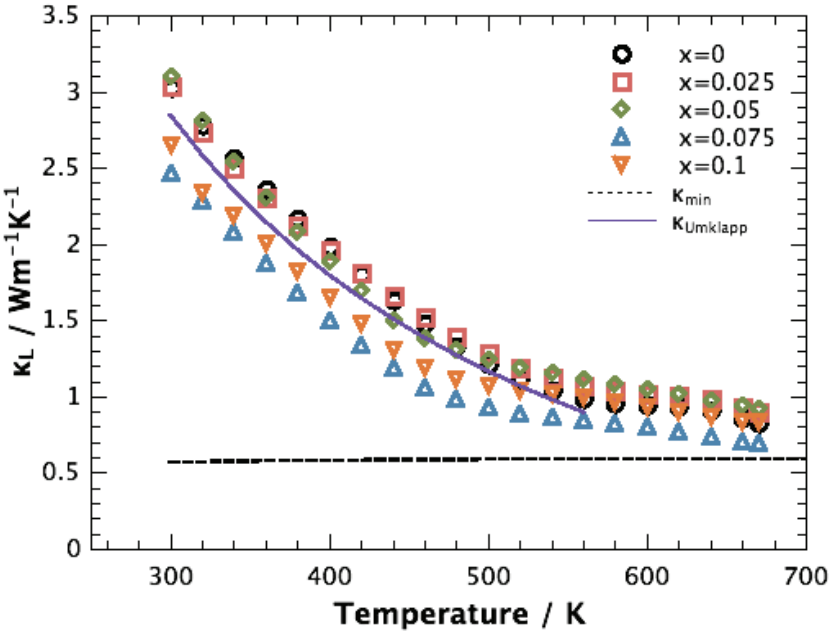

Figure 5.5: Temperature dependence of the lattice thermal conductivity κ_L of $Cu_{2+x}Zn_{1-x}GeSe_4$. κ_L exhibits a $1/T$ temperature dependence (purple line) attributed with phonon-phonon Umklapp scattering, slowly approaching the glassy limit κ_{min} (dashed line) at higher temperatures.

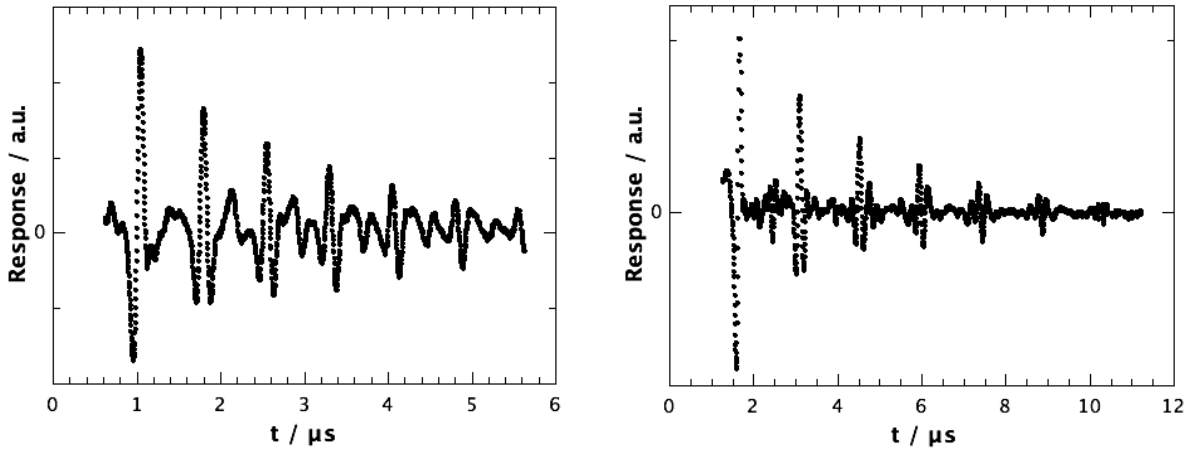

Figure 5.6: Longitudinal (left) and transverse (right) sound response data of an ultrasonic sound/response measurement of $Cu_2ZnGeSe_4$. As expected the longitudinal sound waves propagate faster than the shear modes in a solid.

Room temperature ultrasonic measurements of undoped $Cu_2ZnGeSe_4$ yield the longitudinal v_l and transverse v_t speeds of sound of 4101 m/s and 2154 m/s, respectively. The average speed of sound and the Debye temperature Θ_D of the material of 2409 m/s and 257 K, respectively, can be calculated via Equations 5.14 and 5.13. Respective speed of sound data for $Cu_2ZnGeSe_4$ can be seen in Figure 5.6. As expected the amplitudes decrease with $1/\text{distance}^2$ and the longitudinal speed of sound is faster as the transverse speed of sound in a solid. Differences in the data to other compositions of the solid solution $Cu_{2+x}Zn_{1-x}GeSe_4$ can be assumed to be negligible, again due to the very small mass contrast between Cu and Zn. Furthermore, the differences in grain size and the impurity phases on the grain boundaries are not expected to change the speed of sound significantly since the sound waves of the measurement are very long wavelength phonons.

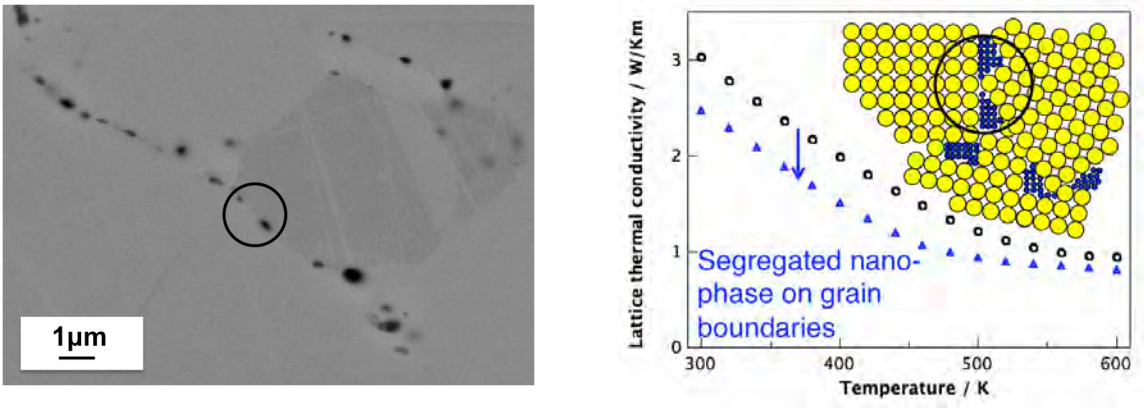

Figure 5.7: SEM micrograph of $Cu_{2.1}Zn_{0.9}GeSe_4$ (left) showing the $Cu_{2-\delta}Se$ as nano sized impurities on the grain boundaries. These impurities lead to enhanced phonon scattering and with it a significant reduction in phonon mean free path. The effect of the reduction leads to a lowering in the lattice thermal conductivity by 15%. (right)

Using Equation 5.16 and the experimental data of the temperature dependent lattice thermal conductivity, a Grüneisen parameter of $\gamma = 0.8$ has been determined for $Cu_2ZnGeSe_4$. This value is reasonable as compared with the room temperature Grüneisen parameter of ZnSe of 0.8,[139] due to similar crystal structures and bonding interactions.

In this material, a statistically significant reduction (see Figures 5.5 and 5.7) in the lattice thermal conductivity can be seen for $x = 0.075$ and 0.1, which can be attributed to the secondary phases at these substitution levels. The nanometer scale impurities are mainly located at the grain boundaries leading to an enhanced phonon scattering and therefore a significant reduction in phonon mean free path. The effect of the reduction leads to a lowering in lattice thermal conductivity of 0.3-0.5 $Wm^{-1}K^{-1}$ at room temperature, with κ_L approaching the minimum value of 0.6 $Wm^{-1}K^{-1}$ at higher temperatures.

5.4 $Cu_2Zn_{1-x}Fe_xGeSe_4$

This section is an adapted reproduction, from *J.* Am. Chem. Soc **2013** - accepted manuscript.[56] Reproduced with permission of the American Chemical Society Copyright 2013.

The total thermal conductivity was calculated from the measured thermal diffusivity using $\kappa = dDC$ where d = thermal diffusivity, D = geometric density, C = specific heat capacity. Here, use of the Dulong-Petit approximation for the heat capacity is likely to result in an underestimation ($\sim$ 10%) of the thermal conductivity at high temperatures.[136] The temperature dependence of the total thermal conductivity is shown in Figure 5.8 and the effect of the previously mentioned phase transformation can be seen at around 450 K. It has to be emphasized that the atomic structure for the thermal conductivity calculations described below are guided by the structure of the room temperature phase and not the unknown high temperature phase.

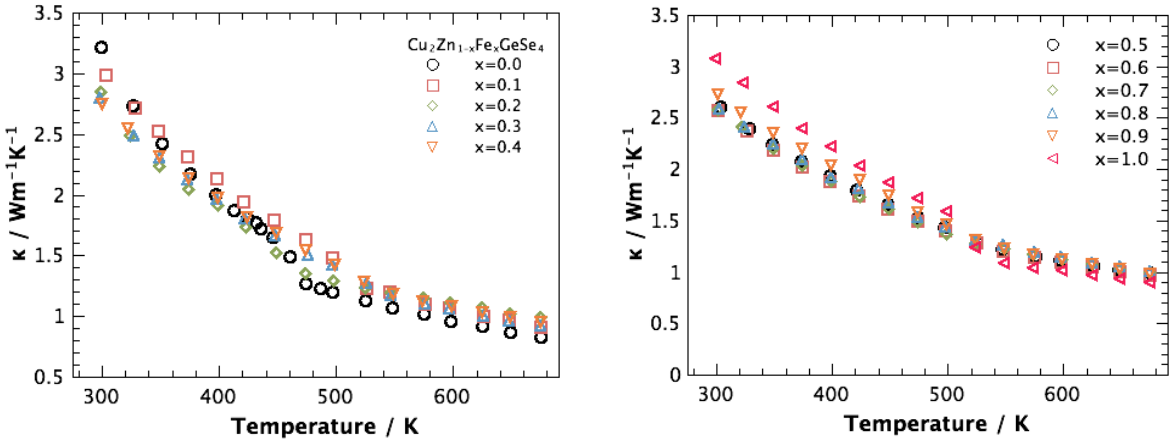

Figure 5.8: Total thermal conductivity κ of $Cu_2Zn_{1-x}Fe_xGeSe_4$ for $x = 0.0$ - 0.4 (left) and $x =$ 0.5 - 1.0 (right), as a function of temperature.

Temperature dependent Lorenz numbers L (see Figure 5.9 top) were calculated within the single parabolic band approximation using Equation 5.30 under the assumption of acoustic phonon scattering ($\lambda = 0$). And Lorenz numbers are smaller than the value for the free

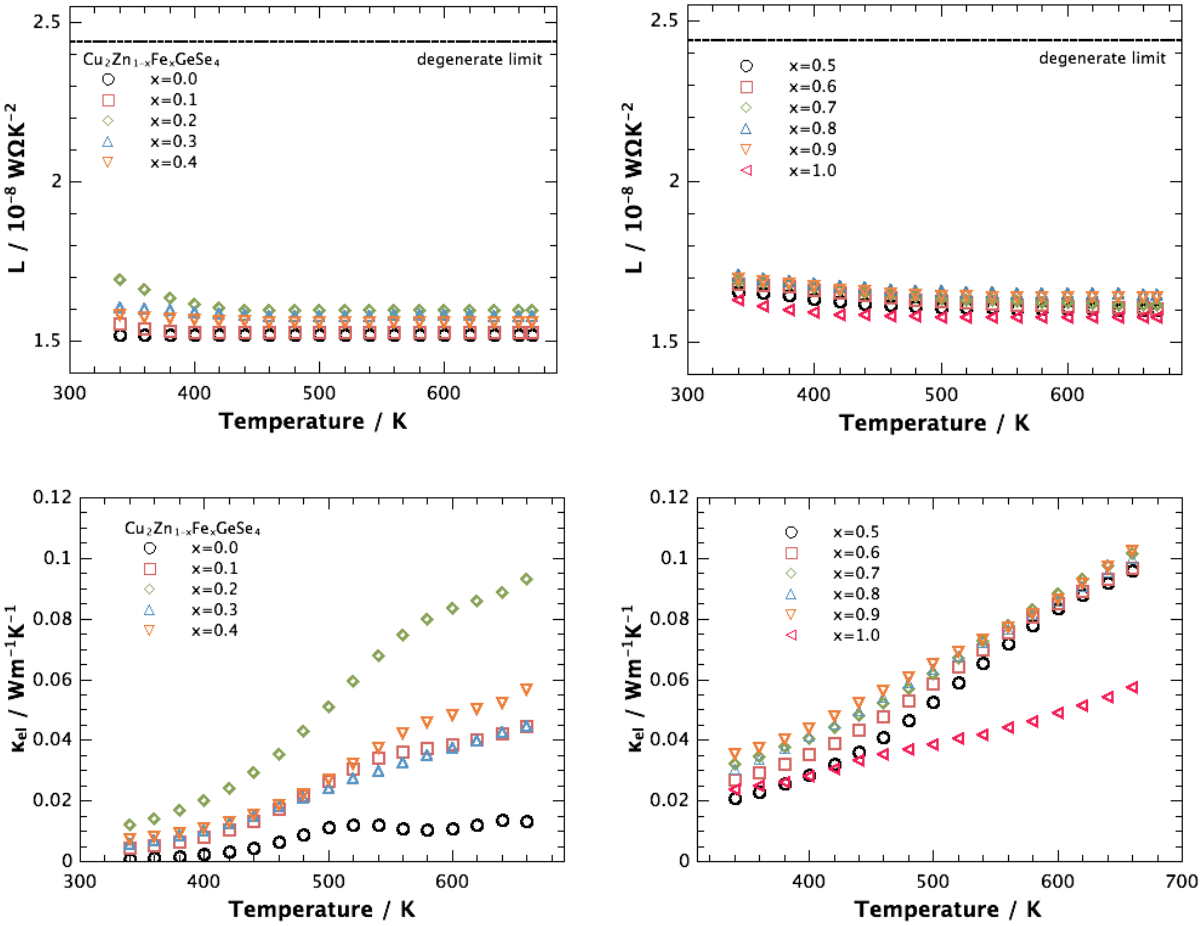

Figure 5.9: Temperature dependent Lorenz numbers (top) and electronic thermal conductivity (bottom) of $Cu_2Zn_{1-x}Fe_xGeSe_4$. The degenerate limit of the Lorenz number is indicated and the calculated Lorenz numbers are close to the non-degenerate limit.

electron model of $2.44\,W\Omega K^{-2}$. The temperature dependent electronic contribution to the thermal conductivity (see Figure 5.9 bottom) has been calculated via the Wiedemann-Franz relation with the measured electrical resistivities and the calculated temperature dependent Lorenz numbers.

Subtraction of κ_{el} from κ leaves the lattice and bipolar contribution of the thermal conductivity Figure (5.10). As expected for this wide band gap semiconductor there is no evidence of a significant bipolar contribution to the total thermal conductivity in this temperature range, which would be visible as an upturn in the data at higher temperatures, and the resulting thermal conductivity is hereafter referred to as lattice thermal conductivity. The temperature dependence of κ_L is well described by a 1/T dependence attributed to phonon-phonon Umklapp-scattering (see Equation 5.16). The temperature dependence of κ_{min} is given in Figure 5.10 calculated via Equation 5.25.

Room temperature ultrasonic measurements of $Cu_2Zn_{0.5}Fe_{0.5}GeSe_4$ and $Cu_2FeGeSe_4$ yield the longitudinal v_l and transverse v_t speeds of sound of 4230 m/s and 2225 m/s for $Cu_2Zn_{0.5}Fe_{0.5}GeSe_4$, and 4371 m/s and 2166 m/s, respectively. The average speeds of sound and the Debye temperatures Θ_D of the materials are 2488 m/s and 265 K

(for 50 % Fe content) and 2430 m/s and 260 K (for 100 % Fe content), respectively. All values are well within the measurement uncertainty of the speed of sound measurements. The similar speeds of sounds and Debye temperatures throughout this solid solution leads to the very similar κ_{min} as seen in Figure 5.10. Respective sound response data for $Cu_2Zn_{0.5}Fe_{0.5}GeSe_4$ and $Cu_2FeGeSe_4$ can be found in the Supporting Information (Chapter 8).

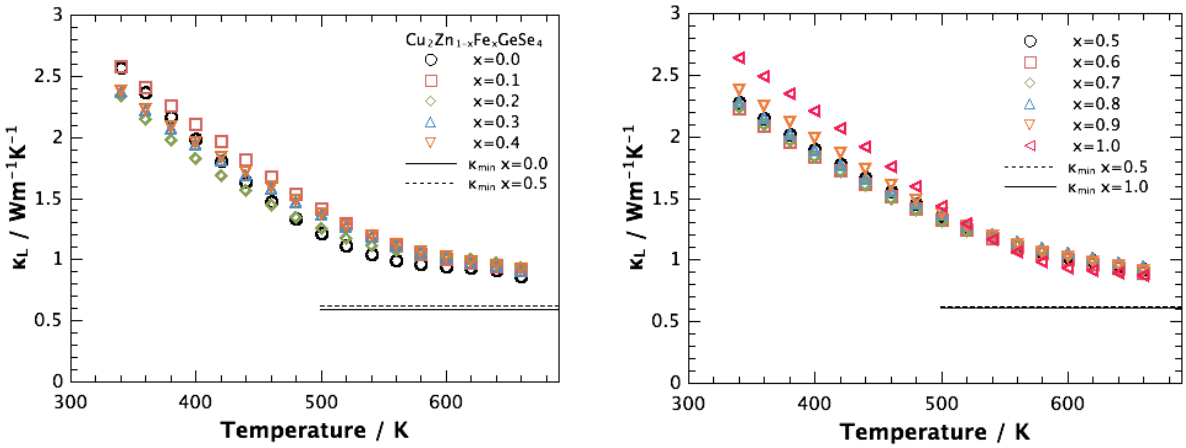

Figure 5.10: Lattice thermal conductivity κ_L of $Cu_2Zn_{1-x}Fe_xGeSe_4$ for x = 0.0 - 0.4 (left) and x = 0.5 - 1.0 (right), decreasing with temperature due to Umklapp-scattering processes. The calculated minimum lattice thermal conductivities are indicated. κ_L does not fully approach κ_{min} at the low temperatures yet. The differences in κ_{min} for different samples of the solid solution is negligible.

The lattice thermal conductivity κ_L at room temperature (see 5.11) was evaluated by subtracting the electronic contribution ($\kappa_{el} = LT\rho^{-1}$, where L = 1.5 x $10^{-8}W\Omega K^{-2}$ for non degenerate materials,[10]) i.e. $\kappa_L = \kappa - LT\rho^{-1}$. While the measurement uncertainty for the laser flash diffusivity measurement is 3 % we have assumed a combined uncertainty for κ_L of 5 % at room temperature, taking into account a 5 % error for the resistivity measurement. Upon substitution with Fe the lattice thermal conductivity decreases with increasing Fe content until a minimum value is reached at 70 % Fe content, where this trend reverses. Since the mass difference between Fe and Zn is small, this statistically significant reduction of the lattice thermal conductivity cannot be explained by the mass contrast only, as indicated in Figure 5.11, where the expected κ_L has been calculated within the Callaway model.[33, 34, 37] Furthermore, effects of the microstructure can be ruled out since similar microstructures and no impurity phases are apparent in the SEM micrographs.

The structural change that correlates with this dramatic reduction in thermal conductivity at 70 % Fe is the 3-stage cation restructuring process described in Figure 3.8 where the highest local anisotropic structural disorder occurs at at 70 % Fe content. This disorder apparently reduces the lattice thermal conductivity by 15 % resulting in a minimum for the composition $Cu_2Zn_{0.3}Fe_{0.7}GeSe_4$ due to scattering of phonons by local anisotropic strain. As the disorder scattering of the phonons, due to mass fluctuation and isotropic strain is expected to be very small from these similar mass and similar volume ions, this shows the potential of significant point defect scattering due to local anisotropic strain. As seen in Figures 5.10 and 5.11

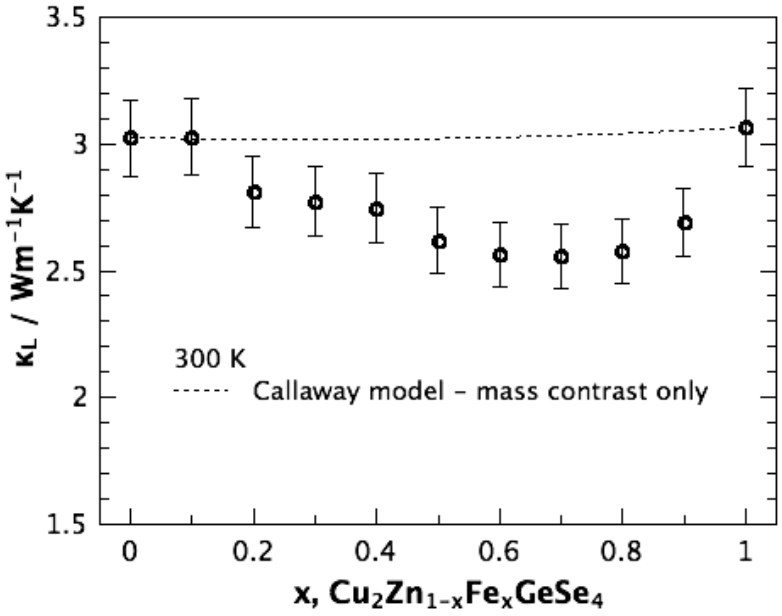

Figure 5.11: Lattice thermal conductivity κ_L of $Cu_2Zn_{1-x}Fe_xGeSe_4$ at room temperature showing a 15% reduction due to disorder scattering. An error of 5% is assumed for κ_L at room temperature. The broken line indicates the calculated influence of the mass contrast between Fe and Zn on the lattice thermal conductivity which shows that the strain related to the lattice constant change has a significant effect on the lattice thermal conductivity.

the reduction of the lattice thermal conductivity by point defect scattering is more effective at lower temperatures. With increasing temperatures the high frequency phonons get scattered mainly by phonon-phonon processes reducing their phonon mean free path. In other words, the dominant scattering mechanism at higher temperatures is phonon-phonon Umklapp scattering and point defect scattering does not contribute hugely to the lattice thermal conductivity.[103]

5.5 $Cu_{2+x}Zn_{1-x-y}Fe_yGeSe_4$

The total thermal conductivity was calculated from the measured thermal diffusivity using $\kappa = dDC$ where d = thermal diffusivity, D = geometric density, C = specific heat capacity. Here, use of the Dulong-Petit approximation for the heat capacity is likely to result in an underestimation ($\sim$ 10%) of the thermal conductivity at high temperatures.[136] The temperature dependence of the total thermal conductivity can be found in the Supporting Information in Chapter 8. It has to be emphasized that the atomic structure for the thermal conductivity calculations described below are guided by the structure of the room temperature phase and not the unknown high temperature phase.

Temperature dependent Lorenz numbers L, the electronic contribution to the thermal conductivity and lattice thermal conductivities can be found in the Supporting Information in

Chapter 8. As seen in Section 5.4 the calculated Lorenz numbers are smaller than the value for the free electron model of 2.44 $W\Omega K^{-2}$. As expected for this wide band gap semiconductor there is no evidence of a significant bipolar contribution to the total thermal conductivity in this temperature range and the temperature dependence of κ_L is well described by a 1/T dependence attributed to phonon-phonon Umklapp-scattering (see Equation 5.16).

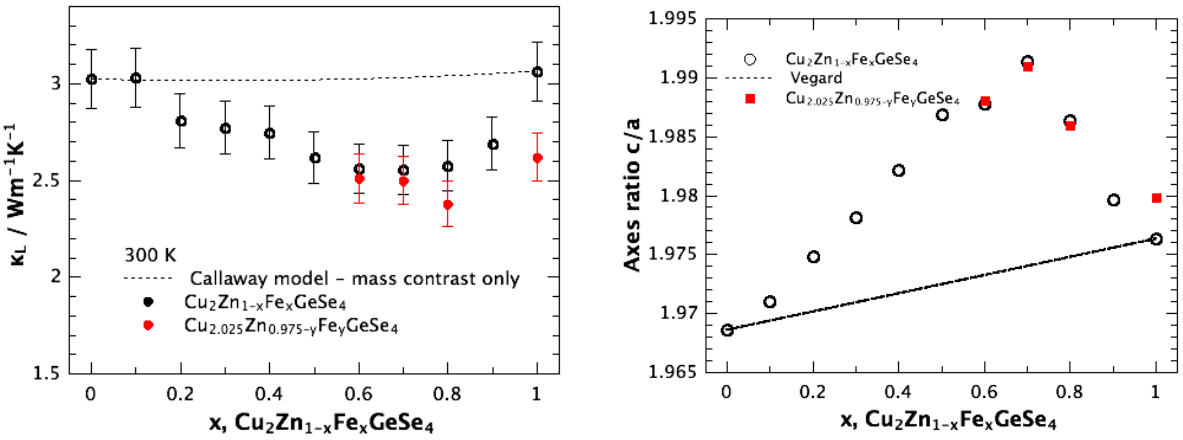

Figure 5.12: Left: Lattice thermal conductivity κ_L of $Cu_{2.025}Zn_{0.975-y}Fe_yGeSe_4$ at room temperature showing a 15% reduction due to disorder scattering. For comparison the data of $Cu_2Zn_{1-x}Fe_xGeSe_4$ has been included (black circles) and the x-axis has been labeled in respect to this solid solution. The broken line indicates the calculated influence of the mass contrast between Fe and Zn on the lattice thermal conductivity which shows that the strain related to the lattice constant change of c/a (right) has a significant effect on the lattice thermal conductivity. Right: Lattice parameter ratio c/a with composition y of $Cu_{2.025}Zn_{1-y}Fe_yGeSe_4$ (red data points), from a Pawley refinement. The broken line indicates the expected behavior following Vegard's law. For comparison the data of $Cu_2Zn_{1-x}Fe_xGeSe_4$ has been included (black circles) and the x-axis has been labeled in respect to this solid solution. A 3-stage cation restructuring process of Cu^+, Fe^{2+}, and Zn^{2+} results in the trend of the lattice parameters.

The lattice thermal conductivity κ_L at room temperature (see 5.12 (left)) was evaluated by subtracting the electronic contribution ($\kappa_{el} = LT\rho^{-1}$, where L = 1.5 x $10^{-8}W\Omega K^{-2}$ for non degenerate materials,[10]) i.e. $\kappa_L = \kappa - LT\rho^{-1}$. While the measurement uncertainty for the laser flash diffusivity measurement is 3 % we have assumed a combined uncertainty for κ_L of 5 % at room temperature, taking into account a 5 % error for the resistivity measurement. As seen in Section 5.4, upon substitution with Fe the lattice thermal conductivity decreases with increasing Fe content until a minimum value is reached at 70 % Fe content, where this trend reverses. The mass difference between Fe and Zn is small, this statistically significant reduction of the lattice thermal conductivity cannot be explained by the mass contrast only, as indicated in Figure 5.11, where the expected κ_L has been calculated within the Callaway model.[33, 34, 37]

This reduction in the lattice thermal conductivity has been attributed to the structural change in this material, which is due to a 3-stage cation restructuring process described in Figure 3.8 where the highest local anisotropic structural disorder occurs at at 70 % Fe con-

tent. The solid solution $Cu_{2.025}Zn_{0.975-y}Fe_yGeSe_4$ supports this explanation, since the lattice parameter ratio c/a (see Figure 5.12 (right)) and the lattice thermal conductivity reproduce the results of Section 5.4 fairly well, with a high c/a-ratio leading to a lowering of κ_L due to to scattering of phonons by local anisotropic strain.

5.6 Ca_3AlSb_3 and Sr_3GaSb_3

This section is an adapted reproduction, from *J*. Mater. Chem **2012** 22, 9826-9830 and *E*nergy Environ. Sci. **2012**, 5, 9121-9128.[96, 100] Reproduced with permission of The Royal Society of Chemistry Copyright 2012.

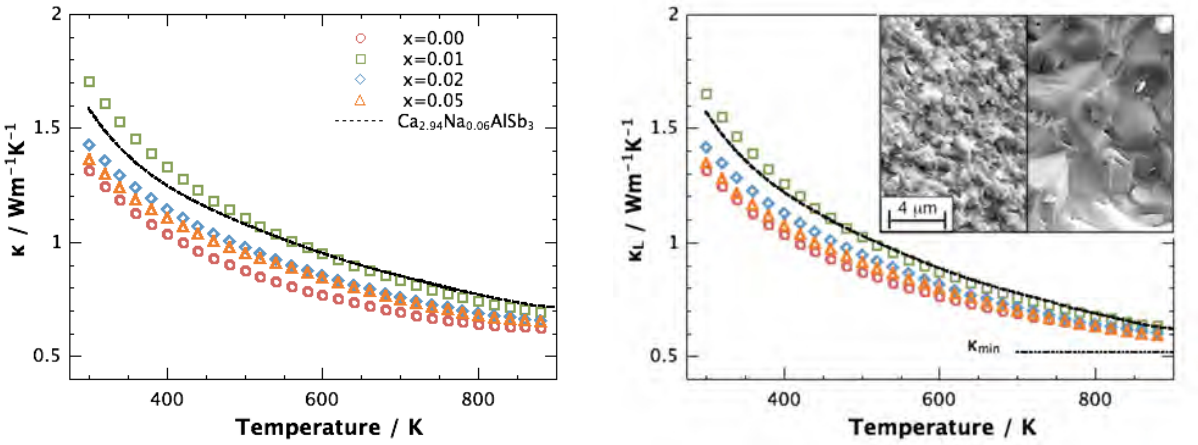

Figure 5.13: Total thermal conductivity (left) and lattice thermal conductivity (right) of $Ca_3Al_{1-x}Zn_xSb_3$ with temperature, with the theoretical minimum lattice thermal conductivity at higher temperatures. The inset illustrates the different grain sizes of the samples. Smaller grains (left) for the compositions with x = 0.00, 0.02, and 0.05 and larger grain sizes for x = 0.01 (right). The scale bar is representative for both micrographs. While the lattice thermal conductivity approaches κ_{min} at higher temperatures, the grain size influences the thermal transport at lower temperatures. Larger grains lead to higher lattice thermal conductivities due to less boundary scattering of the phonons.

The total thermal conductivities of Ca_3AlSb_3 (see Figure 5.13) and Sr_3GaSb_3 (see Figure 5.14), were calculated using $\kappa = dDC$ where d = thermal diffusivity, D = geometric density, C = specific heat capacity. The specific heat capacity was estimated using the Dulong-Petit law. While generally accurate at room temperature, the Dulong Petit heat capacity often underestimates C_p at high temperature by as much as 10 %, leading to an overestimation of zT.[136] The electronic contribution κ_{el} to the total thermal conductivity can be estimated from the Wiedemann-Franz relation ($\kappa_{el} = LT/\rho$). In this study, the Lorenz numbers L are calculated from the experimental Seebeck coefficients using a single parabolic band model as described in Section 5.2.3 and Equation 5.30. The electronic thermal conductivities and Lorenz numbers for $Ca_3Al_{1-x}Zn_xSb_3$ and $Sr_3Ga_{1-x}Zn_xSb_3$ can be seen in the Supporting Information in Chapter 8.

Subtracting the electronic term from the total thermal conductivity leaves the lattice ther-

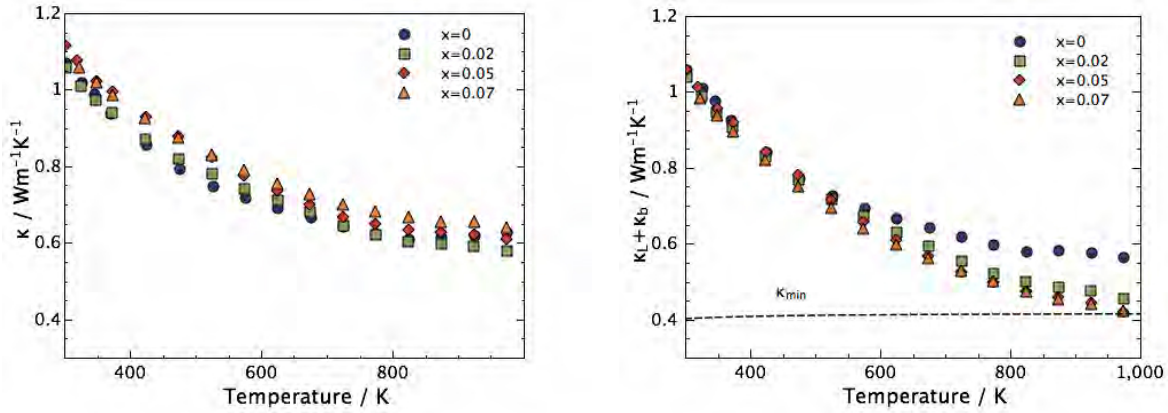

Figure 5.14: Total thermal conductivity (left) and lattice thermal conductivity (right) of $Sr_3Ga_{1-x}Zn_xSb_3$. The calculated minimum lattice thermal conductivity κ_{min} is shown as a broken line, with the theoretical minimum lattice thermal conductivity at higher temperatures. The undoped composition with $x = 0$ exhibits a significant bipolar contribution, evidenced by the increase in $\kappa_L + \kappa_b$ at high temperatures relative to the doped samples.

mal conductivity and the bipolar contribution. No significant bipolar contribution can be observed for Ca_3AlSb_3 (see Figure 5.13) in this temperature range, which would be visible as an upturn in the data at higher temperatures. Of the samples in these studies, only the undoped Sr_3GaSb_3 exhibits a significant bipolar contribution, evidenced by the increase in $\kappa_L + \kappa_b$ at high temperatures relative to the doped samples, as seen in Figure 5.14.[10] In all other remaining compositions for Ca_3AlSb_3 and Sr_3GaSb_3 the lattice thermal conductivity is the dominant term, decreasing with a T^{-1} temperature dependence expected when scattering is dominated by Umklapp processes (Equation 5.16).[130] In all samples, the lattice thermal conductivities approach the minimum thermal conductivity κ_{min} (Figure 5.13), which was calculated using speed of sound measurements and Cahill's formula for disordered crystals (Equation 5.25).

Room temperature ultrasonic measurements of undoped Ca_3AlSb_3 (see Supporting Information Chapter 8) yield longitudinal and transverse speeds of sound of 4170 m/s and 2440 m/s respectively. From these, a mean speed of sound of 2710 m/s and an effective Debye temperature of 261 K are calculated using Equations 5.13 and 5.14.

The influence of Zn on the lattice thermal conductivity seems to be negligible in these materials, as reported in the sodium doped Ca_3AlSb_3.[95] However, the sample with nominal composition $Ca_3Al_{0.99}Zn_{0.01}Sb_3$ exhibits a higher thermal conductivity at lower temperatures. This can be attributed to the larger grains in this sample (see Figure 5.13). The larger grains lead to less grain boundary scattering and hence longer phonon mean free paths compared to the sub-micron grains in the other samples and thus higher lattice thermal conductivities at lower temperatures. At higher temperatures the effect of the grain boundaries becomes less pronounced. Phonon-phonon processes reduce the phonon mean free path with increasing temperature. At higher temperature the phonon mean free path is smaller than the average grain size and scattering events take place before phonons could become scattered at the boundaries, leading to a nearly grain size independent lattice thermal conductivity at higher

temperatues. In conclusion the influence of grain boundary scattering is seen on the thermal transport with larger grain sizes exhibiting less scattering, which in turn leads to higher lattice thermal conductivities.

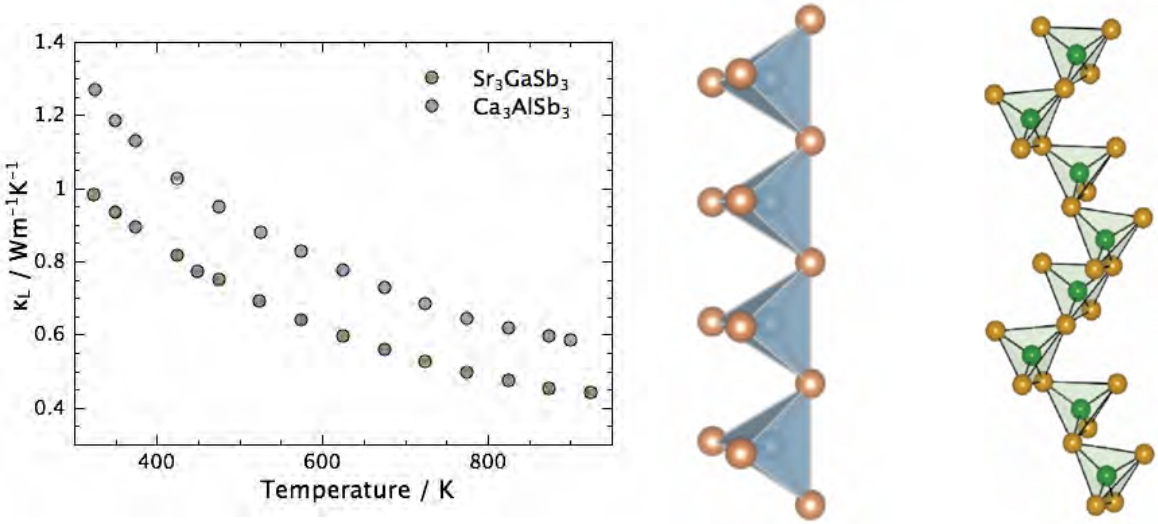

Figure 5.15: Left: Lattice thermal conductivities of Ca_3AlSb_3 and Sr_3GaSb_3 with temperature. Right: The distinct chain-like poly-anions formed by the Zintl-antimonides Ca_3AlSb_3 and Sr_3GaSb_3. Sb (orange) resides at the tetrahedral corners, while either Ga (green) or Al (blue) resides in the centers. The difference in the crystal structures and densities lead to the difference of $0.2\,Wm^{-1}K^{-1}$.

The large number of atoms per unit cell in Sr_3GaSb_3 (N=56), lead, by definition, to a phonon dispersion with 3 acoustic modes and 55×3 optical modes. Such complexity in the dispersion leads to both enhanced Umklapp scattering and flattened, low velocity optical modes that contribute very little to heat transport.[101, 102] These features, combined with the small grain size in our Sr_3GaSb_3 samples (see Supporting Information in Chapter 8), lead to the extremely low lattice thermal conductivity observed in this material.

To estimate the minimum lattice thermal conductivity κ_{min} for Sr_3GaSb_3, and thus to determine whether further nano structuring would be beneficial, we have employed Cahill's formula for disordered crystals (see Equation 5.25).[143] κ_{min} is dependent on the longitudinal and transverse sound velocities, which were determined from ultrasonic measurements to be 3750 m/s and 2130 m/s, respectively. These yield an estimated Debye temperature of θ_D = 243 K and κ_{min} = $0.43\,Wm^{-1}K^{-1}$. At high temperature, the lattice thermal conductivity of Sr_3GaSb_3 approaches the estimated κ_{min}, in common with Ca_3AlSb_3, adding to the growing body of evidence suggesting that large unit cell size leads to the glass-like high temperature κ_L observed in a number of thermoelectric materials.

In the left panel of Figure 5.15 are the lattice thermal conductivities of Ca_3AlSb_3 and Sr_3GaSb_3, estimated from the measured diffusivity of Zn-doped samples. Though both compounds exhibit an identical temperature dependence indicative of Umklapp-scattering, κ_L in Sr_3GaSb_3 is about 25% lower across the entire temperature range. Accounting for traditional

factors such as $\bar{M}$, V, and sound velocity explains only $\sim$10% of the disparity. This assumes that the Grüneisen parameter does not vary greatly between these three compounds (see Equation 5.16), which is reasonable given the same tetrahedral symmetry and the bonding interaction. The remaining difference in κ_L can be explained by the exceptionally large unit cell of Sr_3GaSb_3 (N= 56), which is twice the size of Ca_3AlSb_3 (N= 28) and thus significantly reduces the acoustic lattice thermal conductivity (Equation 5.20). The resulting large unit cell and comparatively high density in Sr_3GaSb_3 combine to yield the exceptionally low lattice thermal conductivity observed in this material (with κ_L = 0.45 $Wm^{-1}K^{-1}$ at 1000 K).

6 Thermoelectric Efficiency

6.1 Summary

This chapter focuses on the thermoelectric performances of the materials discussed in this thesis: $Cu_{2+x}Zn_{1-x}GeSe_4$, $Cu_2Zn_{1-x}Fe_xGeSe_4$, $Cu_{2+x}Zn_{1-x-y}Fe_yGeSe_4$, Ca_3AlSb_3 and Sr_3GaSb_3.

The chapter begins with a short review of the thermoelectric figure of merit, which has been extensively introduced in the Introduction in Chapter 1. Then the important equations which have been used for the transport modeling will be introduced, with the goal to assess the optimum carrier concentration in the materials discussed.

As seen in Chapter 4 the substitution of Zn^{2+} with Cu^{+} introduces holes as charge carriers in $Cu_2Zn_{1-x}GeSe_4$ leading to a lower thermopower and higher electrical conductivities. The resulting carrier concentrations result in an increased power factor compared to the "undoped" material. This, in combination with the lower lattice thermal conductivity, due to a nano sized phase segregation of $Cu_{2-\delta}Se$, leads to an increased figure of merit of 0.45 at 670 K for x = 0.075.

In the solid solutions of $Cu_2Zn_{1-x}Fe_xGeSe_4$ and $Cu_{2+x}Zn_{1-x-y}Fe_yGeSe_4$ the increased band effective mass (see Chapter 4) and higher valley degeneracy, and therefore increased Seebeck coefficients lead to an increased intrinsic figure of merit zT of 0.3 at 670 K for x = 0.6, 0.7 and 0.8 compared to the end members $Cu_2ZnGeSe_4$ (0.1 at 670 K) and $Cu_2FeGeSe_4$ (0.1 at 670 K).

In Ca_3AlSb_3 and Sr_3GaSb_3, doping with zinc increases the figure of merit due to increased carrier concentrations, leading to a zT of 0.5 at 900 K for Ca_3AlSb_3. However the peak zT values of the sodium doped Ca_3AlSb_3[95] material cannot be achieved with zinc due to the lower carrier concentrations, which are well below the optimum carrier concentration. The doping of $Sr_3Ga_{1-x}Zn_xSb_3$ with zinc leads to an increase in the maximum zT from 0.4 for x = 0 to greater than 0.9 when x = 0.07. The improved peak zT of Sr_3GaSb_3 compared with Ca_3AlSb_3 can be attributed almost entirely to its lower lattice thermal conductivity, resulting from the larger unit cell and comparatively high mass density in Sr_3GaSb_3.

6.2 Thermoelectric Efficiency

The efficiency of a thermoelectric material is assessed through the materials dimensionless figure of merit zT (see Chapter 1 and Equations 1.8 and 1.9):

$$zT = \frac{\alpha^2\sigma}{\kappa}T$$

and

$$zT = \frac{\alpha^2\sigma}{\kappa_L + \kappa_{el}} T \ ,$$

with the power factor $PF = \alpha^2\sigma$, determined by the Seebeck coefficient α, the electrical conductivity σ, the Lorenz number L, and the lattice κ_L and electronic contribution κ_{el} to the total thermal conductivity κ.

The figure of merit has a maximum at a given optimum carrier concentration as seen in Figure 1.3. It is therefore necessary to determine the optimum carrier concentration in a given material to be able to tune the zT to a maximum value at a certain temperature. The figure of merit can be written as a function of the reduced electrochemical potential η (see Section 4.2):[21]

$$zT = \frac{\alpha^2}{L + (\psi\beta)^{-1}} \ , \tag{6.1}$$

where

$$\beta = \frac{\mu_0 (m^*/m_e)^{3/2} T^{5/2}}{\kappa_L} \ , \tag{6.2}$$

$$\mu_H = \mu_0 \frac{(1/2 + 2\lambda) F_{2\lambda - 1/2}(\eta)}{(1+\lambda) F_\lambda(\eta)} \ , \tag{6.3}$$

and

$$\psi = \frac{8\pi e}{3} \left(\frac{2 m_e k_B}{h^2} \right)^{3/2} (1+\lambda) F_\lambda(\eta) \ . \tag{6.4}$$

The values of α and L can be calculated via Equations 4.20 and 5.30, respectively. The electron mass m_e and μ_0 can extracted from μ_H at the temperature of interest.[21]

This method is based on the assumption of a single parabolic band and is used for the Zintl phases in this Chapter under the assumption of acoustic phonon scattering (λ = 0).

6.3 $Cu_{2+x}Zn_{1-x}GeSe_4$

This section is an adapted reproduction, from *J.* Am. Chem. Soc **2012**, 134, 7147-7154.[55] Reproduced with permission of the American Chemical Society Copyright 2012.

The power factor and figure of merit are shown in Figure 6.1. The carrier concentration of 7.7x10^{19} cm^{-3} of x = 0.025 leads to the highest power factor in the material, while higher doping levels introduce too many charge carriers (see Section 4.3). This doping level seems to achieve the optimum carrier concentration for this material. However, the figure of merit of the samples with x = 0.075 are higher than those with x = 0.025 due to a statistically significant reduction of the lattice thermal conductivity induced by the nano sized impurities located at the grain boundaries (see Section 5.3). The material exhibits the highest figure of merit of 0.45 at 670 K for x = 0.075. The maximum zT is not yet reached in this temperature range, because the wide band gap of these compounds effectively suppresses the thermal activation of minority charge carriers. Additionally, the incorporation of a protective coating to prevent

the evaporation of selenium will stabilize the material for use and measurement at higher temperatures that should result in higher figure of merit values as seen for $Cu_2ZnSnSe_4$ (zT = 0.45 at 700 K and 0.9 at 860 K).[57, 59]

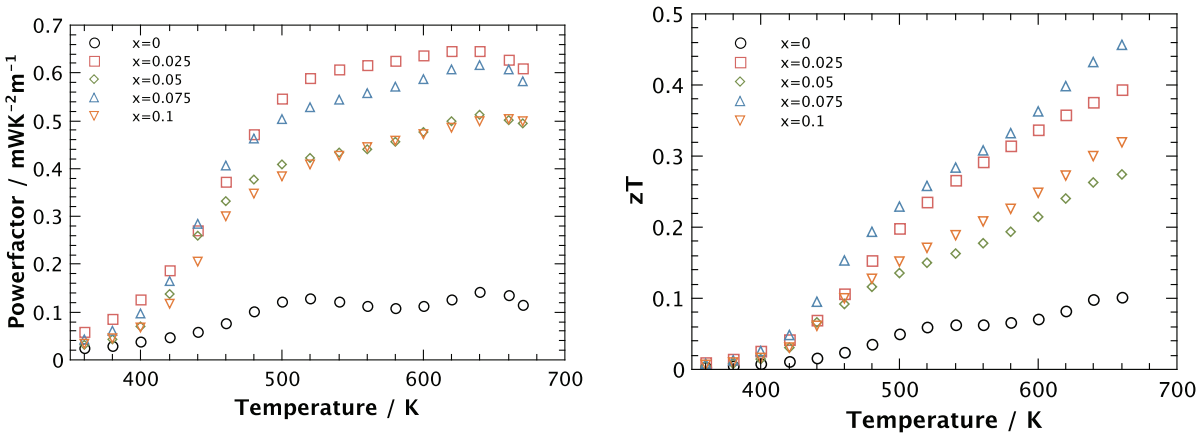

Figure 6.1: Temperature dependence of the power factor PF (left) and figure of merit zT (right) for the solid solutions $Cu_{2+x}Zn_{1-x}GeSe_4$. The highest power factor is achieved for the carrier concentration at the doping level of x = 0.025, but the highest figure of merit is for x = 0.075 due to the reduction of lattice thermal conductivity by nano sized impurities.

6.4 $Cu_2Zn_{1-x}Fe_xGeSe_4$ and $Cu_{2+x}Zn_{1-x-y}Fe_yGeSe_4$

Power factors and figure of merits with temperature of the solid solution $Cu_2Zn_{1-x}Fe_xGeSe_4$ are shown in Figure 6.2 and 6.3, respectively. The data for the solid solution $Cu_{2+x}Zn_{1-x-y}Fe_yGeSe_4$ can be found in the Supporting Information in Chapter 8.

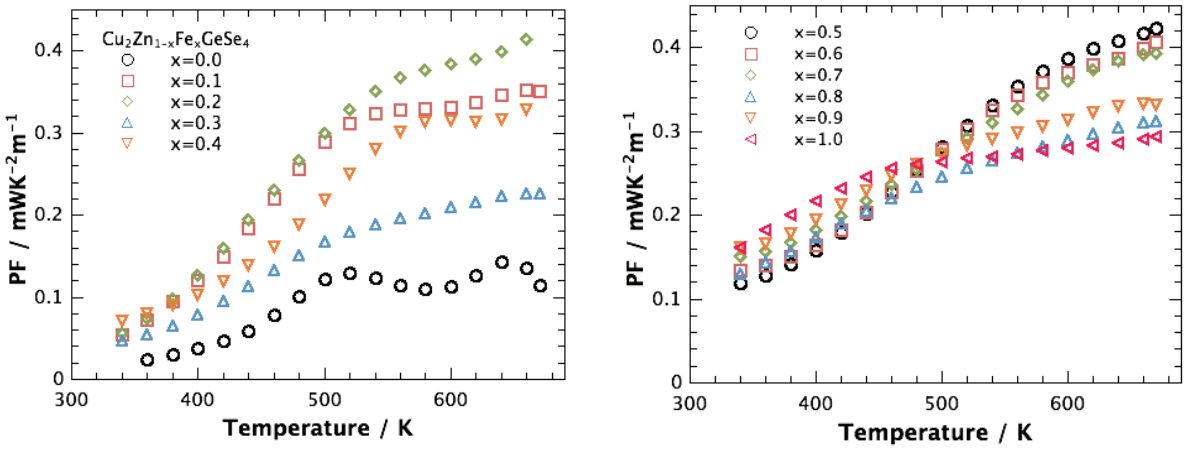

Figure 6.2: Temperature dependence of the power factor PF of $Cu_2Zn_{1-x}Fe_xGeSe_4$ for x = 0.0 - 0.4 (left) and x = 0.5 - 1.0 (right). The highest power factors are achieved for the materials compositions which exhibit the highest effective masses and Hall carrier concentrations.

The increased Hall carrier concentration due to the defects and the multi-band behavior from Fe substitution result in an increase of the power factor from 0.1 $mWK^{-2}m^{-1}$ at 670 K for $Cu_2ZnGeSe_4$ to a maximum of $\sim$ 0.4 $mWK^{-2}m^{-1}$ for x = 0.2, 0.5, 0.6, and 0.7, respectively. As expected, the highest power factors are achieved for the compositions with the highest Hall carrier concentrations and highest effective masses showing the high influence on the transport.

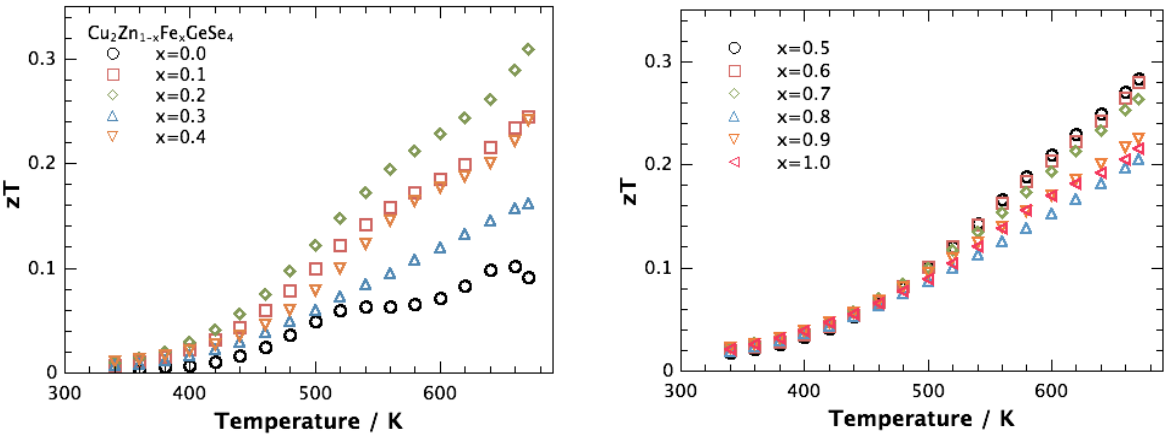

Figure 6.3: Temperature dependence of the figure of merit zT of $Cu_2Zn_{1-x}Fe_xGeSe_4$ for x = 0.0 - 0.4 (left) and x = 0.5 - 1.0 (right). The high power factors resulting from high effective masses at higher Hall carrier concentrations in combination with the reduction of the lattice thermal conductivities due to anisotropic strain lead to a figure of merit of nearly 0.3 at 670 K for these intrinsic solid solutions.

The combination of the reduced lattice thermal conductivities due to anisotropic structural disorder resulting from the 3-stage cation restructuring process (as seen in Section 5.4), showing a minimum at x = 0.7, with the high power factors results in the reasonable high figure of merits of $\sim$ 0.3 for an intrinsic semiconductor.

In conclusion we have seen an enhancement of the figure of merit in the intrinsic solid solutions $Cu_2Zn_{1-x}Fe_xGeSe_4$ and $Cu_{2+x}Zn_{1-x-y}Fe_yGeSe_4$ due to a reduction of the lattice thermal conductivity combined with higher effective masses from Fe substitution.

6.5 Ca_3AlSb_3

This section is an adapted reproduction, from *J.* Mater. Chem **2012** 22, 9826-9830.[96] Reproduced with permission of The Royal Society of Chemistry Copyright 2012.

The figure of merit of $Ca_3Al_{1-x}Zn_xSb_3$ is shown in Figure 6.4 (right). Doping with zinc increases the figure of merit, leading to a zT of 0.5 at 900 K for x = 0.01. Compared with the Na-doped samples of the previous investigation,[95] all of the Zn-doped samples exhibit enhanced zT at intermediate temperatures, which can be attributed to their higher carrier mobilities. The x = 0.01 sample, which has the largest grain size and thus the highest mobility, shows the largest degree of zT enhancement. However, the peak zT values of the sodium doped Ca_3AlSb_3 samples cannot be achieved with zinc due to its limited dopant effectiveness when compared to Na (see Chapter 4), as seen in Figure 6.4 (left).

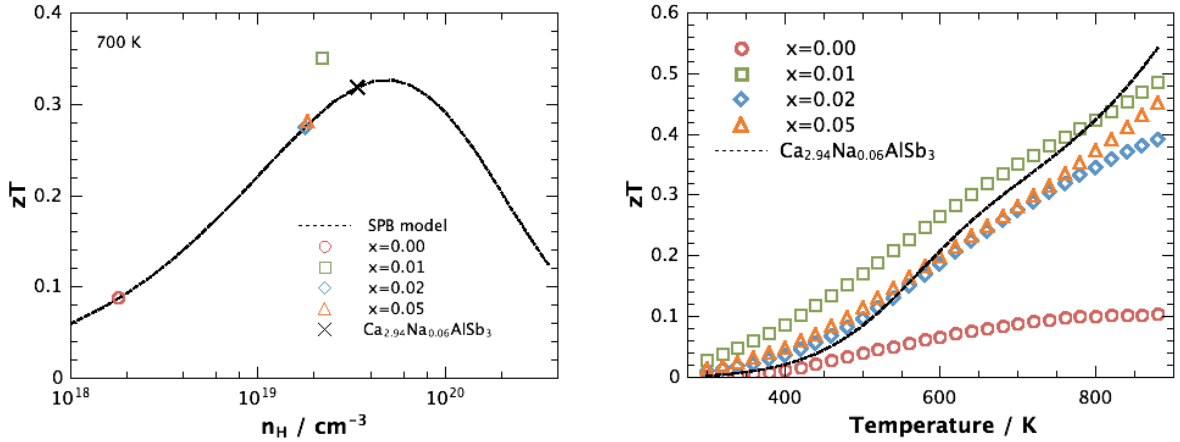

Figure 6.4: Left: Calculated zT vs carrier concentration (broken line) with the experimental zT values at 700 K. The dashed line was generated using a single parabolic band model, with an effective mass of 0.8 m_e, an intrinsic mobility of 15 $cm^2V^{-1}s^{-1}$ and lattice thermal conductivity of 0.78 $Wm^{-1}K^{-1}$. Both Zn and Na[95] doped materials are well described by the same model, suggesting that using Zn as a dopant does not affect the band structure of the compound. It can be seen, that the peak zT values of the sodium doped Ca_3AlSb_3 samples can not be achieved with zinc due to its limited dopant effectiveness when compared to Na. The deviations of the samples with $x = 0.01$ are due to the higher intrinsic mobility due to the larger grain size. Right: Experimental figure of merits zT of $Ca_3Al_{1-x}Zn_xSb_3$. The reduction of grain boundary surface area improves the figure of merit at intermediate temperatures, seen for $x = 0.01$. Experimental data is compared to $Ca_{2.94}Na_{0.06}AlSb_3$ data (black line).[95]

This study shows the effect of different grain sizes on the thermoelectric transport properties, with larger grains leading to higher thermal conductivities and higher mobilities at lower temperatures, due to reduced scattering of phonons and electrons at the grain boundaries. Ultimately, we find that while larger grain size has little effect on the high temperature properties, the reduction of grain boundary surface area improves the figure of merit at intermediate temperatures. This work shows the common strategy to use nano structured materials does not always lead to an improved figure of merit. Other competing factors such as a reduction in mobility may overwhelm the improvement of the lattice thermal conductivity.

6.6 Sr_3GaSb_3

This section is an adapted reproduction, from *E*nergy Environ. Sci. **2012**, 5, 9121-9128.[100] Reproduced with permission of The Royal Society of Chemistry Copyright 2012.

The figure of merit of $Sr_3Ga_{1-x}Zn_xSb_3$ is shown in Figure 6.5 as a function of temperature. The transition from nondegenerate behavior to degenerate semiconducting behavior upon doping with zinc leads to an increase in the maximum zT from 0.4 for $x = 0.0$ to greater than 0.9 when $x = 0.07$. To provide a rough estimate of the optimum carrier concentration in this material we have employed an SPB model at 700 K (see Figure 6.5). At 700 K, it is reasonable to assume that extrinsic carriers still dominate transport and acoustic phonons are the

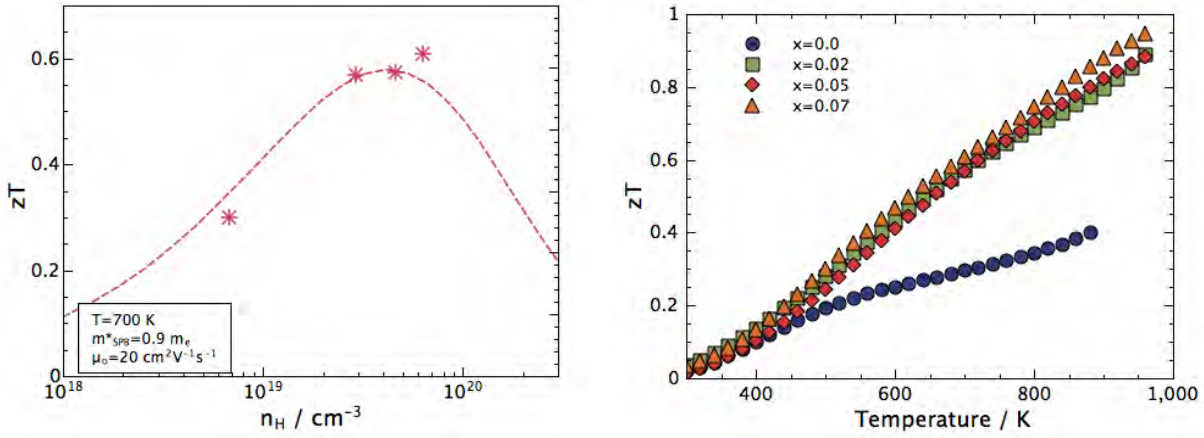

Figure 6.5: Left: zT with carrier concentration approximately according to an SPB model at 700 K. The broken curve represents the predicted SPB behavior of zT, respectively, assuming $m^* = 0.9\,m_e$, $\mu_0 = 17\,\mathrm{cm^2V^{-1}s^{-1}}$ and $\kappa_L = 0.55\,\mathrm{Wm^{-1}K^{-1}}$. The optimum carrier concentration for a maximum zT has been obtained in these doping levels. Right: The measured figure of merit of $Sr_3Ga_{1-x}Zn_xSb_3$ exceeds 0.9 when heavily doped.

primary scattering source. Using input parameters $m^* = 0.9\,m_e$, $\mu_0 = 17\,\mathrm{cm^2V^{-1}s^{-1}}$ and $\kappa_L = 0.55\ \mathrm{Wm^{-1}K^{-1}}$, the predicted optimum carrier concentration is approximately $5\mathrm{x}10^{19}\,\mathrm{h^+/cm^3}$. The doped samples in this study have carrier concentrations clustered around this optimum, explaining their similar zT values.

Relative to the Zintl compound Ca_3AlSb_3, Sr_3GaSb_3 exhibits a higher figure of merit across the entire measured temperature range. The improved peak zT of Sr_3GaSb_3 ($zT \sim 0.9$ at 1000 K) compared with Ca_3AlSb_3 ($zT \sim 0.75$) can be attributed almost entirely to its lower κ_L. Shown in Figure 5.15 are the lattice thermal conductivities of each compound, estimated from the measured diffusivity of Zn-doped samples. Though all three compounds exhibit an identical temperature dependence indicative of Umklapp scattering, κ_L in Sr_3GaSb_3 is about 25% lower across the entire temperature range. Accounting for traditional factors such as $\bar{M}$, V, and sound velocity explains only ~10% of the disparity, assuming that the Grüneisen parameter does not vary greatly between these three compounds (see Equation 5.16). The remaining difference in κ_L can be explained by the exceptionally large unit cell of Sr_3GaSb_3 (N= 56), which is twice the size of Ca_3AlSb_3 and thus significantly reduces the acoustic lattice thermal conductivity.

In conclusion, doping with Zn^{2+} on the Ga^{3+} site leads to degenerate semiconducting behavior, allowing us to obtain p-type carrier concentrations near the optimum value predicted by a single parabolic band model. The combination of low lattice thermal conductivity, reasonable electronic mobility, and a sufficiently large band gap to maintain degenerate behavior at high temperature leads to a zT of 0.9 at 1000 K. Compared with previously studied chain-based Zintl compounds, both the peak zT and integrated zT of Zn-doped Sr_3GaSb_3 samples are significantly higher.

7 Conclusion

This thesis focuses on the structural and thermoelectric properties of quaternary copper selenides and Zintl compounds and tries to link the materials structures to their transport properties.

The thermoelectric and structural properties of the solid solution $Cu_{2+x}Zn_{1-x}GeSe_4$ and the effect of substitution of Zn^{2+} with Cu^{+} have been investigated. A phase transition at 450 K has been identified, and it has an influence on the transport properties in this material, leading to an insulator-to-metal transition. Temperature dependent X-ray diffraction does not reveal a structural phase transformation suggesting that this phase transformation is an electronic phase transition only. The substitution introduces holes as charge carriers, but also leads to the formation of impurities by phase segregation, due to a charge imbalance in this material, which greatly influences the charge carrier concentration. No striking influence on the mobilities and effective masses of the charge carriers can be detected suggesting that the impurities do not affect the percolation of the holes. However, these nanometer sized impurities are primarily located at the grain boundaries causing a reduction of the lattice thermal conductivity by $\sim$15 % due to enhanced phonon scattering at the grain boundaries, ultimately leading to an enhanced figure of merit in this material.

Furthermore, the systematic substitution of Zn^{2+} with Fe^{2+} has been considered in the solid solution $Cu_2Zn_{1-x}Fe_xGeSe_4$. While the intrinsic electronic nature of the material is not changed upon substitution with Fe^{2+}, a distinct change in the lattice parameter c/a-ratio has been observed, which can be explained by a 3-stage cation restructuring and disordering process of Fe, Zn, and Cu. The differences in bonding interaction between the cations and the anions lead to different bond lengths and bond angles, resulting in the observed trend in the lattice parameters. The restructuring leads to a reduction of the lattice thermal conductivity by 15 % at 70 % Fe content. As the disorder scattering of the phonons, due to mass fluctuation and isotropic strain is expected to be very small from these similar mass and similar volume ions, this work shows the potential of significant point defect scattering due to local anisotropic strain that also results in a change in c/a-ratio.

The thermoelectric properties of zinc-doped Ca_3AlSb_3 were compared to a previously reported study on sodium as a dopant. A similar band mass and lattice thermal conductivity is observed regardless of whether Zn or Na is the dopant. However, zinc exhibits a lower solubility limit than sodium resulting in lower carrier concentrations and a lower peak figure of merit, because the optimum carrier concentration for this material cannot be reached via doping with zinc. This study also shows the effect of different grain sizes on the thermoelectric transport properties, with larger grains leading to higher thermal conductivities and higher mobilities at lower temperatures, due to reduced scattering of phonons and electrons at the grain boundaries. Ultimately, we find that while larger grain size has little effect on the

high temperature properties, the reduction of grain boundary surface area improves the figure of merit at intermediate temperatures. This work shows the common strategy to use nano structured materials does not always lead to an improved figure of merit. Other competing factors such as a reduction in mobility may overwhelm the improvement of the lattice thermal conductivity.

At last, we have described a new thermoelectric material, Sr_3GaSb_3, which has a crystal structure characterized by chains of corner-linked tetrahedra, similar to the polyanions found in the previously studied Zintl compounds, $Ca_5Al_2Sb_6$ and Ca_3AlSb_3. The large unit cell and comparatively high density in Sr_3GaSb_3 combine to yield the exceptionally low lattice thermal conductivity observed in this study ($\kappa_L = 0.45\,\mathrm{Wm^{-1}K^{-1}}$ at 1000 K). High temperature transport measurements reveal that Sr_3GaSb_3 is a nondegenerate p-type semiconductor, with a relatively large band gap and high electronic mobility. Substitution of Ga with Zn leads to degenerate semiconducting behavior, allowing us to obtain p-type carrier concentrations near the optimum value predicted by a single parabolic band model. The combination of low lattice thermal conductivity, reasonable electronic mobility, and a sufficiently large band gap to maintain degenerate behavior at high temperature leads to a zT of 0.9 at 1000 K. Compared with previously studied chain-based Zintl compounds, both the peak zT and integrated zT of Zn-doped Sr_3GaSb_3 samples are significantly higher.

Ultimately, this thesis shows the potential and need of understanding the structure-to-property relationships in materials for new thermoelectric materials and their improvement. Especially the different bonding environments, the elemental chemistry, and the crystal structures have to be considered to understand these properties and to further design new thermoelectrics.

8 Supporting Information

8.1 X-ray Diffraction

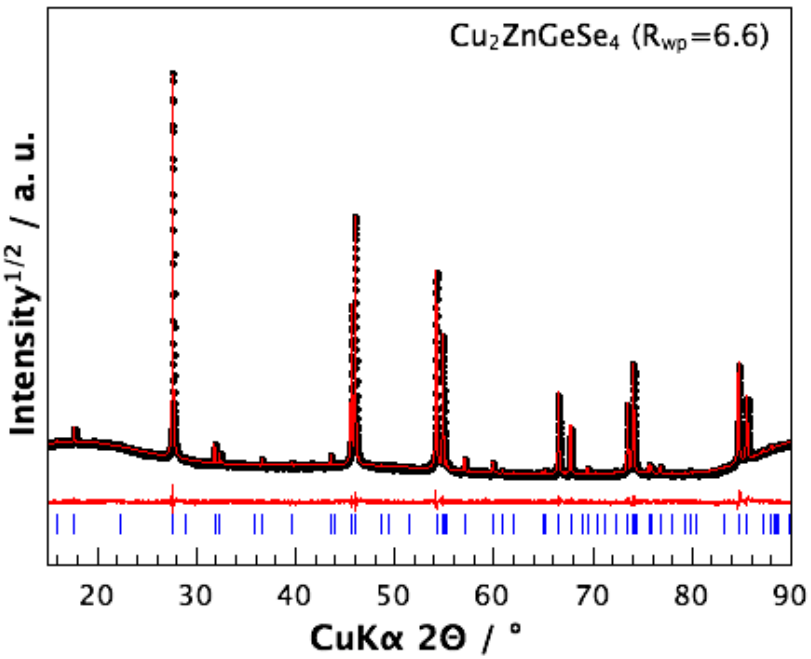

Figure 8.1: X-ray diffraction data including profile fit, profile difference, and profile residuals of the corresponding Rietveld fit of phase pure $Cu_2ZnGeSe_4$.

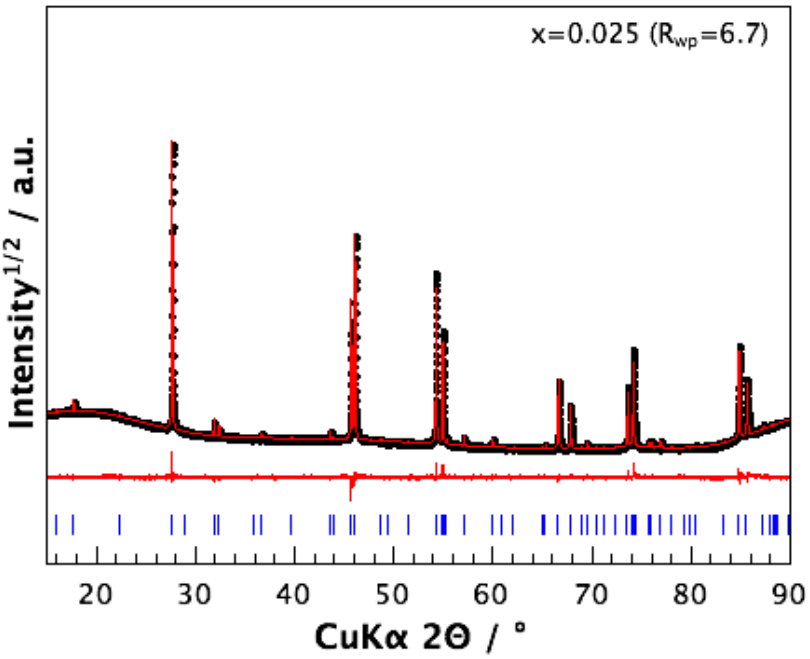

Figure 8.2: X-ray diffraction data including profile fit, profile difference, and profile residuals of the corresponding Rietveld fit of phase pure $Cu_{2+x}Zn_{1-x}GeSe_4$.

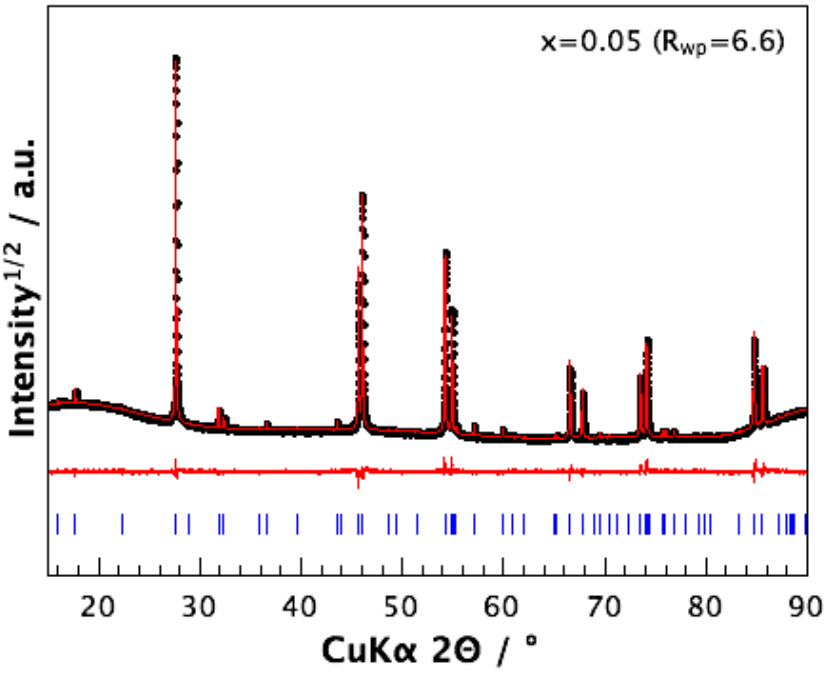

Figure 8.3: X-ray diffraction data including profile fit, profile difference, and profile residuals of the corresponding Rietveld fit of phase pure $Cu_{2+x}Zn_{1-x}GeSe_4$.

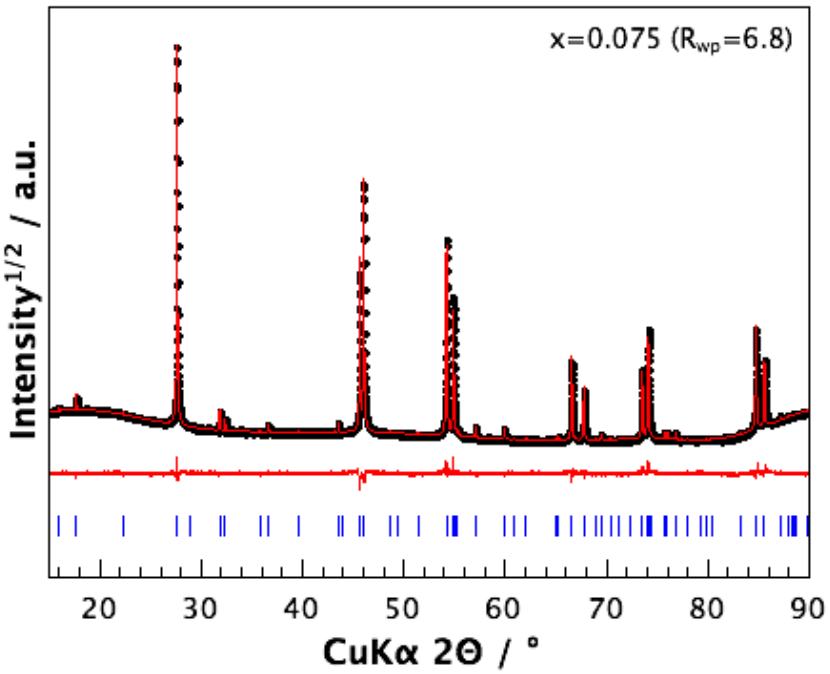

Figure 8.4: X-ray diffraction data including profile fit, profile difference, and profile residuals of the corresponding Rietveld fit of phase pure $Cu_{2+x}Zn_{1-x}GeSe_4$.

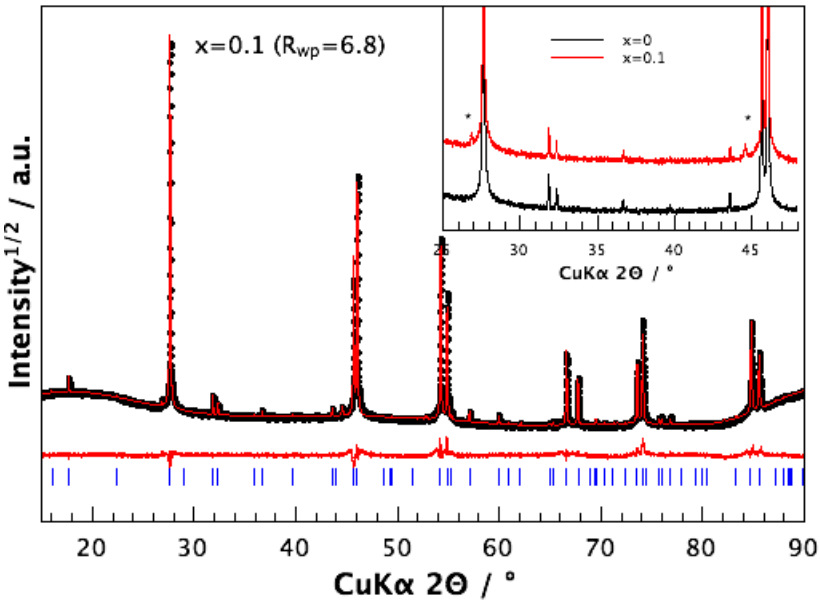

Figure 8.5: X-ray diffraction data including profile fit, profile difference, and profile residuals of the corresponding Rietveld fit of $Cu_{2.1}Zn_{0.9}GeSe_4$. The inset shows the extra reflections indexed to $Cu_{2-\delta}Se$.

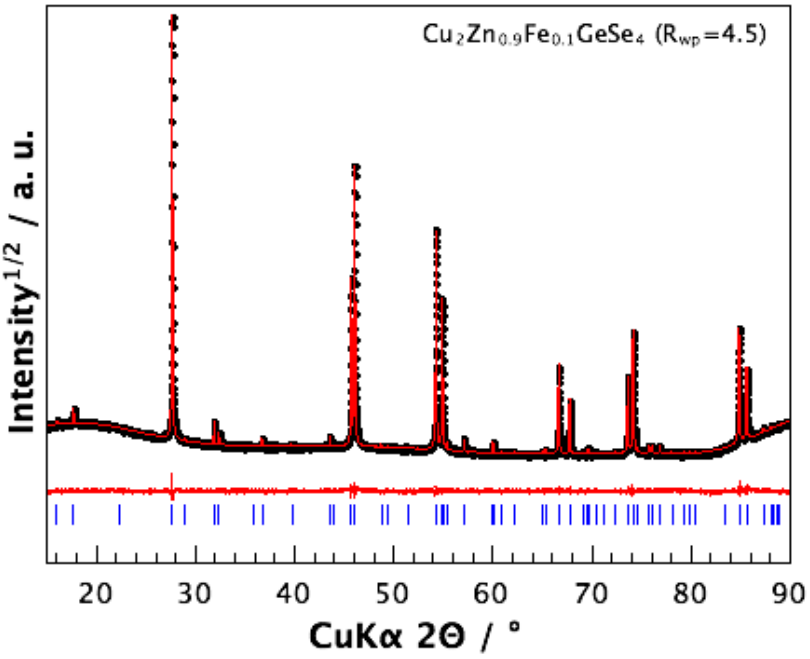

Figure 8.6: X-ray diffraction data including profile fit, profile difference, and profile residuals of the corresponding Pawley fit of phase pure $Cu_2Zn_{1-x}Fe_xGeSe_4$.

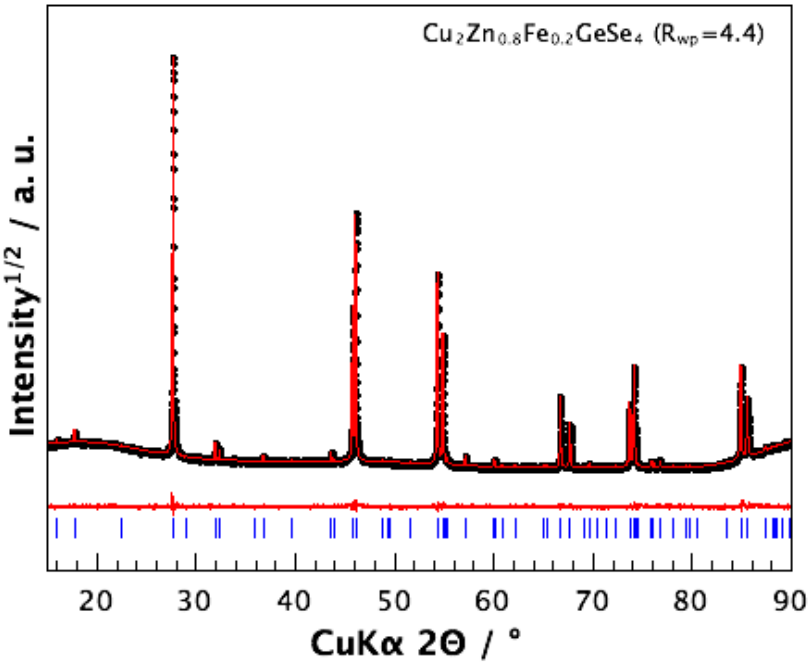

Figure 8.7: X-ray diffraction data including profile fit, profile difference, and profile residuals of the corresponding Pawley fit of phase pure $Cu_2Zn_{1-x}Fe_xGeSe_4$.

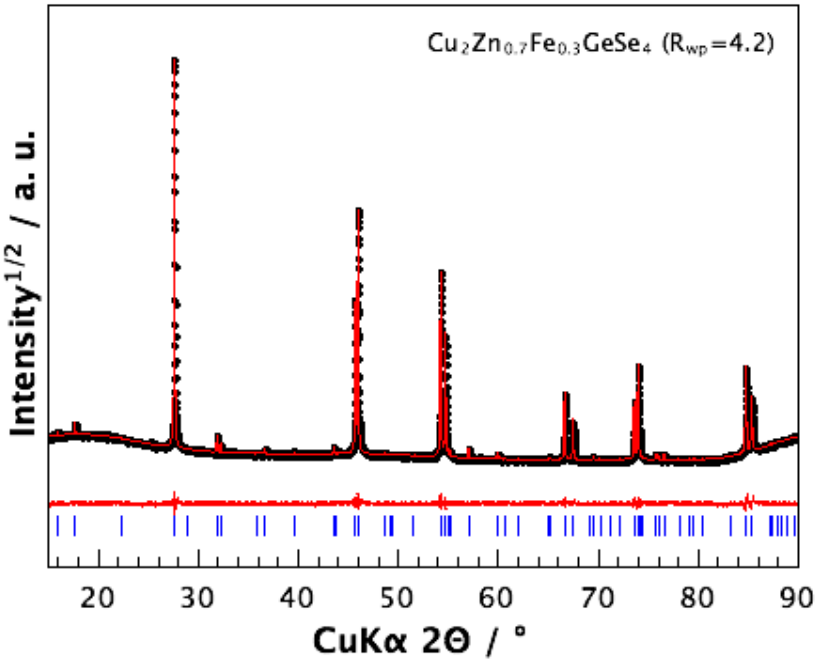

Figure 8.8: X-ray diffraction data including profile fit, profile difference, and profile residuals of the corresponding Pawley fit of phase pure $Cu_2Zn_{1-x}Fe_xGeSe_4$.

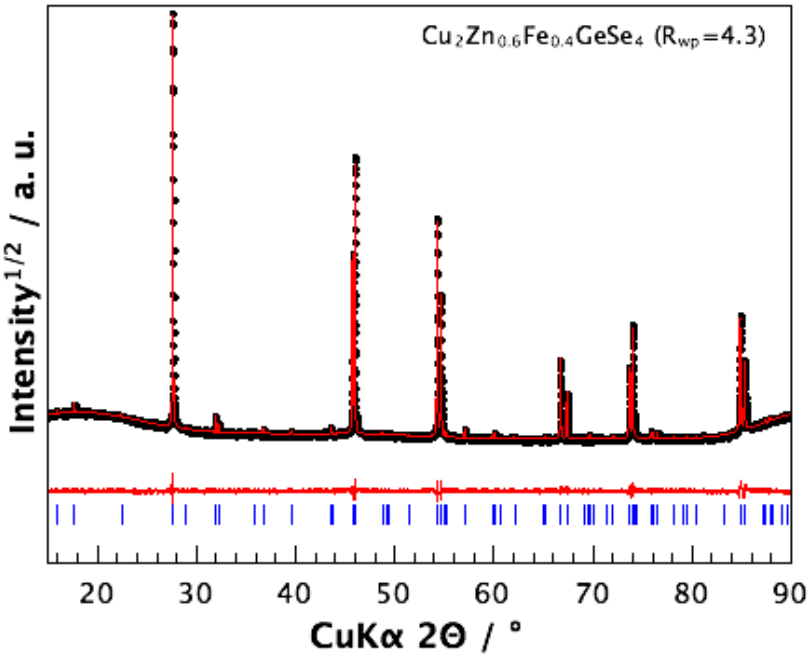

Figure 8.9: X-ray diffraction data including profile fit, profile difference, and profile residuals of the corresponding Pawley fit of phase pure $Cu_2Zn_{1-x}Fe_xGeSe_4$.

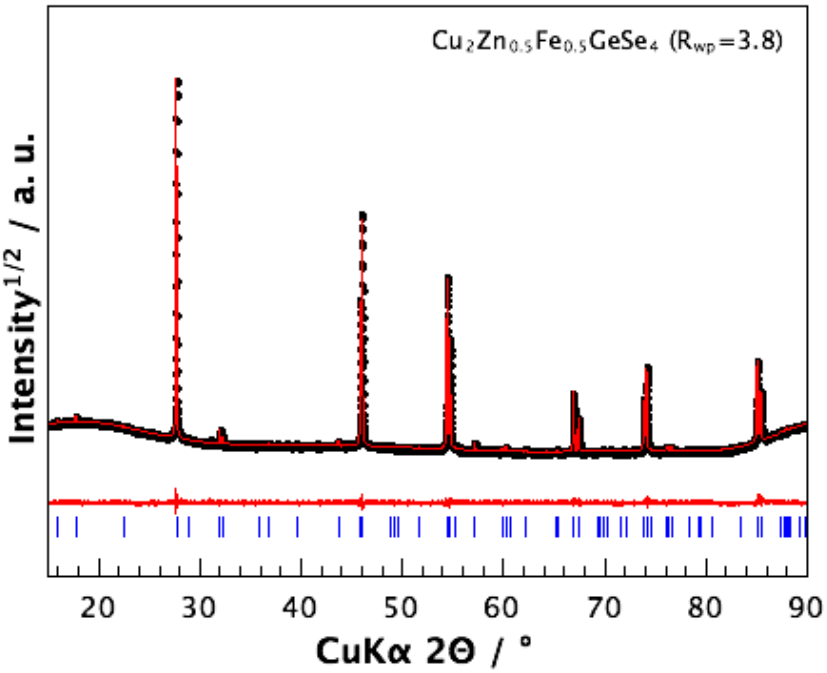

Figure 8.10: X-ray diffraction data including profile fit, profile difference, and profile residuals of the corresponding Pawley fit of phase pure $Cu_2Zn_{1-x}Fe_xGeSe_4$.

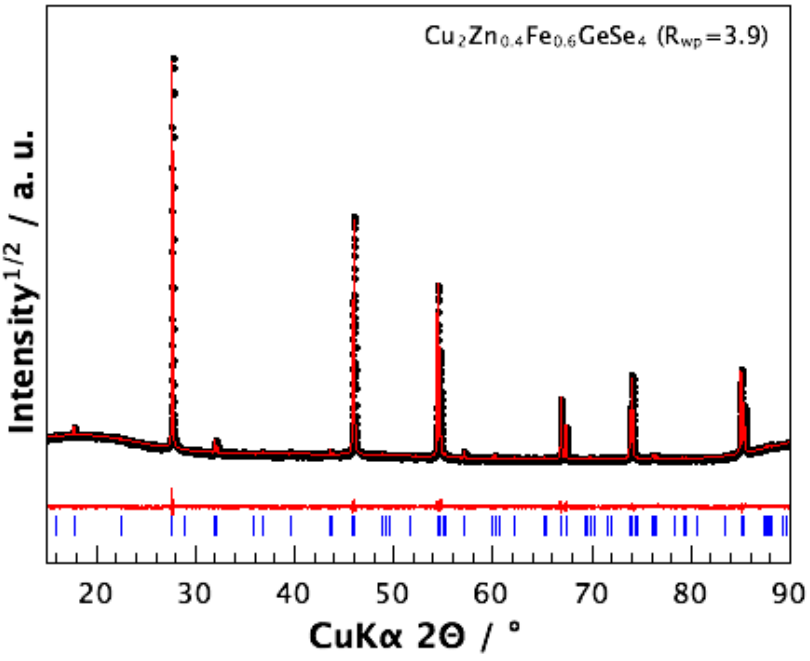

Figure 8.11: X-ray diffraction data including profile fit, profile difference, and profile residuals of the corresponding Pawley fit of phase pure $Cu_2Zn_{1-x}Fe_xGeSe_4$.

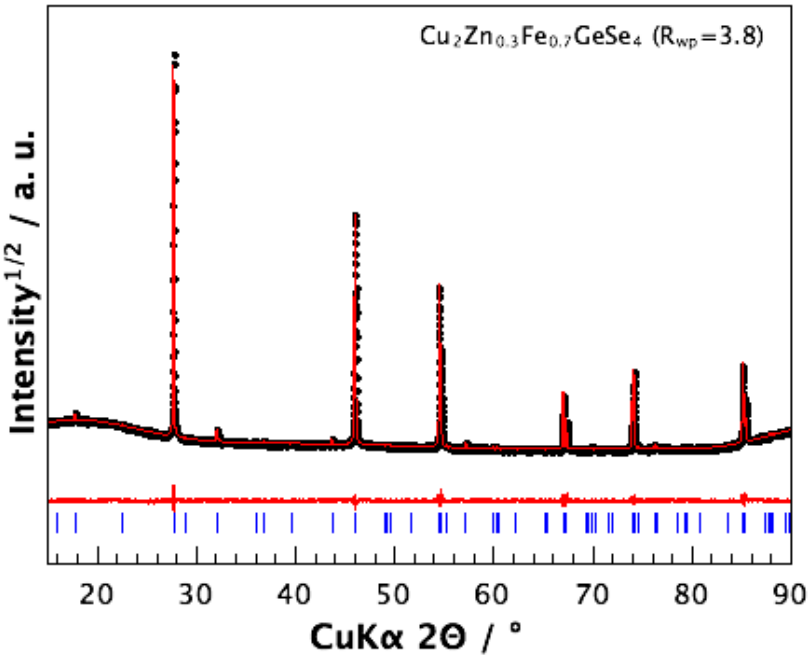

Figure 8.12: X-ray diffraction data including profile fit, profile difference, and profile residuals of the corresponding Pawley fit of phase pure $Cu_2Zn_{1-x}Fe_xGeSe_4$.

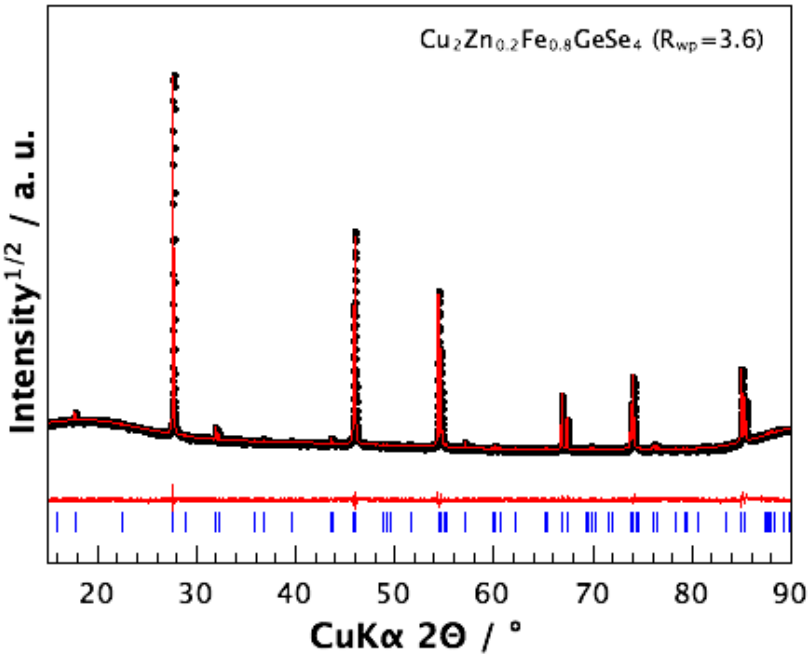

Figure 8.13: X-ray diffraction data including profile fit, profile difference, and profile residuals of phase pure $Cu_2Zn_{1-x}Fe_xGeSe_4$.

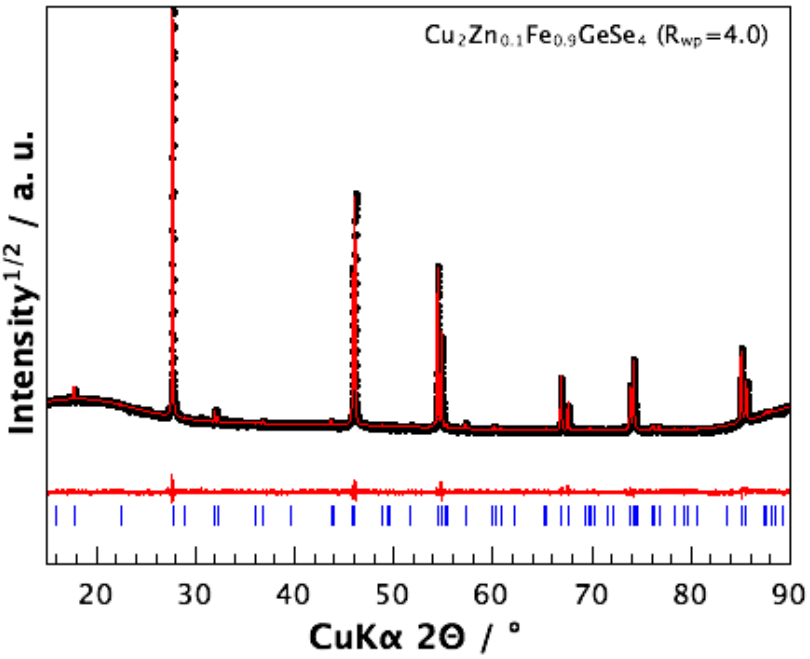

Figure 8.14: X-ray diffraction data including profile fit, profile difference, and profile residuals of phase pure $Cu_2Zn_{1-x}Fe_xGeSe_4$.

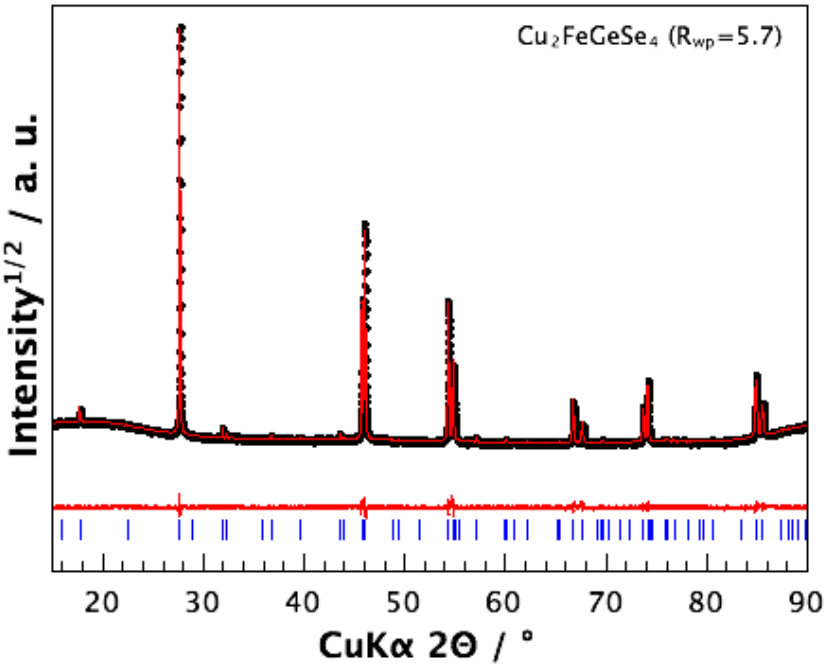

Figure 8.15: X-ray diffraction data including profile fit, profile difference, and profile residuals of phase pure $Cu_2Zn_{1-x}Fe_xGeSe_4$.

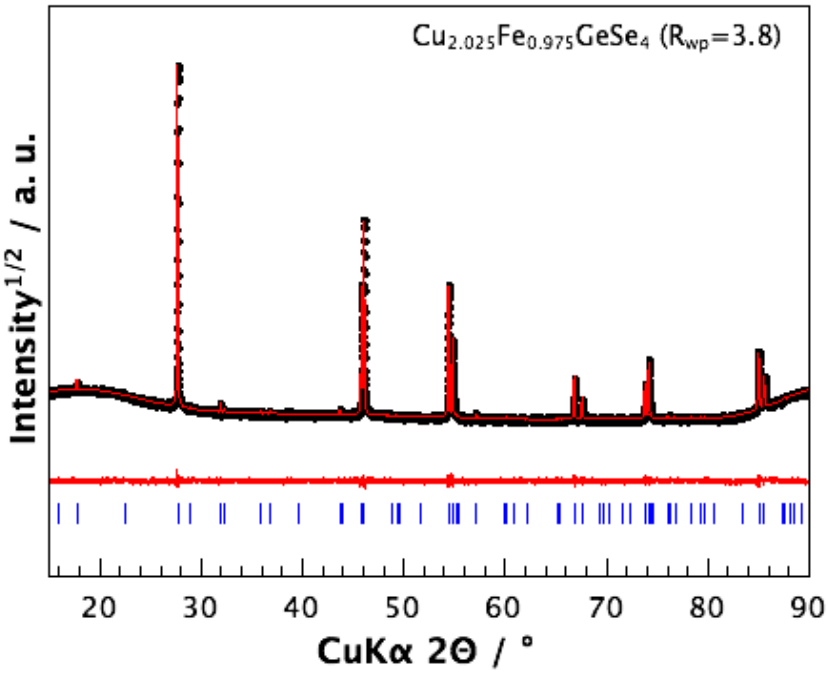

Figure 8.16: X-ray diffraction data including profile fit, profile difference, and profile residuals of phase pure $Cu_{2+x}Zn_{1-x-y}Fe_yGeSe_4$.

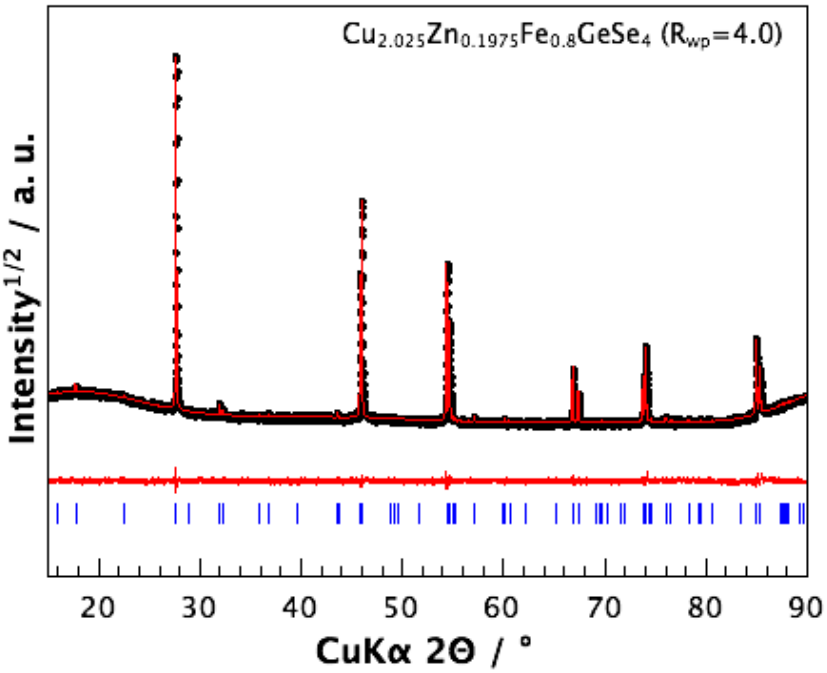

Figure 8.17: X-ray diffraction data including profile fit, profile difference, and profile residuals of phase pure $Cu_{2+x}Zn_{1-x-y}Fe_yGeSe_4$.

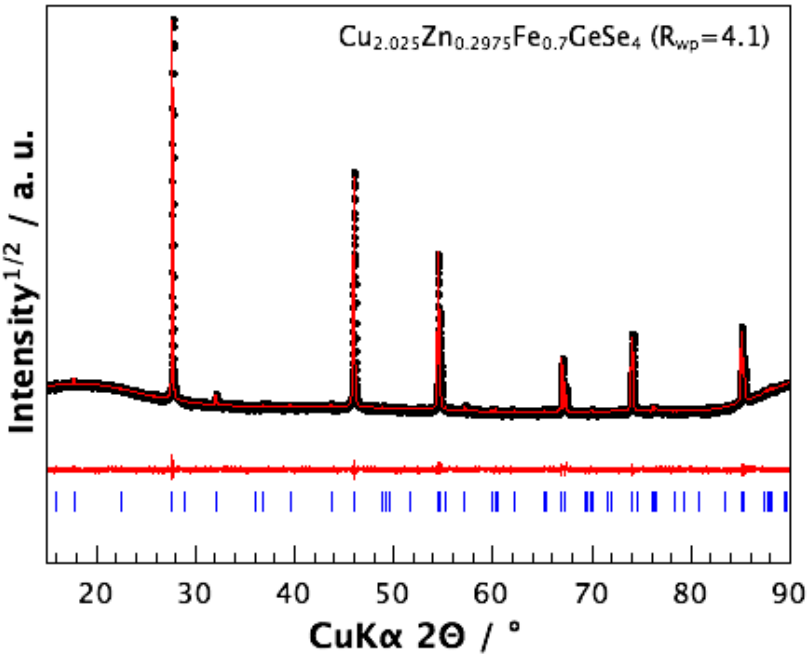

Figure 8.18: X-ray diffraction data including profile fit, profile difference, and profile residuals of phase pure $Cu_{2+x}Zn_{1-x-y}Fe_yGeSe_4$.

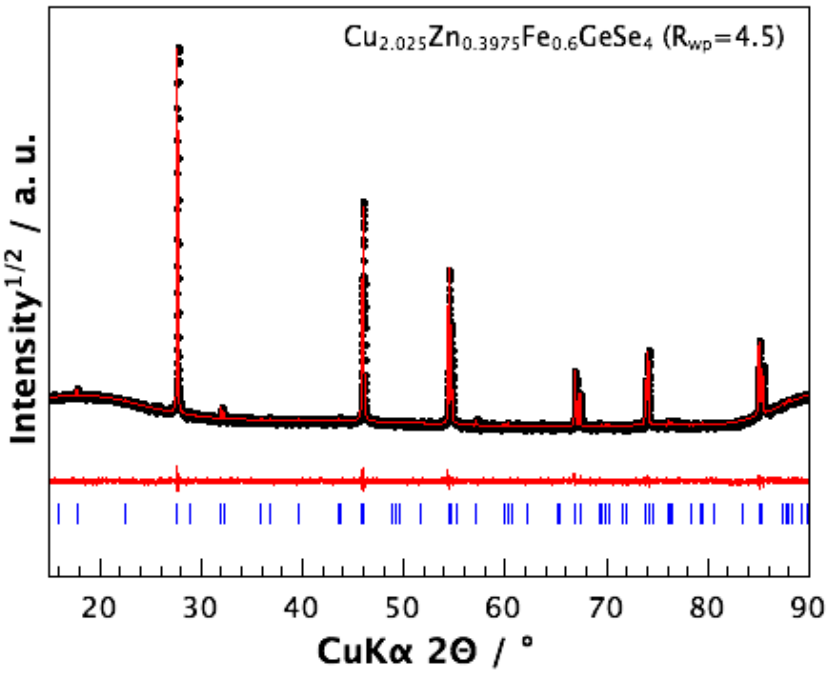

Figure 8.19: X-ray diffraction data including profile fit, profile difference, and profile residuals of phase pure $Cu_{2+x}Zn_{1-x-y}Fe_yGeSe_4$.

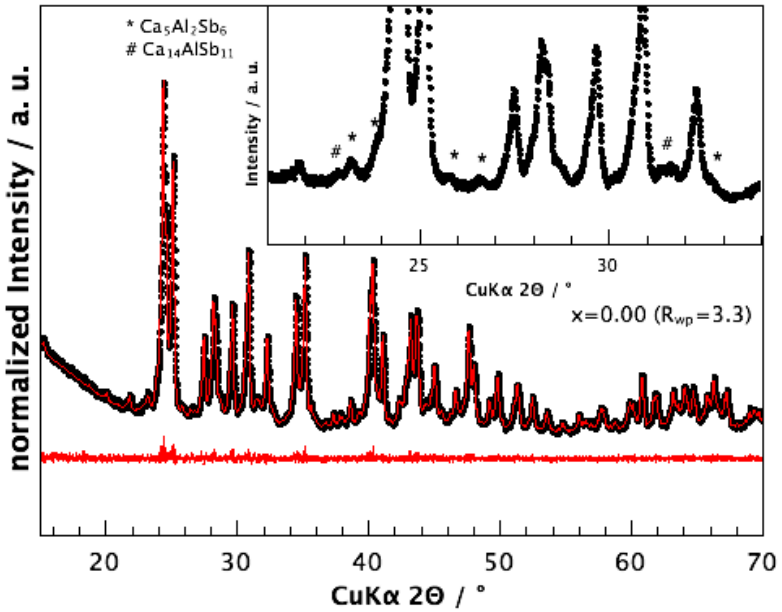

Figure 8.20: X-ray diffraction data for $Ca_3Al_{1-x}Zn_xSb_3$ including profile fit, profile difference, and profile residuals from the corresponding Pawley refinement including the secondary phases of $Ca_5Al_2Sb_6$ and $Ca_{14}AlSb_{11}$. The inset shows the reflections indexed to the impurity phases, observed in all samples.

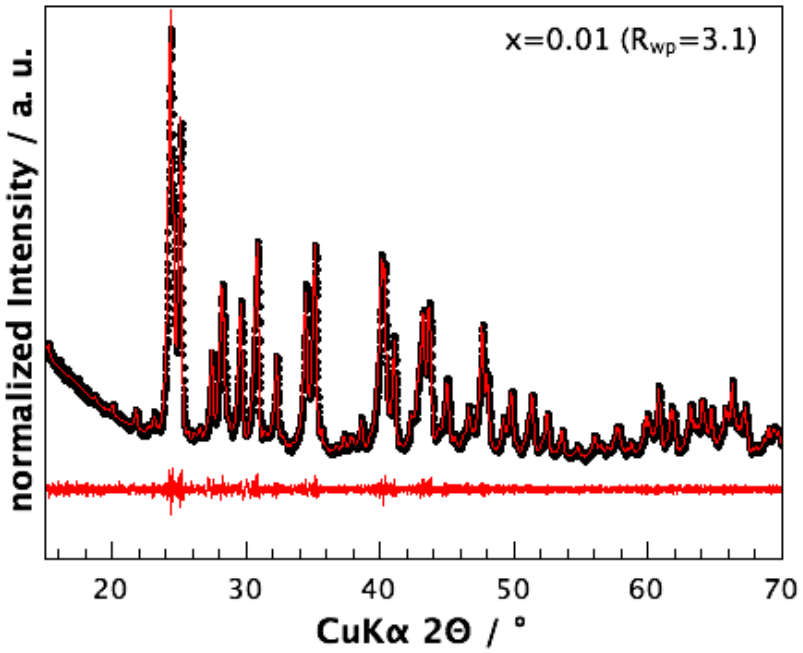

Figure 8.21: X-ray diffraction data for $Ca_3Al_{1-x}Zn_xSb_3$ including profile fit, profile difference, and profile residuals from the corresponding Pawley refinement including the secondary phases of $Ca_5Al_2Sb_6$ and $Ca_{14}AlSb_{11}$.

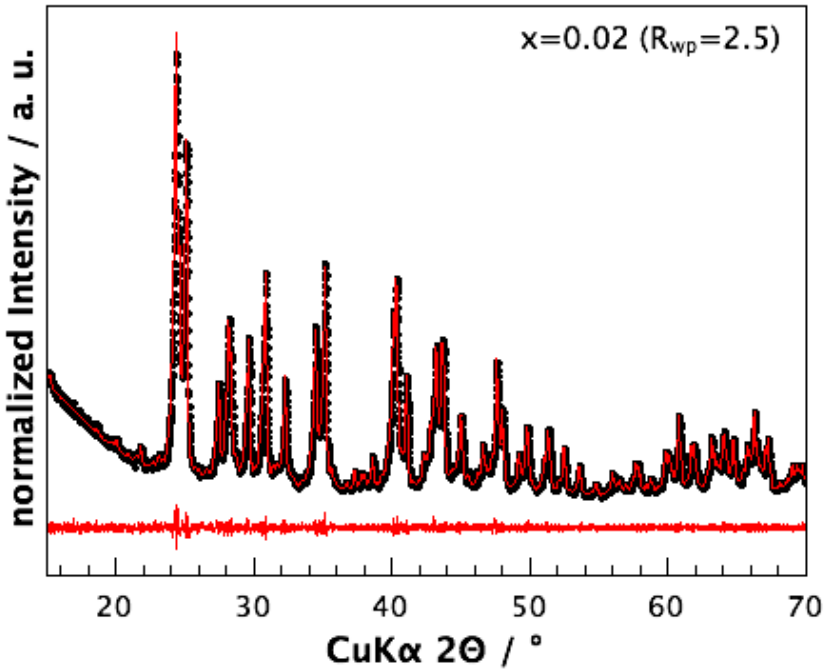

Figure 8.22: X-ray diffraction data for $Ca_3Al_{1-x}Zn_xSb_3$ including profile fit, profile difference, and profile residuals from the corresponding Pawley refinement including the secondary phases of $Ca_5Al_2Sb_6$ and $Ca_{14}AlSb_{11}$.

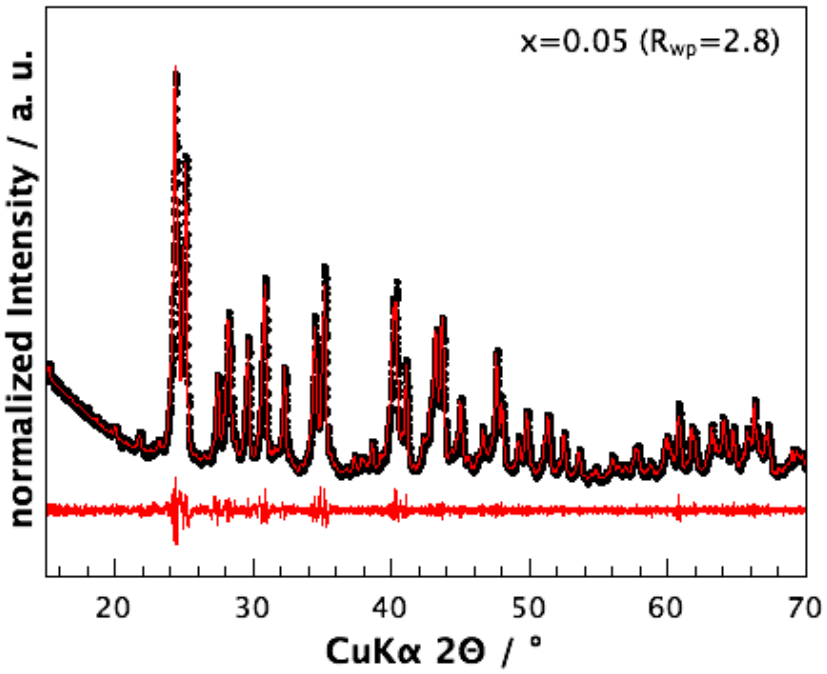

Figure 8.23: X-ray diffraction data for $Ca_3Al_{1-x}Zn_xSb_3$ including profile fit, profile difference, and profile residuals from the corresponding Pawley refinement including the secondary phases of $Ca_5Al_2Sb_6$ and $Ca_{14}AlSb_{11}$.

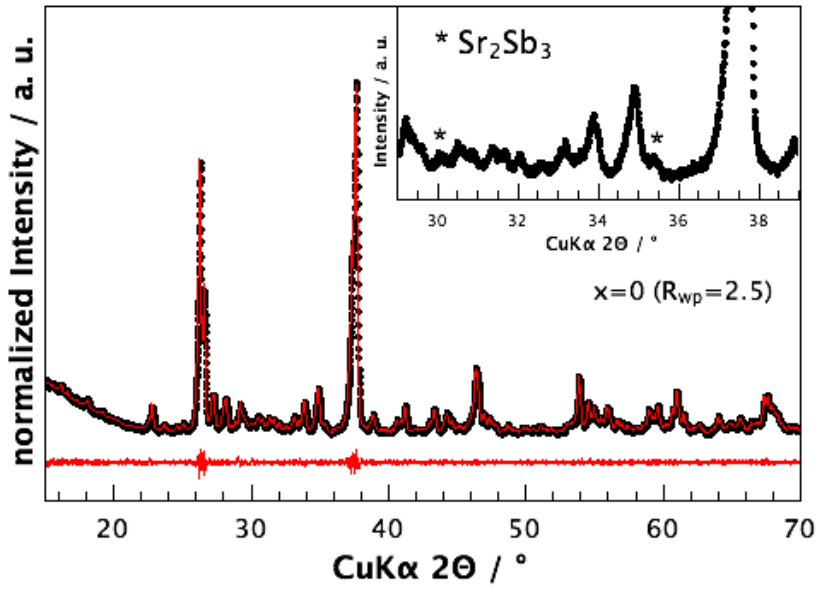

Figure 8.24: X-ray diffraction data for $Sr_3Ga_{1-x}Zn_xSb_3$ including profile fit, profile difference, and profile residuals from the corresponding Pawley refinement including the secondary phase Sr_2Sb_3. The inset shows the reflections indexed to the impurity phase marked by asterisks.

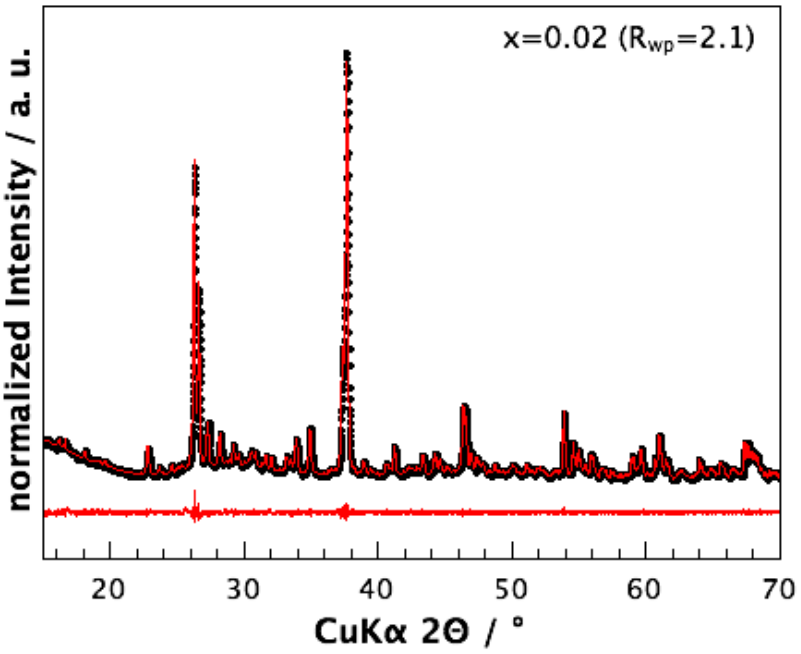

Figure 8.25: X-ray diffraction data for $Sr_3Ga_{1-x}Zn_xSb_3$ including profile fit, profile difference, and profile residuals from the corresponding Pawley refinement including the secondary phase Sr_2Sb_3.

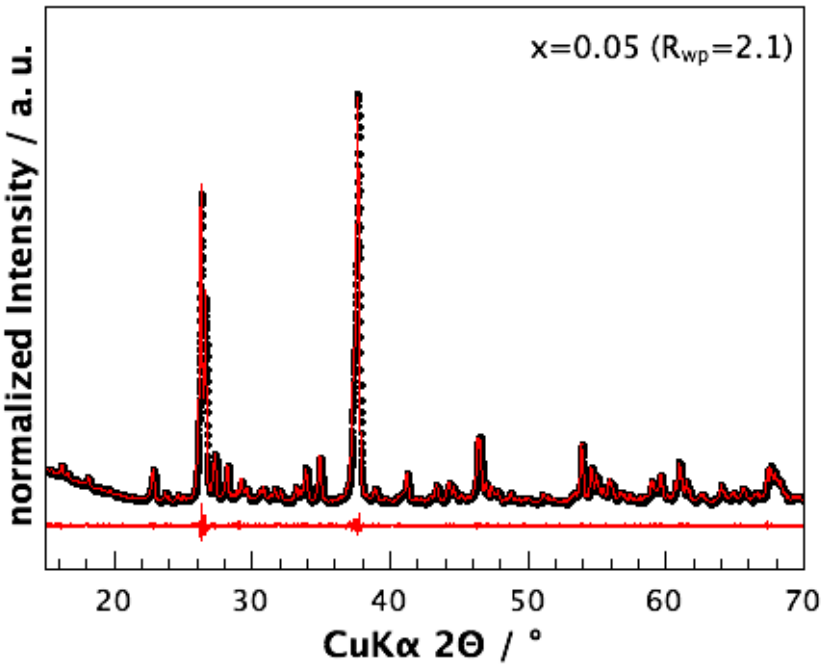

Figure 8.26: X-ray diffraction data for $Sr_3Ga_{1-x}Zn_xSb_3$ including profile fit, profile difference, and profile residuals from the corresponding Pawley refinement including the secondary phase Sr_2Sb_3.

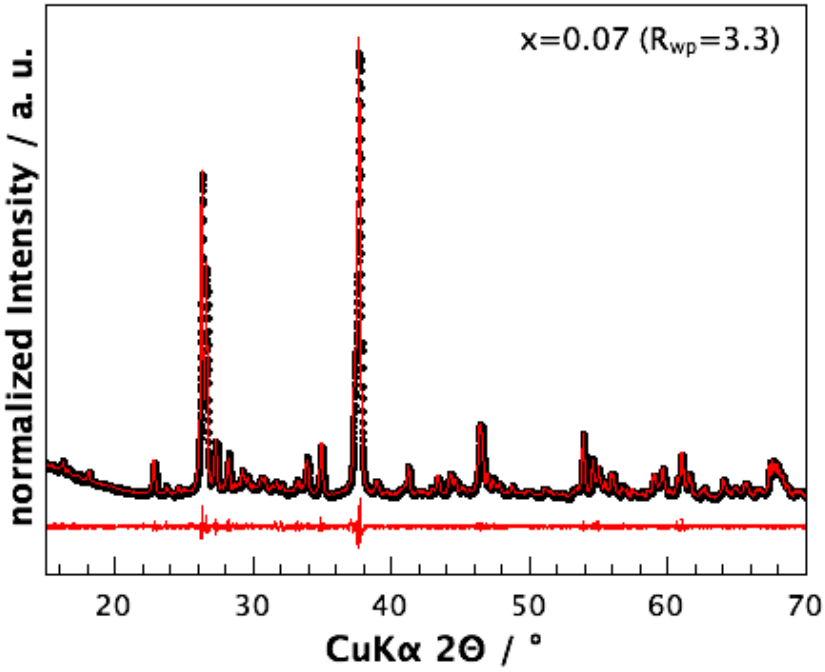

Figure 8.27: X-ray diffraction data for $Sr_3Ga_{1-x}Zn_xSb_3$ including profile fit, profile difference, and profile residuals from the corresponding Pawley refinement including the secondary phase Sr_2Sb_3.

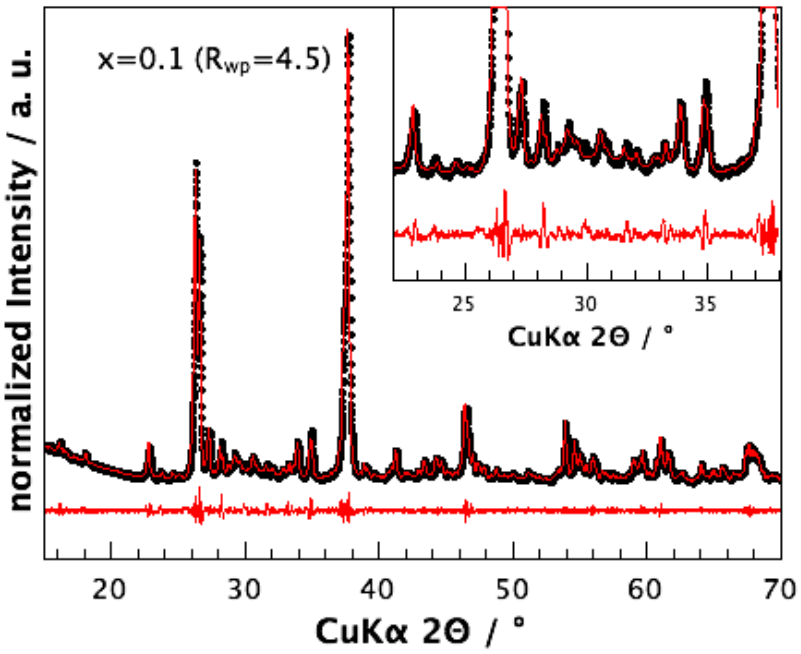

Figure 8.28: X-ray diffraction data for $Sr_3Ga_{1-x}Zn_xSb_3$ including profile fit, profile difference, and profile residuals from the corresponding Pawley refinement. The inset shows the impurities at lower Bragg angles.

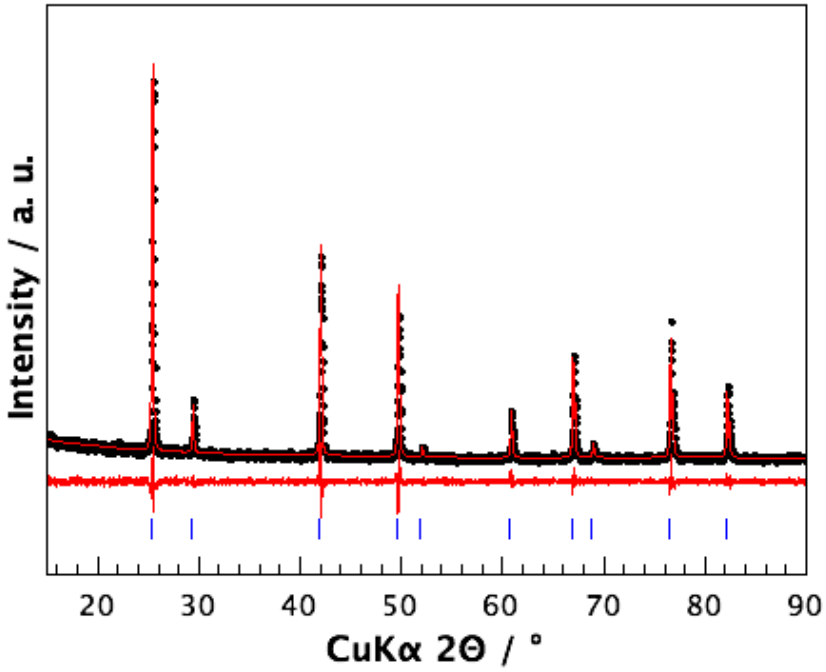

Figure 8.29: X-ray diffraction data for GaSb including profile fit and profile difference, showing a phase pure precursor GaSb.

8.2 Scanning Electron Microscopy

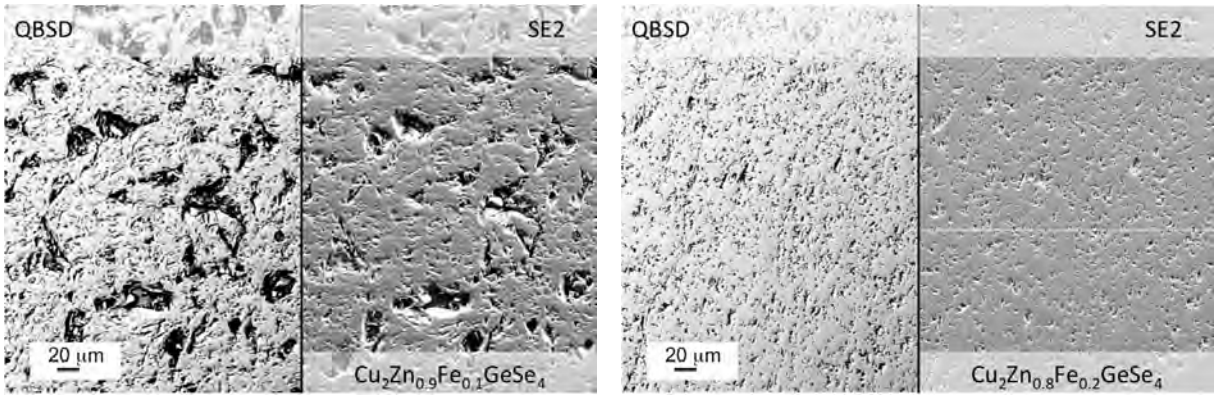

Figure 8.30: SEM micrographs of $Cu_2Zn_{1-x}Fe_xGeSe_4$ in backscattered (QBSD) and secondary electron mode (SE2).

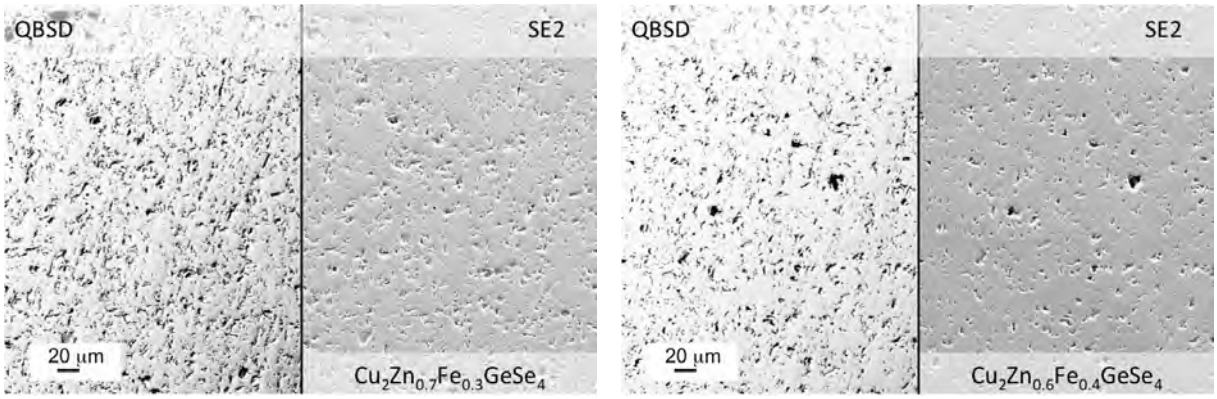

Figure 8.31: SEM micrographs of $Cu_2Zn_{1-x}Fe_xGeSe_4$ in backscattered (QBSD) and secondary electron mode (SE2).

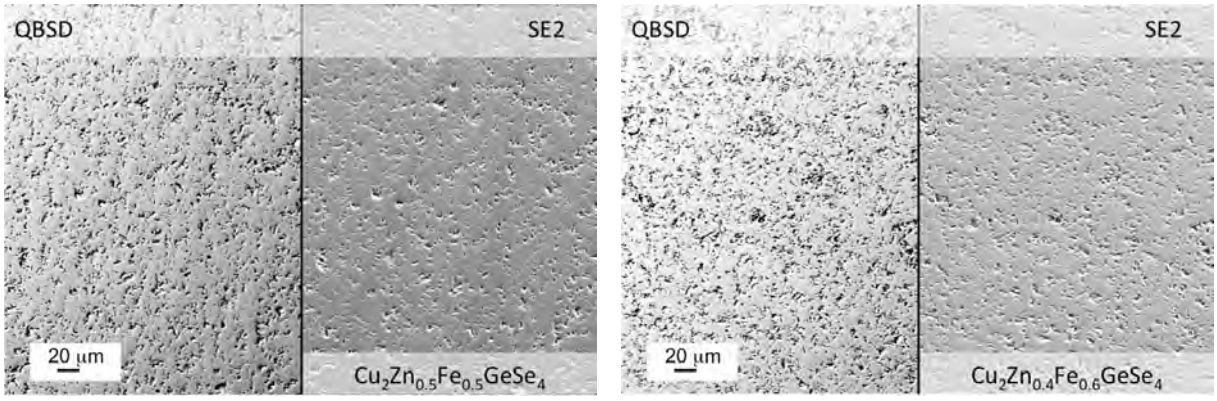

Figure 8.32: SEM micrographs of $Cu_2Zn_{1-x}Fe_xGeSe_4$ in backscattered (QBSD) and secondary electron mode (SE2).

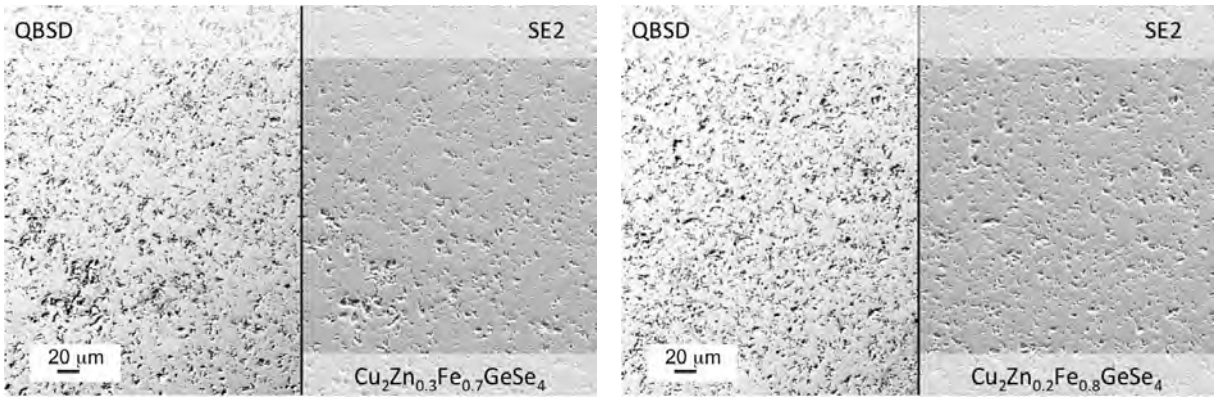

Figure 8.33: SEM micrographs of $Cu_2Zn_{1-x}Fe_xGeSe_4$ in backscattered (QBSD) and secondary electron mode (SE2).

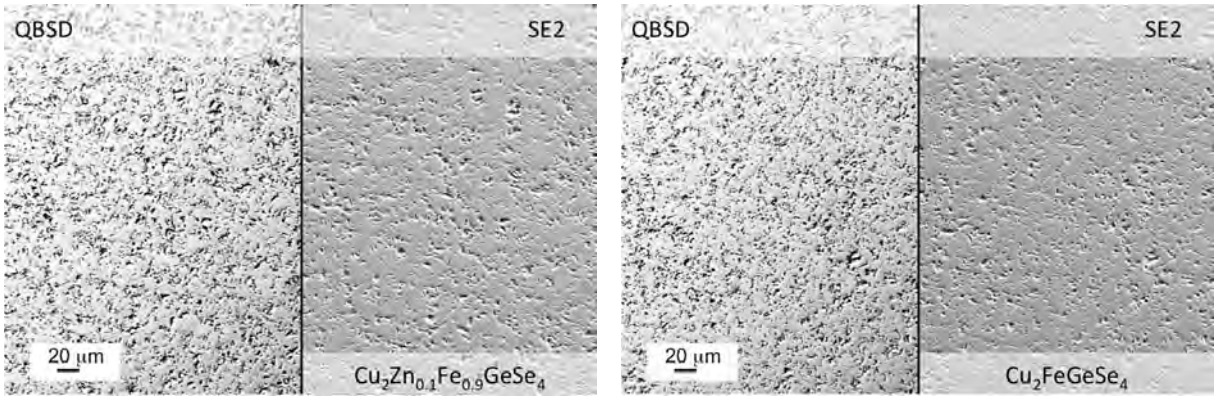

Figure 8.34: SEM micrographs of $Cu_2Zn_{1-x}Fe_xGeSe_4$ in backscattered (QBSD) and secondary electron mode (SE2).

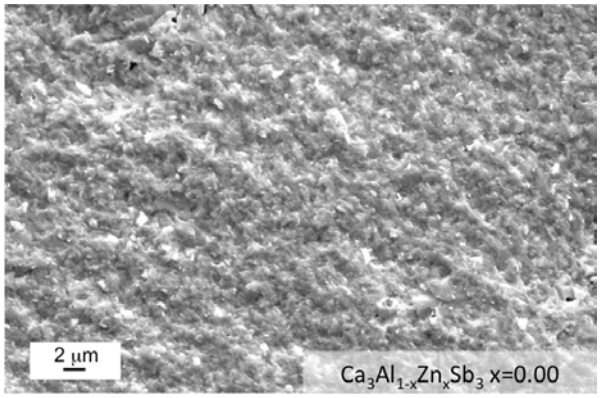

Figure 8.35: SEM micrograph of a fractured surface of $Ca_3Al_{1-x}Zn_xSb_3$ in secondary electron mode.

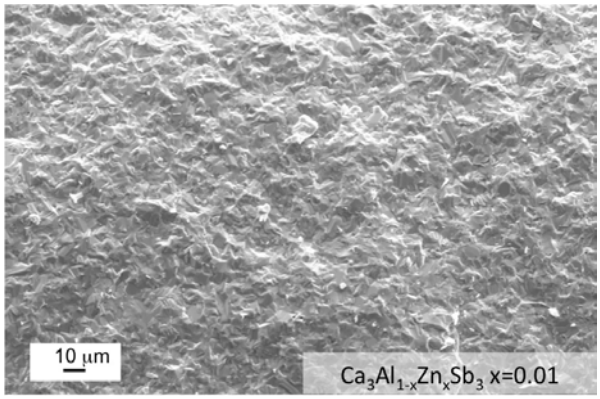

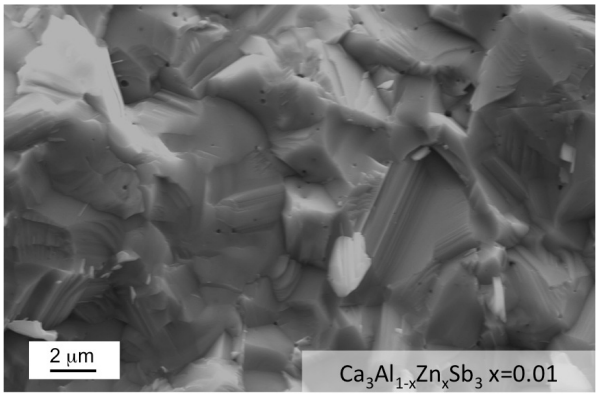

Figure 8.36: SEM micrographs of fractured surfaces of $Ca_3Al_{1-x}Zn_xSb_3$ in secondary electron mode.

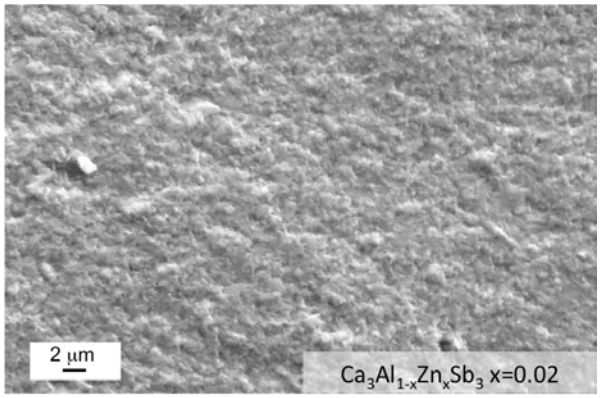

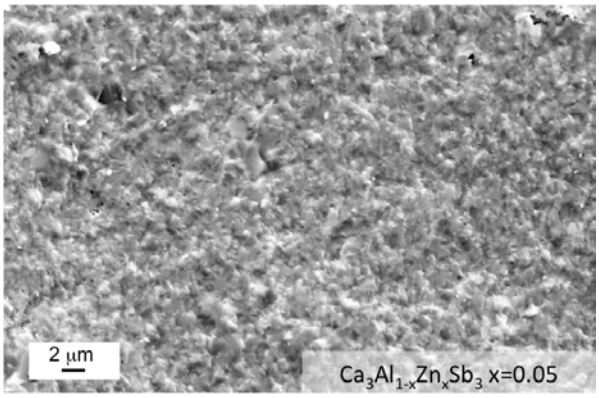

Figure 8.37: SEM micrographs of fractured surfaces of $Ca_3Al_{1-x}Zn_xSb_3$ in secondary electron mode.

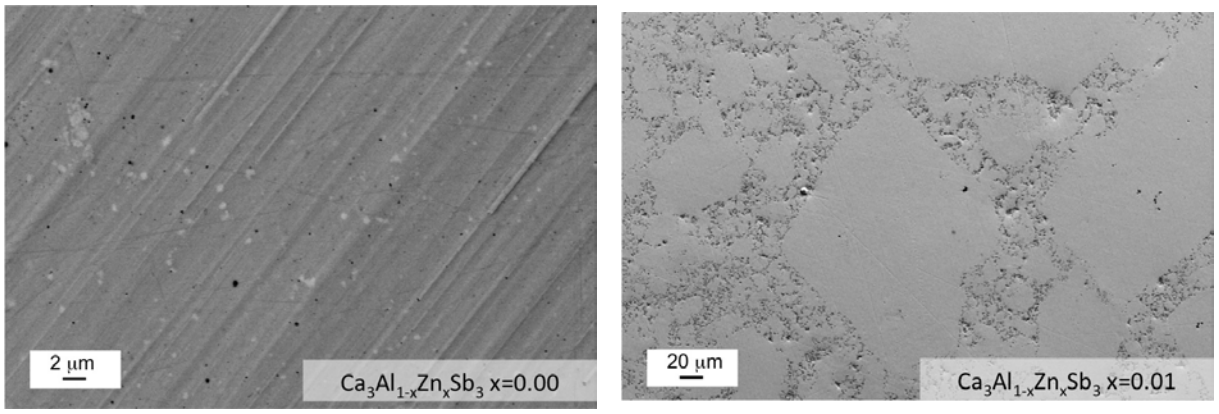

Figure 8.38: SEM micrographs of polished surfaces of $Ca_3Al_{1-x}Zn_xSb_3$ in secondary electron mode.

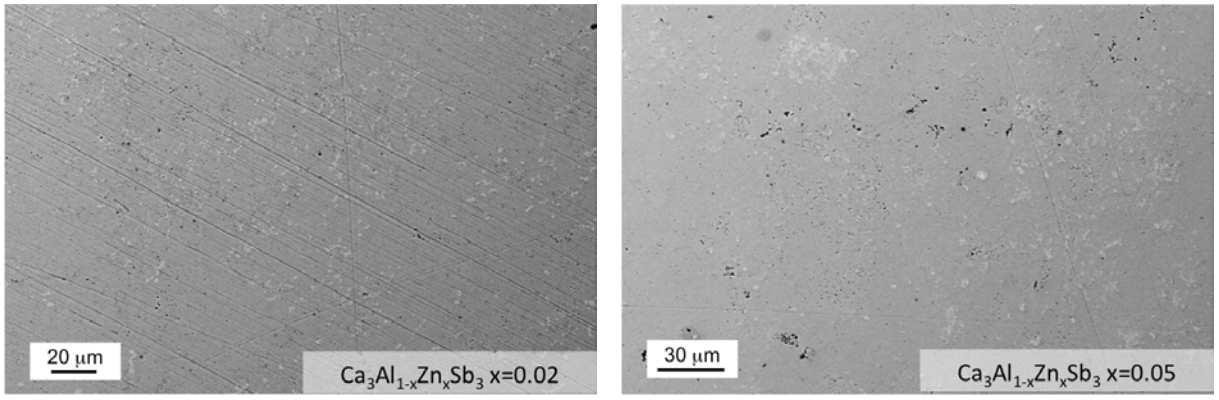

Figure 8.39: SEM micrographs of polished surfaces of $Ca_3Al_{1-x}Zn_xSb_3$ in secondary electron mode.

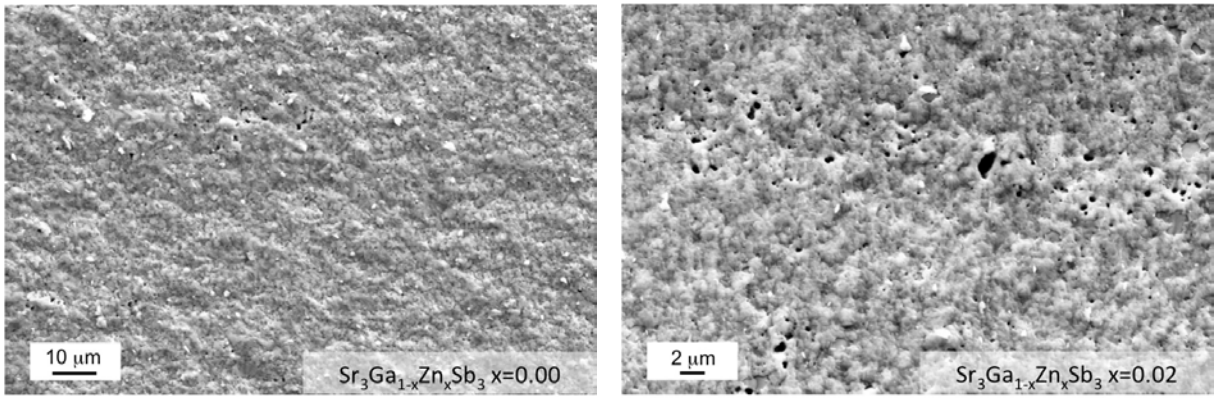

Figure 8.40: SEM micrographs of fractured surfaces of $Sr_3Ga_{1-x}Zn_xSb_3$ in secondary electron mode.

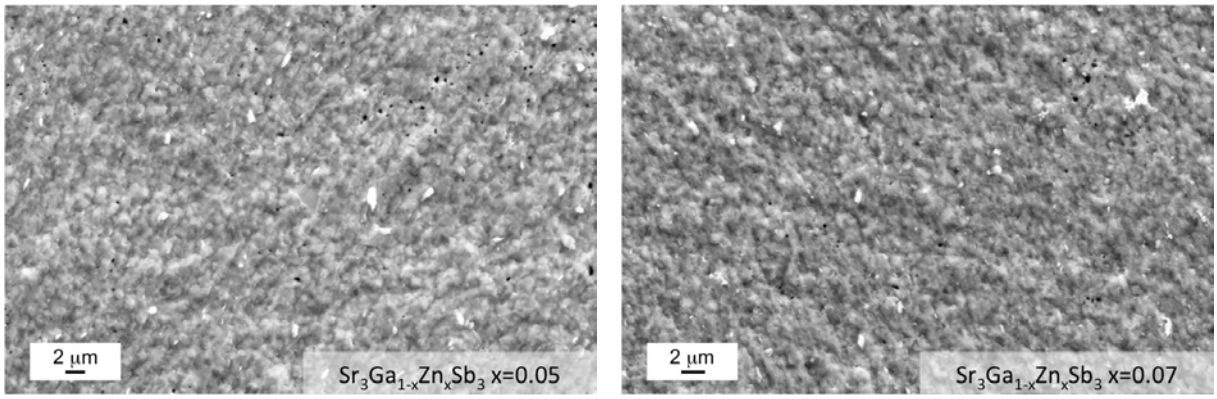

Figure 8.41: SEM micrographs of fractured surfaces of $Sr_3Ga_{1-x}Zn_xSb_3$ in secondary electron mode.

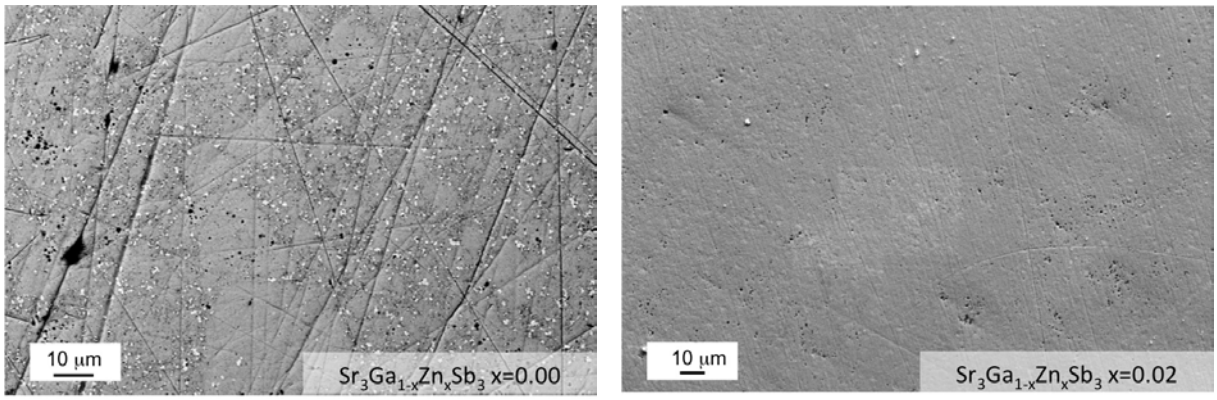

Figure 8.42: SEM micrographs of polished surfaces of $Sr_3Ga_{1-x}Zn_xSb_3$ in secondary electron mode.

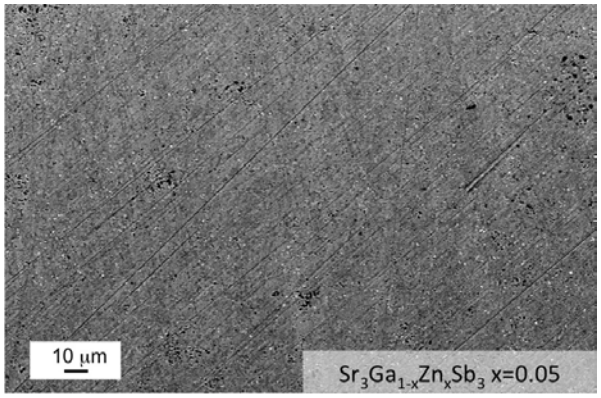

Figure 8.43: SEM micrograph of polished surfaces of $Sr_3Ga_{1-x}Zn_xSb_3$ in secondary electron mode.

8.3 Speed of Sound Data

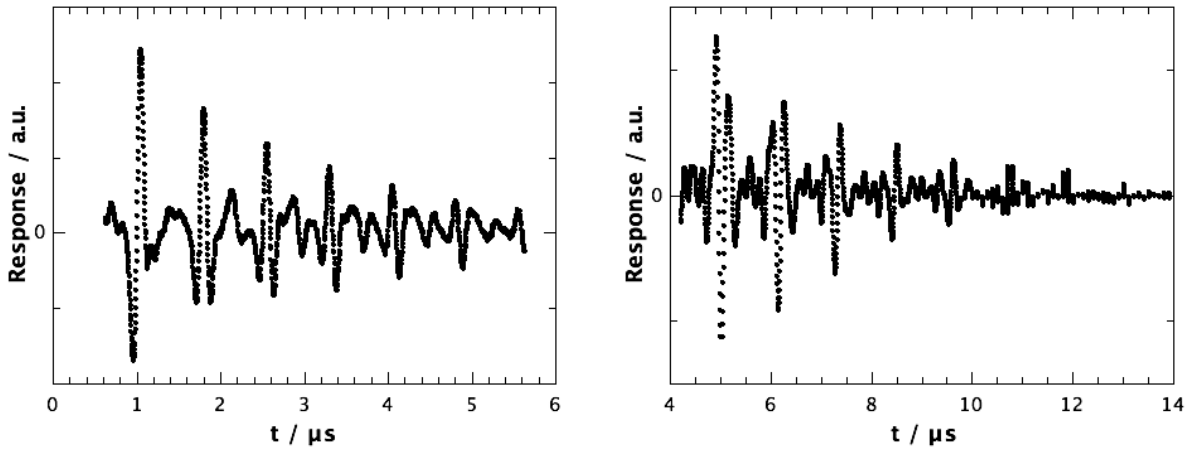

Figure 8.44: Respective longitudinal (left) and transverse (right) sound response data of an ultrasonic sound/response measurement of $Cu_2Zn_{0.5}Fe_{0.5}GeSe_4$.

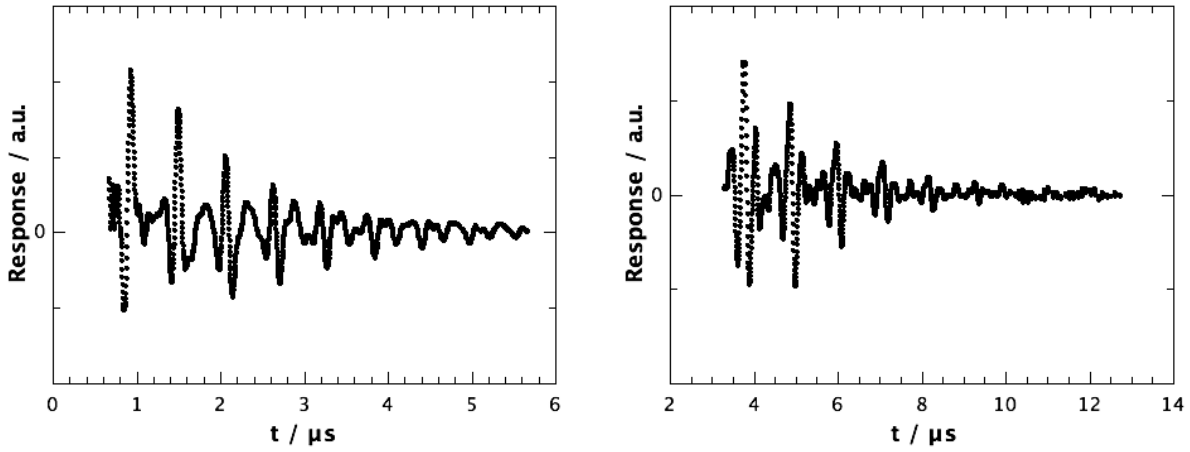

Figure 8.45: Respective longitudinal (left) and transverse (right) sound response data of an ultrasonic sound/response measurement of $Cu_2FeGeSe_4$.

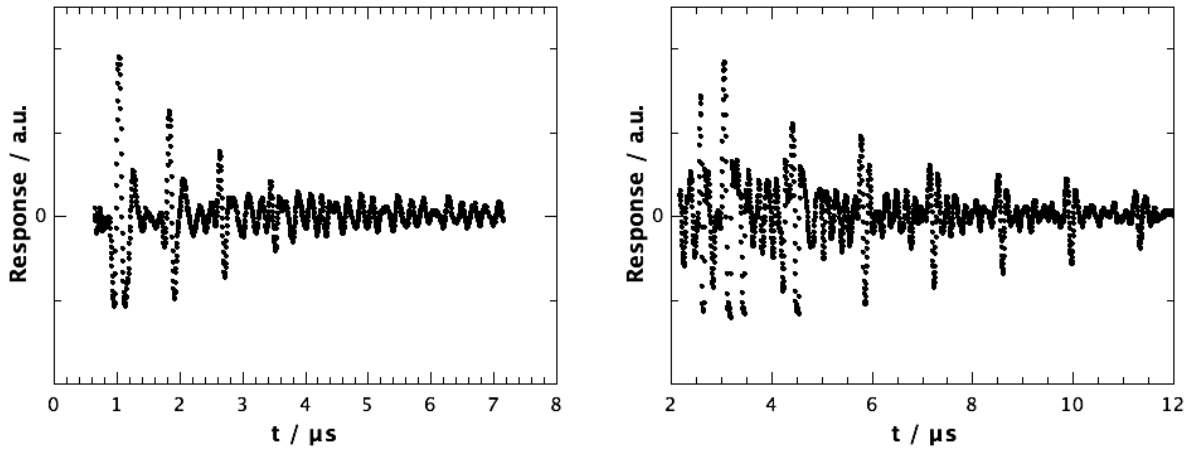

Figure 8.46: Respective longitudinal (left) and transverse (right) sound response data of an ultrasonic sound/response measurement of Ca_3AlSb_3.

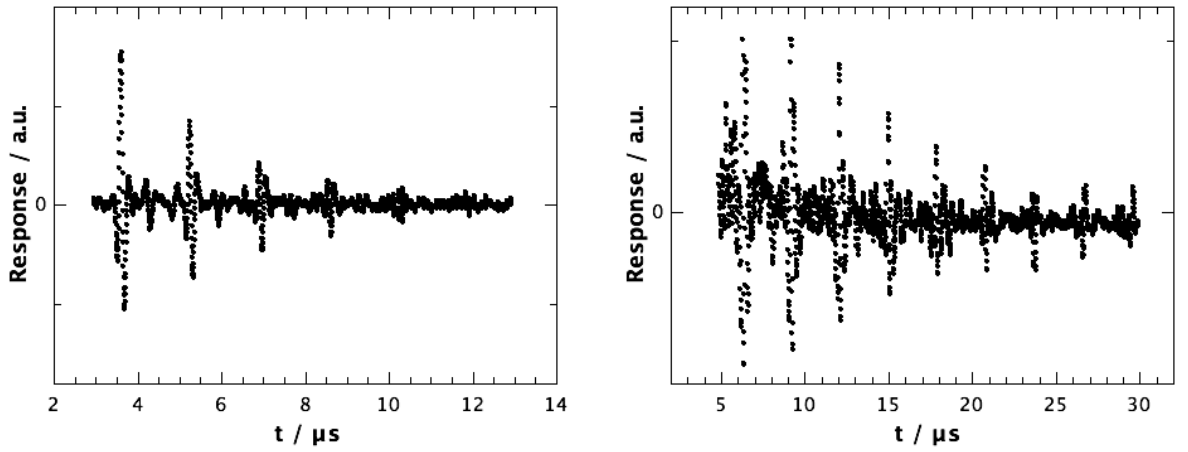

Figure 8.47: Respective longitudinal (left) and transverse (right) sound response data of an ultrasonic sound/response measurement of Sr_3GaSb_3.

8.4 Additional Transport Data

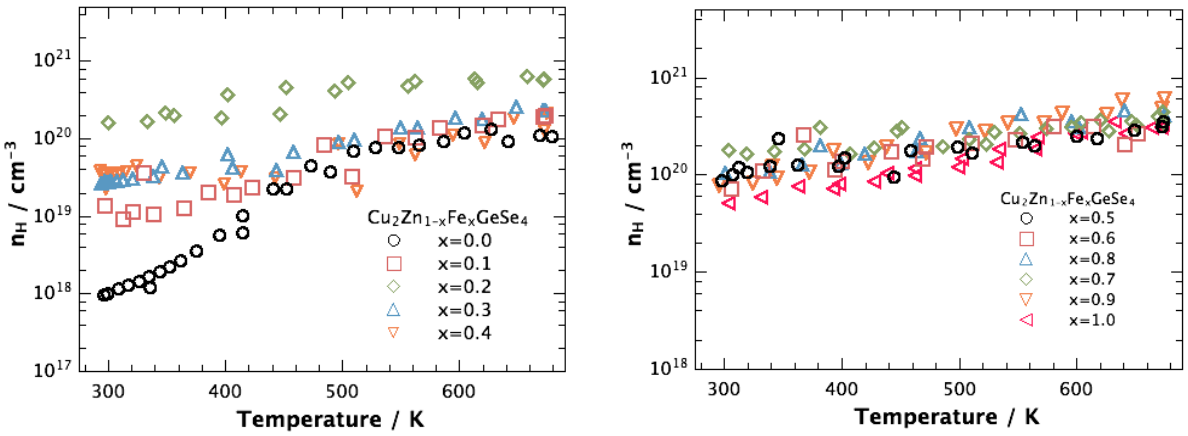

Figure 8.48: Temperature dependent Hall carrier concentrations n_H of $Cu_2Zn_{1-x}Fe_xGeSe_4$ for x = 0.0 - 0.4 (left) and x = 0.5 - 1.0 (right).

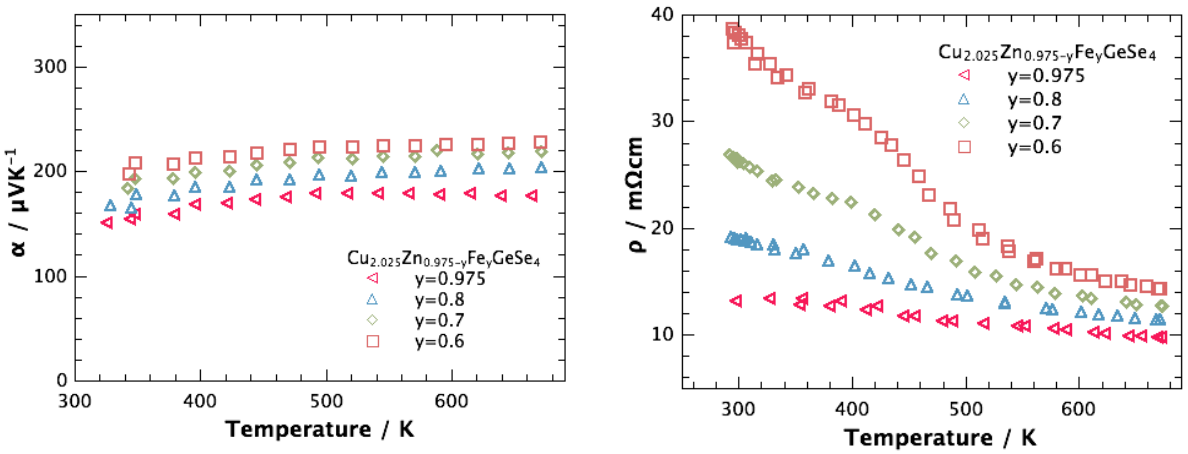

Figure 8.49: Temperature dependence of the Seebeck coefficients α (left) and resistivities ρ (right) of $Cu_{2.025}Zn_{0.975-y}Fe_yGeSe_4$.

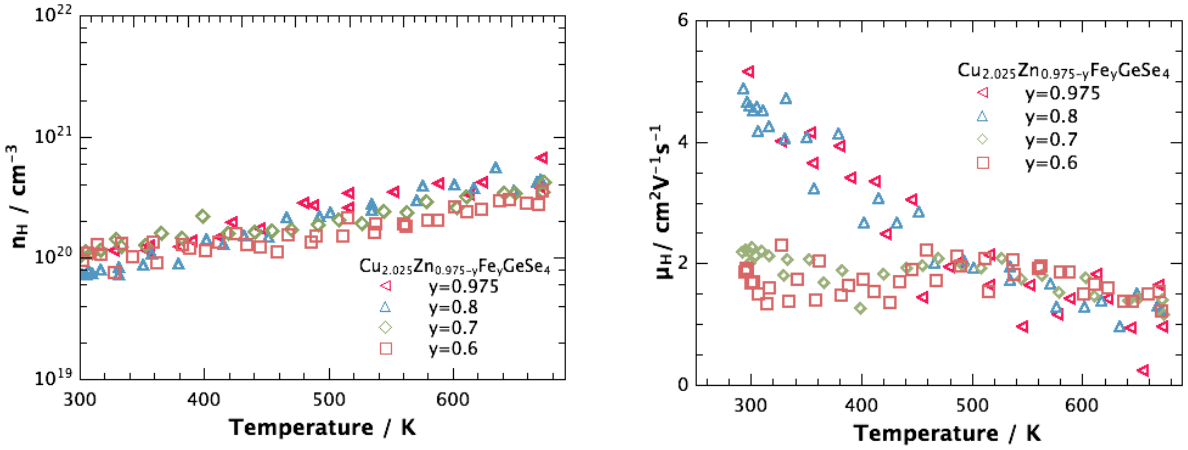

Figure 8.50: Temperature dependence of Hall carrier concentrations n_H (left) and Hall mobilities μ_H (right) of $Cu_{2.025}Zn_{0.975-y}Fe_yGeSe_4$.

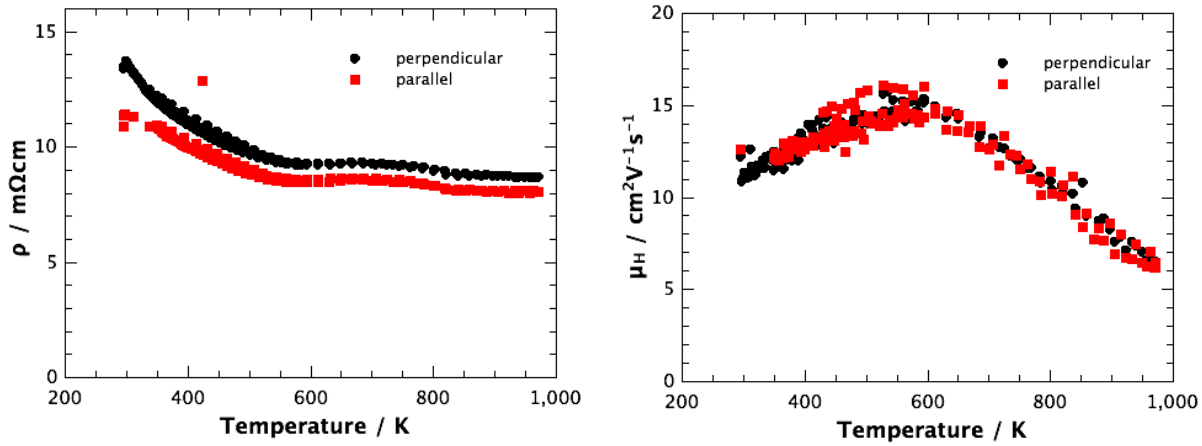

Figure 8.51: Resistivities ρ and Hall mobilities μ_H of $Sr_3Ga_{0.93}Zn_{0.07}Sb_3$ measured on disks cut in different directions (perpendicular and parallel to the hot pressing direction).

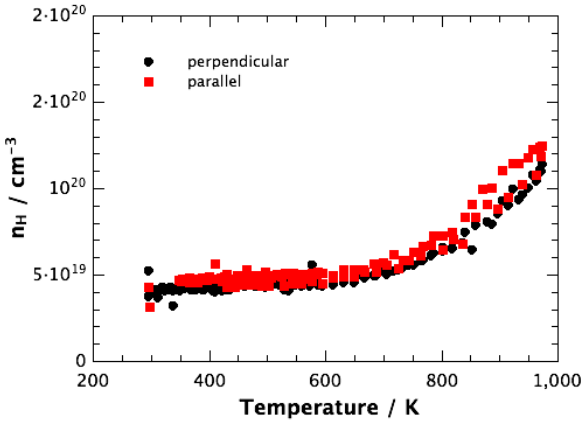

Figure 8.52: Hall carrier concentrations n_H of $Sr_3Ga_{0.93}Zn_{0.07}Sb_3$ measured on disks cut in different directions (perpendicular and parallel to the hot pressing direction)

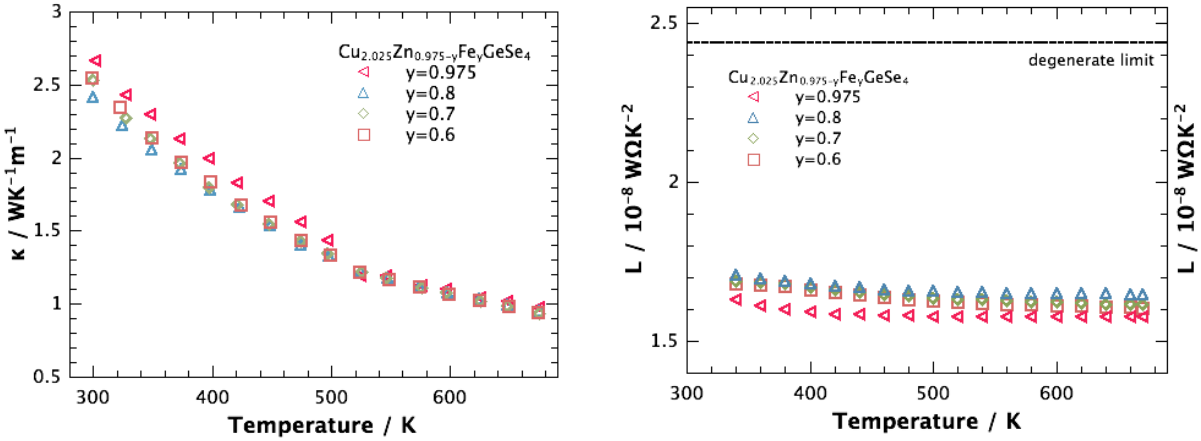

Figure 8.53: Temperature dependence of the total thermal conductivity κ (left) and Lorenz numbers L (right) of $Cu_{2.025}Zn_{0.975-y}Fe_yGeSe_4$.

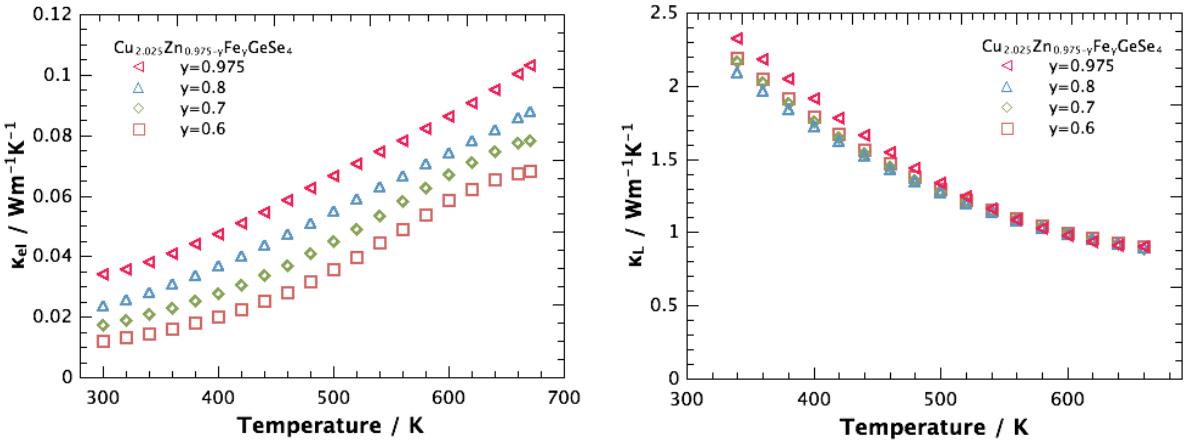

Figure 8.54: Temperature dependence of electronic thermal conductivity κ_{el} (left) and lattice thermal conductivity κ_L (right) of $Cu_{2.025}Zn_{0.975-y}Fe_yGeSe_4$.

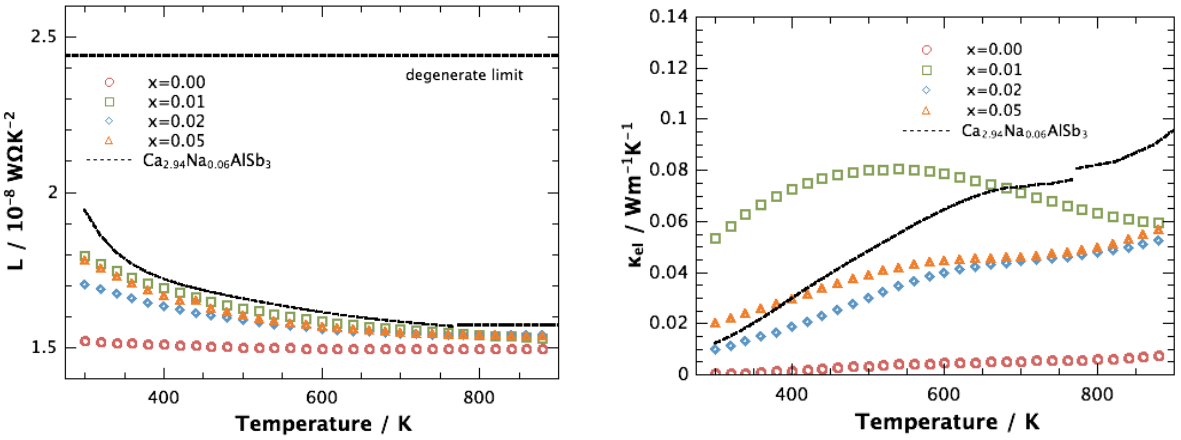

Figure 8.55: Temperature dependence of calculated Lorenz numbers (left) and electronic thermal conductivity κ_{el} (right) of $Ca_3Al_{1-x}Zn_xSb_3$.

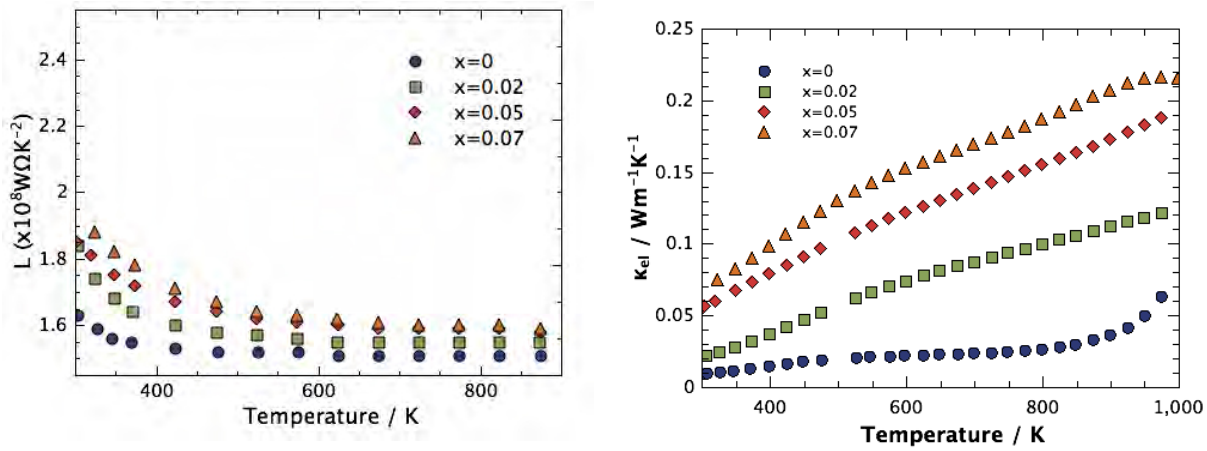

Figure 8.56: Temperature dependence of calculated Lorenz numbers L (left) and electronic thermal conductivity κ_{el} (right) of $Sr_3Ga_{1-x}Zn_xSb_3$.

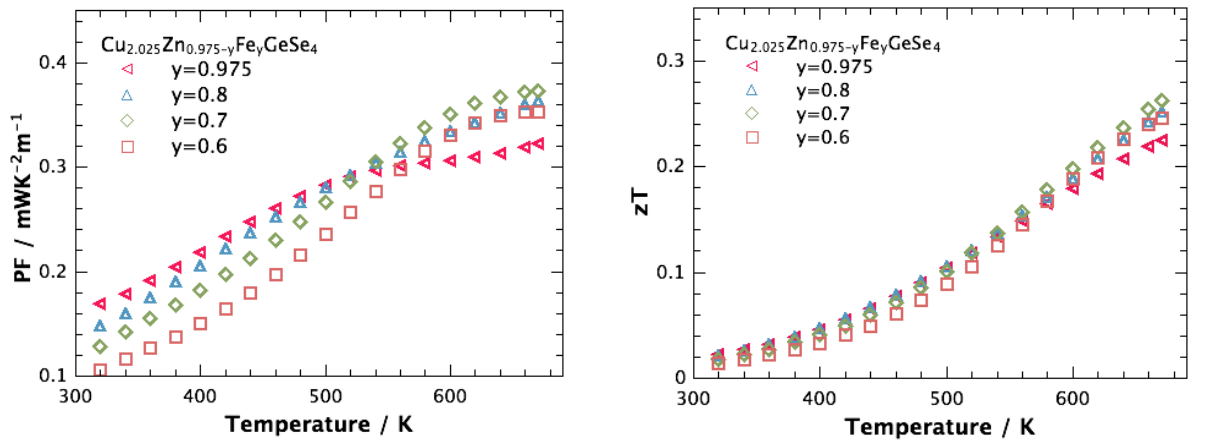

Figure 8.57: Temperature dependence of power factor (left) and figure of merit (right) of $Cu_{2.025}Zn_{0.975-y}Fe_yGeSe_4$.

8.5 Additional Pictures and Images

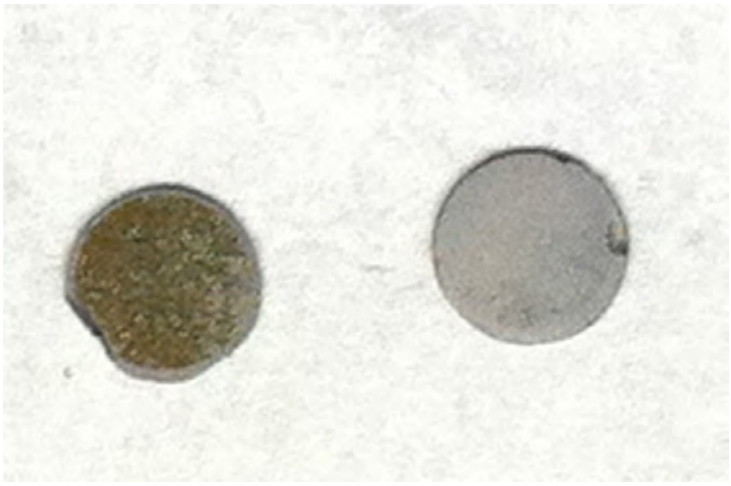

Figure 8.58: Surface of consolidated disks of $Cu_2ZnGeSe_4$ after a laser flash diffusivity measurement up to 723 K (left) and 673 K (right). Above 673 K significant evaporation of selenium takes place, resulting in the yellowish color of the ternary phases.

Bibliography

[1] DiSalvo, F. J. *Science* **1999**, *285*, 703–706.

[2] Bell, L. E. *Science* **2008**, *321*, 1457–1461.

[3] Snyder, G. J.; Toberer, E. S. *Nat. Mater.* **2008**, *7*, 105–114.

[4] Tritt, T. M.; Subramanian, M. A. *Mater. Res. Bull.* **2006**, *31*, 187–198.

[5] MacDonald, D. K. C. *Thermoelectricity - An Introduction to the Principles*; Dover Publications: London, 2006.

[6] Ziman, J. M. *Electrons and Phonons. The Theory of Transport Phenomena in Solids*; Oxford University Press: London, 1963.

[7] Ashcroft, N. W.; Mermin, N. D. *Solid State Physics*; Thomson Learning Inc.: United States of America, 1976.

[8] Wood, C. *Rep. Prog. Phys.* **1988**, *51*, 459–539.

[9] Goldsmid, H. J. *Thermoelectric Refrigeration*; Plenum Press: New York, 1964.

[10] Goldsmid, H. J. *Applications of Thermoelectricity*; Butler & Tanner Ltd: London, 1960.

[11] Rowe, D. M. In *Thermoelectrics Handbook: Macro to Nano*; Rowe, D. M., Ed., 2nd ed.; CRC Press: Boca Raton, 2006, Chapter 1.

[12] Zeier, W.; Panthöfer, M.; Janek, J.; Tremel, W. *Chem. Unserer Zeit* **2011**, 188–200.

[13] May, A. F. *Ph.D. Thesis*, California Institute of Technology, 2010.

[14] Goldsmid, H. J. *Introduction to Thermoelectricity*; Springer Verlag: Berlin, 2009.

[15] Snyder, G. J. *Electrochem. Soc. Interface* **2008**, *Fall*, 54–56.

[16] Snyder, G. J. *Appl. Phys. Lett.* **2004**, *84*, 2436–2438.

[17] Snyder, G. J. In *Thermoelectrics Handbook: Macro to Nano2006*; Rowe, D. M., Ed., 2nd ed.; CRC Press: Boca Raton, 2006, Chapter 9.

[18] LaLonde, A. D.; Pei, Y.; Wang, H.; Jeffrey Snyder, G. *Mater. Today* **2011**, *14*, 526–532.

[19] Toberer, E. S.; May, A. F.; Snyder, G. J. *Chem. Mater.* **2010**, *22*, 624–634.

[20] Eliott, S. R. *The Physics and Chemistry of Solids*; John Wiley & Sons: Chichester, 1998.

[21] May, A. F.; Snyder, G. J. In *Thermoelectrics Handbook: Thermoelectrics and its Energy Harvesting*; Rowe, D. M., Ed.; CRC Press: Boca Raton, 2012, Chapter 11.

[22] Mahan, G. D.; Sofo, J. O. *Proc. Natl. Acad. Sci.* **1996**, *93*, 7436–7439.

[23] Wang, H.; Pei, Y.; Lalonde, A. D.; Snyder, G. J. *Proc. Natl. Acad. Sci.* **2012**, *109*, 9705–9709.

[24] Pei, Y.; Wang, H.; Snyder, G. J. *Adv. Mater.* **2012**, *24*, 6125–6135.

[25] Pei, Y.; LaLonde, A. D.; Wang, H.; Snyder, G. J. *Energy Environ. Sci.* **2012**, *5*, 7963–7969.

[26] Pei, Y.; LaLonde, A.; Iwanaga, S.; Snyder, G. J. *Energy Environ. Sci.* **2011**, *4*, 2085–2089.

[27] Heremans, J. P.; Jovovic, V.; Toberer, E. S.; Saramat, A.; Kurosaki, K.; Charoenphakdee, A.; Yamanaka, S.; Snyder, G. J. *Science* **2008**, 554–557.

[28] Zhang, Q.; Wang, H.; Liu, W.; Wang, H.; Yu, B.; Zhang, Q.; Tian, Z.; Ni, G.; Lee, S.; Esfarjani, K.; Chen, G.; Ren, Z. *Energy Environ. Sci.* **2012**, *5*, 5246–5251.

[29] Jaworski, C.; Heremans, J. *Phys. Rev. B* **2012**, *85*, 033204.

[30] Nielsen, M.; Levin, E.; Jaworski, C.; Schmidt-Rohr, K.; Heremans, J. *Phys. Rev. B* **2012**, *85*, 045210.

[31] Pei, Y.; Shi, X.; LaLonde, A.; Wang, H.; Chen, L.; Snyder, G. J. *Nature* **2011**, *473*, 66–69.

[32] Liu, W.; Tan, X.; Yin, K.; Liu, H.; Tang, X.; Shi, J.; Zhang, Q.; Uher, C. *Phys. Rev. Lett.* **2012**, *108*, 166601.

[33] Callaway, J.; Baeyer, H. C. *Phys. Rev.* **1960**, *126*, 1149–1154.

[34] Yang, J.; Meisner, G. P.; Chen, L. *Appl. Phys. Lett.* **2004**, *85*, 1140–1142.

[35] Meisner, G.; Morelli, D.; Hu, S.; Yang, J.; Uher, C. *Phys. Rev. Lett.* **1998**, *80*, 3551–3554.

[36] Zhou, Z.; Uher, C.; Jewell, A.; Caillat, T. *Phys. Rev. B* **2005**, *71*, 235209.

[37] Alekseeva, G. T.; Efimova, B. A.; Ostrovskaya, L. M.; Serebryannikova, O. S.; Tsypin, M. I. *Soviet Physics - Semiconductors* **1971**, *4*, 1122–1125.

[38] Abeles B., *Phys. Rev.* **1963**, *131*, 1906–1911.

[39] Steigmeier, E.; Abeles B., *Phys. Rev.* **1964**, *136*, 1149–1155.

[40] Callaway, J. *Phys. Rev.* **1959**, *111*, 1046–1051.

[41] Zebarjadi, M.; Esfarjani, K.; Dresselhaus, M. S.; Ren, Z. F.; Chen, G. *Energy Environ. Sci.* **2012**, *5*, 5147–5162.

[42] Pei, Y.; Heinz, N. A.; LaLonde, A.; Snyder, G. J. *Energy Environ. Sci.* **2011**, *4*, 3640–3645.

[43] Pei, Y.; Lensch-Falk, J.; Toberer, E. S.; Medlin, D. L.; Snyder, G. J. *Adv. Funct. Mater.* **2011**, 241–249.

[44] Johnsen, S.; He, J.; Androulakis, J.; Dravid, V. P.; Todorov, I.; Chung, D. Y.; Kanatzidis, M. G. *J. Am. Chem. Soc.* **2011**, *133*, 3460–3470.

[45] Minnich, A. J.; Dresselhaus, M. S.; Ren, Z. F.; Chen, G. *Energy Environ. Sci.* **2009**, *2*, 466–479.

[46] Poudeu, P. F. P.; D'Angelo, J.; Downey, A. D.; Short, J. L.; Hogan, T. P.; Kanatzidis, M. G. *Angew. Chem. Int. Ed.* **2006**, *45*, 3835–3839.

[47] Slack, G. A. In *Handbook of Thermoelectrics*; Rowe, D. M., Ed.; CRC Press: Boca Raton, 1995, p 407.

[48] Sales, B.; Mandrus, D.; Williams, R. *Science* **1996**, *272*, 1325–1328.

[49] Nolas, G. S.; Poon, J.; Kanatzidis, M. G. *Mater. Res. Bull.* **2006**, *31*, 199–205.

[50] Shi, X.; Yang, J.; Salvador, J. R.; Chi, M.; Cho, J. Y.; Wang, H.; Bai, S.; Yang, J.; Zhang, W.; Chen, L. *J. Am. Chem. Soc.* **2011**, *133*, 7837–7846.

[51] Zebarjadi, M.; Esfarjani, K.; Yang, J.; Ren, Z.; Chen, G. *Phys. Rev. B* **2010**, *82*, 195207.

[52] Nolas, G.; Cohn, J.; Dyck, J.; Uher, C.; Yang, J. *Phys. Rev. B* **2002**, *65*, 165201.

[53] Toberer, E. S.; Christensen, M.; Iversen, B.; Snyder, G. *Phys. Rev. B* **2008**, *77*, 075203.

[54] May, A. F.; Toberer, E. S.; Saramat, A.; Snyder, G. J. *Phys. Rev. B* **2009**, *80*, 125205.

[55] Zeier, W. G.; LaLonde, A.; Gibbs, Z. M.; Heinrich, C. P.; Panthöfer, M.; Snyder, G. J.; Tremel, W. *J. Am. Chem. Soc.* **2012**, *134*, 7147–7154.

[56] Zeier, W. G.; Pei, Y.; Pomrehn, G.; Day, T.; Heinz, N. A.; Heinrich, C. P.; Snyder, G. J.; Tremel, W. *J. Am. Chem. Soc.* **2013**, accepted– DOI: 10.1021/ja308627v.

[57] Shi, X. Y.; Huang, F. Q.; Liu, M. L.; Chen, L. D. *Appl. Phys. Lett.* **2009**, *94*, 122103.

[58] Liu, M.-L.; Chen, I.-W.; Huang, F.-Q.; Chen, L.-D. *Adv. Mater.* **2009**, *21*, 3808–3812.

[59] Liu, M.-L.; Huang, F.-Q.; Chen, L.-D.; Chen, I.-W. *Appl. Phys. Lett.* **2009**, *94*, 202103.

[60] Sevik, C. *Appl. Phys. Lett.* **2009**, *95*, 112105.

[61] Schäfer, W.; Nitsche, R. *Mater. Res. Bull.* **1974**, *9*, 645–654.

[62] Guen, L.; Glaunsinger, W. *J. Solid State Chem.* **1980**, *35*, 10–21.

[63] Guen, L.; Glaunsinger, W.; Wold, A. *Mater. Res. Bull.* **1979**, *14*, 463–467.

[64] Schleich, D. M.; Wold, A. *Mater. Res. Bull.* **1977**, *12*, 111–114.

[65] Matsushita, H.; Ichikawa, T.; Katsui, A. *J. Mater. Sci.* **2005**, *40*, 2003 – 2005.

[66] Matsushita, H.; Maeda, T.; Katsui, A.; Takizawa, T. *J. Cryst. Growth* **2000**, *208*, 416–422.

[67] Quintero, E.; Tovar, R.; Quintero, M.; Morocoima, M.; Ruiz, J.; Delgado, G. *Physica B* **2002**, *320*, 384–387.

[68] Quintero, M. *Phys. Stat. Sol. (b)* **1998**, *209*, 135–143.

[69] Bernert, T.; Zabel, M.; Pfitzner, A. *J. Solid State Chem.* **2006**, *179*, 849–854.

[70] Gallardo, G.; Quintero, M.; Barreto, A.; Ruíz, J. *Adv. Mat. Sci & Tech.* **1998**, *1*, 01–12.

[71] Sachanyuk, V. P.; Fedorchuk, a. O.; Olekseyuk, I. D.; Parasyuk, O. V. *Phys. Stat. Sol. (b)* **2007**, *244*, 1288–1295.

[72] Sachanyuk, V. P.; Olekseyuk, I. D.; Parasyuk, O. V. *Phys. Stat. Sol. (b)* **2006**, *203*, 459–465.

[73] Todorov, T. K.; Reuter, K. B.; Mitzi, D. B. *Adv. Mater.* **2010**, *22*, E156–E159.

[74] Tanaka, K.; Fukui, Y.; Moritake, N.; Uchiki, H. *Sol. Energy Mater. Sol. Cells* **2010**, *95*, 838–842.

[75] Wang, K.; Shin, B.; Reuter, K. B.; Todorov, T.; Mitzi, D. B.; Guha, S. *Appl. Phys. Lett.* **2011**, *98*, 051912.

[76] Wei, H.; Ye, Z.; Li, M.; Su, Y.; Yang, Z.; Zhang, Y. *Cryst. Eng. Comm.* **2011**, *13*, 2222.

[77] Barkhouse, D. A. R.; Gunawan, O.; Gokmen, T.; Todorov, T. K.; Mitzi, D. B. *Prog. Photovolt: Res. Appl.* **2012**, 6–11.

[78] Green, M. A.; Emery, K.; Hishikawa, Y.; Warta, W.; Dunlop, E. D. *Prog. Photovolt: Res. Appl.* **2012**, 12–20.

[79] Schorr, S. *Thin Solid Films* **2007**, *515*, 5985–5991.

[80] Hall, S. R.; Ssymanski, J. T.; Stewart, J. M. *Can. Mineral.* **1978**, *16*, 131–137.

[81] Schorr, S.; Hoebler, H.-J.; Tovar, M. *Eur. J. Mineral.* **2007**, *19*, 65–73.

[82] Schorr, S. *Sol. Energy Mater. Sol. Cells* **2011**, *95*, 1482–1488.

[83] Bonazzi, P.; Bindi, L.; Bernardini, G. P.; Menchetti, S. *Can. Mineral.* **2003**, *41*, 639–647.

[84] Caldera, D.; Quintero, M.; Morocoima, M.; Quintero, E.; Grima, P.; Marchan, N.; Moreno, E.; Bocaranda, P.; Delgado, G.; Mora, A.; Briceño, J.; Fernandez, J. *J. Alloys Comp.* **2008**, *457*, 221–224.

[85] Zeier, W. G. *Diploma Thesis*, Johannes Gutenberg-University Mainz, 2010.

[86] Schäfer, H.; Eisenmann, B.; Müller, W. *Angewandte Chemie* **1973**, *85*, 742–760.

[87] Meyer, H.-J. In *Moderne Anorganische Chemie*; Riedel, E., Ed., 2nd ed.; Walter de Gruyter: Berlin, 2003, Chapter 3, pp 427–434.

[88] Müller, U. *Anorganische Strukturchemie*, 6th ed.; Teubner: Wiesbaden, 2008.

[89] Kauzlarich, S. M.; Brown, S. R.; Snyder, G. J. *Dalton Trans.* **2007**, *21*, 2099–2107.

[90] Toberer, E. S.; Brown, S. R.; Ikeda, T.; Kauzlarich, S. M.; Snyder, G. J. *Appl. Phys. Lett.* **2008**, *93*, 062110.

[91] Toberer, E. S.; Cox, C. A.; Brown, S. R.; Ikeda, T.; May, A. F.; Kauzlarich, S. M.; Snyder, G. J. *Adv. Funct. Mater.* **2008**, *18*, 2795–2800.

[92] Brown, S. R.; Kauzlarich, S. M.; Gascoin, F.; Snyder, G. J. *Chem. Mater.* **2006**, *18*, 1873–1877.

[93] Fisher, I.; Bud'ko, S.; Song, C.; Canfield, P.; Ozawa, T.; Kauzlarich, S. *Phys. Rev. Lett.* **2000**, *85*, 1120–1123.

[94] Gascoin, F.; Ottensmann, S.; Stark, D.; Haile, S. M.; Snyder, G. J. *Adv. Funct. Mater.* **2005**, *15*, 1860–1864.

[95] Zevalkink, A.; Toberer, E. S.; Zeier, W. G.; Flage-Larsen, E.; Snyder, G. J. *Energy Environ. Sci.* **2011**, *4*, 510–518.

[96] Zeier, W. G.; Zevalkink, A.; Schechtel, E.; Tremel, W.; Snyder, G. J. *J. Mater. Chem.* **2012**, *22*, 9826–9830.

[97] Cordier, G.; Schäfer, H.; Stelter, M. *Z. Naturforsch.* **1984**, *39b*, 727–732.

[98] Cordier, G.; Schäfer, H. *Angewandte Chemie* **1981**, *93*, 474.

[99] Cordier, G.; Schäfer, H.; Stelter, M. *Z. Naturforsch. B* **1987**, *42*, 1268–1272.

[100] Zevalkink, A.; Zeier, W. G.; Pomrehn, G.; Schechtel, E.; Tremel, W.; Snyder, G. J. *Energy Environ. Sci.* **2012**, *5*, 9121–9128.

[101] Slack, G. A. *Solid State Physics*, 34th ed.; Academic Press: New York, 1979.

[102] Toberer, E. S.; Zevalkink, A.; Snyder, G. J. *J. Mater. Chem.* **2011**, *21*, 15843–15852.

[103] Toberer, E. S.; May, A. F.; Melot, B. C.; Flage-Larsen, E.; Snyder, G. J. *Dalton Trans.* **2010**, *39*, 1046–1054.

[104] Wang, X. J.; Tang, M. B.; Chen, H. H.; Yang, X. X.; Zhao, J. T.; Burkhardt, U.; Grin, Y. *Appl. Phys. Lett.* **2009**, *94*, 092106.

[105] Cao, Q. G.; Zhang, H.; Tang, M. B.; Chen, H. H.; Yang, X. X.; Grin, Y.; Zhao, J. T. *J. Appl. Phys.* **2010**, *107*, 053714.

[106] Chakoumakos, B. C.; Sales, B. C.; Mandrus, D. G.; Nolas, G. S. *J. Alloys Comp.* **2000**, *296*, 80–86.

[107] LaLonde, A. D.; Ikeda, T.; Snyder, G. J. *Rev. Sci. Instrum.* **2011**, *82*, 025104.

[108] Cohelo, A. *TOPAS Academic V4.1*, 2004.

[109] Iwanaga, S.; Toberer, E. S.; LaLonde, A.; Snyder, G. J. *Rev. Sci. Instrum.* **2011**, *82*, 063905.

[110] Martin, J.; Tritt, T.; Uher, C. *J. Appl. Phys.* **2010**, *108*, 121101.

[111] Borup, K. A.; Toberer, E. S.; Zoltan, L. D.; Nakatsukasa, G.; Errico, M.; Fleurial, J.-P.; Iversen, B. B.; Snyder, G. J. *Rev. Sci. Instrum.* **2012**, *82*, 123902.

[112] Tritt, T. M. In *Thermoelectrics Handbook: Macro to Nano*; Rowe, D. M., Ed., 2nd ed.; CRC Press: Boca Raton, 2006, Chapter 23.

[113] Blaha, P.; Schwarz, K.; Madsen, G.; Kvasnicka, D.; Luitz, J. *WIEN2k: An Augmented Plane Wave plus Local Orbitals Program for Calculating Crystal Properties*; Institute of Physical and Theoretical Chemistry, TU Vienna, 2001.

[114] Perdew, J. P.; Burke, K.; Ernzerhof, M. *Phys. Rev. Lett.* **1996**, *77*, 3865–3868.

[115] Tran, F.; Blaha, P. *Phys. Rev. Lett.* **2009**, *102*, 226401.

[116] Koller, D.; Tran, F.; Blaha, P. *Phys. Rev. B* **2011**, *83*, 195134.

[117] Bernardini, G. P.; Bonazzi, P.; Corazza, M.; Corsini, F.; Mazzetti, G.; Poggi, L.; Tanelli, G. *Eur. J. Mineral.* **1990**, *2*, 219–225.

[118] Elbschütz, M.; Hermon, E.; Shtrikman, *J. Phys. Chem. Sol.* **1967**, *28*, 1633–1636.

[119] Cox, P. A. *The Electronic Structure and Chemistry of Solids*; Oxford University Press: New York, 1987.

[120] Whangbo, M.-H.; Canadell, E. *Chem. Rev.* **1991**, *91*, 965–1034.

[121] Hoffmann, R. *Angew. Chem.* **1987**, *99*, 871–906.

[122] Fistful, V. I. In *Heavily Doped Semiconductors*; Plenum Press: New York, 1969, Chapter 3, pp 77–202.

[123] Porras, A.; Quintero, M.; Barrios, R.; Gonzalez, J.; Tovar, R. *Phys. Stat. Sol. (b)* **1999**, *1067*, 1067–1073.

[124] Toberer, E. S.; Zevalkink, A.; Crisosto, N.; Snyder, G. J. *Adv. Funct. Mater.* **2010**, *20*, 4375–4380.

[125] Zevalkink, A.; Toberer, E. S.; Bleith, T.; Flage-Larsen, E.; Snyder, G. J. *J. Appl. Phys.* **2011**, *110*, 013721.

[126] Ravich, Y. I.; Efimova, B. A.; Smirnov, I. A. *Semiconducting Lead Chalcogenides*; Plenum Press: New York, 1970.

[127] Zunger, A. *Appl. Phys. Lett.* **2003**, *83*, 57–59.

[128] Petritz, R. L. *Phys. Rev.* **1956**, *104*, 15081516.

[129] Goldsmid, H. J.; Sharp, J. W. *J. Electron. Mater.* **1999**, *28*, 869–872.

[130] Yang, J. In *Thermal Conductivity-Theory, Properties and Applications*; Tritt, T. M., Ed.; Kluwer Academic / Plenum Publishers: New York, 2004, Chapter 1.1, pp 1–20.

[131] Murashov, V.; White, M. A. In *Thermal Conductivity-Theory, Properties and Applications*; Tritt, T. M., Ed., 1st ed.; Kluwer Academic / Plenum Publishers: New York, 2004, Chapter 1.3, pp 93–104.

[132] Roufosse, M.; Klemens, P. *Phys. Rev. B* **1973**, *7*, 5379.

[133] Blake, N. P.; Latturner, S.; Bryan, J. D.; Stucky, G. D.; Metiu, H. *J. Chem. Phys.* **2001**, *115*, 8060–8073.

[134] Züchner, H. *Vorlesungsmanuskript Statistische Thermodynamik*, Westfälische Wilhelms-Universität Münster, 1998.

[135] Göpel, W.; Wiemhöfer, H.-D. *Statistische Thermodynamik*; Spektrum Akademischer Verlag GmbH: Heidelberg, 2000; pp 204–210.

[136] Delaire, O.; May, A. F.; McGuire, M. A.; Porter, W. D.; Lucas, M. S.; Stone, M. B.; Abernathy, D. L.; Ravi, V. A.; Firdosy, S. A.; Snyder, G. J. *Phys. Rev. B* **2009**, *80*, 184302.

[137] Drabble, J. R.; Goldsmid, H. J. *Thermal Conduction in Semiconductors*; Pergamon Press: New York, 1961.

[138] Klemens, P. G. *Solid State Physics*, 7th ed.; Academic Press: New York, 1958.

[139] Soma, T. *Solid State Comm.* **1980**, *34*, 927–932.

[140] Dames, C.; Chen, G. In *Thermoelectrics Handbook: Macro to Nano*; Rowe, D. M., Ed.; CRC Press: Boca Raton, FL, 2006, Chapter 42.

[141] Ambegaokar, V. *Phys. Rev.* **1959**, *114*, 488–489.

[142] Klemens, P. G. *Proc. Phys. Soc.* **1955**, *68*, 1113–1128.

[143] Cahill, D.; Watson, S.; Pohl, R. *Phys. Rev. B* **1992**, *46*, 6131–6140.